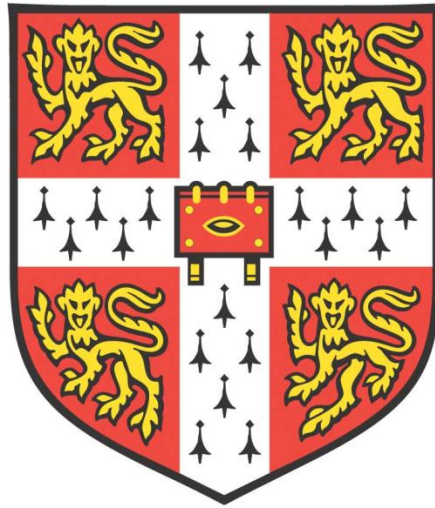


DIGITALLY ENABLED SURFACE FUNCTION
MODIFICATION FOR WIDE AREA
APPLICATIONS



James Macdonald

Darwin College

Department of Engineering

University of Cambridge

This dissertation is submitted for the degree of Doctor of Philosophy

March 2021

DECLARATION

This dissertation is the result of my own work and includes nothing, which is the outcome of work done in collaboration except where specifically indicated in the text. It has not been previously submitted, in part or whole, to any university or institution for any degree, diploma, or other qualification.

In accordance with the Department of Engineering guidelines, this thesis is does not exceed 65,000 words, and it contains less than 150 figures.

Signed:

[Signature redacted]

Date:

09/03/2021

James Macdonald

ABSTRACT

The aim of this work is to produce a digital manufacturing strategy to tailor surface wettability and control fluid deposition to the modified surfaces. The studies combine surface function modification by digitally enabled additive coatings with wide-area laser processing. Nano and femtosecond laser texturing have been used to modify surface topography and chemical functionality. Additive functional coating techniques included delivering materials by vapour transfer, laser induced reverse transfer and inkjet printing.

Laser texturing can be used to modify the wettability of stainless steel from complete water affinity (superhydrophilicity) to repulsion (superhydrophobicity). A focus of experiments was to explore the knowledge gaps around the chemical mechanism of hydrophobic transition after laser texturing. This allowed the development of a manufacturing approach to improve the acceleration of the time-consuming transition period and to produce surfaces with application-tailored superhydrophobic functionality. XPS analysis of surface chemistry produced new insight into the role of organic compound adsorption in the hydrophobic transition process.

The capability to produce a high level of control of surface wettability and understanding of the underpinning surface science is vital for inkjet printing to glass surfaces. Preconditioning surface treatments were investigated for inkjet deposition of functional material. An emerging industrial trend is the switch to 'green' water-based printing inks. However, the use of these inks poses challenges for functional material printing due to their properties such as high surface tension. Shadow masked corona discharge plasma and ultrafast laser ablation of glass were used for localised patterning of wettability which enabled precise control of fluid spreading on the glass surfaces. Another key industrial concern linked to surface energies is the durability of the printed deposits which was investigated through adhesion and abrasion experiments. Typically, conductive tracks printed to flat glass are rapidly removed by abrasion, by using a laser texturing pretreatment the deposit retained conductive properties after exposure to abrasion cycles.

Finally, a novel process of laser induced reverse transfer deposition of low resistivity material was developed. A recently developed capability of holographic phase contrast imaging at nanosecond temporal resolution was used to report the morphology of the confined ablation plume during material transfer and patterning. This revealed previously unobserved phenomena such as the influence of the rebounding pressure wave and the longer plasma lifetime of a confined plume of 230 μs compared to 125 μs for the unconfined case. This showed the importance of plume shielding and incubation effects for applications. 3 common conductive materials: silver, graphite and copper, were tested to assist with materials selection. Silver and graphite were shown to produce conductive deposits with resistivities of 0.03 $\mu\Omega\text{ m}$ and 340 $\mu\Omega\text{ m}$ respectively.

ACKNOWLEDGEMENTS

I would first like to thank my supervisor Dr Ronan Daly, without whom this work would not be possible. His guidance and support over the past four years has inspired and nurtured the ideas which form this thesis.

Thanks go to Dr Cristina Rodriguez-Rivero, Susannah Evans and Dr Niamh Fox for their assistance with laboratory characterisation. I would like to thank Pete Atkin, Jack Cook, Dr Jason Ten, Dr Martin Sparkes and Prof Bill O'Neill from the Centre for Industrial Photonics for their assistance with laser processing experiments. Dr Weiwei Li, Dr Adam Brown and Dr Carmen Fernandez Posada for their assistance with XPS measurements. Paul Warren and Su Varma from Pilkington NSG for their guidance and support. Dr Alexandra Rutz and Dr Chris Truscott for their guidance with wettability characterisation. Dr Jack Alexander Webber and Sammi Mahdi for their assistance with electrical characterisation. Dr Richard Langford and Eric Tapley for help with electron microscopy experiments. Dr Ainara Rodriguez, Dr Aldara Pan Cabo and Julen Azkona from the laser manufacturing research group at CEIT for hosting me during a research visit.

During the 2nd year of the PhD programme I co-supervised an MRes student Henry De Fossard on a 4 month mini project I proposed entitled 'Laser Induced Transfer of Graphite'. I was directly involved with the planning, execution of experiments and analysis of results. Nadeem Gabbani assisted in setting up the holographic camera imaging system. Dr Krste Pangovski provided the analysis code to interpret the captured data. Henry De Fossard carried out the experiments and processed the data as part of the project noted above.

The research into laser processed superhydrophobic surfaces continued from an MRes long project 'Wide Area Laser Manufacturing of Self Cleaning Surfaces'. I would like to thank Adam Rosowski from SPI Lasers and Richard Segar from Thurne for helping to develop this aspect of the research.

I acknowledge funding support from EPSRC, Centre for Doctoral Training in Ultra-Precision Engineering, Centre for Doctoral Training in Nanotechnology, The Worshipful Company of Engineers and Pilkington NSG.

My time at the Institute for Manufacturing and in the research community at Cambridge University has been an incredibly interesting and enriching experience. I'd like to thank those who have contributed to this including all of the Fluids in Advanced Manufacturing research group, the committee members I worked with at Cambridge University Nanotechnology Society, collaborators at BluSci Technology magazine and the many fellow punting enthusiasts of Darwin College.

Finally, I would like to thank my family who have always been there for support and guidance.

RESEARCH OUTPUTS

Publications Resulting From This Work

- J.Macdonald, H.Fossard, N.Gabbani, W.O'Neill, R.Daly. (2020). Material ejection dynamics in direct-writing of low resistivity tracks by laser-induced reverse transfer. *Applied Surface Science*. <https://doi.org/10.1016/j.apsusc.2020.147924>
- J. Macdonald, C.Rodriguez-Rivero, A.Rodriguez, Ronan Daly. (2021) Direct Write Laser Surface Wettability Modification for Fluidic Manufacturing Processes. *Proc. SPIE. 11674-27, Laser-based Micro- and Nanoprocessing XV. Submitted.*
- J.Macdonald, A.Rodriguez, R. Daly. Hydrophobic agent adsorption dynamics of laser textured superhydrophobic metallic surfaces. *In preparation.*

Other Publications

- Ong Hui Chong, J., Zhao, J., Levy, G. K., Macdonald, J., Justin, A. W., & Markaki, A. (2020). Functionalisation of a heat-derived and bio-inert albumin hydrogel with extracellular matrix by air plasma treatment.. *Scientific reports*, 10 (1), 12429. <https://doi.org/10.1038/s41598-020-69301-7>
- Ding, L., Joshi, P., Macdonald, J., Parab, V., Sambandan, S., Self-Healing Thin-Film Transistor Circuits on Flexible Substrates. *Advanced Electronic Materials*. 2021, 2001023. <https://doi.org/10.1002/aelm.202001023>
- Y. Shams, C. Durkan, J.Ten, D.Copic, J.Macdonald, M.Sparkes & R. Daly. (2021). Direct-Write technology to digitally tune nano-catalyst for CNT architectures. *In preparation*

To disseminate the industrial focus of my PhD I have contributed to press release publications with my industrial sponsor in magazines such as The Manufacturer and other trade journals

- <https://www.themanufacturer.com/articles/exploring-technologies-for-customisation-at-scale/>
- <https://www.pilkington.com/en-gb/uk/news-insights/latest/nsq-group-and-university-of-cambridge-sowing-seeds-for-future-glass-applications>

Conference Presentations

- Digitally-enabled surface function modification for wide area applications. *Institute for Manufacturing First Year PhD Conference. May 2018*

- Biomimetic surface engineering: manufacturing functional surfaces using digital processing technologies *Darwin College Science and Technology Seminar Series, University of Cambridge*. **Nov 2018**
- Taming the chemical transition of laser processed superhydrophobic surfaces *Laser-based Micro- and Nanoprocessing, SPIE Photonics West*. **Feb 2019**
- Surface Reorganisation of Atoms & Molecules. *Nanophotonics Winter School, Montafon*. **Mar 2019**
- Laser Induced Reverse Transfer of Functional Micropatterns. *Lasers In Manufacturing, World of Photonics Congress*. **Jun 2019**

CONTENTS

1	INTRODUCTION.....	1
1.1	TECHNOLOGY TRENDS IN SURFACE MODIFICATION	1
1.2	SURFACE FUNCTIONALITIES IN THE STEEL AND GLASS INDUSTRIES	2
1.3	DIGITAL FABRICATION TECHNOLOGIES - EMERGENCE AND INDUSTRIAL ADOPTION ..	7
1.4	RESEARCH AIMS	11
1.5	THESIS OUTLINE	12
2	EXPERIMENTAL TOOLS AND ANALYTICAL TECHNIQUES	13
2.1	MATERIALS.....	13
2.2	LASER PROCESSING	14
2.3	INKJET PRINTING	15
2.4	CHARACTERISATION.....	16
3	EFFECT OF LASER PARAMETERS ON SURFACES	20
3.1	CHAPTER INTRODUCTION	20
3.2	DESIGN OF EXPERIMENTS	32
3.3	METHOD	33
3.4	RESULTS AND DISCUSSION	36
3.5	CONCLUSION.....	49
4	PROGRESS IN FUNDAMENTAL UNDERSTANDING OF LASER TEXTURING FOR SUPERHYDROPHOBICITY.....	51
4.1	CHAPTER INTRODUCTION	51
4.2	LITERATURE REVIEW.....	51
4.3	DESIGN OF EXPERIMENTS	59
4.4	EXPERIMENTAL APPROACH AND METHODOLOGY	60
4.5	RESULTS AND DISCUSSION	62
4.6	CONCLUSION.....	78
5	WETTABILITY MODIFICATION OF GLASS FOR INKJET DEPOSITION OF FUNCTIONAL MATERIAL.....	80
5.1	INTRODUCTION	80
5.2	LITERATURE REVIEW.....	81
5.3	DESIGN OF EXPERIMENTS	94
5.4	METHOD	95
5.5	RESULTS & DISCUSSION	99
5.6	CONCLUSION.....	120
6	LASER INDUCED REVERSE TRANSFER OF FUNCTIONAL MATERIAL	122
6.1	INTRODUCTION	122
6.2	LITERATURE REVIEW	123
6.3	DESIGN OF EXPERIMENTS	129
6.4	EXPERIMENTAL APPROACH AND METHODOLOGY	130
6.5	RESULTS AND DISCUSSION	132

6.6	CONCLUSION.....	150
7	RESEARCH OUTCOMES AND FUTURE WORK	152
7.1	RESEARCH OUTCOMES	152
7.2	FUTURE WORK	154
8	REFERENCES	157
	APPENDIX A	182
	A1 - LIPSS HATCH SPACING	182
	A2 - IN-VOLUME MODIFICATION	182
	APPENDIX B	183
	B1 - HEAT TREATMENT	183
	B2 - TERMINAL GROUP VARIANCE.....	183
	B3 - CHAIN LENGTH VARIANCE	184
	B4 - DEPOSITION OF 1-OCTANOIC ACID	185

LIST OF ABBREVIATIONS AND ACRONYMS

2D	2 Dimensional
3D	3 Dimensional
CAD	Computer-Aided Design
DLT	Direct Laser Texturing
EDX	Energy Dispersive X-Ray Spectroscopy
HAZ	Heat Affected Zone
IPA	Isopropanol
LIFT	Laser Induced Forward Transfer
LIPSS	Laser Induced Periodic Surface Structures
LIRT	Laser Induced Reverse Transfer
NA	Numerical Aperture
OM	Optical Microscopy
PDMS	Polydimethylsiloxane
Ra	Average Roughness
Rt	Total Profile Height
SEM	Scanning Electron Microscopy
TRL	Technology Readiness Level
UV	Ultraviolet
WLI	White Light Interferometry
XPS	X-Ray Photoelectron Spectroscopy

1 INTRODUCTION

The research presented in this thesis focuses on developing digital, non-contact techniques for tuning or patterning surface functionality on glass and steel surfaces. The work builds the underpinning knowledge around a range of techniques while also examining their suitability for scaling to an industrially relevant environment. Here, the motivation for this work is introduced by describing the trends in technologies and targeted functionalities that have led to a broad industrial interest in this topic. This is followed by the research objectives and the structure of the thesis that will present findings for each objective.

1.1 Technology trends in surface modification

Many ancient civilisations made their early experiments in technology through modification of engineering surfaces. Archaeological remains have shown that the Mycenaean Greeks used cooking equipment covered with fine holes to provide a non-stick surface for bread baking [1]. The first written evidence of thermal treatment to improve the toughness and strength of metal weapons dates from 880 B.C in Homer's *Odyssey* dating to 1400-1200 B.C [2].

Society has also long recognised functional surfaces produced in the natural world. The 2000 year old Hindu religious text the *Bhagavad Gita* documents the self-cleaning lotus leaf; a biological surface exhibiting a naturally superhydrophobic surface wettability [3]. Studying these surfaces and surface interaction has historically been limited by technology. In 1876 Worthington was able to progress the studies of patterns of liquid drops upon impact through direct observation with the naked eye using the technique of spark illumination to freeze the image [4]. The intensive research efforts in 20th and start of the 21st century have engendered discovery and adoption of functional surfaces. In 1965 the first commercial SEM was sold by the Cambridge Scientific Instrument Company, and by 1977 the nanoscale structure underpinning the self-cleaning superhydrophobicity of the lotus leaf had been discovered using an SEM [5]. A commonly used non-stick coating Teflon was accidentally discovered by a research chemist at DuPont in 1938 [6], only 6 years later DuPont were producing and selling over 900 tons of Teflon annually.

The future of engineered, functional surfaces brings both challenges which motivate research, and opportunities enabled by new engineering capabilities. There are a wide range of trends driving research in this area, with a few examples including:

- It is estimated that by 2025, 1.8 billion people will have scarce access to water [7]. This will drive the growth in demand for water efficient technologies, such as self-cleaning surfaces.
- Wang's law for the display industry [8] describes the display panel performance doubling every 36 months for a given price point. This is anticipated to involve significant manufacturing innovation involving advanced fluid manufacturing techniques to engineer surfaces.
- It is estimated that the average UK citizen owns 15 internet connected devices [9]. This is growing dramatically in the industrial space also, and drives demand for surfaces engineered with embedded electronics and smart, responsive or functional capabilities.

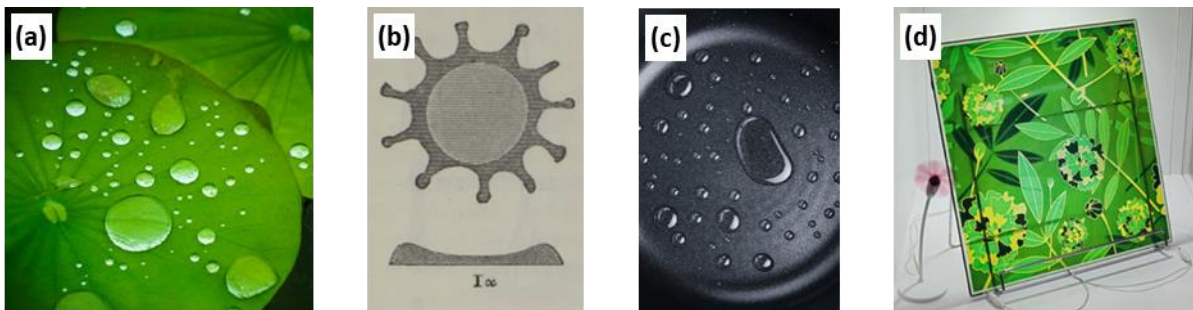


Figure 1.1: (a) The lotus leaf was revered in ancient Hindu society for its superhydrophobic self-cleaning properties. (b) Scientific research into fluid surface interaction [4] has enabled new products such as non-stick cookware (c). (d) Printing to surfaces may enable customisation of glass products with devices such as embedded solar cells as demonstrated in this prototype solar-window pane [10]. While the trends are clearly very broad, covering many sectors and materials, this thesis focuses on research in the functionalising of steel and glass, which will be introduced in the next section.

1.2 Surface functionalities in the steel and glass industries

This section aims to illustrate the market ‘pull’ factors and motivation for the research into new production technologies in the stainless-steel and flat glass industries. The history and current challenges in manufacturing and business have important implications for technology innovation and development. The markets for stainless steel and flat glass are established and the major processes used in modern production were defined during the 20th century. The business networks involved are now colossal and globally distributed with significant macroeconomic implications and dependencies. Figure 1.2 shows the global market share for stainless steel [11] and flat glass [12] by application. A theme in the 21st century has been the depression of the steel and glass industries with the migration of these markets to lower cost Asian producers. In response to this trend [13], two available strategies for Western producers are to:

- Reduce manufacturing costs, potentially through automation and energy efficiency
- Offer products with unique selling points and advanced functionalities

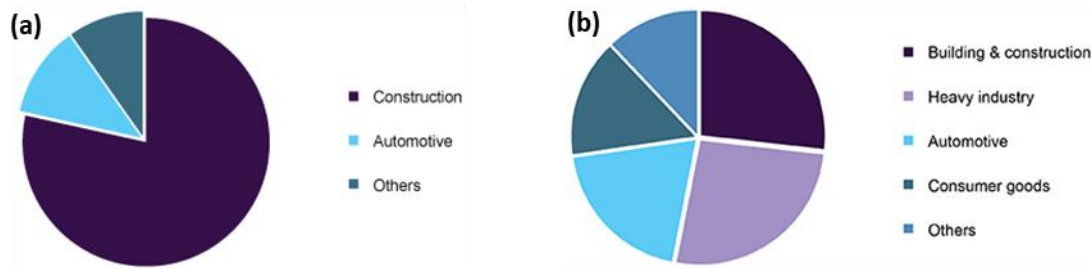


Figure 1.2 (a) Sectors of stainless steel industry [11], (b) Sectors of flat glass industry [12]

Stainless steel can be considered first, to show an example of a market ‘pull’ effect. In 2016, the global stainless-steel market was valued at \$85bil with a predicted annual growth rate of 5.2% over the following ten years [11]. The market for stainless steel is split into a diverse set of applications with major segments involving construction, heavy industry and automotive. Stainless steel is selected for use due to a range of properties including manufacturability, toughness and corrosion resistance. The first major commercial application of stainless steel was between the years of 1919-1923 as a replacement of carbon steel to produce surgical scalpels, cutlery and tools [14]. Today in the food processing industry stainless steel is widely used due to its resistance to corrosion and ease of cleaning. However, in even a medium size dairy production facility cleaning can typically cost £1m per year with this cost majorly composed of lost production time, labour, water and energy consumption. This provides commercial impetus to develop functionalised materials which further reduce the high cost and resource usage of cleaning [15], for example self-cleaning food-grade materials.

Glass can be considered for a second example of a market ‘pull’ effect. Glass making is an ancient technology, with the first cast glass used by the Romans dating to 100 AD [16]. The invention of the float glass production process in 1952 allowed highly flat glass to be produced, modern capabilities of float glass production allow for thicknesses of 0.4-25 mm with widths of up to 3 metres [12]. There are around 260 float glass production lines globally producing a combined output of about 800,000 tonnes per week [17]. Additional manufacturing techniques involve rolled glass to make patterned or wired security glass, and fusion drawing to make ultra-thin glass for smart phone displays. The major sectors for glass manufacturing are in the construction and automotive sectors where glass is selected for its high toughness and transparency. Emerging markets involve applications in solar energy and display technology. The global flat glass market size was estimated to be \$82.2 bn in 2016 with a predicted annual growth rate of 7.1% up to 2025. Although segments such as vehicle building are expected to show consistent long term growth [18], the European automotive market is depressed

following the 2008 financial crisis and has lost overseas trade to cheaper Asian producers. There is significant potential for UK & European producers to offer advanced functionalities on glass following promising developments in responsive ‘smart’ glass and self-cleaning glass [13]. This is driving research into local, digital technologies for delivering electronics or surface chemistry control on commercial glass surfaces. In the cases of stainless steel and glass there are clear drivers towards self-cleaning and also integration of electronics or devices, which will be explored briefly in the next subsections.

1.2.1 Manufacture of superhydrophobic self-cleaning surfaces

Nature abounds with examples of surfaces which have adapted wetting functionalities to prosper in their natural environment, from widely disseminated examples such as the self-cleaning superhydrophobic lotus leaf [5] or lesser researched examples such as the water directing grooves of the rice leaf [19] or wetland insects who trap pockets of air for underwater respiration [20].

Superhydrophobicity can be described as an extreme state of surface wettability where aqueous liquid cannot adhere to the surface but instead is freely mobile, exhibiting both a high sessile contact angle ($>150^\circ$) and low roll off angle ($<10^\circ$). The theory which explains this property is outlined in section 2.4.4 Here, the fabrication approaches to make superhydrophobic surfaces are briefly noted and opportunities for research using digital manufacturing approaches are outlined.

Superhydrophobic surfaces have attracted significant research attention since the first publications which explored artificially reproducing its effect in the late 1990s [21]. The superhydrophobic property requires the combination of both a low surface energy chemistry and a rough surface structure. This combination is essential, as for a perfectly flat surface the most hydrophobic contact angle possible is 120° which was demonstrated experimentally based on surface chemistry consisting of hexagonal packed $-\text{CF}_3$ groups [22].

Most procedures for superhydrophobic surface fabrication involve single step roughening of a low surface energy material or inducing a surface roughness either additively or subtractively which is then coupled with a hydrophobic chemical treatment [23]. One example of roughening a low surface energy material is sand blasting of PTFE [24]. This low-cost approach was demonstrated to have a fast-areal modification rate and effective superhydrophobicity. However, it is inherently limited to specific materials such as fluorinated polymers, which brings limitations for some engineering applications. Metal and glass surfaces are not suitable for direct roughening because their chemistry is intrinsically polar and therefore hydrophilic. Modification of the surface roughness with the addition of chemical deposition has been shown through anodising [25] and plasma treatment [26]. Laser

ablation is to-date the only process in which both roughening and chemical transformation can be achieved in a single processing step [27,28].

Mature additive superhydrophobic modification approaches have involved sol-gel silica coatings [29], solution deposition of hydrophobically functionalised nanoparticles [30] and gas phase chemical vapour deposition of nanostructured coatings [31]. Overall, there has been a significant progression in the research field from initial exploratory laboratory demonstrations to low cost, scalable manufacturing methods [23]. Commercial spray applied self-cleaning coatings are available as consumer goods for products such as clothing, domestic appliances, automotive and architectural glass [32–34]. However, the use of fluorinated chemicals has serious safety and environmental concerns due to their aerosol application and degradation [35]. A recent investigation by the UK government's health and safety executive found significant evidence of health concerns associated with lung inflammation due to inhaling of hydrophobic agents when applying hydrophobic coatings through the prevalent spray misting method [36].

The durability of the surface modification is a key concern as the technology is progressed towards real world applications [37]. Durability is broadly a two-fold problem of both mechanical resistance to abrasion and rubbing, as well as the chemical stability of the surface. Recent studies have shown that a hierarchical roughness active across two length scales can maintain a suitable Cassi-Baxter state even after some features have worn away [38]. Durability has received more attention since early-stage research however a standardized test method has not been achieved.

Experimental approaches to engineer patterned surface wettability have targeted applications in water harvesting [39], microfluidics [40] and inkjet printing [41,42]. These works have mainly involved analogue lithography or mask exposure approaches which limits the scalability of the processes. The competing requirements of cost, scalability, durability, desire for patterning and safety bring significant scope for research work into digital processes to modify wettability.

1.2.2 Applications of embedded electronics and sensors

The second main application of surface engineering covered in this thesis is that of functionalisation of sheet glass to deliver embedded electronics. In particular, the application of inkjet printing as a technique to produce these functionalities is outlined, with required material deposition characteristics.

Sheet glass material is used over a wide range of applications and length scales. The float glass process has enabled glass of nanometre roughness with high form flatness to be produced. At a large scale, float glass is used in buildings with a composition selected by required thermal characteristics

for energy efficiency and mechanical properties for strength and weather resistance. Smart windows involve the use of photocatalytic coatings such as TiO_2 to produce a photocatalytic self-cleaning effect or electrochromic coatings which respond to electrical charging to switch between transparency and opaqueness. Similarly, glass is widely used as a casing material to protect silicon photovoltaic cells whilst still ensuring excellent light transmittance. A key stage in solar panel manufacturing technology is screen printing deposition of silver fingers and busbars for electrical circuitry [43]. For glass in automotive applications, there is an emerging demand for displays which show the information produced by vehicle sensors and systems. Ultra-thin, flexible glass is an attractive substrate to produce printed touch panel displays because this enables low cost roll-to-roll processing whilst preserving the hardness and thermal-stability benefits of glass [44,45]. Hybrid processes such as one-step interconnect combine inkjet printing and laser patterning to produce multilayer electronics such as displays and solar panels [46].

To outline some of the emerging functional glass requirements, an example of the sensing and responsive functionalities of a future ‘smart’ car windscreen is shown in Figure 1.3. Table 1.1 links sheet functionalities to applied active materials and research studies. For the creation of these thin films; chemical or physical vapour deposition approaches are currently the most commonly used. However, these techniques are only suitable for large-scale batch manufacturing, whereas digitally enabled techniques allow small batches, rapid production of trial products and personalisation for customers.

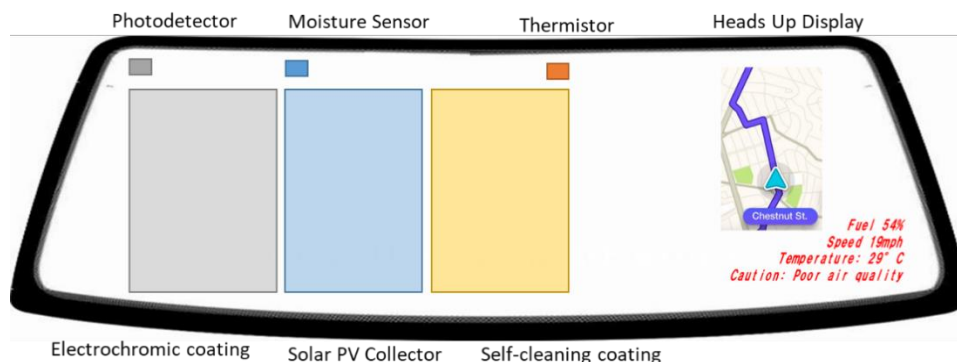


Figure 1.3: Concept sketch of a ‘smart’ automotive windscreen with labels for embedded sensors, surface functionalities and display features

Self-cleaning coatings may involve application of photocatalytic UV responsive metal oxides, or superhydrophobic coatings. A key challenge in the fabrication of superhydrophobic transparent surfaces is the production of a surface texture capable of a Cassi-Baxter wetting state which does not also incur transmittance limiting diffuse reflections or diffractive effects. Electrochromic devices are fabricated through deposition of a transparent conducting oxide, electrochromic film, ion conductor

and a counter electrode. Transition metal oxides such as WO_3 are commonly selected due to their high electrochromic efficiency and short switching times [47].

In addition to sheet surface functionality there is the requirement for complementary embedded electronics and sensors. An example feedback loop may involve a light sensor which triggers an electrochromic response in glare conditions. Sensing devices may involve several components integrating a sensing material which is electrically responsive to a specific condition (such as the presence of a toxic gas) with printed circuitry to process and transmit the electrical signal. A manufacturing challenge is in the industrial scale fabrication of these components on glass substrates with high yield and uniformity.

Table 1.1: Example reports of surface functionalities and enabling active material.

Functionality	Example Active Material	Reference
Self-cleaning (photocatalytic)	TiO_2	[48]
Self-cleaning (superhydrophobic)	PTFE	[49]
Electrochromic	WO_3	[47]
Solar Cell	$\text{Cu}(\text{In,Ga})(\text{S,Se})_2$ (CIGS)	[50]

Again, an important trend is the shift towards digital fabrication of these targeted functionalities, which will be described further in Section 1.3.

1.3 Digital fabrication technologies - emergence and industrial adoption

In this thesis ‘digital fabrication’ is defined by programmable surface modification processes with computer defined patterning, this is closely associated with ‘direct-write processing’ and the terms are used interchangeably in the research literature [51,52]. ‘Digital’ printing contrasts with ‘analogue’ printing techniques such as screen printing, where the pattern is fixed. Digital patterning technologies are highly sought after in niche, low-volume or flexible manufacturing systems for deposition of functional materials, conductive tracks, or interconnects across a wide range of sectors [51]. The benefits of these fabrication techniques are in late-stage product customisation, their ease of scalability and their low material wastage. These are well suited to match the demand for low cost, embedded electronics created by emerging Internet of Things applications [53]. The selection of a specific technique in an industrial setting is determined by the physical parameters of the targeted device such as resolution or substrate material properties, as well as manufacturing parameters such as production rate, cost effectiveness, chemical compatibility, safety and environmental considerations.

Direct write technologies have become more prominent in ultra-precision micro-nano scale manufacturing research with processes possible to suit a range of application length scales. Figure 1.4 shows the minimum line width possible with major direct write fabrication processes. These processes have been delineated as either additive or subtractive processes. Characteristics of these processes are that the track width is from sub-micron to millimetres, the substrate is an integral part of the final product and they are suitable for a range of deposited materials including metals and polymers [53]. Two of the direct write techniques which have received the most industrial attention are inkjet deposition and laser ablation. However, there are challenges with the use of these processes such as adhesion, resolution, uniformity and avoidance of defects. An in-depth understanding of process interaction parameters is required to meet these challenges which is tackled within this thesis.

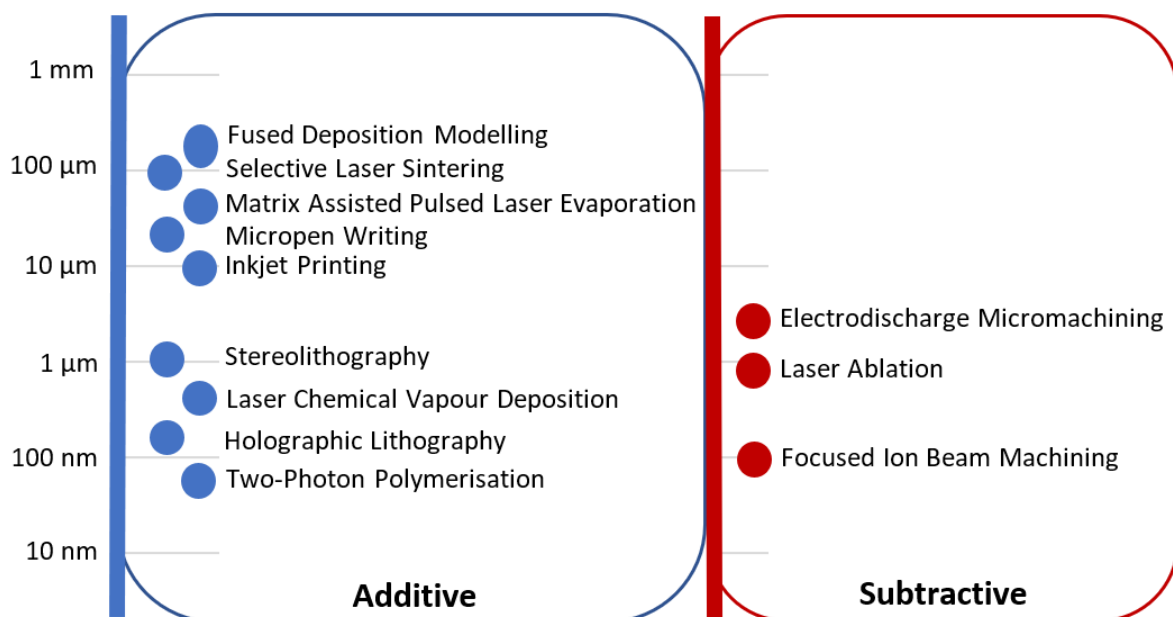


Figure 1.4: A comparison of additive and subtractive direct write fabrication approaches. The reported value is the approximate minimum feature size. [53–56]

Industrial and functional printing applications have been predicted to rise by 50% to a market value of £114.8 bn by 2020 [57]. In the time span 2016-2022, digital printing applications as a share of overall print output was predicted to rise from 10% to 18%. The value of the global inkjet market is predicted to rise by 9.4% to 2023. This growth is driven by opportunities outside the traditional graphics and packaging sectors created by new inkjet inks with functional capabilities such as for electronic or biomedical device fabrication. A particular benefit of inkjet and laser processing is the capability for digital prototyping and design modification. This allows for a design to be created on a computer and a fully functional electronic circuit or component to be rapidly fabricated. This design can then be scaled to pilot production. This process produces a competitive advantage by reducing time to market.

Further cost savings associated with adoption of digital deposition approaches for printed electronics applications include: cost reduction of materials, assembly and machinery, shrinking of supply chain requirements and reduced production of hazardous waste [58].

Figure 1.5 compares the costs of areal printing approaches, showing digital printing approaches (inkjet and laser induced forward transfer (LIFT)) are economic at a very low number of print runs [12,13]. In inkjet, no physical print form is needed which saves both cost and time for machine setup compared to an analogue technique such as screen printing [61]. In the case of subtractive manufacture using laser processing cost savings come from reduction of wear of mechanical parts and cutting tools.

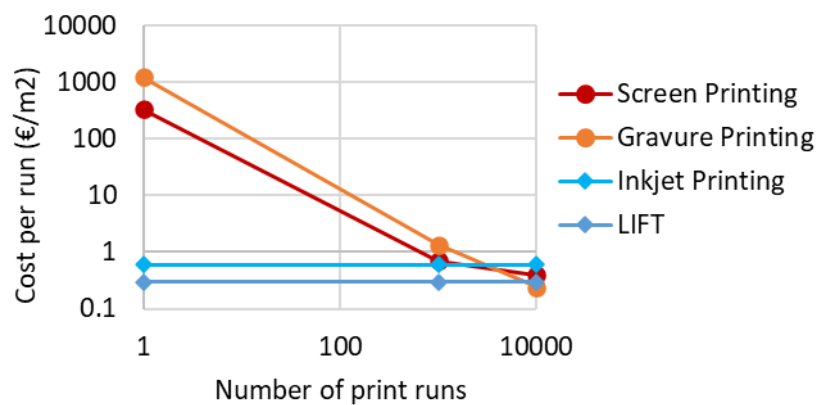


Figure 1.5: A comparison of the cost profile of analogue (red) and digital (blue) printing technologies [12,13]. This comparison does not account for capital costs of the printing system.

In addition to additive processes, subtractive direct-write processes are needed for microfabrication. Pulsed laser ablation has emerged as one of the most important micromachining processes for a diverse range of materials and applications. The first laser was constructed in 1960 by Theodore Maiman using a synthetic ruby as the gain medium and photographic flashlamps as the lasers pump source [62]. Following this innovation, industrial applications of lasers were rapidly discovered. In 1961, a ruby laser was used to destroy a retinal tumour at a Manhattan hospital [63]. In 1964 the first gas-laser cutting experiments were carried out at Bell labs using CO₂ lasers, and by 1967 CO₂ lasers with powers greater than 1kW were possible [64,65]. Since then, high powers lasers have emerged as a ubiquitous industrial tool. The revenues of the materials processing laser industry were worth \$19.8 billion in 2018 and the applications which this market supports adds a substantial multiplier to this value [66].

The use of short-pulse and ultra-short lasers enable ultra-precision modification applications. The first lasers with sub-picosecond pulses were based on organic dyes with a saturable absorber and were used for the early breakthroughs in femtosecond spectroscopy [67]. The current applications of

femtosecond materials processes became accessible with higher power Ti:Sapphire lasers in the 1980s. Ti:Sapphire are based on solid state mode-locked architecture and allowed for peak powers in the MW range [46].

During this stage fibre lasers were also researched but had not been able to achieve the same pulse energy and peak powers. In the last 20 years, industrial fibre lasers have become available with very high average powers, repetition rates and ultrafast pulses [69]. Fibre lasers are based on rare earth metal doped glass fibre as the gain medium. A seed diode laser is amplified through a master-oscillator power amplifier. Fibre lasers are very attractive for industrial applications for several reasons. Because high powers are accessible, this can allow for faster processing rates. The use of simple air-cooling systems instead of specialist chillers means that fibre lasers have higher energy efficiency and take up less floor space. Finally, they have a very long lifetime with 100,000 hours of expected operating time [70].

The functional properties of a surface and its' interfacial behaviour in tribological, wetting and corrosion contexts are determined by a combination of surface structure and chemistry. Laser surface modification processes provide a versatile suite of techniques to produce low friction, wear resistant and self-cleaning metallic surfaces. These techniques may involve subtractive material removal processes such as: laser polishing [71,72] and direct laser texturing [73], laser induced chemical transformations such as laser surface hardening [74], or additive processes to deposit extremely wear resistant materials by laser cladding [75].

The direct-write nature of these digital fabrication techniques provides exciting opportunities for rapid and efficient manufacturing of tuneable, functional surfaces. This thesis has identified key barriers that are currently preventing this adoption and research aims where an improved understanding would help overcome the barriers and deliver scalable manufacturing.

1.4 Research Aims

The introduction chapter presented the demand from industry for digital surface modification processes that will enable scalable customisation and advanced fabrication. In particular, there is a need for innovative strategies combining additive and subtractive approaches to modify surface morphology and chemistry. There is also a major research interest in the use of digital manufacturing for rapid device prototyping. The main motivation for this research is to therefore overcome problems encountered by industry such as long sequences of lithography and expensive laboratory processes for device fabrication through the use of digital fabrication techniques. New capabilities in high-rate pulsed laser processing, plasma surface treatment and inkjet deposition of functional material provide the potential components of such a system.

To explore feasibility in industrially relevant applications a set of research aims were identified, which are reflected in the chapters in this thesis:

- 1 Provide insights through literature analysis and experimentation to identify where progress is needed for direct laser texturing to create superhydrophobic surfaces.
- 2 Examine laser processing of surfaces to better understand the laser-surface interactions that will produce surface micro-structuring and surface chemistry control of stainless steel and float glass surfaces at an industrial scale.
- 3 Explore surface modification approaches to enable functional inkjet printing with enhanced adhesion and durability on glass surfaces.
- 4 Examine the viability of an indirect laser deposition technique, laser induced reverse transfer, using a nanosecond pulsed fibre laser for deposition of functional materials to glass surfaces.

1.5 Thesis Outline

To address these aims, this thesis is structured into 7 chapters and a summary of each chapter is given below.

Chapter 1 introduced the background to this research, highlighting how it has informed the research direction and motivated the development of new digital surface modification processes. As each chapter is focused on quite separate techniques within the overall research goals, a detailed literature review is presented at the start of each separate chapter in Chapters 3 – 6. Each literature review informs the design of experiments addressing knowledge gaps in previous research.

Chapter 2 discusses the common fabrication and characterisation tools used in this work. A range of analytical equipment was used to fulfil surface characterisation requirements of morphology, chemistry, and wettability.

Chapter 3 investigates the laser processing to drive surface restructuring of glass and stainless steel, developing the processing strategies used in chapters 4 and 5. The role of laser parameters is assessed through post-fabrication analysis, and is validated with reference to laser matter interaction theory.

Chapter 4 examines laser texturing specifically for superhydrophobic surface fabrication. These experiments address core challenges such as the laser processing approach for high areal rate patterning, acceleration of the chemical transition after laser processing and probing the chemical pathway of the laser induced hydrophobicity for stainless steel substrates.

Chapter 5 explores the use of functional inkjet deposition for fabrication of microelectronic devices on glass. Experiments focus on surface preparation of glass prior to inkjet printing through cleaning, plasma and chemical treatments. Wettability patterning through laser processing and plasma treatment are also explored.

Chapter 6 presents experimental findings into the use of laser induced reverse transfer. This deposition technique uses direct write laser ablation to pattern metallic deposits on transparent substrates but is relatively unexplored in the literature. Here, insights are provided into the underpinning mechanism through studying deposition from solid targets using a nanosecond pulsed fibre laser.

Chapter 7 summarises the research findings and outlines directions for future research.

2 EXPERIMENTAL TOOLS AND ANALYTICAL TECHNIQUES

This chapter describes the common fabrication and characterisation tools used throughout this research. Detailed descriptions of experimental methodologies relating specifically to certain chapters are included within those separate chapters.

2.1 Materials

2.1.1 Stainless Steel

Experiments used 304 stainless steel supplied either in cold rolled form (Ra 255 nm) or with mirror polished finish (Ra 3 nm) in both cases with thickness 1.0 mm, with an example of these measurements in Figure 2.1. The lower cost cold rolled finish was used for nanosecond pulsed laser texturing where the resultant texture is microstructured. Several operations were used to prepare sample shape involving mechanical cutting, waterjet cutting and laser cutting. Samples were kept in their protective plastic film throughout these operations to preserve surface finish and cleanliness.

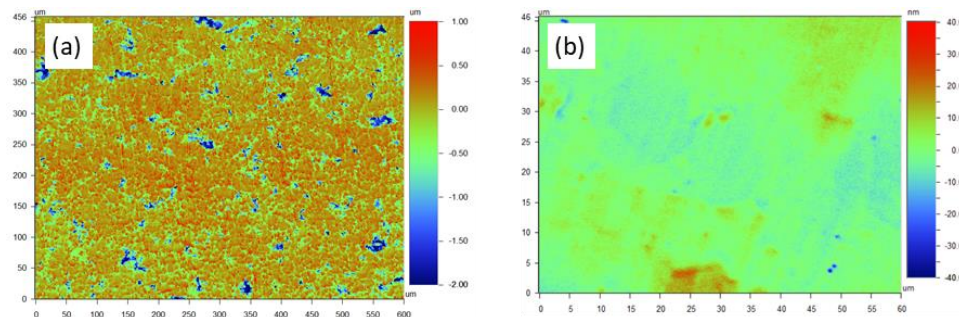


Figure 2.1: White light interferometry surface roughness measurements of stainless steel used for laser processing experiments (a) Cold rolled finish (b) Mirror polished

2.1.2 Glass

The glass used was Pilkington Optiwhite with reduced iron content and 2.1 mm thickness. Vertical scanning interferometry indicated roughness average Ra < 10 nm. The market for this glass is as exterior or interior glazing, furniture or a wide range of other applications [76].

2.2 Laser Processing

2.2.1 G3 Laser Marker Platform

Nanosecond pulsed laser processing experiments were carried out with an SPI™ G3 Yb non-polarized fiber laser with wavelength of 1.064 μm , output beam $M^2 < 2$ and maximum output power of 20 W at a pulse duration of ~200ns with PRF 25 kHz. A Jenoptic™ 03-90FT fused silica lens with focal length of 125 mm was used to produce a focused spot size of 36.4 μm .

2.2.2 Ultrafast Laser Machining Platform

An Amplitude Systems Satsuma laser source configured for sample stage translation patterning was used for the majority of glass processing experiments. The laser has a pulse width of 280 fs, wavelength of 1030 nm and a repetition rate of 500 kHz. Laser power was varied through the modulation efficiency. Power readings were measured using a coherent fieldmaster thermal power meter and a S120C Thorlabs photodiode. Substrates were mounted on an Aerotech air bearing XY stage. The stage has an accuracy of $\pm 3 \mu\text{m}$ in the X/Y directions and $\pm 0.5 \mu\text{m}$ in the Z direction. A 2-axis tilt table is used in combination with a chromatic confocal probe to level the surface. G-code was written to command laser operations and patterning.

2.2.3 Laser4Surf Platform

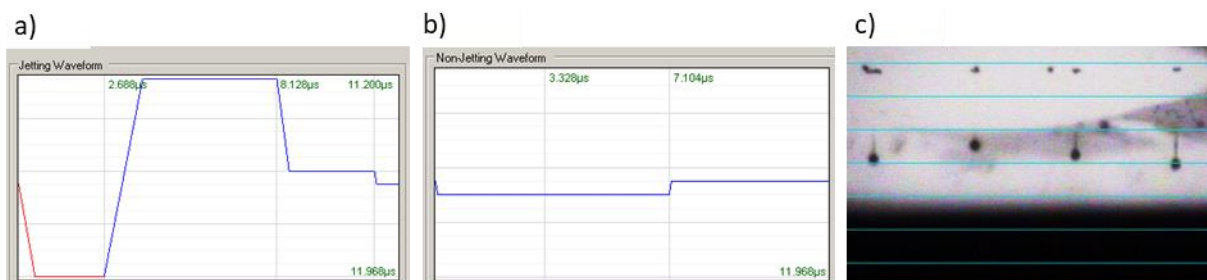
An Amplitude Systems Satsuma laser was also used with a galvanometer scan head to explore high rate patterning of steel and glass. A Satsuma laser system generating 350 fs pulses at 1030 nm was used for laser processing experiments with maximum power of 9 W varied with an optical attenuator. The system was operated with longitudinal polarization. A LASEA-LS LAB scanning system was used to raster the beam across the surface. The optics train involved a beam expander and an F θ lens with a focal length of 100 mm. The beam expansion ratio was varied to produce a focal spot size of 30 μm or 8 μm .

Table (2.1) Summary of the laser parameters and characteristics for the different systems used in experiments.

Laser	SPI G3 (WFM 0)	Satsuma
Pulse Duration	200 ns	280 fs
Wavelength	1064 nm \pm 10 nm	1030 nm \pm 5 nm
Repetition Rate	25 kHz	500 kHz
Quality Factor M2	<2	1.1
Maximum Power	20 W	9W
Pulse Energy	0.8 mJ	10.6 μ J
Optics	XLR8 Scan Head - 36.4 μ m	Thorlabs LMU 10x, Spot-4.81 μ m COMAR 08 0X 05, Spot- 1.92 μ m LASEA-LS LAB Scan Head, Spot – 8:30 μ m
Maximum Scan Speed	1 m/s	50mms/s with stage translation 4m/s with galvanometer platform

2.3 Inkjet Printing

The inkjet printer used was a piezoelectric-actuated drop-on-demand type (Dimatix Materials Printer DMP-2800, Fujifilm). The printer uses cartridges with arrays of 16 individually addressable piezo-actuated nozzles through which fluid is dispensed, the nozzle diameter is 21.5 μ m producing a nominal 10 pL droplets. The Dimatix print settings used were a meniscus setpoint of 0.5 in.-H₂O (124 Pa), a 0.4 mm cartridge height, a room temperature print nozzle temperature and an ejection voltage of 23V was applied to fire four jets. Figure 2.2 shows the jetting and nonjetting waveforms applied to the piezoelectric nozzle actuators. A Sunchemical silver nanoparticle ink U13046/M27359 with surface tension of 0.035 N/m was used for inkjet printing experiments. The ink contained 25-50% ethanediol, 10-20% glycerol and had a concentration of 10-20 silver nanoparticles with the remainder water. The bed was heated to 50°C to aid track coalescence as recommended by ink supplier. Sintering conditions were 150°C for 30 minutes unless otherwise stated. Drop spacing and number of layers were investigated with experimental work.

**Figure 2.2:** Applied (a) jetting waveform and (b) Non-jetting waveform for Dimatix inkjet printing experiments, (c) image of droplets ejected with specified print conditions.

2.4 Characterisation

In order to measure surface structure, surface chemistry and wettability a range of surface characterisation equipment was used as described below.

2.4.1 Surface Structure Characterisation

An Olympus BX51 Optical Microscope with attached digital camera was used to image surface structure and colour. Measurement of surface roughness and topology was carried out with a Veeco Wyko NT3300 optical profiler and interferometer operating in vertical scanning mode.

Imaging of surface morphology at micro-nano scale was carried out with Zeiss Auriga Gemini, Helios NanoLab 600 SEM and FIB. A conductive coating to allow SEM imaging was applied to the glass substrates. This involved sputtering of an Ag/Pd target using an Emitech sputter coater. The current was 65 mA applied for 14 s per sample. From manufacturer guidance this produced a coating thickness of 4.4 nm. A Helium Gas Field Ion Source Zeiss Orion Nanofab with electron flood gun charge neutralisation was used to directly image the morphology of LIRT deposits on glass which avoided the need for anti-charging conductive coating.

2.4.2 Surface Chemistry Characterisation

Energy dispersive X-Ray spectroscopy (EDS) involves the production of characteristic X-rays from a sample irradiated by a high energy electron beam, the X-rays produced have an energy characteristic of the sample elemental composition. An Oxford Instruments X-max EDS system was used. An accelerating voltage of 10 keV was used to minimise the X-ray generation volume and signal produced by the glass substrate.

X-Ray Photoelectron Spectroscopy (XPS) involves the irradiation of a sample with an X-Ray beam and measuring the number and kinetic energy of the electrons which are produced from the top 1-10 nm of the surface. The technique was used to analyse the composition of laser transferred metallic deposit and to probe the changes in surface chemistry after laser texturing for superhydrophobicity. The XPS system had a monochromatic Al K α 1 X-ray source ($h\nu = 1486.6$ eV) using a SPECS PHOIBOS 150 electron energy analyzer with a total energy resolution of 500 meV. Raman spectroscopy of carbonaceous LIRT deposits was carried out at 785 nm, with a beam power of 10 mW and spot size < 10 μ m.

2.4.3 Electrical properties characterisation

Resistivity was measured with a Keithley 4200 SCS Parametric Test Station using a four-point probe test configuration, this parameter was selected to enable comparison with bulk material properties.

Resistivity was calculated according to the formula, $\rho = \frac{RA}{L}$ where R-resistance, A-cross sectional area, L-Length. A measurement error of $\pm 50 \mu\text{m}$ to length was applied to account for probe tip placement error. For later experiments on inkjet printed tracks, a two probe configuration was used with a desktop 1705 True RMS Programmable Multimeter.

2.4.4 Wettability Analysis

Contact angle measurement is a widely used technique to probe the interaction of liquids with solid surfaces and ensure the expected surface chemistry is present. The contact angle of a liquid droplet on a solid surface is an important metric in manufacturing to inform coating adhesion and the cleanness of a surface. It indicates surface tension, surface free energy and the cleanliness of a surface. The technique is used this study to characterise the surface and fluid prior to inkjet printing and to characterise the superhydrophobicity of processed surfaces.

The interaction of a fluid with an ideal surface is a problem of classical mechanics with the chemistry of surface and liquid determining the physical shape of a droplet [77]. Gibbs's equation demonstrates that a droplet will act to minimise its free energy through minimisation of the sum of the interfacial energies acting on the droplet. Figure 2.3 illustrates the different wetting regimes possible.

$$\psi = \sigma_{SV}A_{SV} - \sigma_{SL}A_{SL} + \sigma_{LV}A_{LV} \quad (2.1)$$

A contact angle is defined by the angle formed in a liquid droplet between the liquid-vapour interface and the solid surface. Young's equation describes the contact angle as a result of this interaction for a plane homogenous surface.

$$\sigma_{SV} = \sigma_{LS} + \sigma_{LV}\cos\theta_{eqm} \quad (2.2)$$

On a rough surface, the surface topographical features lead to a total surface area which is larger than the projected area. In this case the effect of roughness is to magnify the intrinsic wettability of the material through the Wenzel model [78].

$$\cos(\theta) = \frac{A_{surface}}{A_{projected}} * \cos(\theta_0) \quad (2.3)$$

For very rough surfaces the liquid does not completely wet the rough surface and composite interface is formed where the liquid droplet is in contact with both air and liquid simultaneously. This

behaviour results in hydrophobicity with increasing roughness as the thin layer of trapped air at the interface reduces the attractive interactions between the solid and liquid [37]. This behaviour is described by the Cassie-Baxter model where f_{LA} is the fraction of the liquid droplet base in contact with air at the interface.

$$\cos(\theta_{CB}) = \frac{A_{surface}}{A_{projected}} f_{LA} \cos(\theta_0) - (1 - f_{LA}) \cos(\theta_0) \quad (2.4)$$

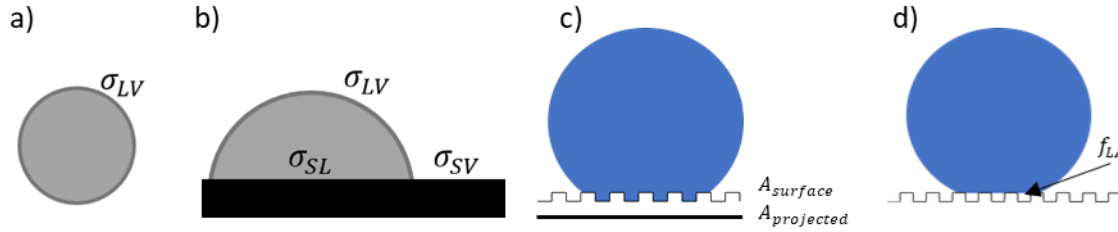


Figure 2.3(a) A droplet in flight forms a spherical shape to minimise free energy. (b) The shape of a sessile droplet on a surface is determined by the balance of the three interfacial surface tensions. (c) the Wenzel wetting regime magnifies the intrinsic wettability of the surface material (d) The Cassi-Baxter regime produces a hydrophobic droplet shape.

To complement sessile drop measurement further measurement techniques are used to assess the dynamic behaviour of droplets. One of the most basic techniques is to measure sliding angle, a drop is dispensed onto a flat surface, the tilt angle is then incrementally increased until the droplet slides or rolls off the surface. The general trend is that sliding angle becomes smaller as contact angle increases because there is less contact area between the drop and surface [79].

Superhydrophobicity is an extreme wetting state with high repulsion of water droplets. This is characterised by sessile droplet contact angles greater than 150° and sliding angle less than 10° [27,80]. Hysteresis describes the difference formed between advancing and receding contact angles. It can be measured by increasing the volume and footprint of a drop on a surface with a syringe or the analysis of sliding droplet shapes. Superhydrophobic surfaces are usually characterised with a sliding angle below 5° and hysteresis below 3° . In the superhydrophobic self-cleaning effect, liquid droplets bead up and roll off at low sliding angles. Because of the high contact angle of superhydrophobic surfaces, the droplet rolls off the surface instead of sliding, as the droplet rolls contaminants are picked up, embedded into the water droplet and removed from the surface [81].

Practically, contact angle analysis involves imaging the profile of a sessile droplet. Figure 2.4 shows a schematic of a typical drop shape imaging system. A dispensing device is used to produce a sessile droplet on the surface and a camera captures the profile of the droplet, subsequent

image processing is used to measure the contact angle formed. Several commercial contact angle testers were used for fluid profile imaging and analysis. Firstly, a Dataphysics OCA15 was used, the system was calibrated to produce a droplet of 2 mm diameter and 4 μL volume. The dropsnake imageJ plugin [82] was selected for image processing on the criteria of versatility, reproducibility and speed of measurement. Further experiments used a Kruss DSA100 system dispensing a 2 μL droplet of deionized water. Static contact angle was measured using the in-built software in tangent-fitting mode. Automated fitting failed for contact angles below 5° and measurement was done a manual ‘box fit’ method. Sliding angles were measured with the stage tilt capability, the stage was tilted at a rate of $1.6^\circ/\text{s}$ and drop shape images were recorded at 24 fps.

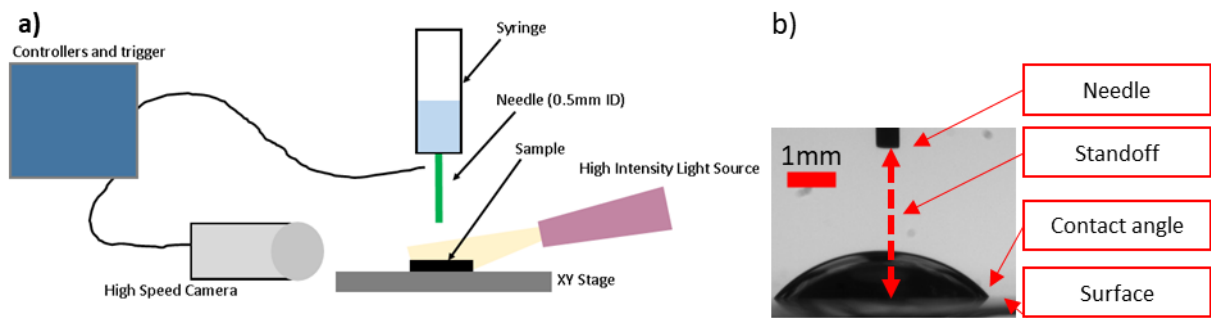


Figure 2.4: (a) Schematic of a typical droplet imaging system. (b) Important characteristics of a drop shape image profile

3 EFFECT OF LASER PARAMETERS ON SURFACES

3.1 Chapter Introduction

Industrial microtechnology applications of pulsed laser ablative processing have flourished over the last two decades. Two technological trends have supported this growth; the emergence of high-power pulsed lasers highlighted in chapter 1 and the effective translation of engineering research through ‘lab to fab’ scale up [83].

In this chapter, a review of background literature is presented focusing on laser ablation processing. Firstly, the relevant theory of laser light absorption and thermal material excitation is discussed, this leads to discussion of surface structuring through laser ablation and laser induced periodic surface structure fabrication. The second half of this literature reviews focuses on the manufacturing aspects of pulsed laser modification with discussion of laser sources, beam scanning apparatus and surface functionalisation.

Creating functional surfaces requires changes to surface properties such as morphology and chemistry, and so we need to identify how to tune laser parameters to deliver this in a scalable way. The results of experimental investigations presented in this chapter are used to establish processes for a stainless-steel surface texture which has superhydrophobic properties and effective laser micro structuring of glass.

3.1.1 Laser materials interaction

This section outlines the relevant theory for the work in this thesis, describing the process of laser light absorption and material removal through ablation. The major factors in this discussion which have experimental impact are the intensity of the laser light and the duration of the laser pulse.

Figure 3.1 shows a timeline of the laser interaction events for a single pulse, this interaction sequence from laser absorption to structural changes is used to define the layout of this section. Critically it is seen that many of the absorption and interaction processes occur within the femto to nanosecond time scales of the laser pulse, which influences the transient interaction mechanisms and processing regime. This theory section examines the key aspects of the laser energy absorption and relaxation mechanics and their relation to the selection of laser parameters. This leads to an introduction of the resulting phenomena of surface modification through ablative structuring and laser induced periodic surface structure (LIPSS) formation.

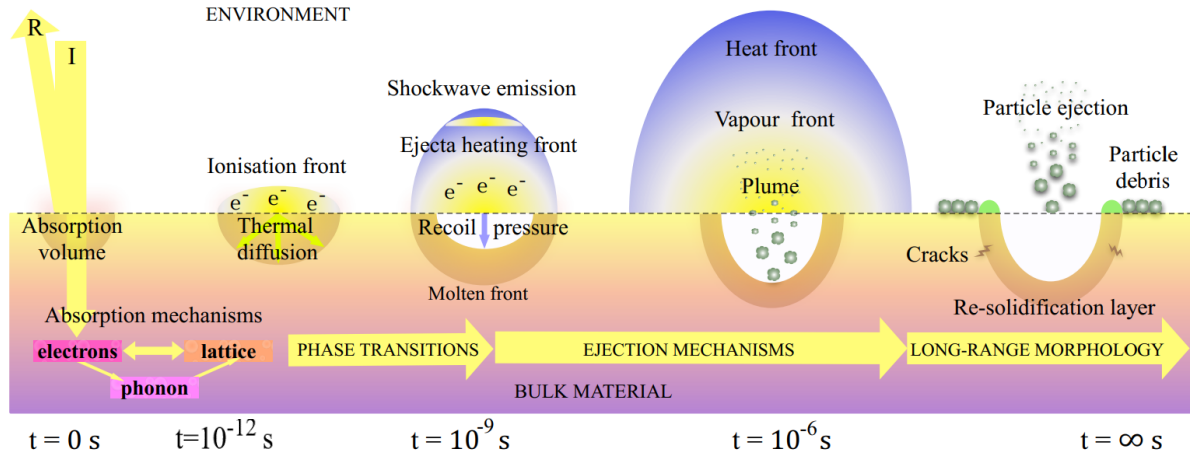


Figure 3.1: Temporal profile of the laser ablation process showing the timeline of laser matter interaction mechanisms resulting in ablative material removal [84].

3.1.1.1 Laser light absorption and excitation mechanisms

Propagation of light into a material begins at the surface interface. The Fresnel equations describe the reflection of light (R) when arriving at an interface between two refractive indices (\tilde{n}_0 & \tilde{n}_1). Light transmitted through the interface (T) is given as the reciprocal of reflected light [85].

$$R = \left(\frac{\tilde{n}_0 - \tilde{n}_1}{\tilde{n}_0 + \tilde{n}_1} \right)^2 \quad (3.1)$$

$$T = 1 - R \quad (3.2)$$

Equation 3.1 defines the absorption coefficient of the material. This determines the rate of attenuation of light in a medium with units of m^{-1} . This coefficient is used in the Beer-Lambert law to determine

the attenuated intensity, I , at depth, Z . The optical penetration depth is calculated from the Beer-Lambert law (equation 3.2) as the depth at which the power of the wave has reduced to $1/e^2$ of its surface value. At 1064 nm incident laser wavelength, iron has a penetration depth of ~22 nm and soda-lime glass 17.2 cm [86]. For metals, absorptivity will typically increase with temperature due to laser heating or as metal oxides are formed during processing [87].

$$\alpha = \frac{4\pi k}{\lambda} \quad (3.3)$$

$$I(z) = I_0 e^{-\alpha z} \quad (3.4)$$

In absorbing materials photons deposit energy through the inverse Brehmstrahlung effect, the energy of a photon (E) is calculated from Planck's equation, as shown in Equation 3.5, where h is Planck's constant, c is the speed of light and λ is the wavelength.

$$\Delta E = \frac{hc}{\lambda} \quad (3.5)$$

In the case of metals, the photon energy is greater than the bandgap energy resulting in direct interband or intraband absorption, as free electrons are present in the conduction band intraband absorption is the most relevant for ablative processing [88]. In the case of dielectric or semiconducting materials, absorption is determined by the photon energy relative to the material bandgap. For wide bandgap materials the photon energy is often less than the bandgap, for example the bandgap of soda lime glass is 3.0 eV[89] and the photon energy of a 1064 nm laser is 1.2 eV. This means that alternative non-linear phenomena are taking place to enable energy absorption in these materials. The previously stated values for absorption depth are incorrect in the case of the non-linear absorption processes as transient metal-like states are induced in the substrate. The mechanism of ultrafast absorption in these wideband gap materials is multiphoton absorption or tunnelling ionization followed by avalanche ionization as illustrated in Figure 3.2. In multiphoton absorption, multiple photons are absorbed simultaneously in virtual states to bridge the bandgap and reach the conduction band [90], this can occur in ultrashort laser pulses due to the high photon density. In tunnelling ionization, the potential barrier between bands can be distorted at high intensities allowing for electron promotion. Keydish *et al.* showed that multiphoton and tunnelling concepts are limits of the same process [91], the ionization probability is determined by the photon density (pulse duration) and the amplitude of the laser field (intensity) respectively.

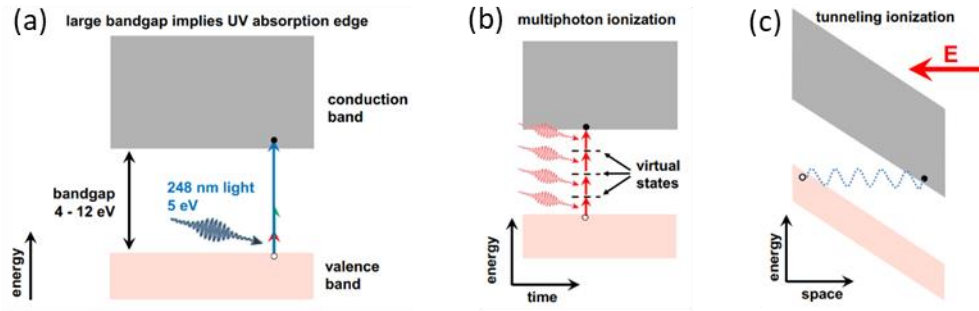


Figure 3.2: Schematic of absorption processes [90] for (a) direct interband absorption of UV light, (b) multiphoton absorption and (c) tunnelling ionization processes.

Once seed electrons are excited to the conduction band they absorb laser energy through the inverse bremsstrahlung effect. Once their energy is higher than the bandgap further electrons in the valence band are ionized and promoted through inelastic scattering resulting in an avalanche process. Eventually a critical density of electrons is reached to initiate ablation effects through thermalization processes [92].

Absorbed laser light is converted to heat through vibrational excitation of the material lattice phonons. Several relaxation mechanisms are involved with the transfer of energy from the excited electrons to the material lattice such as coupling through phonon, ion or neutral atom scattering.

An important aspect of these thermalisation processes is their temporal duration with respect to the laser pulse. There is significant variance in the time to transfer energy to phonons and thermalize depending on the material, in metals thermalization typically occurs in the order of 10^{-12} - 10^{-10} s. If the laser pulse is longer than the thermal coupling rate (e.g. longer than ns pulse duration) the absorbed laser energy can be considered as being directly converted into heat. When the pulse duration and laser-induced excitation rate is shorter than the thermalization rate large excitations can build up in intermediary states allowing for reduction of heat damage through ultra-fast non thermal processing [93].

3.1.1.2 Laser ablation surface structuring

Laser ablation is defined as material removal through irradiation with a laser. Beyond a critical laser intensity threshold, the rapid heating effects result in material transformation and removal through melting, vaporisation, sublimation, and plasma formation processes as well as ejection of solid particles through fragmentation and spallation.

The ablation threshold is determined experimentally for a specific material and is calculated from equation 3.5 in units of J/cm². E_p is the minimum pulse energy to observe ablation, d is the crater diameter and ω_0 is beam waist.

$$F_{th} = \frac{2E_p}{\pi\omega_0^2} \exp\left(-\frac{d^2}{2\omega_0^2}\right) \quad (3.5)$$

The dynamic of the ablation process underpins the resulting morphology and chemistry of the material surface. ‘Gentle’ and ‘strong’ regimes can be identified based on increasing laser fluence [94]. In the ‘gentle’ regime, the ablation depth is correlated with the aforementioned optical penetration depth. At high fluences, higher rates of material removal are observed resulting in ‘strong’ ablation. This regime is shown to be dependent on heat transport characterised by the materials electron diffusion length. Mannion *et al.* found that for femtosecond laser ablation of stainless steel the threshold for strong ablation occurred at around 10x the fluence at which material transformation effects were initially observed in the gentle ablation regime [95], as shown in Figure 3.3(a).

In the ‘gentle’ regime, crater morphology is typically smoother and cleaner as material is sublimated instantaneously to vapour, whereas in the ‘strong’ ablation regime more roughness is observed due to the phase explosion melting and redeposition processes. Although the majority of research attention is given to surface morphology, it can similarly be seen that the chemistry is affected in the case of metals when processed in air environments as investigated by Adams *et al.* [96]. Figure 3.3(b) shows that for nanosecond laser processing of stainless steel the depth of oxide formation increased from 50-500 nm with increasing laser energy dose. In this oxidation region, the stainless-steel composition and structure were significantly changed with observation of diminished Cr concentration and transformation from face-centred cubic austenite into a body-centred ferrite or martensite phase [96].

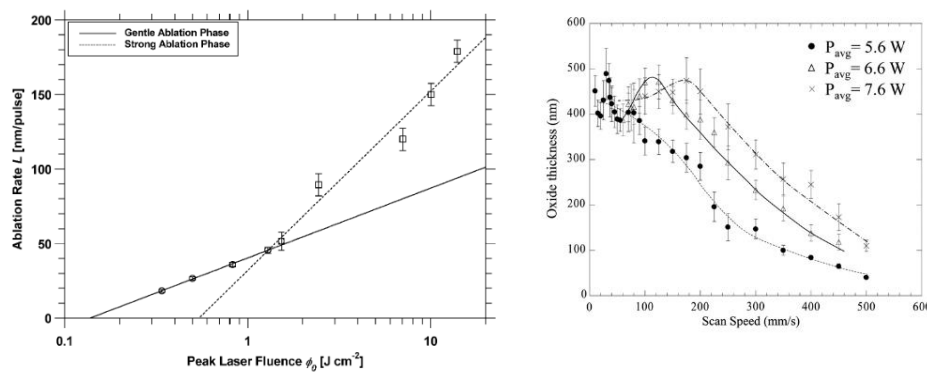


Figure 3.3: (a) Variation of ablation rate with laser fluence showing ‘gentle’ and ‘strong’ ablation regimes [95]. (b) Variation of laser induced oxide thickness with average power and scan speed [96].

In this study, the laser beams used had a Gaussian intensity profile as defined by equation 3.6, this shape is characterised by a sharp peak and wide low intensity tails [97]. Figure 3.4(a) shows the

spatial profile of the beams used. Laser ablation with this intensity profile results in circular crater morphology with the dimensions of the crater determined by the beam radius at which the ablation threshold is exceeded. Figure 3.4(b) illustrates how the spatial intensity profile influences the radius of the surface modification [98]. With careful control of laser parameters, the intensity profile can be manipulated so that only a small band exceeds the ablation threshold to ablated a feature dimension smaller than the laser spot size.

$$I(r, z) = \frac{P}{\pi w(z)^2/2} \exp\left(-2 \frac{r^2}{w(z)^2}\right) \quad (3.6)$$

I Laser intensity, P Power, z distance from beam waist in propagation axis, r radial position, w(Z) distance from the beam axis where the intensity drops to $1/e^2$ of the maximum value.

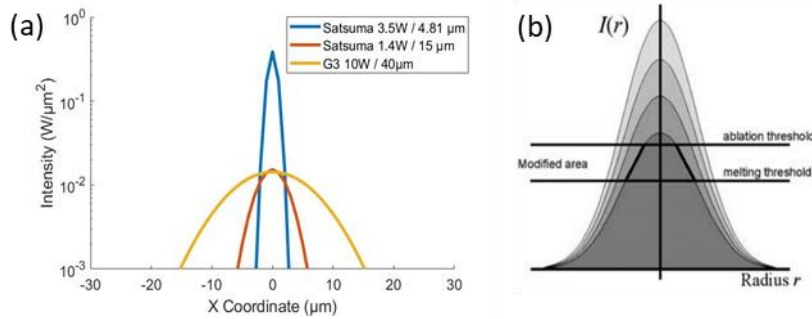


Figure 3.4: (a) Gaussian beam profiles of laser beams used in experiments, (b) illustration of the Gaussian beam profile relative to material processing parameter threshold [98].

Ablation processes have been modelled using approaches such as molecular dynamics simulation [99,100]. Figure 3.5 shows simulation of a 50 fs laser pulse impacting a silicon surface over 0-17.5 ps timescale. However, this approach not yet able to capture an industrial scale event as the computational expense constrains the interaction volume to 10^6 atoms or around 100-200 nm which is very simplified compared to experimental conditions.

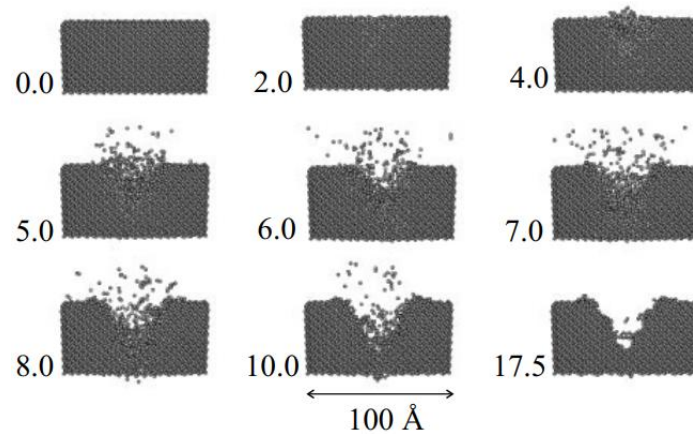


Figure 3.5 Molecular dynamics simulation of a 50 fs laser pulse impact on a silicon surface, the times are given in ps to the left of each frame [99].

Empirical approaches remain the standard method to optimise laser processing operations. It has been shown that based on initial measurements of ablation threshold, a simple logarithmic relationship adequately describes ablation depth with varying fluence as shown in equation 3.7. This can be extended to predict the 3D crater profile by applying the Gaussian intensity profile as described in equation 3.8. Calculating the total incident number of pulses per unit area from beam scanning parameters allows for a full surface topography to be modelled. Figure 3.6 shows the results of this modelling approach with comparison to the profile of a laser textured surface manufactured using a nanosecond regime operating in the ‘strong’ ablation regime [101]. Although this approach accurately predicted the material removal it is not capable of accounting for the raised edge ‘burrs’ formed around the periphery of the laser spot due to molten material flow and accumulation of redeposited particles.

$$D = C \cdot \ln\left(\frac{F}{F_{th}}\right), F \geq F_{th} \quad (3.7)$$

$$D_t(x, y) = \sum_{i=0}^m \sum_{j=0}^n k \cdot C \cdot \ln\left(\frac{F_0 \exp\left(-2\frac{z_i^2 + \eta_i^2}{w_0^2}\right)}{F_{th}}\right) \quad (3.8)$$

D single pulse ablation depth, D_t total ablation depth, C ablation depth at $e \cdot F_{th}$, F_{th} is the ablation threshold fluence. K number of laser passes, $\sum_{i=0}^m \sum_{j=0}^n$ account for the number of incident laser pulses per unit area.

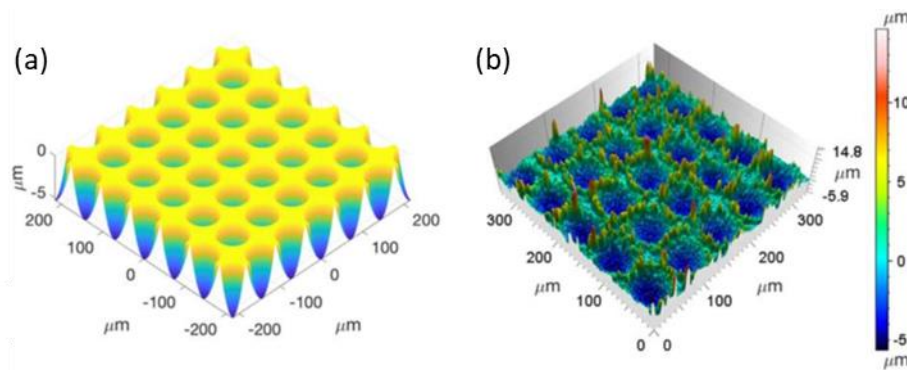


Figure 3.6: Comparison of (a) empirically modelled and (b) measured surface topography for nanosecond pulse laser textured stainless-steel. Adapted from [101].

3.1.1.3 Laser induced periodic surface structure fabrication

Laser induced periodic surface structures (LIPSS) are ripple-like structures appearing with either low spatial frequency (LSFL) with periodicity between ripples close to the incident laser wavelength or high spatial frequency (HSFL) with periodicity much smaller than the laser wavelength. LSFL are generally accepted to be caused by the interference of incident laser light with the surface electromagnetic waves produced by laser irradiation [102]. The intensity pattern produced by this interference results in inhomogeneous energy deposition into the irradiated material. LIPSS are observed with laser intensity close to the ablation threshold to enable local ablation or melting and resolidification without being overpowered by high fluence ablative effects [103]. Figure 3.7 LSFL LIPSS with periodicity of 620 ± 80 nm and are formed with orientation perpendicular to the laser beam polarisation. In the case of HSFL LIPSS the periodicity is 80 ± 20 nm and they are oriented parallel to the polarisation. The height of LIPSS was measured to be 110 ± 20 nm for LSFL and 110 ± 20 nm for HSFL [103].

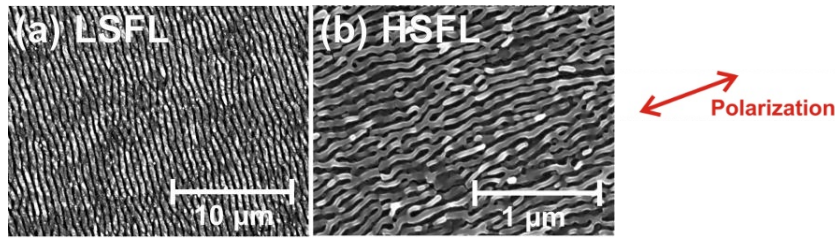


Figure 3.7: SEM images of (a) low spatial frequency and (b) high spatial frequency LIPSS with comparison to incident beam polarisation [103].

LIPSS have been observed for almost any laser pulse duration from continuous wave [104] to ultrafast pulsed sources [105]. The use of ultrafast lasers is particularly attractive because of their capability for precision control of structure. In processing of glass, ultrafast lasers allow for the reduction of heat conduction during ablation which reduces damage due to the low thermal expansion coefficient of glass. Additionally, non-linear absorption characteristics in the ultrafast regime may encourage LIPSS formation. Ultrafast pulses allow direct excitation of surface plasmon polaritons once a critical density of electrons in the conduction band is reached. Important lasing parameters which control LIPSS formation are noted in Table 3.1.

Initial substrate surface finish [106] and heat accumulation during processing [107] impose scale up constraints for wide-area LIPSS manufacturing. Defects or scratches are shown to produce preferential alignment sites for LIPSS to form and usually a very fine level of polishing is required to avoid inhomogeneities. One reported method is to use linear polishing in the direction orthogonal to the intended direction of LIPSS ($R_a \sim 10$ nm), this avoids topographic spatial frequencies of the initial surface finish in the same spatial frequency band of the LIPSS efficacy factor [106]. Heat

accumulation limits the quality of ripple structures formed when moving to higher structuring rates, it was found for processing of 304 stainless steel that when the surface temperature exceeds a critical value of 607°C during processing, a bumpy surface is formed. Analysis of heat accumulation during high rate structuring experiments (10^2 - 10^3 mm²/s) has shown that scanning speed can be controlled to prevent surface temperature from exceeding the critical surface temperature and prevent the structure from transitioning from ripples to ablation [107].

Table 3.1: Influence of laser parameters on LIPSS formation

Parameter	Impact	Condition
Fluence	Formation	LIPSS are possible in both ablative and non-ablative regimes. Generally, fluence close to ablation threshold is used for multiple pulse LIPSS [108].
Number of Pulses	Formation	Initial pulses generate surface roughness which facilitates energy coupling of subsequent pulses. Specific spatial frequencies of roughness encourage absorption producing a positive feedback loop [103].
Polarization	Orientation	LIPSS are generally observed as oriented perpendicular to laser light polarization.
Scanning Direction	Uniformity	Scanning should be oriented perpendicularly or at 45° to polarization direction for high quality and regularity [109].
Spot Size	Uniformity	Spatial coherence of excited surface waves are better preserved in smaller areas[110].
Wavelength	Periodicity	Periodicity of LSFL is usually close to incident laser wavelength.

3.1.2 Pulsed laser surface modification

This section describes the manufacturing considerations in selection of a laser texturing system, then the specific design criteria are discussed for texture modification to produce superhydrophobic functionality.

3.1.2.1 Femto and nano second pulsed laser texturing systems

A major system design factor when selecting a laser for an industrial process is the pulse duration. Several advantages are associated with the use of short and ultra-short pulse lasers. The ablation threshold has been shown to decrease with shorter pulse duration [111,112] allowing for higher ablation efficiency. Because of the potential for nonthermal processing, ultrafast lasers are more suitable for applications where high precision and resolution are required such as laser

micromachining. When an areal modification is the object of process, the reduced thermal input when using ultrafast lasers enables novel nanoscale morphology and a shallower modification depth such as in the production of a LIPSS texture. However, in addition to performance, it is also important to consider the availability and cost.

The most powerful commercial femtosecond laser system at the time of writing is 300W [113] and increasing rapidly. Nanosecond pulsed lasers are now commercially available greater than 1kW. Historically femtosecond pulsed lasers have only been commercially available at low powers and repetition rates. This has meant they were not well suited for wide area surface modification due to slow processing rates. The advent of industrially suitable fibre femtosecond lasers with higher powers has enabled fast areal coverage with the use of beam scanning systems.

Polygon and galvanometer scanners are the two options for scanned beam translation, current models are able to achieve scanning speeds of up to 100 m/s [114]. Figure 3.8 shows the mechanics of galvanometer scanning which is based on two wobbling mirrors and polygon scanning which uses a rotating polygon mirror. Galvanometer scanning has become the industry standard for high accuracy and speeds, whereas polygon scanning may offer a throughput benefit because of its potential for higher speeds in applications where high surface coverage (>80%) or multiple passes are required [115]. Additional emerging optical solutions to wide area processing are laser interference patterning [116], micro lens array [117] and beam splitting with diffractive optical elements [118].

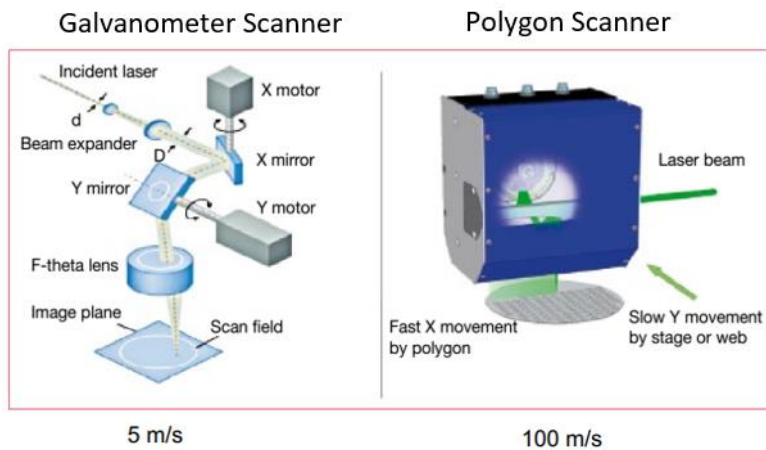


Figure 3.8: System mechanics of polygon and galvanometer scanning, image reproduced from [114]. Galvanometer scanners offer very accurate positioning however the mechanics are more complex and can be slower in some areal modification applications than polygon scanners.

Surface functionalisation using laser texturing involves imparting micro- or nano- scale surface features. Tribological applications of laser textured surfaces involve – low [119,120] and high [121]

friction surfaces, lubricant retention and lifetime enhancement [122]. This has been used for mechanical properties such as enhanced interface adhesion, anti-stick surfaces, wear resistance as well as optical surfaces such as iridescent or polarising surfaces [123]. By controlling both surface structure and chemistry of metals through laser texturing it is possible to alter surface wettability into extreme wetting states such as superhydrophobicity and superhydrophilicity.

3.1.2.2 Superhydrophobic surface modification

Laser direct texturing of superhydrophobic surfaces is a single step treatment which produces a hierarchical roughness and low surface-energy surface chemistry. A rough hierarchical micro-nano surface structure is imparted by ablative removal, the reaction of the surface with air during ablation results in the formation of a metal oxide layer. Metal oxides have very high surface energy and show superhydrophilic behaviour, however this high energy state is unstable and with time decomposes to a low surface energy state [124]. This chapter focuses on the effect of laser parameters on surface structure, subsequent chapters 4 and 5 focus on functional aspects of surface chemistry transition and wettability.

The technique first emerged in 2009 [27], with recent developments addressing the laser processing strategy, the optimisation of surface structure [73,125] and use of different metallic [126] and polymeric materials [127]. Two surface structure modes producing superhydrophobicity have emerged. This is associated with the use of either femtosecond pulsed lasers or nanosecond pulsed lasers. Femtosecond pulsed laser machining is capable of highly precise surface modification, fabrication of microprotrusions and nanoripple features have been demonstrated as shown in Figure 3.9(a) [128]. In high fluence nanosecond pulsed processing, the surface texture is mainly melt driven consisting of microscale trenches and globules as shown in Figure 4.1(b) [8].

To achieve the superhydrophobic Cassi-Baxter wetting regime liquid droplets must be prevented from contacting bare stainless-steel. This requires producing surface asperities which are tall enough to prevent suspended droplets from contacting the base of the surface texture [129]. Additionally, the surface asperities must be closely spaced enough to remove hydrophilic surface. A full surface coverage of surface texture is needed in order to avoid the water adhesion effects documented for hatch separations much greater than processed track diameter [130], whilst also avoiding the poor structure formation with high levels of hatching overlap [107].

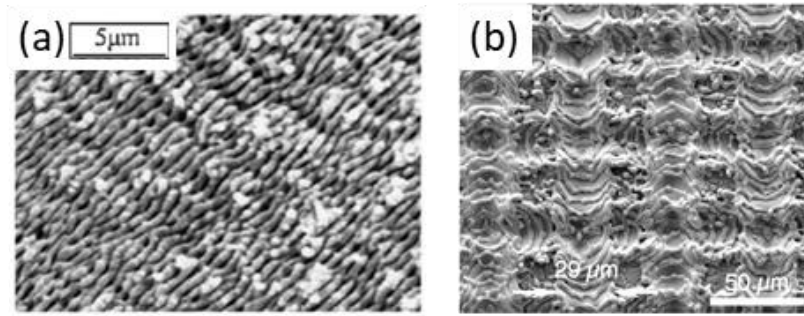


Figure 3.9: Comparison of (a) ripple like surface texture fabricated with a femtosecond laser [128] and (b) hierarchical roughness surface texture fabricated with nanosecond laser [8].

Key concepts for technology scale up involve consideration of the trade-offs between nanosecond pulsed lasers and femtosecond pulsed laser sources [130], wide area texturing through the use of scanning devices [128] and acceleration of the chemical transition mechanism [131].

Multifunctional surfaces have been demonstrated including anti-icing [126,132], anti-corrosion [133,134], anti-biofouling [135,136], enhanced condensation heat transfer [137] and oil filtering [138] functionalities. There have been several industry collaborations which have ran during the course of this PhD to translate laser texturing into industry. In particular, Tres Clean [139] which focused on self-cleaning end-use cases of the food industry and Laser4Surf [140] targeting medical components and batteries.

In this section, the theory and applications of laser surface modification have been discussed. Different ablative material removal regimes were identified based on laser intensity and pulse duration. Although modelling of laser ablation remains complex, empirical modelling can be used to predict ablation morphology for high fluence nanosecond pulsed laser processing based on the material response under threshold conditions. By irradiating stainless steel with a long nanosecond pulse under high fluence, material ejection includes artefacts of thermally driven interaction such as redeposited material and splatter.

The LIPSS surface texturing approach offers novel possibilities for functional surface manufacture due to the nanoscale surface structure and gentler thermal profile of the process. The theoretical understanding and effect of laser parameters on the fabrication of LIPSS was outlined. Currently it is challenging to fabricate LIPSS textures over wide areas due to the high sensitivity to laser parameters such as pulse overlap and beam polarisation. Experiments were led to investigate this manufacturing concern by comparing the fabrication process and functional properties of LIPSS with an industrially accessible high fluence nanosecond laser texturing approach.

The background literature into laser interaction with transparent media highlighted the challenges of ablative processing of glass such as low laser absorption and propensity for crack formation. This led the research direction into ablative processing of glass using a femtosecond laser source. The literature review highlighted the need to design the processing system to trigger non-linear absorption on the surface of the transparent media whilst thermal artefacts at high laser fluence. Femtosecond laser micromachining has historically been very slow due to the limitations of available laser sources. Using state of the art fibre laser sources in combination with beam scanning systems offers a pathway to adopt femtosecond laser glass processing into a high throughput manufacturing application, but research is needed to optimise the material removal mechanics.

3.2 Design of experiments

This section describes the development of research objectives and experimental plan to address the research aim.

3.2.1 Research Aim

- Determine the most effective laser patterning approach to produce scalable surface structuring of flat stainless steel and float glass surfaces.

3.2.2 Research Objectives

The literature review described the energetic pathway by which laser light is absorbed and leads to ablative surface structuring. Nanoscale LIPSS texturing of stainless steel and precision micro structuring of glass with transparent laser wavelengths offer novel functionalities but remain challenging to realise at an industrial scale.

Experimental work first needs to examine the use of a nanosecond pulsed fibre laser to produce microscale crater, track and texture geometry. This is the first step towards a scalable surface texturing strategy, combined with a holistic appreciation of laser material interaction mechanics. Experiments are designed to examine the role of different laser parameters on surface chemistry and surface structure. In particular, we need to better understand the effect of laser intensity on metal oxide formation and the morphology of the ablated region and redeposited material.

At laser intensities close to the ablation threshold it is possible to form submicron laser induced periodic surface structures. However, the literature highlights that this is sensitive to many components of the optical system and requires careful tuning of interaction dynamics. The theoretical basis behind LIPSS formation is examined with a focus on laser selection and manufacturability. A high patterning rate ultrafast laser platform is used to investigate the formation of these nanoscale

structures and then pattern them to form a continuous surface texture with high uniformity and regularity. The regime for LIPSS production was identified in terms of laser intensity and incident number of pulses, a future route to wide area manufacturing was identified.

It is challenging to produce microscale ablation of glass with near infrared lasers because unlike stainless steel the material is not directly absorptive of the laser light. By using ultrafast near infrared laser sources it is possible to trigger ablation through non-linear absorption, this also ensures the heat damage is sufficiently low to avoid thermal shock damage to the glass. However, the delicate window for this interaction mechanism brings concern for manufacturing viability and requires significant experimental optimisation. Experiments are used to investigate the laser parameter range available for precise structuring of glass and explore scaling the patterning approach to wide areas for later experiments focusing on fluid deposition applications.

- Study the effect of laser parameters in pulsed laser ablation of stainless steel on morphological, and compositional properties.
- Develop the theoretical basis and parameter window to manufacture a texture consisting of nanoscale laser induced periodic surface structure.
- Investigate the modification of float glass surface topography through ablative structuring with an ultrafast laser.

3.3 Method

This section introduces the details of the experiments carried out and outlines the how laser parameters and operating conditions were controlled. A full description of glass and stainless-steel substrate materials was given in Section 2.1. The laser systems and characterisation tools used in this chapter were introduced in Sections 2.2 and Section 2.4. Figure 3.9(a) explains the technical terms used in experimental work.

3.3.1 Stainless Steel Laser Processing

In order to address research objectives 2 and 3. A series of laser processing experiments aimed to fabricate a LIPSS type surface texture and a hierarchical surface texture whilst simultaneously generating insight into the laser interaction mechanics. Figure 3.9(b) illustrates the different laser processing experiments carried out on stainless steel. In experiment S1 the SPI G3 marker introduced in Section 2.2.1 was used. The stainless-steel surface was exposed to isolated laser pulses by scanning the laser at 2 m/s to produce a separation between pulses greater than the crater damage radius. The effect of varying laser power was investigated by varying the laser power from the minimum value at which damage occurred up to 15 W in increments of 1 W. The other laser parameters including

repetition rate (25 kHz), spot size ($36.4\ \mu\text{m}$) and pulse duration (200 ns) were kept constant in all experiments.

In experiment S2, continuous tracks were ablated using the SPI G3 laser marker, a scanning speed of 100 mm/s was used resulting in a pulse overlap of 90% and laser power was varied from 10 W to 20 W. Experiment S3 also investigated continuous track formation but in this case using the Laser4Surf ultrafast platform described in Section 2.2.3 in order to fabricate LIPSS. In this case an experimental matrix was executed, this matrix varied power from 0.81-4.1 W in increments of 0.41 W and scan speed from 15 mm/s up to the maximum limit of 4000 mm/s with the value doubling between each matrix increment. In all LIPSS fabrication experiments using the Laser4Surf platform the parameters specified in Section 2.2.3 were used including repetition rate (500 kHz), spot size ($30\ \mu\text{m}$) and pulse duration ($<300\ \text{fs}$)

In experiment S4 the texture types investigated in continuous track experiments in S2 & S3 were compared. Full surface coverage was achieved by scanning the beam with a hatch spacing of $58\ \mu\text{m}$ for the nanosecond laser processed surface and $21\ \mu\text{m}$ for LIPSS fabrication. This spacing was equivalent to the measured diameter of the track profile including the central depression and raised burrs. Small areas of less than $1\ \text{cm}^2$ were fabricated for SEM and XPS analysis. Following these experiments larger samples of dimension $4\times 4\ \text{cm}$ were fabricated for wettability measurement in Chapter 4.

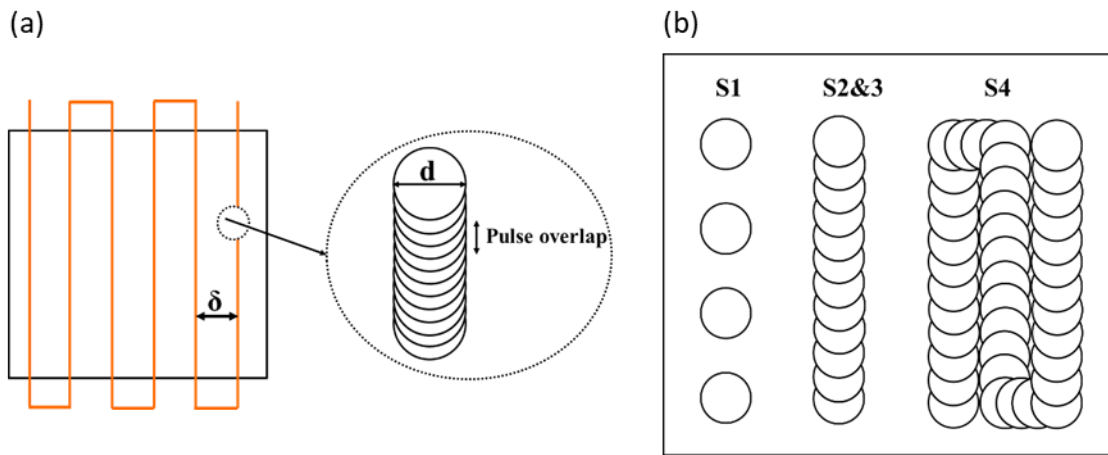


Figure 3.9: (a) Schematic illustrating laser hatch spacing - δ , pulse separation and spot size - d . (b) Overview of scanning patterns in stainless steel experiments.

3.3.2 Glass Laser Processing

Objective 3 concerned the development of a process for microstructuring of flat glass using ultrafast laser ablation. Figure 3.10 summarises the experiments conducted to achieve this objective.

Experiment G1 explored the selection of laser objective whilst operating in near ablation threshold conditions. The ultrafast laser processing platform and objectives used in experiments were described in Section 2.2.2. The beam power and vertical offset of the objective from the focal position were varied and the range of values for which ablation occurred was measured with an optical microscope. The beam power was reduced from 1.05 W in increments of 0.07 W until no ablation was observed. At each power level the vertical offset was varied firstly in increments of 1 μm and then in units of 0.5 μm as the vertical tolerance for ablation became smaller at low power.

In experiment G2, the profile of the laser ablated tracks with varying laser power was measured using interferometry to find the cross-sectional area and calculate the material removal rate. This section compared the material removal of the samples processed with stage translation to those processed with galvanometer scanning. In this experiment the same Satsuma laser sources were used operating at constant wavelength 1030 nm, pulse duration <300 fs and repetition rate 500 kHz.

Once these fundamental interaction experiments were completed the next stage was to develop a processing approach for creation of a micro structured topology with a millimetre scale footprint using multiple passes and hatching. In experiment G3, the laser power of 3.1 W, spot size of 4.81 μm and scan speed of 10 mm/s and other operating parameters were kept constant. The effect of scanning multiple passes (1x, 5x and 10x passes) and hatched tracks (5 μm 10 μm) was tested in order to produce freeform design of surface topology.

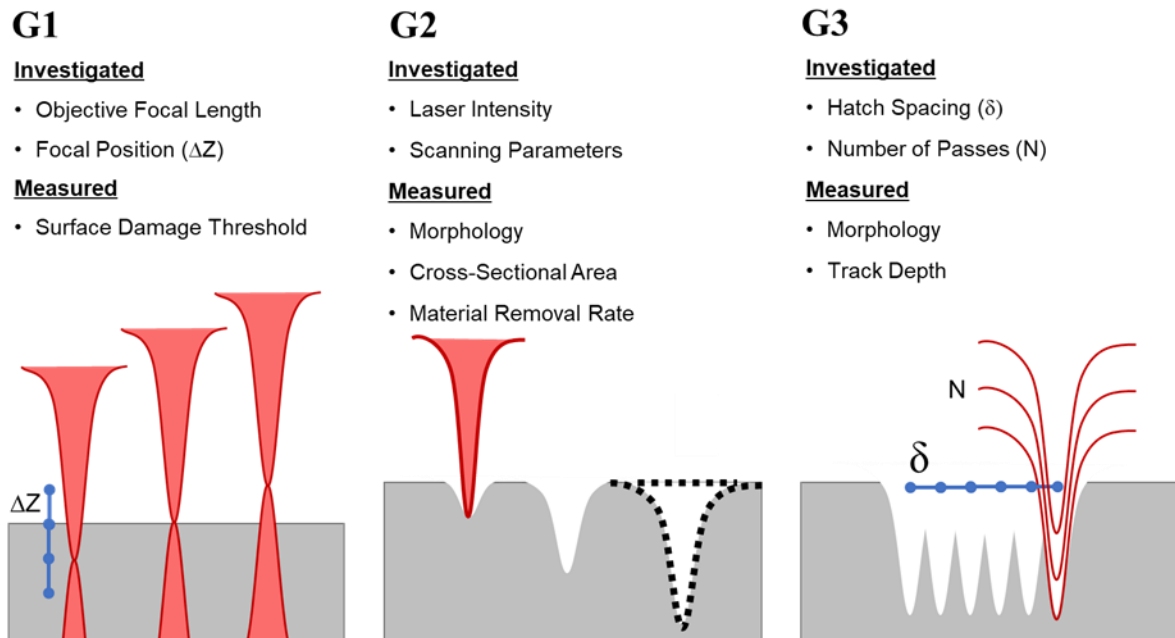


Figure 3.10: Overview of glass laser processing experiments showing experiment: G1- Identifying ablation threshold and depth of focus, G2 - Effect of varying laser fluence on etching of tracks and G3- Surface topology micro structuring with variation of scanning parameters.

3.4 Results and Discussion

3.4.1 Development of laser processing strategy for surface functionalisation of stainless steel

A laser texturing approach was developed which used a 200 ns pulsed fibre laser operating at 1064 nm, the laser was focused with a galvanometer scan head as described in method Section 2.2. The final laser texturing process involves scanning the beam in a serpentine pattern over the stainless-steel surface. Initial experiments looked at the interaction of a single pulse to assess material removal mechanics and morphology variance as applied laser intensity was increased.

3.4.1.1 Ablation of stainless steel using isolated nanosecond laser pulses

Laser intensity was increased from the minimum power for which ablation occurred from 3 W to 15 W in steps of 1 W, the resultant surface structure was characterised using SEM, EDS and WLI in order to characterise pulse crater morphology, surface chemistry, ablation crater profile and depth. The minimum laser intensity for which ablation was observed with a power of 3W or fluence of 9.55 J/cm^2 . When this threshold was exceeded ablative material removal was observed. As seen in SEM images presented in Figure 3.11, the centre of the ablation crater in all cases was observed to be smoother than the cold-rolled stainless-steel substrate. This is attributed to smoothing effects of laser induced surface melting followed by solidification. In the laser polishing process a thin surface layer is molten and surface tension causes material flow from peaks to valleys resulting in a smooth surface structure. Literature reports suggest that when long pulse durations with a longer thermalisation profile are used, LIPSS formation is inhibited by the dynamics of molten material flow and redistribution [108].

In addition to crater formation, SEM imaging highlighted thermal artefacts of the process. The presence of redeposited burrs was observed at all laser fluences. At low fluence, the burr structure was a continuous raised ring around the perimeter of the crater. At high fluence redeposited material was ejected explosively from the ablation crater redepositing onto the subject as spatter. This is attributed to the thermal effect of the long nanosecond laser pulse [141,142]. In the experimental system, the laser pulse duration (10^{-8} s) is longer than the thermal relaxation time (10^{-10} s) of the substrate material, this causes heat diffusion into the material lattice over the length of the laser pulse and result in a thermally driven interaction [143].

EDS mapping showed that after single pulse laser processing the surface chemistry remained unchanged from the stainless-steel substrate. No changes were observed and any colour changes

visible in Figure 3.11 are artefacts from the in-built analysis software of the EDS system. Less than 0.5% surface oxygen content was detected in all experiments. Literature reports show metal oxide formation due to reaction with air, however this is only observed for film texturing or when high numbers of pulses are used [144]. The relatively short exposure duration of single pulses and absence of thermal incubation means there is a lower surface temperature and less energy to trigger the reaction.

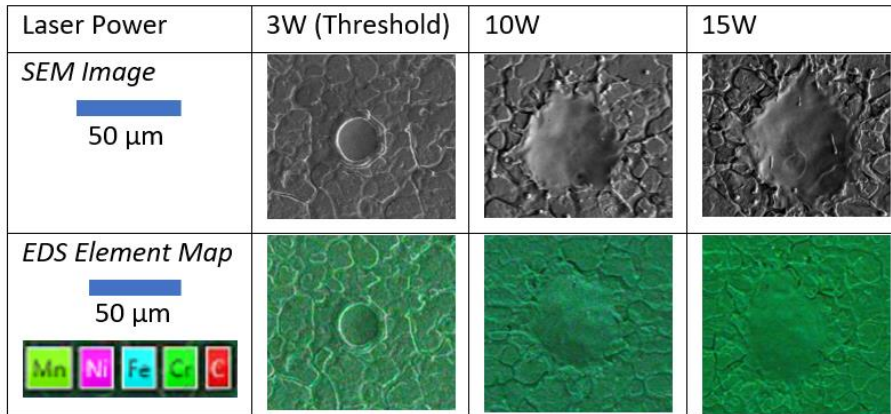


Figure 3.11 SEM images and EDS maps of single pulse laser ablation experiments. In the EDS element map the grey scaled SEM image is overlaid with colours corresponding to the location of elements detected in the EDS scan. This corresponds to the elements Manganese (Mn), Nickel (Ni), Iron (Fe), Chromium (Cr) and Carbon (C).

Interferometry was used to capture the topology profile of the ablation craters. The predictive model described by equation 3.8 was used to predict crater depth and profile variance with increasing laser intensity. The measured damage threshold conditions of (fluence - 9.55 J/cm^2 , crater depth - $1.73 \mu\text{m}$) were substituted into the model. Figure 3.12(a) compares the topology contours of the surfaces and the 2D crater profile. In the topology contours, the hemispherical shape and presence of redeposited material and splatter was consistent with the SEM observations. With increasing laser intensity from 3 W – 15 W, It was found that the crater depth increased from $1.73 \mu\text{m}$ up to $4.77 \mu\text{m}$. The width of the central ablation crater was also observed to increase with applied laser fluence from $25.0 \mu\text{m}$ at 3 W up to $44.1 \mu\text{m}$ at 15 W. This was attributed to the tails of the beam intensity profile exceeding the observed laser intensity threshold as highlighted by the predicted crater profiles.

Figure 3.12(b) compares the measured ablation crater depth to predicted results produced using equation 3.8. The effect of increasing laser fluence produces an increase in crater depth, the rate of this increase decays exponentially which is attributed to optical absorption and heat flow. The simple logarithmic relationship for crater depth and profile with limited experimental data showed good agreement with experimental results.

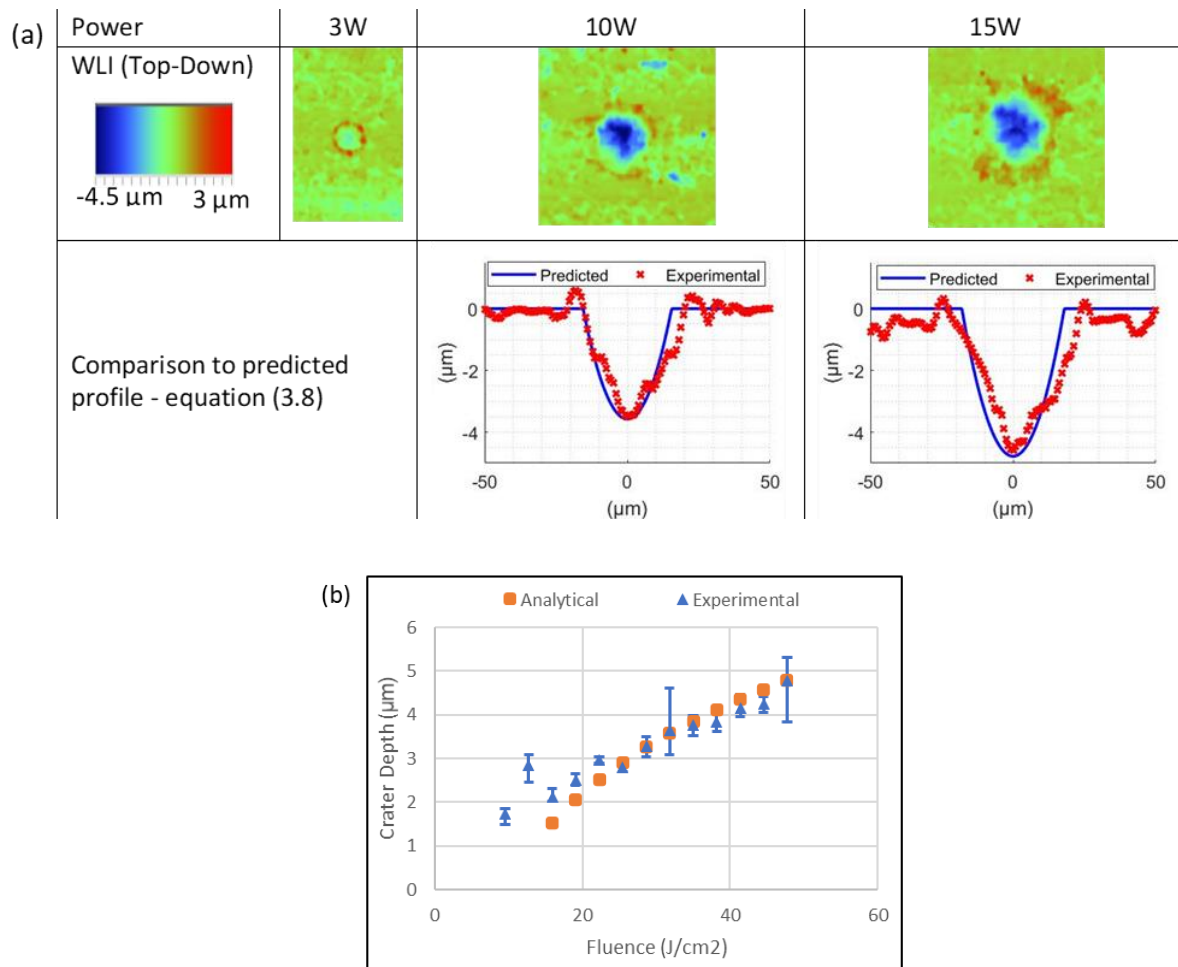


Figure 3.12 (a) Contours and measured profile from white light interferometry measurements of single pulse experiments. **(b)** Ablation depth measurement and comparison to predicted values

3.4.1.2 Production of continuous laser machined linear features

In the texturing process a full surface coverage is produced with a serpentine scan of continuous tracks as highlighted in Figure 3.9 shown in the method section. Continuous tracks were machined with varying power (10,15,20W) and with constant pulse duration (200 ns), repetition rate (25kHz) and scan speed (100mm/s). The aim of this stage of experiments was to provide an informed design of the areal surface texturing approach. The effect of modifying power and pulse duration on surface topology was assessed. As shown in Figure 3.12 (a) The profile of the continuous features consisted of: 1. Unmodified stainless-steel substrate, 2. Ablation groove with negative surface profile 3. Burr formation with positive surface profile. The height and width characteristics of three profiles were measured using interferometry. Crater depth was measured as the distance between the lowest point of the profile and the baseline height of the unmodified substrate. Crater width was measured as the width of the negative surface profile terminated on each side where the crater became burrs at the baseline height of the unmodified substrate. Burr height was measured from the highest point of the

burr to the baseline height of the unmodified substrate. ‘Width of Burrs’ was measured as the distance between where the positive burrs met the baseline of the unmodified substrate minus the crater width.

For the equivalent applied power and pulse energy used in the single pulse ablation experiments, the laser ablated tracks were observed to be deeper and wider. This was attributed primarily to the higher applied overall energy dose as well as accumulation of thermal energy in the scanning direction. The overlapping rate of pulse separation as a percentage of laser spot diameter was calculated as 90%, producing 10 laser pulses per spot. Additionally higher surface temperatures as a result of thermal incubation provide a smaller temperature gap to reach vaporisation temperature [145]. Multiple pulse burst processing has also been shown to produce a lower ablation threshold and temporary enhancement of absorptivity after the first pulse [146].

Figure 3.12(b) plots surface structure measurements with comparison to laser power. From 10-20W applied power, the track depth (H1) increased from an average value of $18.1 \pm 1.4 \mu\text{m}$ to $38.1 \pm 6.9 \mu\text{m}$. In this range, the burr height (H2) remained relatively constant increasing from $11.7 \pm 1.6 \mu\text{m}$ to $14.8 \pm 1.5 \mu\text{m}$. This meant the ratio of ablated track depth to redeposited burr height (H1/H2) increased with power. The track width (W1 - $30.24 \mu\text{m}$) was larger than the width of the burrs at W2- $19.6 \mu\text{m}$) producing a width ratio (W2/W1) of 0.65. With increasing power, the burr size became much larger resulting in a (W2/W1) ratio of 1.4. This analysis found that with increasing fluence the overall volume of material removed from the crater increases substantially, primarily through the increased depth of track. Material which redeposits forms burrs, and it is observed that with increasing fluence the burrs tend to grow in width rather than height .

After full surface coverage with tracks the effect of varying laser intensity on surface chemistry was investigated using EDS as shown in Figure 3.12(c-d). At low fluence close to ablation threshold (3.7 W) the composition remained close to the original substrate. At high fluence in the strong ablation regime, around 7% oxygen content was measured which indicated formation of metal oxides. This corroborates with the work of Lawrence *et al.* who found that in nanosecond laser texturing of stainless steel, metal oxide films of up to 489 nm thickness were formed, and the thickness of the oxide film reduced with applied laser fluence [147].

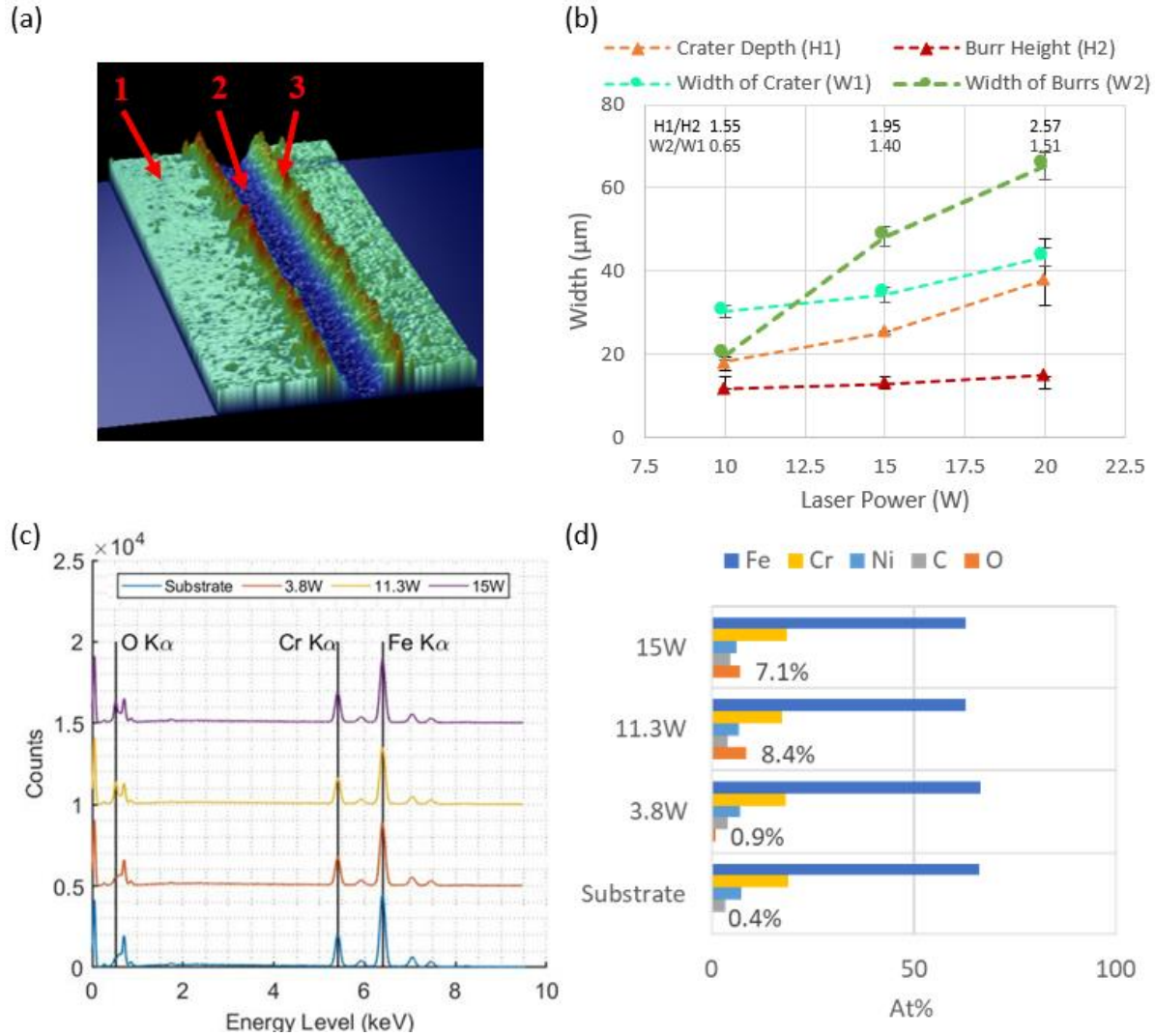


Figure 3.13 (a) 3D visualisation of ablated track morphology using parameters of average power 10W, and scan speed 100 mm/s, (b) Measurement of track morphology parameters with increasing laser fluence, (c) EDS Spectrums with major peaks labelled (d) Composition breakdown of EDS measurements in At%.

3.4.1.3 Production of ripple surface of high density and uniformity

Nanosecond laser ablation at high fluence resulted in a rough microscale surface texture based on direct write ablation and burr formation. The literature review highlighted an alternative emerging laser texturing process to fabricate surfaces with a nanoscale LIPSS texture. The characteristics of this texture are that it is shallow covering of nanoscale ripples with high density and aspect ratio.

Section 3.1.1 identified the influences on LIPSS formation from the research literature. A mirror polished substrate was used to investigate nanoscale features. This is because LIPSS have been shown to be affected by the original surface morphology [106]. Typically, femtosecond lasers are used for

LIPSS formation because the fluence must be near the surface damage threshold to avoid domination of ablation effects. Optical parameters such as the number of incident pulses and beam polarisation are used to control periodicity and orientation of LIPSS.

The Laser4Surf femtosecond laser platform was used to investigate LIPSS formation. The effect of single laser passes to produce linear tracks was explored with varying scanning speed and average power as detailed in Section 3.3.1. Visualising individual pulse ablation craters was not possible for the high repetition rate femtosecond laser system used. Four processing regimes were observed with increasing fluence which are identified as nanobubbles, LIPSS, spikes and ablation in Figure 3.14.

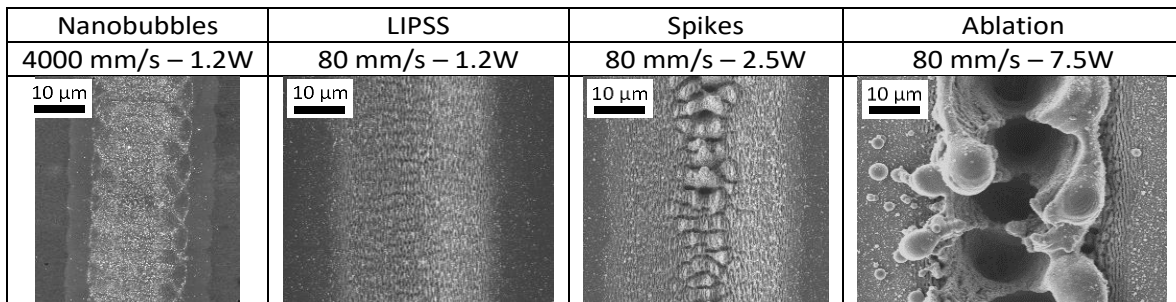


Figure 3.14: SEM images of example surfaces and laser parameters for the identified processing regimes in production of LIPSS through femtosecond laser processing of stainless steel

The most-gentle modification regime of nanobubbles was observed at very rapid beam scanning with parameters of 4m/s scanning speed and 1.2 W average power. The hemispherical outline of the beam spot is visible corresponding to a beam overlap of 73.3%. Formation of ripples were visible however they were not dense or consistent in shape. By lowering the scan speed to 80 mm/s resulting in a pulse overlap of 99.5% the optimum LIPSS regime was found shown in Figure 3.13. This consisted of mild ablation with micro channels of depth 1-2 μm , the microchannels were decorated with high density LIPSS. The period of the LIPSS was measured using a Matlab program [148] and was found to average 747 nm indicating they are categorised as low-spatial frequency LIPSS. The LIPSS were oriented in the path of beam scanning and perpendicular to beam polarisation which is consistent with literature reports [103]. When the fluence was increased further ablation became the dominant effect first resulting in a protruding spiky central channel and then in strong ablative material removal.

These findings showed that to produce LIPSS requires careful control of the energy dose and number of incident pulses, as a narrow processing window is available to produce high density LIPSS whilst avoiding ablation. In order to scale the LIPSS fabrication parameters to wide areas the number of incident pulses is critical. For example, to scale 6250 pulses per mm to a scan rate of 1 m/s a repetition rate of 6.3 MHz is needed. This is within the range of current cutting edge high power-high

repetition rate femtosecond fibre lasers [149,150] demonstrating a viable pathway for industrial adoption.

3.4.1.4 Comparison of surface texture modification approaches

To fabricate a surface texture a hatched pattern of tracks is used as shown earlier in method Section 3.3.1. A full surface coverage of LIPSS was created and compared to a hierarchical surface texture fabricated with a nanosecond laser. Surfaces were textured by scanning in a serpentine pattern using the parameters developed through individual track machining experiments. For the nanosecond laser processed texture, the hatch separation between tracks was specified as the total width of the crater and burrs shown in Figure 3.12(b) +10% to account for deviation. For the LIPSS surface the hatch spacing was adjusted experimentally and a hatch spacing of 21 μm was selected as the surface with the best uniformity and density of LIPSS. These processes were developed firstly to investigate surface structure of the two texture modification approaches and enable later functional experiments concerning the wettability of surfaces after texturing. Appendix A shows the surfaces with different hatch spacings. Table 3.2 summarises the laser parameters used to create these surfaces.

Table 3.2: Summary of laser processing parameters used for surface texturing experiments

Parameter Set	Pulse Duration	Power	Repetition Rate	Scan Speed	Spot Size	Hatch Spacing
Hierarchical	200 ns	10W	25 kHz	350 mm/s	39	58 μm
LIPSS	350 fs	1.5W	500 kHz	80 mm/s	15	21 μm

Clear distinctions were observed between the micro and nanoscale topology of the two texturing approaches as illustrated in SEM images shown in Figure 3.14 and roughness measurements in Figure 3.15. The LIPSS surface texture was mainly rough only on the submicron length scale of the ripples with measured roughness of R_a 0.68 μm . The nanosecond laser processed surface resulted in a hierarchical roughness with R_a 2.94 μm . This consisted of microscale trenches covered with redeposited molten particles. At the nanoscale, the surface was covered with fine hairlike structures which have been shown to be caused by metal oxidation [144]. This change in chemistry through oxidation was shown in Section 3.4.1.2 using EDS experiments. In laser texturing of LIPSS on stainless steel Gomez-Arandzi *et al.* also found that oxidation occurs however it is less pronounced at low fluences [148].

As reported in Figure 3.14(c) the topography factor was calculated from the ratio of surface area to projected area. This is a key factor for the wettability of rough surfaces as outlined in discussion of the

Wenzel model 2.4.4. Although the LIPSS surface measured with interferometry showed a slightly high topography factor of 1.35 compared to 1.17 for the hierarchical surface, this doesn't fully account for the nanoscale influence which would cause the surface area to be substantially higher in both cases.

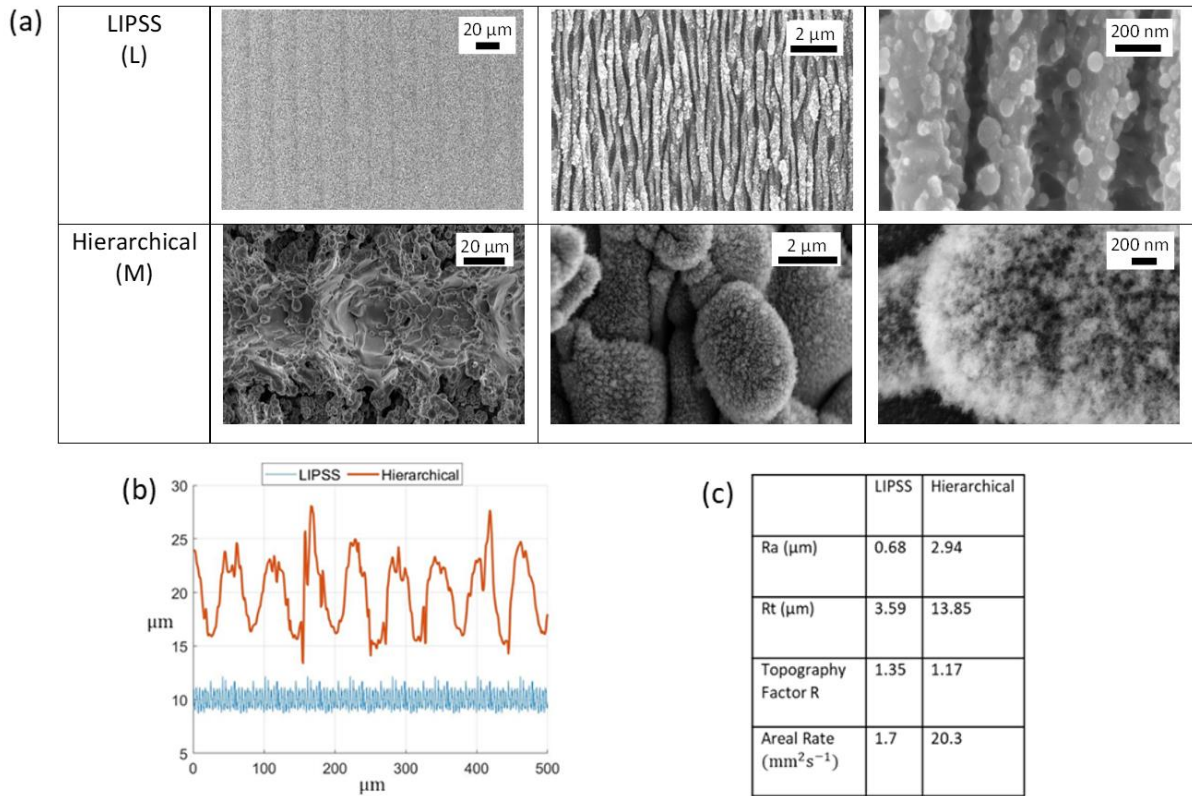


Figure 3.15: (a) Comparison of SEM images of LIPSS and hierarchical surface textures. (b) Superimposed interferometry surface profile of the two texture types. (c) Summary of roughness measurements.

It is particularly important to assess the overall manufacturability of the two processing approaches in terms of the time to fabricate the surfaces, durability of the modification and industrial feasibility. Although the use of a galvanometer scanner enabled relatively fast production of LIPSS (1.7 mm²/s), the areal processing rate of the nanosecond processing technique remained substantially higher (20.3 mm²/s). This could be balanced in future work as more powerful femtosecond lasers with MHz repetition rates become available or with the use of alternative optics configurations such as line focused beam profile [106].

Because a LIPSS surface texture has a smaller modification depth and lower thermal input to the material it could be used to texture thinner substrates than the nanosecond processing technique. Experimentally a LIPSS texture was fabricated onto stainless-steel foils with thickness 100 μm whereas with high fluence nanosecond laser texturing the minimum thickness was 300 μm after which

the sheet became buckled. However, LIPSS fabrication is sensitive to surface finish and the initial mirror polishing stage may add expense to the overall process. Clearly, very different attributes were found when comparing the two laser texturing approaches. Chapter 4 explores how these surface textures modification approaches compare in terms of functionality as superhydrophobic surfaces.

3.4.2 Development of laser processing strategy for ablation of float glass using a femtosecond NIR laser

The literature review highlighted that laser ablation of clear soda-lime glass is challenging with near infrared fibre lasers because of its low absorption at the laser wavelength. One approach is to use femtosecond lasers which trigger non-linear absorption processes in the transparent media through tunnelling ionization or multiphoton ionization. However, achieving the very high photon density for these effects necessitates the use of pulse durations less than 10 picoseconds and focusing the laser to a tight spot through high numerical apertures machining objectives [151].

In order to develop a laser processing strategy and determine the optimal parameters for material removal several experiments were carried out. The tolerance bands for machining operations were examined. The use of different laser objectives and scanner configurations were assessed for their material removal rate. By analysing laser machined tracks the cross section could be observed and the material removal rate was calculated. Following these investigations into manufacturing viability, a multipass structuring approach to ablate microchannels into flat glass surfaces was used to produce topology and wettability patterned surfaces for fluid deposition experiments in chapter (6).

When operating at high repetition rates, incubation effects between laser pulses means that a lower threshold for ablation occurs in comparison to single pulses. To assess the multipulse threshold for ablation of glass using the Satsuma laser a processing speed of 1 mm/s and repetition rate of 500kHz were applied with varied fluence and objective focal length.

3.4.2.1 Identifying ablation threshold and depth of focus

Short focal length lasers are needed to achieve the high photon density to ablate glass however this means they have a short depth of focus. The depth of focus in which ablation was possible for a given optics configuration was assessed through a geometric method [152].

A series of tagged snake patterns were machined into the glass substrates. At each section of the snake, marked by the diagonal or vertical tags in Figure 3.16(b), the working distance between objective and substrate was decreased by ΔZ . The resultant surface damage indicated the interaction at different working distances. The strongest ablation occurs at the focal point, and the depth of focus

was judged by the vertical range of objective positions for which ablation was observed. The laser intensity was lowered from 2.1 μJ pulse energy until below threshold.

Two laser objectives were tested for machining, the input beam diameter was ~ 6 mm. Firstly, the Comar 08-0X-05 22x with 8 mm focal length and calculated spot diameter 1.92 μm . Secondly, the Thorlabs LMU 10x with 20 mm focal distance and 4.81 μm spot diameter. Figure 3.16 shows the results of varying laser intensity on depth of focus for which surface damage was observed.

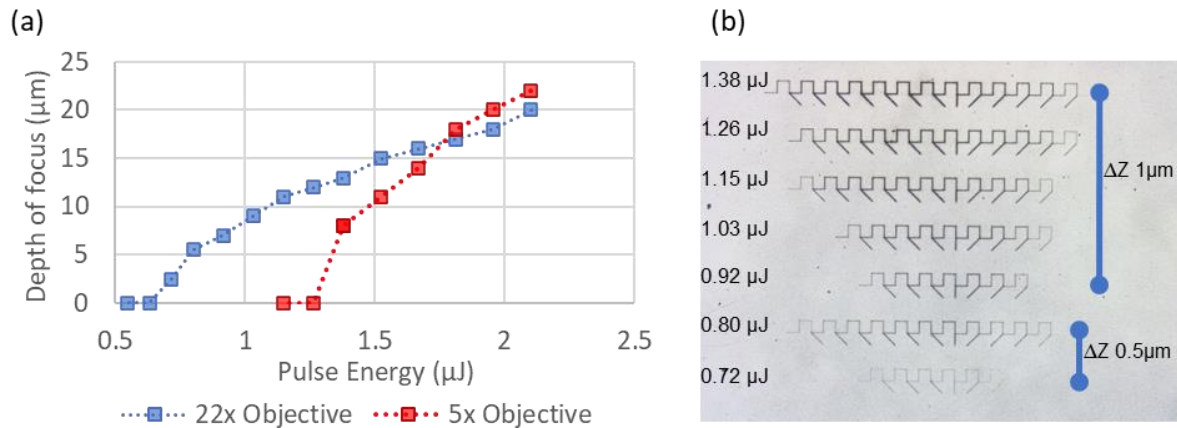


Figure 3.16: (a) Plot of depth of focus over which ablation occurred for 22x and 5x laser objective (b) Images used for geometric depth of focus determination with the 22x laser objective.

The Comar 22x objective presented a lower surface damage threshold of 0.716 μJ or threshold fluence value of 12.4 J/cm^2 , at this laser intensity there was a very tight depth of focus of 2.5 μm . In these near threshold conditions using the high numerical aperture objective there was some evidence of emerging ripple-like structures, however extreme sensitivity to depth of focus at low fluence made this technique difficult to investigate consistently experimentally, particularly when wide area modification was desired.

The Thorlabs objective required a higher pulse energy to achieve ablation of 1.38 nJ, the calculated fluence of 3.80 J/cm^2 due to the larger beam spot size and a longer threshold depth of focus of 8 μm was measured. The surface structure observed in these conditions indicated ablation in the strong fluence regime. For both objectives, the use of higher intensity beams led to a greater depth of focus with a Z-range tolerance of 20 μm or greater measured for both objectives at 2.1 nJ pulse energy.

This experiment highlighted the sensitivity of the laser process to variations in the Z-axis. A confocal probe was used to assess the flatness of the glass substrate surface, it was found that the sample had a bowed shape with variation in buckling of 8 μm over 30 mm. Future research in near threshold ablation of glass over wide areas requires flatter glass and a better levelling approach as the manual tilt table was insufficient to achieve high precision tilt alignment. The Comar depth of focus at the

ablation threshold of $2.5\ \mu\text{m}$ equates to a 0.06° tilt tolerance over a $1\ \text{cm}$ area, the equivalent tilt tolerance for the Thorlabs objective operating at threshold conditions was $8\ \mu\text{m}$.

3.4.2.2 Effect of varying laser fluence on etching of tracks

Next the effect of modifying laser fluence and incorporating rapid beam scanning on material removal was assessed through measurement of track cross-sectional area. 2 machining setups were tested, firstly using the Comar 22x optic with stage translation at $1\ \text{mm/s}$, secondly a galvanometer scanned beam with rate of $10\ \text{mm/s}$ and $80\ \text{mm/s}$. Figure 3.17(a) plots the cross-sectional area of tracks machined with the specified conditions and varying laser intensity, Figure 3.17(b) shows the morphology and Figure 3.17(c) the track profile.

In near threshold conditions using the Comar optic the cross-sectional area was measured to be close to zero. The neutral cross sectional area for near threshold ablation for powers less than $1.1\ \text{W}$ was attributed to redeposition and glass swelling which may occur due to chemical outgassing or void formation below the glass surface [153]. There was some indication of ripple-like structures forming as shown at point W ($1.1\ \text{W}$ or $132.2\ \mu\text{Jcm}^{-2}$). As intensity was increased, an ablation trench was formed resulting in a negative cross-sectional area. The largest track cross sectional area of $15.4\ \mu\text{m}^2$ was produced at point X in the surface profile shown in Figure 3.17(c), this track was produced with a laser power of $4.1\ \text{W}$ equivalent to fluence $132.2\ \mu\text{Jcm}^{-2}$.

Using the galvanometer scanner setup, the beam expander in the optics train was set to its highest value to produce the tightest focus possible with $8\ \mu\text{m}$ spot size. A higher damage threshold was observed with $2.1\ \text{W}$ or $4.1\ \mu\text{Jcm}^{-2}$. Laser intensity below this value produced modification in the bulk of the material rather than the surface as observed by [154] and shown in Appendix A. This is attributed to beam self-focusing, the nature of the in-volume modification is through void formation due to thermal effects [155].

For both $10\ \text{mm/s}$ and $80\ \text{mm/s}$ scan speeds the highest cross-sectional area of removed material occurred at power $3.3\ \text{W}$ or fluence $6.6\ \mu\text{Jcm}^{-2}$. The highest cross sectional area value for each set of scanning parameters was used to calculate the optimal material removal rate as annotated on Figure 3.17 (a). The use of a galvanometer scanner improved the material rate by 2 orders of magnitude to $1.2\ \text{mm}^3\text{s}^{-1}$ demonstrating that rapid ablation of float glass is possible in future research. A high power was required to trigger surface absorption which meant all ablation occurred in the strong fluence regime.

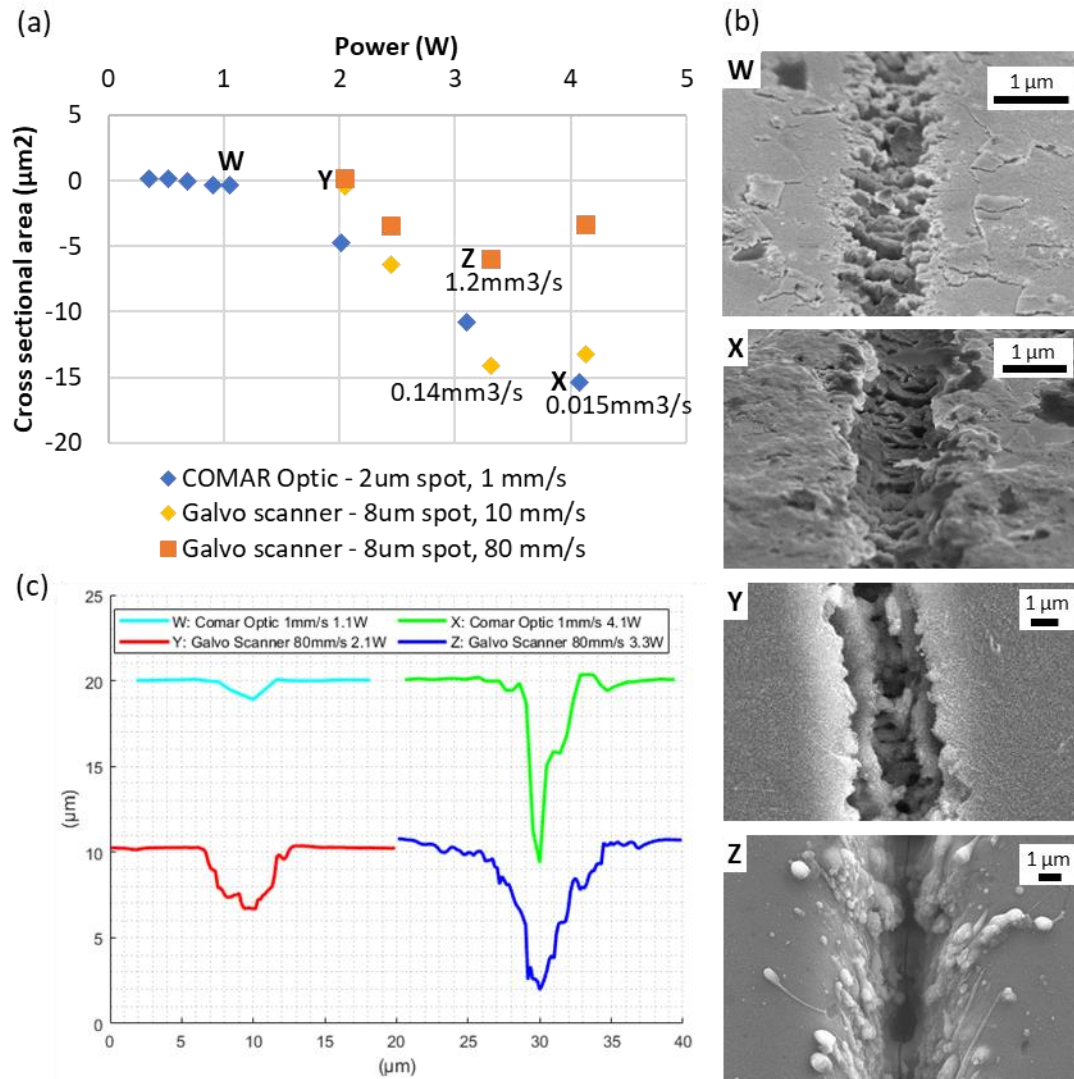


Figure 3.17: (a) Plot of track cross sectional area variance with power for the laser optics configurations explored. (b) SEM microstructure images of points W-Z. (c) Interferometry profiles of points W-Z.

3.4.2.3 Surface topology microstructuring with varying hatch spacing and number of scanning passes

The initial investigation into single pass track ablation was used to develop a strategy to etch microchannels into glass with free selection of pattern size ultimately targeting a pattern geometry of 10x1 mm. To produce microchannels with these dimensions required multiple scanning passes. The effect of scanning strategy on surface structure was tested using interferometry and SEM imaging. The number of scanned layers (1,5,10) at constant focal position and hatch spacing in intervals equivalent to 1x and 2x of the beam spot size ($\sim 5 \mu\text{m}$) were tested. The Thorlabs LMU 10x objective at 10 mm/s scan speed operating in the strong ablation regime with power of 3.1 W was used because

of the high depth of focus and material removal rate at high fluence. Otherwise, constant laser parameters were applied as outlined in Section 3.3.2.

Figure 3.18 presents the profile and morphology produced by this investigation. Track morphology was clearly in the strong fluence regime for all cases due to the surface roughness and redeposited material. From 1-5 passes scanned in a single track, the peak track depth was found to increase from 0.6 μm to 2.6 μm , after 10 scans the depth was 3.6 μm . Very similar track depths were also obtained when tracks were patterned with a 10 μm hatch spacing as there was no interaction between hatching passes. When a hatch spacing of 5 μm with 5 passes was applied, the track depth was 5.8 μm which was substantially larger than without overlapped hatching.

This interaction is attributed to stronger laser absorption and interaction with the diffuse rough surface created by the first pass compared to the flat glass. Although the depth of tracks was within the measured depth of focus ($>20 \mu\text{m}$) for all test cases, to machine deeper channels in future work may require adjustment of the focal position with each pass.

For the target dimensions of 10x1 mm tracks, the overall processing time with 5 μm hatch spacing, 5 passes and scan speed of 10 mm/s was 17 minutes, although this was slow future work could utilise the proof-of-concept results for high fluence ablation with galvanometer scanning to enhance the material removal rate.

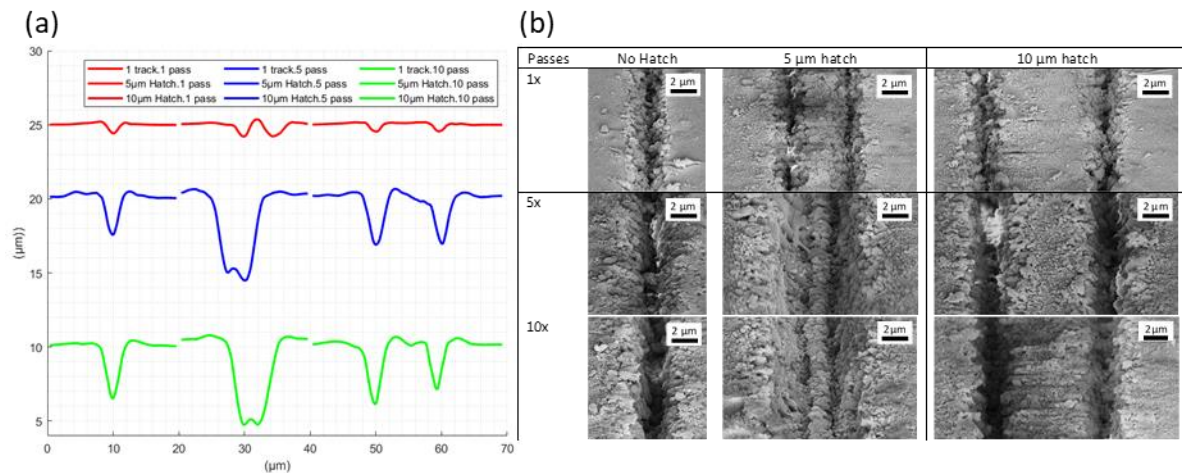


Figure 3.18: (a) WLI topological profiles and (b) SEM images at 45° imaging angle of surfaces with varying laser hatch spacing and number of passes.

The processing approach developed for micromachining of glass was limited by equipment availability to the use of femtosecond NIR laser beams. To progress the approach developed in this thesis towards industrial applications calls for further improvement in processing rate and freedom of topology control. The use of picosecond lasers is attractive for high rate glass micromachining because of their high peak power and industrial availability. Additionally they are significantly less complex, more reliable and lower cost than typical femtosecond lasers [156]. Picosecond lasers have seen strong adoption by industry for applications in micromachining of chemically strengthened glasses and thin glass [157]. Using an alternative wavelength with high laser absorption by the glass substrate could avoid the need for nonlinear laser interaction and improve process elements such as the high sensitivity to laser depth of focus observed in section 3.4.2.1. Shin *et al.* recently demonstrated crack-free groove formation using a UV nanosecond pulsed laser [158]. In this study they used a laser with a fundamental wavelength of 1064 nm, third-harmonic generation was used to produce a laser beam of 355 nm wavelength. This is attractive compared to an ultrafast laser approach because of the lower cost per output power and high material removal rate.

3.5 Conclusion

In this chapter, the fundamental theory underpinning pulsed laser materials was outlined, this highlighted direct and linear absorption processes and the impact of laser parameters such as pulse duration and wavelength on absorption. Processing regimes such as strong and gentle ablation were identified and the mechanism of LIPSS formation was discussed with respect to manufacturing considerations such as initial surface finish and areal patterning rate.

Single pulse ablation experiments were used to investigate material response in a simplified experimental system. At the threshold fluence of 9.55 J/cm^2 an ablation crater of $1.73 \text{ }\mu\text{m}$ depth was formed. An empirical model showed that this foundational information could be used to predict the crater depth at high fluences due to the logarithmic decay of laser light. This led to processing of track and texture geometries with direct write laser ablation.

Using a 200 ns laser pulse, raised edged burrs were formed due to material thermalisation. The height and width of the burrs with respect to the dimensions of the laser ablated channel were analysed. With increasing laser fluence the laser ablated tracks became deeper whilst maintaining width close to the beam spot size, the burrs tended to grow laterally whilst showing a relatively small increase in height. The measurements of single tracks were used to develop a laser texturing process with maximum surface coverage and feature aspect ratio to enable superhydrophobic properties. Laser patterning in near-threshold conditions using a linearly polarised femtosecond laser source was used to investigate formation of a LIPSS surface texture. The optimum parameters for fabrication of LIPSS on stainless steel were power of 1.2 W with an overlapping rate of 6.3 pulses per μm . The period of

the LIPSS was analysed as 747 nm and a full surface coverage was created by optimising the laser hatch spacing to 21 μm which resulted in an overlapped region 60% of beam spot size.

Laser processing of glass firstly explored the intensity and focusing tolerance band available to trigger non-linear absorption using a femtosecond near-infrared laser source. Ripple-like structures were found in near threshold conditions of 0.13 mJcm^{-2} laser fluence using an 8 mm focal length objective, however the short 5 μm depth of focus in these conditions created a high sensitivity to variations in surface form. Microchannels were ablated into the flat glass surface using a longer focal length lens objective operating in the strong ablation regime, the use of overlapped hatched laser passes allowed for deeper channel depth of up to 5.8 μm . The use of a galvanometer scanning system was investigated in order to facilitate future research scale up of the laser processing technique. A key finding here was that although the track cross sectional area and aspect ratio were smaller when fast scanning was used, the material removal rate was 2 orders of magnitude greater.

4 PROGRESS IN FUNDAMENTAL UNDERSTANDING OF LASER TEXTURING FOR SUPERHYDROPHOBICITY

4.1 Chapter Introduction

In this chapter, experiments are described to investigate the fabrication of superhydrophobic surfaces through laser texturing. The primary focus of this work is to impart a self-cleaning functionality to stainless steel 304. The approach has been the subject of significant international attention, but the research presented here focuses on an area where there is still significant uncertainty, the fundamental understanding of transient surface chemistry reported after laser processing. The general studies and findings presented are further developed with application-focused experiments exploring hybrid laser-chemical treatment. Finally, to analyse the industrial viability of laser texturing, the technical challenges to enable wide area manufacturing are explored and the position of this approach in the landscape of technology readiness and competing approaches is described.

4.2 Literature Review

Chapter 3 introduced the use of laser texturing to control surface structure and chemistry, some of the manufacturing considerations in fabricating superhydrophobic surfaces through laser texturing were outlined. Now, the research literature concerning the functional impact of the laser processing technique is examined.

4.2.1 Initial observations of hydrophobic transition and early papers

The first studies demonstrating laser texturing of superhydrophobic surfaces, noted in the previous chapter, showed that after laser processing the surfaces did not immediately have a superhydrophobic response but required an ageing process [27]. This transitional period for the surface wetting behaviour of the laser processed metallic surfaces to shift from hydrophilic to a stable hydrophobic state with exposure to ambient air is now widely reported, as detailed in table 4.1.

4.2.2 Duration of transition

A wide range in the length of transition periods has been observed, the ageing times to reach a steady state wetting angle varied significantly from just a few days to over a month. Kietzig in particular showed that the regression coefficient used to describe the rate of transition varied substantially both in terms of substrate material and applied laser fluence [27].

Table 4.1: Summary of laser texturing of stainless steel for superhydrophobicity studies

Study Citation	Stainless Steel Grade	Structure type & Pulse duration	Final Contact Angle	Transition Period
Bizi-bandoki <i>et al.</i> 2013 [159]	X40Cr14Az	Ripples, 125 fs	130°	3 days
Kietzig <i>et al.</i> 2009 [27]	304L	Ripples, 150 fs	146°	5.25 days (calculated)
Tian <i>et al.</i> 2016 [160]	304	Hierachical 34ns	154°	10 days
Ta <i>et al.</i> 2016 [130]	304S15	Hierachical, 200ns	154°	13 days
Gregorčič <i>et al.</i> 2017 [144]	316L	Hierachical, 95 ns	153°	30 days
Trdan <i>et al.</i> 2017 [80]	316L	Hierachical 40 ns	168°	1 month

Table 4.1 collates the reported transition periods for a number of studies showing laser texturing of stainless steel for superhydrophobicity. Several studies have reported continual trends such as longer transition duration with increasing laser fluence [27,130]. However, the far larger difference in transition duration between ripples and hierarchical surface structures has not previously been established. Some of the variance is likely to be multi-faceted in origin due to the large number of potential surface chemistry influences. Current studies have not effectively reported the environmental conditions during storage. Several studies have shown that small variances in storage conditions may cause significant variance in wettability such as storage in polyethylene bags, solvent exposure [161] and cleaning process [162] and composition of storage atmosphere [163].

4.2.3 Chemical mechanism of transition

The research field is in general agreement that the morphology of the laser textured surface does not change with air exposure, this indicates that the cause of the transition is due to chemical reaction of the surface with air. However, the chemical pathway of this transition continues to be contentious. Recent investigations have pointed towards adsorption of airborne organic material to be responsible, although a nuanced understanding has not been achieved [1][131].

Potential chemical processes underlying the transition are summarised:

- Partial surface deoxidation
- Removal of surface water and creation of hydrophobic functional groups
- Decomposition of CO₂
- Adsorption of airborne organic molecules

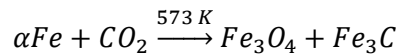
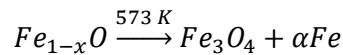
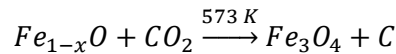
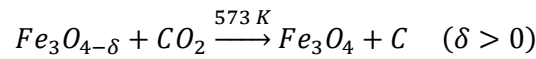
Immediately after laser processing of steel in ambient conditions, the metal oxides formed have a highly polar electronic structure induced by coordinate unsaturation of the metal elements. This favours the formation of hydrogen bonds with interfacial water, high adhesion forces and consequently a hydrophilic response [165]. It has been shown that this hydrophilic property can be maintained permanently by attaching hydrophilic functional groups to the surface or through a simple water boiling treatment process [166]. The action of water boiling treatment has been shown to further oxidize the underlying metal and attach polar hydroxyl groups to the surface. A relevant study examined the interaction of pristine aluminium oxide wafers with water vapour [167]. The pristine surface was shown to be composed of unsaturated Al atoms acting as Lewis acid sites and unsaturated oxygen atoms acting as Lewis base sites, when exposed to water vapour these sites are quickly hydroxylated and effectively passivated. This is the suggested cause of the stability of the superhydrophilicity in the case of boiling water treatment. It has a further implication for contact angle measurement, once a surface has been exposed to water in the measurement process it will be transformed chemically.

Deoxidation has been proposed as a potential mechanism for laser texturing of copper as XPS experiments have shown the ratio of CuO to Cu₂O increased over time after last processing [73,168]. However, all metal oxides are intrinsically hydrophilic [124] and therefore not solely responsible for the hydrophobic transition mechanism. The behaviour of laser induced metal oxides during hydrophobic transition has been investigated further in experimental work for the case of stainless steel.

In a study comparing superhydrophobic laser texturing of aluminium and steel [159], XPS measurements were compared before processing and six days after processing. The study found that the surface carbon content of stainless steel actually decreased during this time period from 68% to 58% and attributed the hydrophobic transition to removal of a thin film of water. However, it is very likely that the surface before processing had some adventitious carbon contamination which was removed by laser processing. Even though the initial surface had a high content of nonpolar carbon, it was smooth and no functional properties were observed, as explained by the wetting regime theory outlined in Section 2.3. This means a valid experiment should have included an XPS measurement immediately after laser processing.

4.2.4 CO₂ decomposition

CO₂ decomposition to form amorphous carbon is another proposed mechanism to explain the transition period. The laser texturing process results in the formation of surface-active magnetite Fe₃O_{4-δ} (0 < δ < 1) which is a non-stoichiometric oxygen deficient iron oxide scale. Active magnetite has been found to catalyse the dissociative adsorption of carbon dioxide [169]. Carbon monoxide and carbon are formed with oxygen anions transferred into the lattice vacancies to form a stoichiometric metal oxide such as Fe₃O₄. This reaction has been shown to happen very slowly at room temperature which explains the gradual transition. Wan suggested the reaction pathway for this mechanism under low temperature heat treatment [170]:



CO₂ reduction on metal oxide surfaces has been experimentally proven possible [171]. In this study an amorphous carbon thin film was shown to form at FeO sites when exposed to a partial pressure of CO₂ gas, the thickness of this layer was found to increase with CO₂ pressure and exposure time up to a maximum of 3.7 nm. The authors of the study noted that in their XPS measurements the C 1s peak of the deposited film was 285 eV which is closer to a typical hydrocarbon peak (285 eV) than an amorphous carbon or graphite peak (284.4 eV).

These findings suggest that CO₂ reduction is evidentially possible. However, it does not necessarily mean that the process underpins the superhydrophobic transition. The primary argument against this

mechanism is that CO₂ is a very stable molecule with a high activation energy, this suggests the process is unlikely to occur in air or would require a very long time.

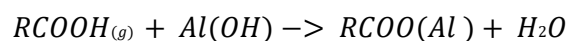
4.2.5 Hydrocarbon adsorption

Adsorption of atmospheric hydrocarbon contaminants occurs readily for a variety of materials [172–175] and systems, it is typically associated with a small increase in contact angle for a smooth surface. It is anticipated that this well-observed process also occurs during air exposure of laser textured metals and is responsible for the hydrophobic transition.

The surface formed after laser irradiation of metallic substrates is highly non-equilibrium, possesses a lot of defect sites and high surface energy, which gives rise to the initial hydrophilic response [133]. Chemical and physical adsorption processes are driven by reducing the Gibb's free energy of the surface and diminishing surface energy [124]. The high surface energy and presence of polar sites in the laser textured surface and terminal groups of airborne organic molecules drive an energetically favourable adsorption process [126,164,176]. This means polar metal oxide sites allow chemisorption of polar groups such as alcohol, carboxylate and carbonyl.

Long *et al.* [131] studied the wettability transition of laser textured aluminium stored in a range of atmospheres. When the textured samples were kept in N₂, O₂ and CO₂ atmospheres no wettability transition occurred, and the substrate maintained superhydrophilic properties. A superhydrophobic response was observed when the surfaces were stored in air and in a hydrocarbon rich atmosphere. The hydrocarbon rich atmosphere was created by storing a drop of a volatile organic (4-MethylOctanoic Acid) in a sealed container. The hydrocarbon rich atmosphere additionally showed a much faster transition of only 8 days compared to 30 days in air.

After laser processing of aluminium Cardosa *et al.* found that the surface was hydroxylated with exposure to ambient water vapour as OH- groups were detected through XPS [177]. The surface density of OH- groups has been shown to be a major factor governing the adsorption of organic substances to metal oxide films [178]. This suggested the following reaction for carboxylic acid chemisorption to the metal surface through interaction with the OH- groups:



It is hypothesized that this process is not unique to aluminium but common to other laser textured metals including the focus of experimental work on stainless steel. Evidentially it is seen that although varying in duration, the same form of superhydrophilic-superhydrophobic transition with air exposure has been observed for a number of metals and alloys each with

different chemical, catalytic activity and crystallographic structure [27,124,179]. There are some important differences between studies, with stainless steel Kietzig *et al.* [27] did not observe the same inhibitive effect when storing in a CO₂ atmosphere as Long *et al.* did with aluminium, Kietzig *et al.* actually observed a more hydrophobic final contact angle compared to air exposure. It is important to ascertain whether this is due to a different chemical mechanism in stainless steel or error such as unintended introduction of hydrocarbon species. Previous authors have observed that small amounts of hydrocarbons may be introduced by oils and lubrication in vacuum pumps and seals [180].

4.2.6 Heat treatment

Several approaches have been shown to improve the rate of transition such as variation of the storage atmosphere [131], storage in high vacuum conditions [71] and heat treatment in air [166] or in solvent immersion [162]. Heat treatment in air is a particularly attractive approach due to exhibiting the shortest cycle time, and safety in addition to manufacturing integration benefits of equipment availability and simplicity.

The effect of accelerating the rate of hydrophobic transition of nanosecond laser processed surfaces through heat treatment has been shown by several studies using temperatures in the range of 100-240°C. Heat treatment at 100°C for 8 hours after laser processing of stainless steel was shown to substantially accelerate the wetting transition period from several weeks to 20 hours [181]. In the case of aluminium an optimised heat treatment temperature of 200°C formed superhydrophobic properties in 6 hours [182]. Chun *et al.* [168] showed the fast fabrication of superhydrophobic surfaces on copper using a nano second laser. By annealing at 100°C both with and without immersion in ethanol, a much faster transition to superhydrophobicity was observed occurring in less than 4 hours. Anhe *et al.* found that if the superhydrophobic property was modified to hydrophilic through ultrasonic cleaning, further cycles of heat treatment in ethanol could renew the hydrophobic property [183].

It is possible that there is an optimum temperature beyond which the hydrophobic transition is impeded. Moradi *et al.* [184] showed that heat treatment at 700°C for 30 minutes of flat and laser processed stainless steel surfaces resulted in higher level of oxidation for both, hydrophilic contact angles of <10° were reported for the laser processed surface. Heat treatment at 240°C after laser texturing has even been recently shown to allow modify intrinsically superhydrophilic glass surfaces to produce superhydrophobic surfaces [185]. In this case the heat treatment was suggested to accelerate the adsorption of organic material to the surface.

Although these studies were effective in showing a rapid enhancement of transition rate, they did not explore the stability or durability of superhydrophobic properties in comparison to ambient transition or a chemically treated superhydrophobic surfaces. Additionally, the reported chemical mechanism has varied between with each paper reporting different mechanisms, respectively deoxidation for laser processed copper [168,183], hydrocarbon adsorption for aluminium [182] and CO₂ decomposition for stainless steel [181].

4.2.7 Hybrid laser texturing processes

A hybrid laser texturing process is defined for the purposes of this thesis as a 2-step process involving first laser texturing and then a post-process chemical treatment differentiated from single step laser texturing and exposure to ambient conditions. Chemical treatment can be applied through several physical and chemical deposition approaches such as drop casting, adsorption from solution, vapour transfer, chemical vapour deposition and sputtering. This approach has been used both as an investigative approach to probe adsorption dynamics on laser textured surfaces and also to impart novel ‘designer’ functionalities by applying different chemical treatments to laser processed surfaces.

The most well established process is to introduce a hydrophobic fluorinated-alkyl-silane chemical to a laser textured surface [186]. The CF₂ group in the perfluorinated alkyl group has a very low bond polarity and therefore offers an easy route to superhydrophobicity. In addition, the silane group has been shown to form very strong bonds with the laser textured surface [187]. The major drawback preventing this approach from industrial-scale usage is the safety of the fluoro-alkyl-silane chemical as well as their expense and environmental impact.

Boinovich *et al.* tested the behaviour of 4 different surfactants used to make laser textured superhydrophobic surfaces [188]. It was found that only surfaces treated with carboxylic acids and fluorinated alkyl silanes maintained hydrophobic properties with exposure to acid, alkali, water and saline conditions. Both the alkane (docosane) and the fluorinated alkane (perfluoropentadecane) were shown to lose hydrophobic properties indicating that the binding of surfactant terminal group to the laser processed surface is key in the durability of the superhydrophobic property. Ruan *et al.* showed that using low concentrations of carboxylic acids to modify rough alumina coatings could be used to make superhydrophobic anti-icing surfaces [189]. It was found specifically that modifying the chain length of the fatty acid from 4-12 methyl groups resulted in higher contact angles although this finding was not investigated further.

Surfaces with switchable wettability are highly sought in applications such as condenser surfaces, oil water separation and microfluidic channels [190]. Yong *et al.* showed that laser modification of titanium allowed for photoinduced switchable wetting based on the formation of photoactive TiO₂

[191]. To the authors knowledge there has not been a demonstration of a switchable wetting surface for laser texturing of non-photoactive metals such as stainless steel and a hybrid process is required. Ryu *et al.* showed that a temperature switchable hydrophilic-hydrophobic surface could be fabricated by depositing a pNIPAM methacrylic acid co-polymer to a chemically etched aluminium surface. The surface exhibited switchable wettability from hydrophilicity (10° SCA) to hydrophobicity (120° SCA) [192].

The literature review highlights the myriad of factors which can influence the fabrication procedure for single step laser texturing of steel for superhydrophobicity. These factors are collected into groups pertaining to the substrate, laser processing and post processing to produce a table of influences to guide experimental work.

Table 4.2: Experimental factors influencing the wettability response of a laser textured surface

Group	Subgroup	Influence
Substrate	Chemistry	Initial surface polarity, tendency to oxidize, alloy components
	Heat dissipation	Thermal properties, thickness & volume
Laser Processing	Laser material interaction	Surface roughness, reflectivity, damage threshold, laser wavelength,
	Laser ablation characteristics	Fluence, pulse duration, number of pulses, areal rate of processing, scanning pattern (linear or hatched)
	External	Atmospheric composition, shielding gas, particle extraction
Post-Processing	Cleaning	Sonication, debris removal, solvent
	Storage Environment	VOC percentage & type, temperature, humidity, exposure to water, sealed, plastic bags type if used
	Wettability measurement	Drop size, test type, standoff, drop dispense rate, curve fitting model, environmental conditions

4.3 Design of experiments

This section describes how the research aim and literature findings were used to formulate research objectives and experimental approach.

4.3.1 Research Aim

Provide insight through literature analysis and experimentation to progress direct laser texturing of superhydrophobic surfaces towards an industrially realisable technology.

4.3.2 Research Objectives

The literature review highlighted different approaches to produce superhydrophobic stainless steel using laser texturing. Nanosecond pulsed laser processing to produce hierarchical surface structures is currently a more accessible technique in industry. Recently, the increased availability in lower cost and higher performance ultrafast fibre lasers has made production of nanoscale LIPSS surface texture at a high areal patterning rate a viable future strategy. Research is needed to understand the functional attributes of the two approaches and their differences for manufacturing.

A key factor highlighted in the literature review is the contention over the chemical mechanism involved in the post-processing stage which underpins the hydrophobic transition after laser processing. A series of experimental objectives were formulated to produce an optimised fabrication process and address the major gaps of knowledge highlighted in the literature review. Firstly, the surface chemistry changes and resultant wettability after air exposure were analysed. Building on this finding, the effect of modifying composition by exposing the surface to different carbonaceous atmospheres was tested. In further detailed experiments, the effect of modifying the surfaces with adsorbed hydrocarbons with different terminal groups and chain length was investigated. Several different techniques to accelerate the transition which may be used in manufacturing including heat treatment and solution deposition were assessed in terms of mechanism and durability. This aim and the key research gaps noted above can be addressed by tackling the following objectives:

1. Assess the effectiveness of the hierarchical roughness texture produced by nanosecond laser processing technique compared to a high-density nanoscale LIPSS texture.
2. Analyse the chemical pathway of the hydrophobic transition of stainless steel in air after laser processing by varying the terminal group and chain length of adsorbed hydrocarbons.
3. Explore techniques to accelerate the transition process involving heat treatment, control of storage atmosphere and solution deposition of hydrophobic chemical.

4.4 Experimental approach and methodology

This section outlines the materials, equipment and experimental procedure used.

4.4.1 Acceleration of hydrophobic transition

Several post-processing treatment techniques were assessed for their capability to accelerate the hydrophobic transition after laser processing.

4.4.1.1 Heat treatment

Samples were stored in a Memmert oven at 250°C for up to 24 hours, the dimensions of the oven were 22x24x40cm ~21L. After heat treatment, the samples were stored in ambient conditions until contact angle measurement.

4.4.1.2 Control of storage atmosphere

To test the role of CO₂ gas in the transition process, a positive pressure system was created as shown in Figure 4.2(a). Firstly, the conical flask was purged with CO₂ and then a balloon was placed over the tubing and filled with CO₂ gas to ensure a positive pressure of gas. The balloon was periodically refilled.

For silanization tests, a low surface energy fluoroalkyl silane was deposited by vapour transfer. ~25 uL of Trichloro(1H,1H,2H,2H-perfluorooctylsilane) (Sigma 448931-10G) was pipetted onto a glass slide, the slide and the sample were stored overnight in a vacuum desiccator pumped to 7 mBarr.

In initial hydrocarbon transfer tests, following the process of [131], 14 µL of 4-Methyloctanoic acid were pipetted onto a glass slide in a 0.2 L petri dish container. The textured steel sample was placed into the petri dish and parafilm was wrapped around the lid to create a sealed environment as shown in Figure 4.2(b). The sample was stored for 4 days in these conditions at room temperature. Following these experiments, the type of hydrocarbon was varied to test the effect on wettability, the chemicals used in this experiment are shown in Table 4.3. Due to a supplier problem 4-methyl-octanoic acid was substituted in some experiments for 1-octanoic acid. The wettability measurement tests were, repeated using 1-octanoic acid, these results were very similar and are included in Appendix A.

Table 4.3: List of chemicals used in hydrocarbon terminal group variance experiments

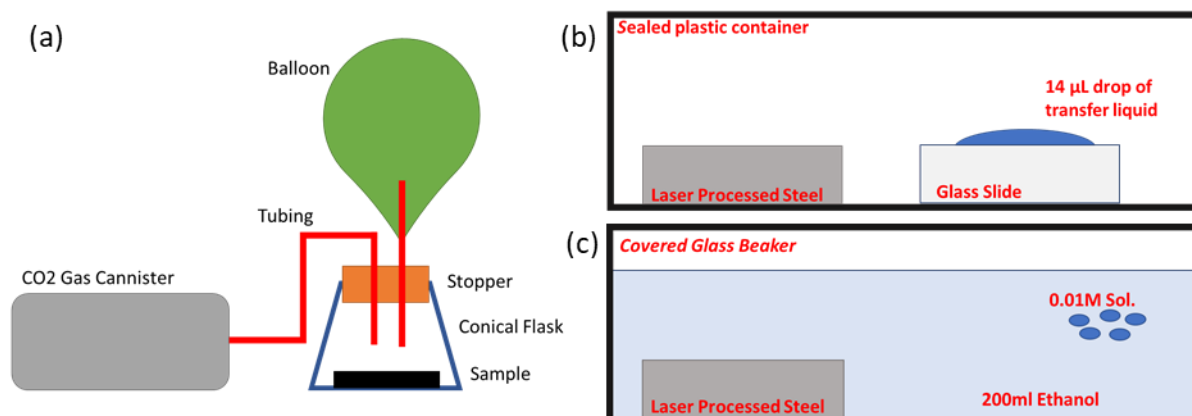
Name	Functional Group	Functional Group Formula	Supplier Code	CAS Number
Octane	Alkane	CH ₃	Sigma-296988	111-65-9
Octanol	Alcohol	COH	Sigma-95446	111-87-5
4-Methyl Octanoic Acid	Carboxylic Aid	COOH	Alfa-Aesar-B22616.06	54947-74-9
Octanoic Acid	Carboxylic Aid	COOH	Sigma-C2875	124-07-2
Trichloro(octyl)silane	Silane	SiCl ₃	Sigma-235725	5283-66-9

4.4.1.3 Solution deposition

A 0.01 mL solution of stearic acid was created by dissolving 0.569 g in 200 mL of ethanol. The sample was immersed for 2 hours followed by rinsing with ethanol and analytical reagent grade water and drying with compressed air. After solution deposition the samples were stored in ambient conditions exposed to air until contact angle measurement. This process was repeated for 0.01M solutions with varying chain length and immersion time. The chemicals used in this experiment are described in Table 4.4. This approach is illustrated in Figure 4.2(c)

Name	Chain Length	Supplier Code	CAS Number
Butyric Acid	4	Sigma-B103500	107-92-6
Octanoic Acid	8	Sigma-C2875	124-07-2
Stearic Acid	16	Sigma-S4751	57-11-4

Lignoceric Acid	24	Sigma-L6641	557-59-5
-----------------	----	-------------	----------

Table 4.4: List of chemicals used in solution deposition experiments**Figure 4.2:** (a) Experimental arrangement for CO₂ gas sample exposure. (b) Vapour transfer approach. (c) Solution deposition approach

4.5 Results and Discussion

Chapter 3 involved development of the LIPSS and hierarchical stainless steel laser texturing processes. The hierarchical surface involved far more thermal damage to the material and a rougher surface was formed, whereas the LIPSS surface texture consisted of a dense covering of nanoscale ripples. So far in chapter 4, the literature into these laser modification processes for superhydrophobic functionality has been discussed, a difference in the transition rate of the two modification modes was observed, additionally there is a need for deeper understanding of the mechanism of the chemical transition after laser processing. In the following report of experimental work, detailed analysis of surface properties was used to build an understanding of the chemical transition and hydrophobic functionality of the two texturing approaches.

4.5.1 Analysis of the hydrophobic transition in air

After nanosecond laser processing the changes in surface chemistry and wettability with air exposure were characterised. In the XPS data presented below, 'Sample 1' was measured less than 1 hour after laser processing, 'Sample 2' after ageing for 3 weeks with air exposure. It was found that the laser textured surfaces accumulated surface carbon and transitioned in wetting behaviour from superhydrophilic to hydrophobic. Figure 4.3 shows XPS spectra of the major elements present in the surface chemistry of the samples. Table 4.5 breaks down the atomic percentage composition with comparison to the substrate.

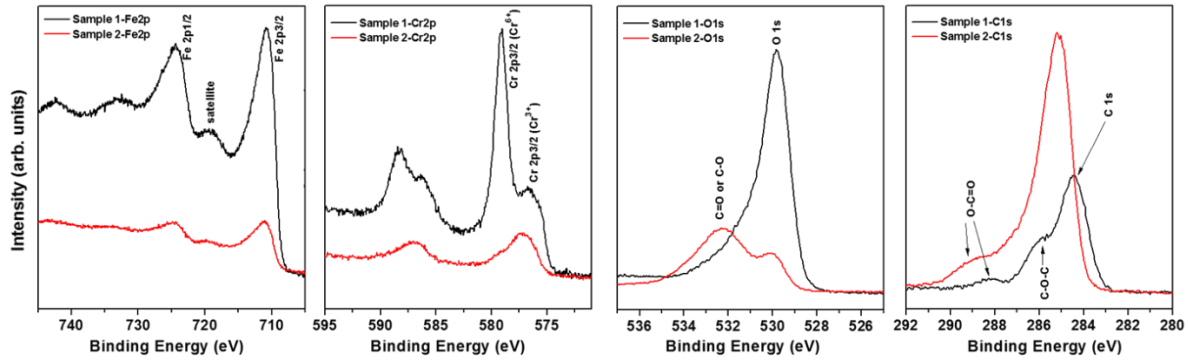


Figure 4.3: XPS Spectra after nanosecond laser processing scans for element narrow scans (a) Fe (750-700 eV), (b) Cr (595-550 eV), (c) O (538-524 eV), (d) C (292-280 eV).

XPS measurement showed that the surface atomic percentage carbon content after air exposure increased from 27.9% to 70.6% for the nanosecond laser processed surface. An XPS survey immediately after processing was not possible for the LIPSS processed surface. The main binding energy range accounting for this rise was the C 1s peak (284.4 eV) which is attributed to the C-H bond. The metal elements were largely unchanged although minor effects were observed including a lower ratio of Cr to Fe (4.8 to 2.5) and change in the iron valence state after air exposure, it is noted that Chromium segregates to the surface of stainless steel at high temperatures which may influence the measured composition with a surface sensitive technique [193]. Although minor changes in metal elements may contribute to the hydrophobic transition by far the major effect observed is the accumulation of surface carbon. In particular, it was observed that the main oxygen peak in the ALP sample was metal oxide (530 eV) whereas in the AAE sample the peak was mainly organic C-O (533 eV) and C=O (531.5). Furthermore, the ratio of carbon to oxygen increased with air exposure suggesting that the metal oxide produced after laser processing had been shielded with carbon.

Table 4.5: Summary of elemental composition of surface at different stages of fabrication process

Sample	Fe2p (At%)	Cr2p (At%)	Ratio Fe/Cr	C1s (At%)	O1s (At%)	Ratio C/O	Other Elements
304 Stainless Steel Substrate from reference [194]	69.4	18.4	3.8	0.0	0.0		Balance
After nanosecond Laser Processing (ALP)	15.7	3.3	4.8	27.9	53.2	1.9	Not Detected

After Air Exposure (AAE)	1.6	0.6	2.5	70.6	27.1	0.4	Not Detected
-----------------------------	-----	-----	-----	------	------	-----	-----------------

Many hydrocarbons with large differences in electronic and atomic structures have C1s binding energies at or very close to 285eV, whereas amorphous carbon or graphite typically has C1s binding energy near to 284.4eV [171]. The peak at 284.4 eV in our experimental study for sample AAE is sufficiently displaced to suggest that some hydrogens are associated with each carbon site and that the deposit is primarily composed of hydrocarbons.

Figure 4.4(a) shows the change in contact angle of the nanosecond and femtosecond laser processed surfaces over time, labelled to describe the surface texture type as Hierarchical and LIPSS respectively. The unprocessed steel substrate showed a hydrophilic contact angle of 40.5°. After laser processing both approaches showed superhydrophilic responses with contact angles of 0° which slowly changed to hydrophobic responses with air exposure. The nanosecond processed surface took around 4 days to transition from a fully wetting non-measurable contact angle to a measurable hydrophilic droplet profile and 21 days to form a hydrophobic contact angle of 123°. The steady state contact angle after 3 months of air exposure was 152°. This lengthy transition period is inhibitive to industrial value. Although other researchers have shown faster transition periods in the region of 7-15 days for nanosecond laser processing [46], it was not possible to replicate these results in any experiments, this may result from natural variation of the potential influences on the process outlined in Table 4.2, such as differences in the air composition between labs.

The femtosecond laser textured LIPSS surface required a much shorter period of around 6 days to reach a contact angle of 138°, the steady state contact angle measured after 2 months was 159°. Evidentially the hydrophobic transition of the LIPSS surface occurred much more quickly than the nanosecond processed surface. It was observed in section 3.4.1 that the nanosecond laser processing approach results in a much rougher surface with a higher surface area and larger amounts of laser induced metal oxide. It is possible that these effects explain the difference in transition durations. The much higher surface area of the rougher nanosecond processed texture requires a longer time to ensure a full coverage of hydrophobic surface chemistry, particularly if the mechanism is hydrocarbon adsorption which is limited by the availability of suitable hydrocarbons in the atmosphere and their transport to the surface. Additionally, the higher degree of oxidation and production of redeposited metal oxide particles presents a more hydrophilic barrier to overcome. In both cases the air exposed surfaces showed hydrophobic high adhesion behaviour with no measurable roll-off behaviour observed, this indicated that the surface chemistry was heterogenous as some hydrophilic entities remained on the surface causing interfacial bonding to water molecules. The combination of structure and chemistry underpinning these effects was explored in further experiments.

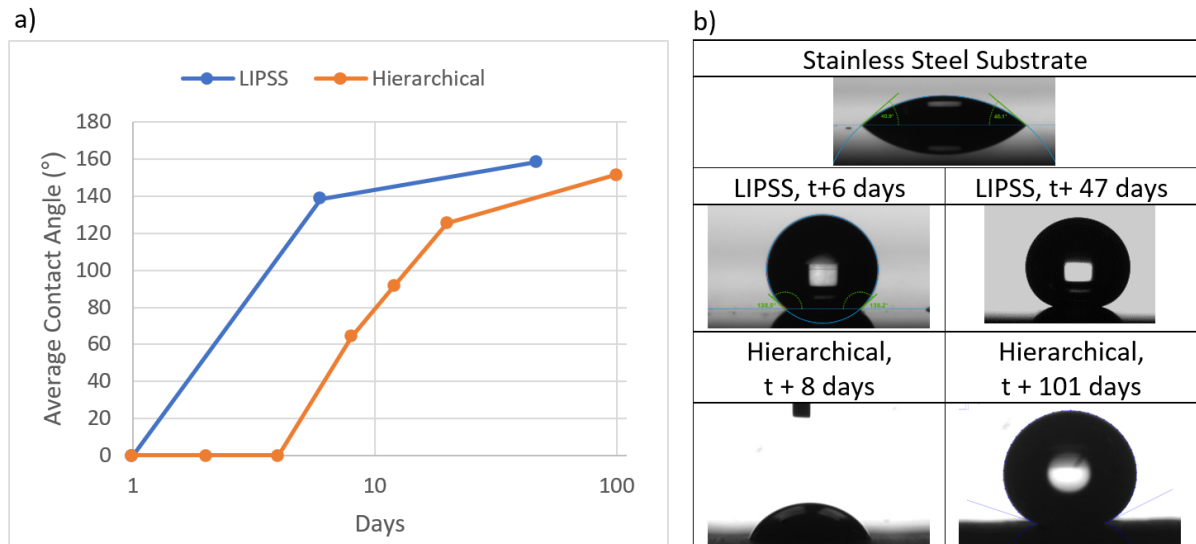


Figure 4.4: (a) Change in water contact angle over time with air exposure for the two laser processing approaches LIPSS (fs laser) and Hierarchical (ns laser) (b) Droplet profile images used for sessile contact angle measurements over the transition period.

4.5.2 Acceleration of hydrophobic transition

Increasing the rate of hydrophobic transition would be very valuable to advance the direct laser texturing technique to a usable manufacturing process. Post-process heat treatment was tested initially. This adaption showed the ability to change the wettability of the surface however there were issues with consistency and durability which suggested the need for further fundamental study of the hydrophobic transition. The composition of the gaseous environment which the laser textured surface was stored in was thought to be a major influence on these difficulties, so this was investigated further.

4.5.2.1 Heat Treatment Acceleration

Heat treatment acceleration tests were carried out with the nanosecond laser processing approach described in section (3.3). After laser processing the surfaces were heat treated in a natural convection oven at 250°C, the surfaces were removed from the oven in intervals of 4 hours up to a maximum treatment time of 24 hours, the surfaces were then left exposed to air for a further 24 hours before wettability testing. The atmosphere in the oven was not controlled, the convection oven intakes the ambient air from the room.

Figure 4.5 shows how the measured contact angle varied on each surface with length of annealing period. As the treatment time was increased, the wetting response of the surfaces showed a continuous transition between superhydrophilic and highly hydrophobic responses. For 0-8 hours of annealing a

superhydrophilic response was measured where droplets fully spread over the surface. From 8-20 hours the average contact angle measured on the surface increased, although the range of contact angles measured on each sample varied considerably. For example, after 20 hours the surface exhibited both a hydrophilic response (SCA 56°) and superhydrophobic response (SCA 154°) at different locations on the surface. After 24 hours of annealing all tested droplets showed a contact angle greater than 144° with average measurement of 154° . Highly hydrophobic behaviour was observed for samples with heat treatment duration greater than 24 hours.

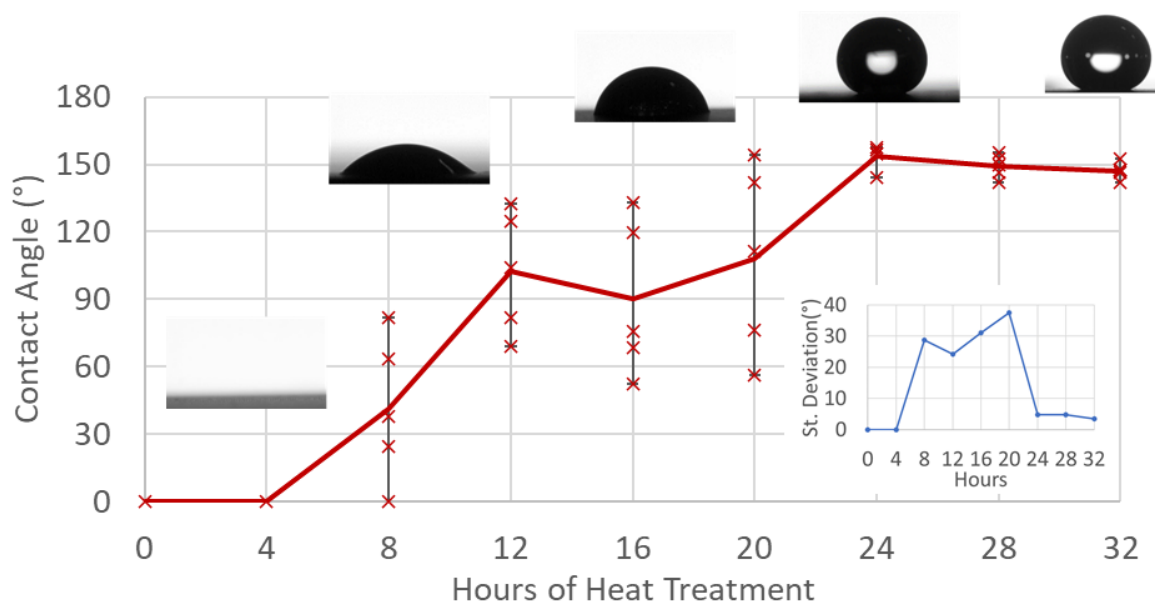


Figure 4.5: Change in contact angle and corresponding drop shape images for heat treatment of the nanosecond laser processed surface. The standard deviation of the contact angle measurement is inset.

XPS spectra were obtained for surfaces immediately after laser processing (SCA 0°), after ambient air exposure over a period of 3 weeks (SCA 120°), and after heat treatment for 24 hours (SCA 154°). Figure 4.6 shows the normalized spectra and elemental scans of carbon and oxygen regions in the XPS survey. Immediately after laser processing the surface exhibited a large formation of metal oxides shown in Figure 4.6(c) (529-530 eV). After heat treatment the C1s peak (284.8 eV) remained of similar magnitude however new peaks appeared in the spectrum for organic elements specifically the Organic C=O/C-O bond in the O1s spectrum at 531.5-533 eV and the C-O bond (286) in the C1s bond. This indicates a slightly higher presence of organic material after heat treatment. After 25 days of exposure to air the surface showed a higher intensity of C 1s and hydrophobic properties as seen in earlier experiments. XPS was not able to give a full picture of the mechanism underpinning the heat treatment acceleration however the presence of peaks related to organic material suggest there may be accelerated adsorption [182].

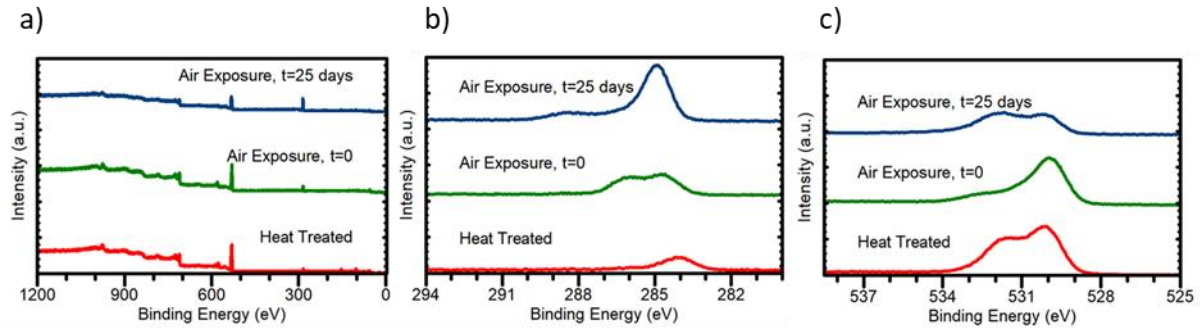


Figure 4.6: XPS Spectra of nanosecond laser processed surfaces immediately after laser processing ($t=0$), after air exposure ($t=25$ days) and after 24 hours heat-treatment (a) survey scan (b) Carbon element scan (294-279 eV) (c) Oxygen element scan (538-525 eV).

Substantial variance was observed during wettability measurements of the heat-treated surfaces. To investigate the process further the spatial variance of wettability change was assessed. A quadrant grid was patterned on top of the laser textured surface to map the contact angle across a 4x4cm surface.

Heat treatment was anticipated to accelerate the thermodynamics of reaction with natural airborne contaminants, this means characterising a surface midway through the heat treatment process allowed for a figurative window into the reaction. Figure 4.7 shows the contact angle map of the surface after heat treating at 250°C for 24 hours. The results suggest that wettability transition initiates at defects, spatial variance may occur due to this nucleation and growth mode of transition [73,124] as well as natural variances in the composition of the atmosphere within the oven. There is some indication that nucleation may be initiated at the edges of the sample, this may be linked to less redeposited material and reduced oxide depth.

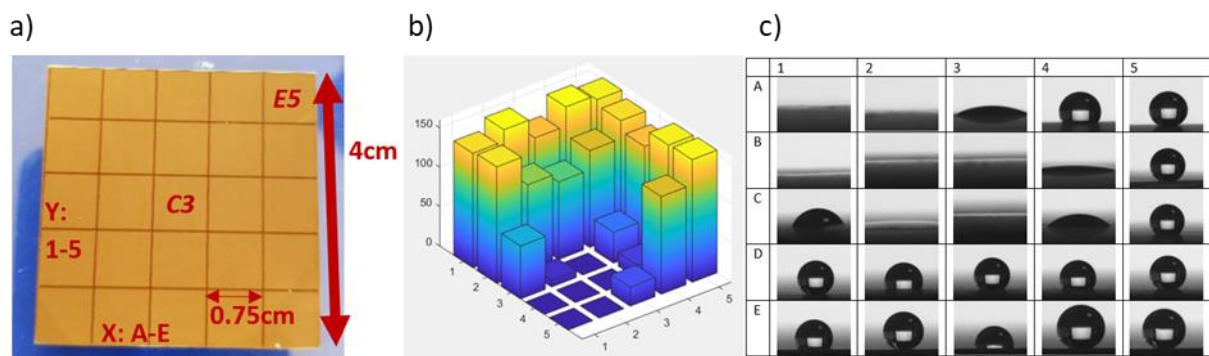


Figure 4.7: (a) Laser marked grid on nanosecond laser processed surface for mapping of spatial variance in contact angle (b) Bar chart of contact angle spatial variance (c) Corresponding table of droplet profile images.

Although it was not possible to clearly pin the species involved with this heat treatment process. The results presented fit the theory of adsorption rate enhancement. The kinetics of adsorption are

endothermic, but species availability is increased with temperature [195]. Significant variances between tests of heat treatment suggest the process is reliant on the air composition in the oven and is not repeatable without controlling this factor. The inconsistency with earlier measurements when the surface was fully mapped suggests there may be significant variance within a heat-treated surface. This measurement could be repeated in future work with different exposure durations to show full evolution of the surface during processing. This type of test is experimentally difficult because once the surface has been exposed to water it is effectively contaminated. Water can act to form polar OH-groups on the surface, as well as to remove adsorbed materials.

Figure 4.8 shows the change in contact angle of the surfaces heat treated for 24 hours through measurements over 20 days. This aimed to test the stability of the heat treated surface and record any further wettability transition. Although the samples heat treated for 24 hours initially showed hydrophobic behaviour, after several runs of contact angle testing a hydrophilic response was measured. The minimum average contact angle of 24.4° was measured 8 days after sample fabrication. This figure shows that the hydrophobic heat treated surface is not stable and after multiple sessile contact angle measurements changes back to hydrophilicity. The direct outcome of these results is that the measurement of contact angle on freshly annealed surfaces influences subsequent measurement results. One possible conclusion was that this influence was due to reticence of surface water. However, this effect was seen even with an oven drying step between measurements suggesting a reactive pathway is more likely.

With air exposure the surfaces gradually regained hydrophobicity, an average contact angle of 90.5° was measured 20 days after sample fabrication. The linear rate of increase from the minimum value (8 days) to the last measurement (20 days) was 5.5° per day. This compares to 7.6° per day for an equivalent surface exposed to air after laser processing without heat treatment (91.1 after 12 days air exposure, section 4.5.1). The similar rate of change in wettability between these two samples suggests there is an equivalent adsorption mechanism.

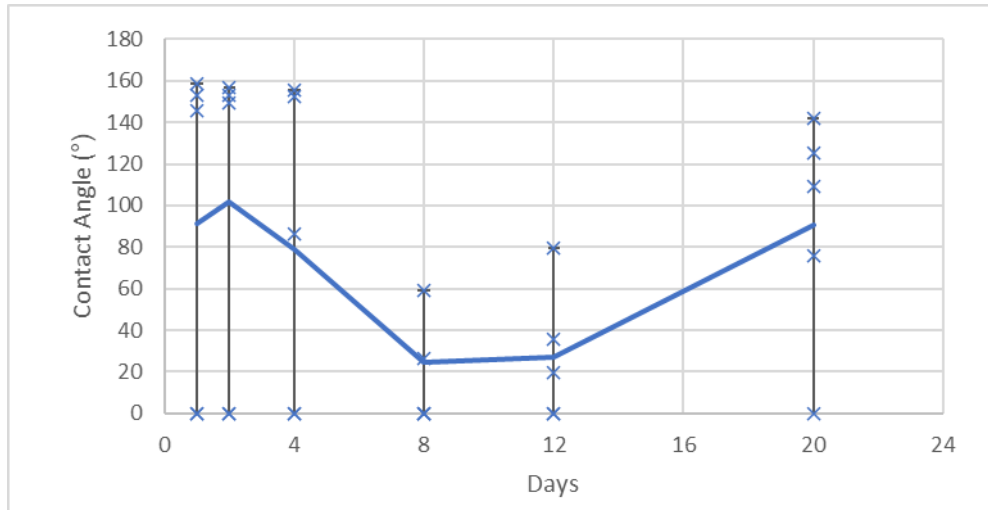


Figure 4.8: Variance in contact angle after heat treatment of the nanosecond laser processed surface over 20 days.

Heat treatment was also tested for the LIPSS surface producing a contact angle of 119° after 24 hours of treatment at 250°C . Heat treatment produced a less hydrophobic surface than ageing in air. It is thought that this effect could be due to the composition of air in the oven varying from previous experiments and from reports in literature. These results, although informative did not suggest that heat treatment acceleration was a promising avenue to continue with experimentally due to poor repeatability, lack of stability and only high adhesion superhydrophobicity observed. Literature reports into high adhesion superhydrophobicity suggest that liquid forms a Cassie impregnating wetting state [196], this is associated with heterogenous surface chemistry composition [197].

4.5.2.2 Control of storage atmosphere

The literature review highlighted that there can be substantial variance in the final contact angle and the rate of contact angle change for apparently similar laser processing approaches when the surfaces are stored in ambient conditions. Several studies have shown that varying the composition of the storage atmosphere can accelerate this transition period [27,80,163], however differing theories have been used to explain their observations. In this section, the storage atmosphere was varied to assess the chemical mechanism underpinning the transition.

One reported mechanism highlighted in the literature review was that exposure to CO_2 gas results in dissociative adsorption of adventitious carbon catalysed by the active magnetite produced by laser processing. This theory was tested by exposing the laser processed surface to an atmosphere of CO_2 by the method shown in Section 4.4. In this case a higher rate of hydrophobic transition was not observed, and the surface maintained hydrophilic properties after 3 weeks of measurement. Vapour transfer of a low surface energy fluoro-alkyl silane chemical caused a change to hydrophobicity.

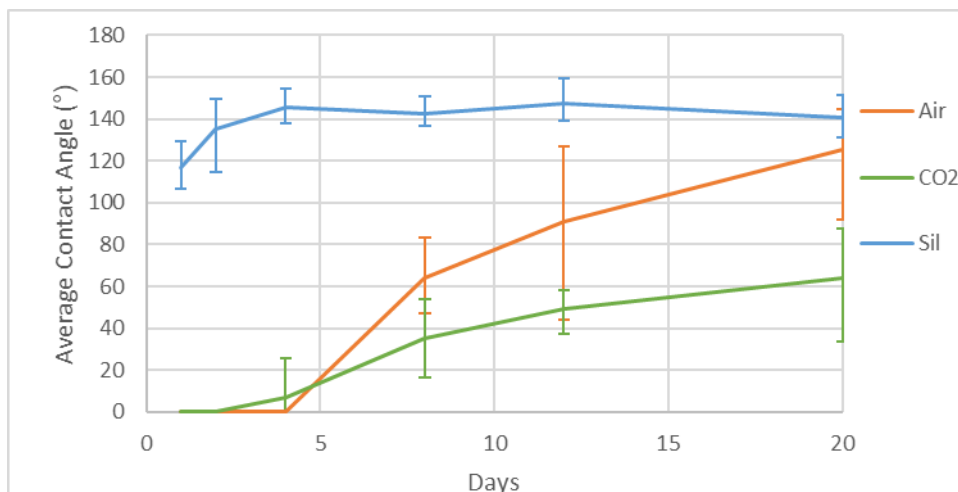


Figure 4.9: Wettability transition over time of nanosecond laser processed surface when stored in air (Air), CO₂ gas (CO₂), and with fluoroalkylsilane deposition (Sil)

To further test the potential role of amorphous carbon, a graphite target was used to sputter carbon onto the surface immediately after laser processing. Approximately 50 nm of carbon was deposited. No substantial change in wetting was observed and superhydrophilic properties were maintained. A limitation of this study was that because sputtering is line of sight it may not truly replicate an essentially conformal chemical mechanism. The sputtering process has however been previously used to produce controlled surface chemical states on rough laser textured surfaces [198], but in this cited report the surface treated was one which already had transitioned to hydrophobic properties. This indicates that a thin film of amorphous carbon alone is insufficient to shield the influence of the laser induced superhydrophilic metal oxide.

During the optimisation of the LIPSS laser processing technique, the exposure of the surface to different post-process conditions was tested. Applying the already discussed approaches of air exposure for 3 weeks, heat treatment, silanization as well as stearic acid solution deposition and storage in a hydrocarbon rich atmosphere at detailed in method section 4.4.

Figure 4.10 (a) plots the effect of post-process condition on static contact angle. Both the hydrocarbon atmosphere and stearic acid treatment methods showed very hydrophobic responses on the laser textured areas. The full surface coverage of LIPSS showed the low adhesion conditions required by the definition of ‘superhydrophobicity’. The sequence of images in figure 4.10(b) shows that a 2 μ L drop would not stick to the surface. To measure contact angle instead an 8 μ L drop was dispensed onto the surface from a needle using a standoff greater than the drop diameter.

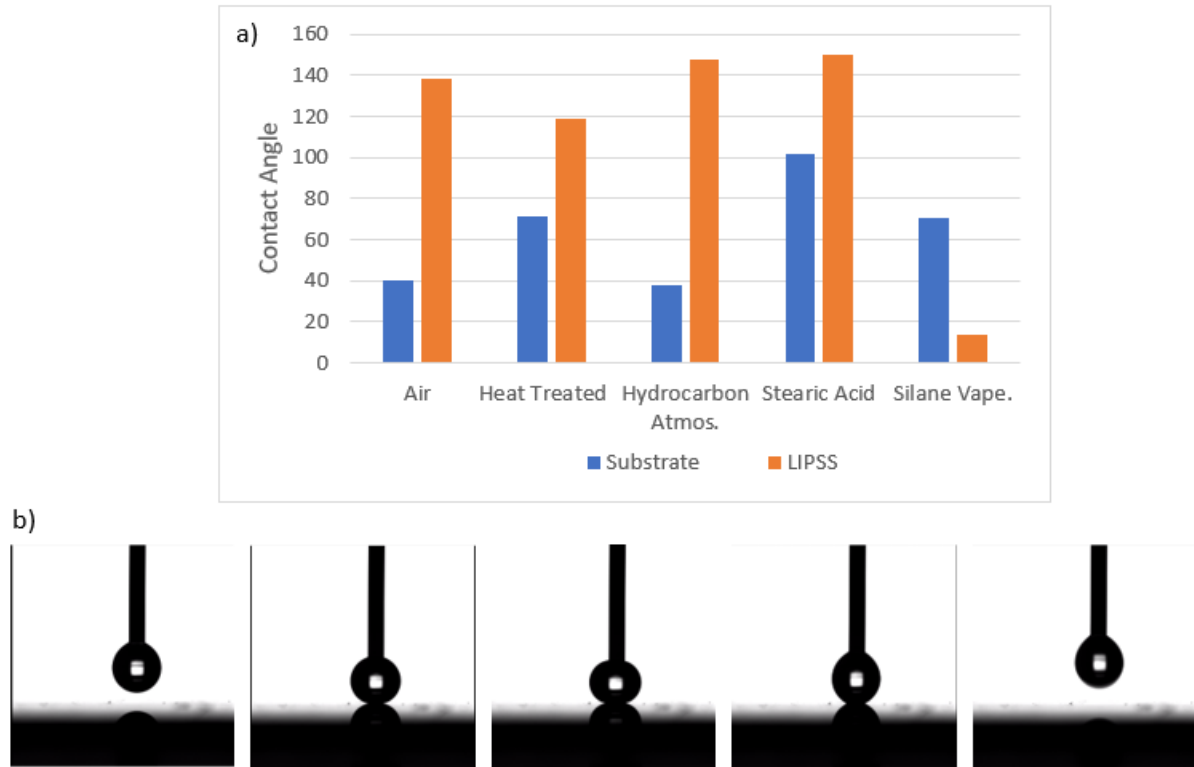


Figure 4.10: (a) Variance of static contact angle with post-processing condition for LIPSS surface (b) Sequences of images showing low adhesion to superhydrophobic LIPSS surface created through storage in hydrocarbon atmosphere.

Whereas the deposition of stearic acid by immersion in solution made the steel substrate significantly more hydrophobic (102°), the storage in a hydrocarbon atmosphere did not cause a significant change in contact angle to the steel substrate (38°). This could suggest that the laser textured areas provided preferential sites for adsorption of the hydrocarbon and that storing in a hydrocarbon rich environment is a more suitable replica for the airborne ageing process.

The next series of experiments tested the hypothesis that the carboxylic acid hydrocarbon species were responsible for the transition process. The terminal group of species with equivalent chain length was varied. Liquid drop of hydrocarbons with fixed chain length and varying terminal group were stored in a sealed container with the laser processed stainless steel for 7 days. The binding groups investigated were alcohol (COH), alkane (CH₃), carboxylic acid (COOH) and trichloro-silane (SiCl₃).

The different reagents used have different vapour pressures so produce different atmospheric concentrations. During experiments it was observed that the carboxylic acid showed some liquid still present on the glass slide whereas the others evaporated completely. As the carboxylic acid atmosphere showed a full hydrophobic transition the difference in evaporation rates was not a limiting step as enough molecules were available in the atmosphere for hydrophobicity.

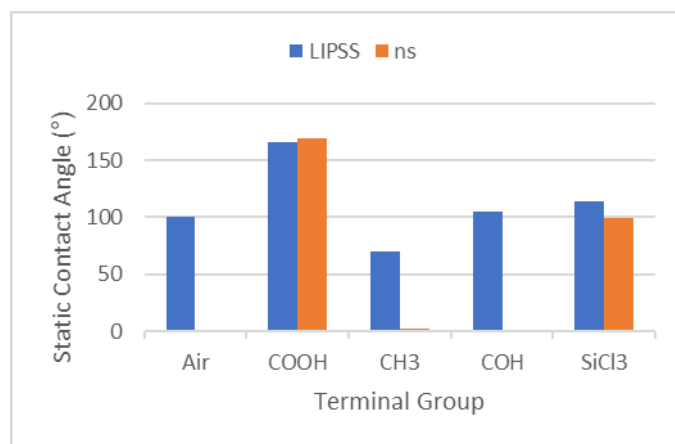


Figure 4.11: Comparison of the measured contact angle of the LIPSS and nanosecond laser processed surfaces after exposure to different atmospheres for 8 days.

Only the carboxylic acid rich atmosphere produced a superhydrophobic response, indicating the preferential binding hypothesized. Treatments with alkane and alcohol groups did not show a significant difference from the surface exposed to air. In most cases the nanosecond laser processed surface showed a superhydrophilic contact angle of 0°. The silane treatment showed a hydrophobic response, however the steel surface was significantly corroded.

XPS surface chemistry analysis was used to assess the origin of the differences between the wettability's. 1x1 cm sections of stainless-steel foil were used to be compatible with the XPS system, the LIPSS texturing approach was used to limit thermal deformation of the foil. Figure 4.12 compares the overall spectra and the individual element peaks of Carbon and Oxygen for each surface.

Figure 4.12(d) shows the elemental composition of each surface. Spectra for Iron and Chromium are shown in Appendix A. Additional alloying elements Mn (11.98%) and Ni (1 2.07%) were detected in the air exposed sample. Si (4.74%) and Cl (3.49%) peaks were also detected in the Silane treated sample.

The elemental composition analysis did not provide a clear explanation of the differences in surface wettability due to varying the hydrocarbon terminal group. As all of the LIPSS surfaces displayed contact angles of at least 70° it is anticipated that some carbon adsorbed to all of the surfaces. It is postulated that the carboxylic acid group allowed for more ordered binding and organisation to the surface driven by its high polarity. The terminal group with the lowest polarity (methyl) also recorded the lowest contact angle.

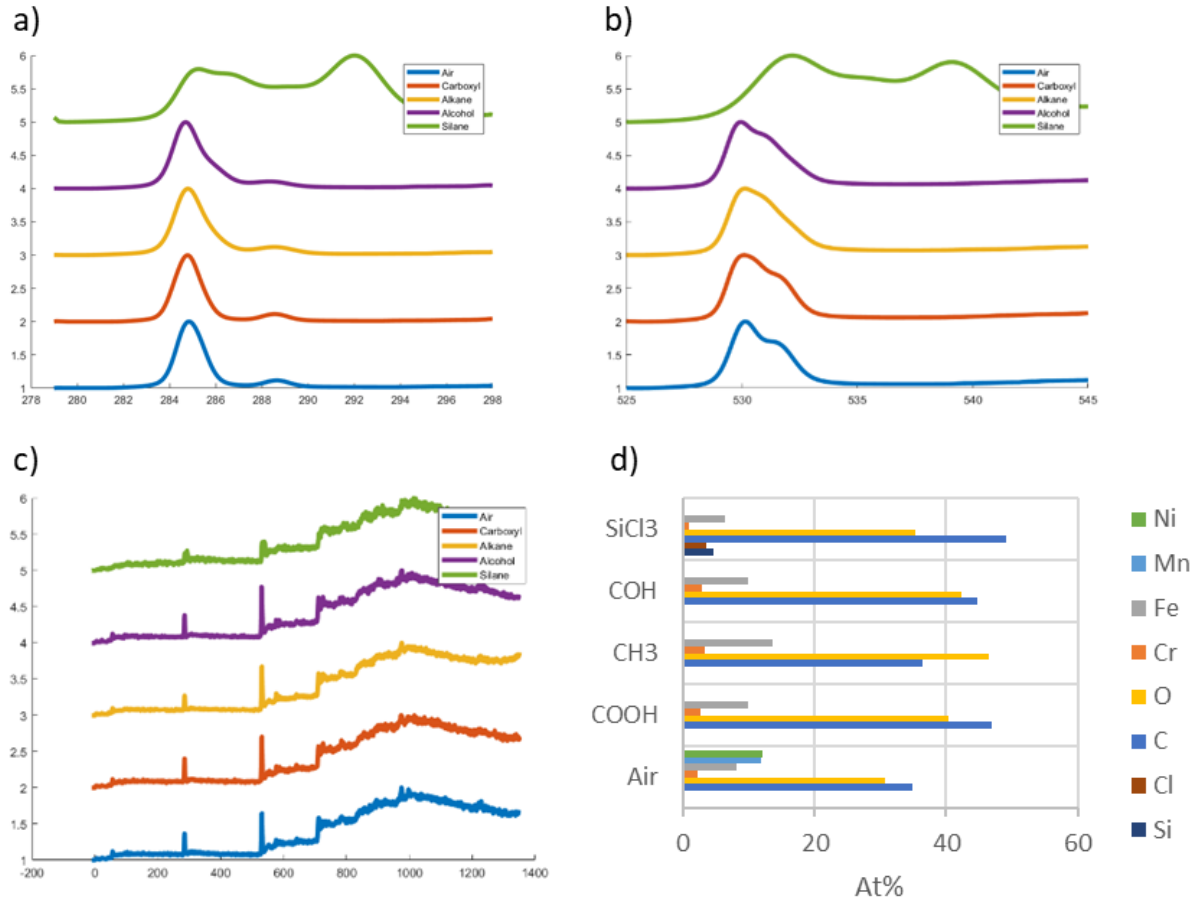


Figure 4.12: XPS spectra of LIPSS surfaces after exposure to different storage atmospheres. **(a)** C element scan spectra **(b)** O element scan spectra **(c)** survey spectra **(d)** At% composition breakdown of each surface

By comparing the individual element peaks, several interesting observations were made. Firstly, the C1s peak at 284.8 eV indicates adventitious carbon sources from organic contamination, no distinctive difference in carbon bonding was observed between hydrocarbon atmospheres. The oxygen spectra showed some differences, the main peak at 530 eV observed in all cases is associated with metal oxide bonding, the presence of the second peak at 531.5-532.2 eV indicated a C=O peak which could account for the carboxyl group. The alkane group showed far less of a peak in this area. The air exposed surface showed a significant C=O peak indicating the presence of carboxylic acids in the air. The Fe (570-590 eV) and Cr (705-740 eV) spectra regions are included in Appendix A, they showed that the underlying metal chemistry was not changed by the treatment approach for organic terminal groups. Exposure to the trichlorosilane terminated hydrocarbons showed significant corrosion of the steel surface and a moderate hydrophobic contact angle.

XPS depth profiling was used to explore the variance of surface composition as material was etched from the surface using an ion gun. The carboxylic acid exposed surface was selected as having given the most hydrophobic properties and equipment access was limited. A milling ion energy of 2000 eV

was applied for 10 hours, this was predicted to give a milling rate of 0.3 nm/s (estimated for Ta₂O₅) producing a depth of over 10.8 μm . In practice, only a small sub-micron milling depth was observed which it was not possible to measure with SEM imaging. Figure 4.13 plots the change in elemental composition over the duration of the depth profiling experiment.

In the initial measurement before any milling, the carbon At% was 39.2%, after 60 seconds of milling this had dropped to 7.3% and then settled at 1-3%. The high carbon is therefore associated with only a thin atomic scale surface layer and is reduced as this surface layer is removed. A more gradual transition was observed with oxygen. Oxygen was the highest concentration element after the surface carbon layer was removed with 51.1 At% at 60s milling time. As the surface is etched further the oxygen content continually decreases with the difference made up through increases in Fe and Cr content. This is attributed to profiling through the heat affected zone into the bulk of the stainless steel.

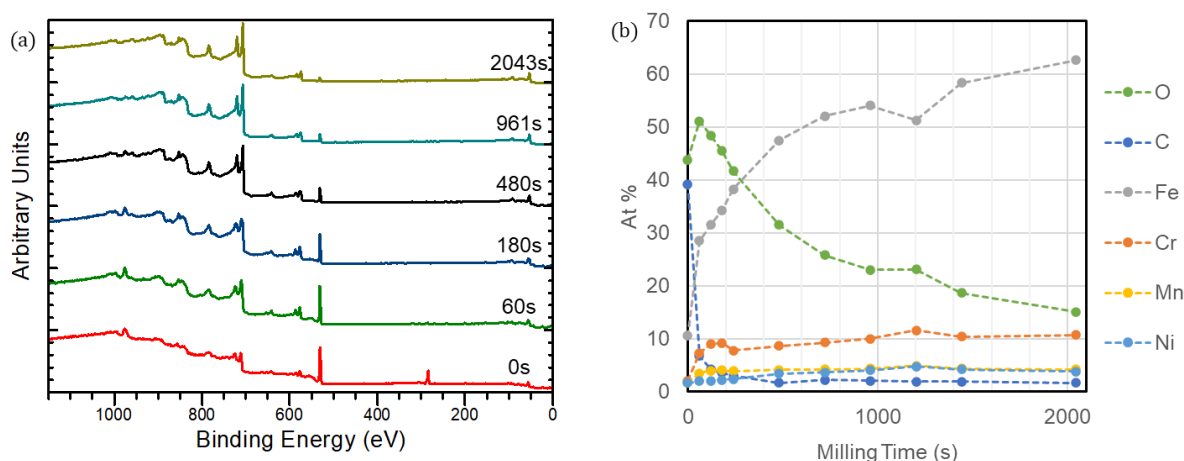


Figure 4.13: Depth profiling of LIPSS surface stored in carboxylic acid hydrocarbon atmosphere: (a) Stacked spectrums at different milling times. (b) Plot of elemental composition variation.

4.5.2.3 Rapid superhydrophobic conversion with solution deposition

The final set of experiments aimed to explore the use of post-process chemical treatment of laser textured surfaces to have tailored functionality. A solution deposition approach was used to rapidly deposit carboxylic acids on laser textured surfaces to produce superhydrophobic stainless steel. To optimise the process for effective superhydrophobicity, the length of carboxylic acid chain and the duration of the immersion was varied.

The length of carboxylic acid chain was varied through deposition of butyric acid (C4), 4-methyl octanoic acid (C9), stearic acid (C16) and lignoceric acid (C24). Ethanol was used as the solvent,

prior research has found it does not form adsorbed monolayers on iron oxide surfaces but instead partitions onto the surface as a liquid phase multilayer structure [199]. This reduces competitive adsorption of the solvent with the surfactant molecule. Additionally, ethanol is low cost, widely available, relatively safe to handle and available in food grade standard. After the deposition process, the surfaces were characterised with contact angle measurement and XPS.

Figure 4.14 plots the static and dynamic wettability responses of the samples compared by the length of the alkyl chain. For the shortest alkyl chain length, butyric acid (C4), a fully wetting response was recorded with the average contact angle less than 10° for both nanosecond laser textured and LIPSS surfaces. This indicates that the solvent removed any carbonaceous material adsorbed to the surface and the deposited butyric acid did not form a hydrophobic layer. As the chain length was increased to 4-methyl octanoic acid (C9) the wetting behaviour transitioned to a highly hydrophobic regime. In contrast to air exposure tests, no roll-off behaviour was observed for solution deposition experiments using 4-methyloctanoic acid. As chain length was increased to 16 and then 24 alkyl groups there was a further development in wetting behaviour to low adhesion superhydrophobicity. This finding is supported by the study of Thorpe *et al.* which showed linear variance of the surface energy and contact angle with the length of the CF_2 chain in fluoroalkyl silane molecules coatings on smooth surfaces [200,201].

Overall, the nanosecond laser processing approach showed more strongly water repelling behaviour with slightly higher contact angle and lower roll off angles recorded although the final wettability's after 24 hours immersion were very similar. It was shown in results section 4.5.1 that the nanosecond laser processed surface has a much higher surface energy than the LIPSS processed surface, when this is coupled with the hypothesis in section 4.5.2.2 that the surface polarity drives the chemisorption of the carboxylic acids it may imply that the energetics of the adsorption process favours adsorption to the more polar nanosecond processed surface.

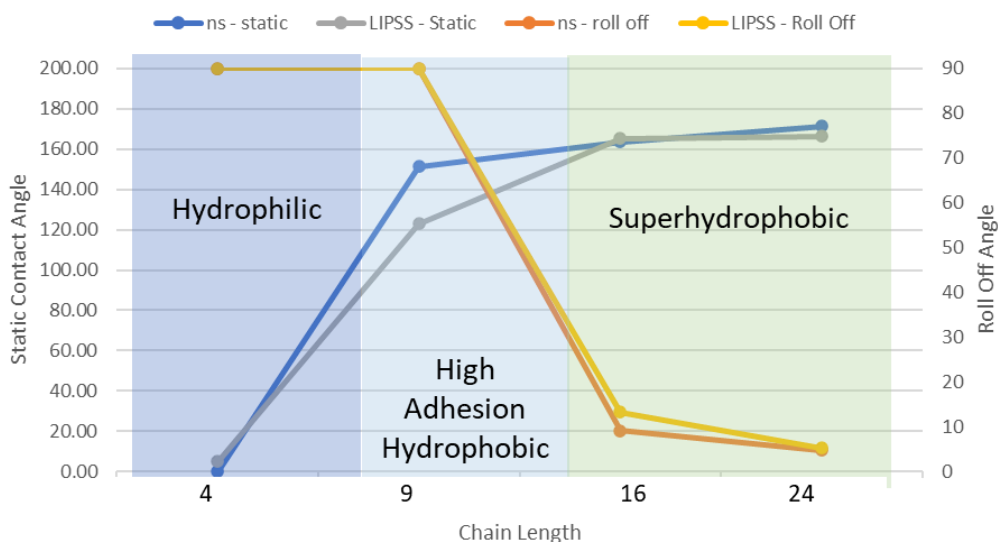


Figure 4.14: Wettability response variance with length of carboxylic acid chain for LIPSS and nanosecond laser processed surfaces

In composition analysis, it was found that the carbon concentration increased continuously with chain length as shown in Figure 4.15(b). In the C1s range of binding energies shown in Figure 4.15(a), it was found the peak at 288.5 eV for the O-C=O bond became smaller with increasing chain length. The percentage composition of oxygen decreased with increasing chain length, this is attributed to shielding of the metal oxide by the adsorbed hydrocarbon layers. In the oxygen spectra shown in Figure 4.15(c), there was variance in the proportion of oxygen occurring from organic sources (531.5-533 eV) compared to metal oxide (529-530 eV) however no clear trend was observed with respect to increasing chain length. The metal elements remained largely unchanged by the deposition process. The XPS study did not fully account for the large differences in observed wetting behaviour between the C4 and C9 surfaces. Although a very small increase in carbon content was observed any potential insight could be masked by the background carbon contamination as the amount is similar to that of the air exposed surface. Both of the superhydrophobic surfaces, C16 and C24 showed much higher carbon content. The surface forces which determine the hydrophobicity rapidly fade towards the interior of the bulk phase and therefore a nanometre thick layer is required to shield the underlying substrate [200,201].

Surface preparation approaches such as plasma cleaning are typically used in XPS measurements to remove carbon contamination. However, as this type of adsorbed organic material is of specific interest, they were not suitable for this investigation. Comparison of normalized elemental spectra indicated that binding was of the same nature between experiments and that the underlying laser textured substrate was not substantially affected by the deposition process.

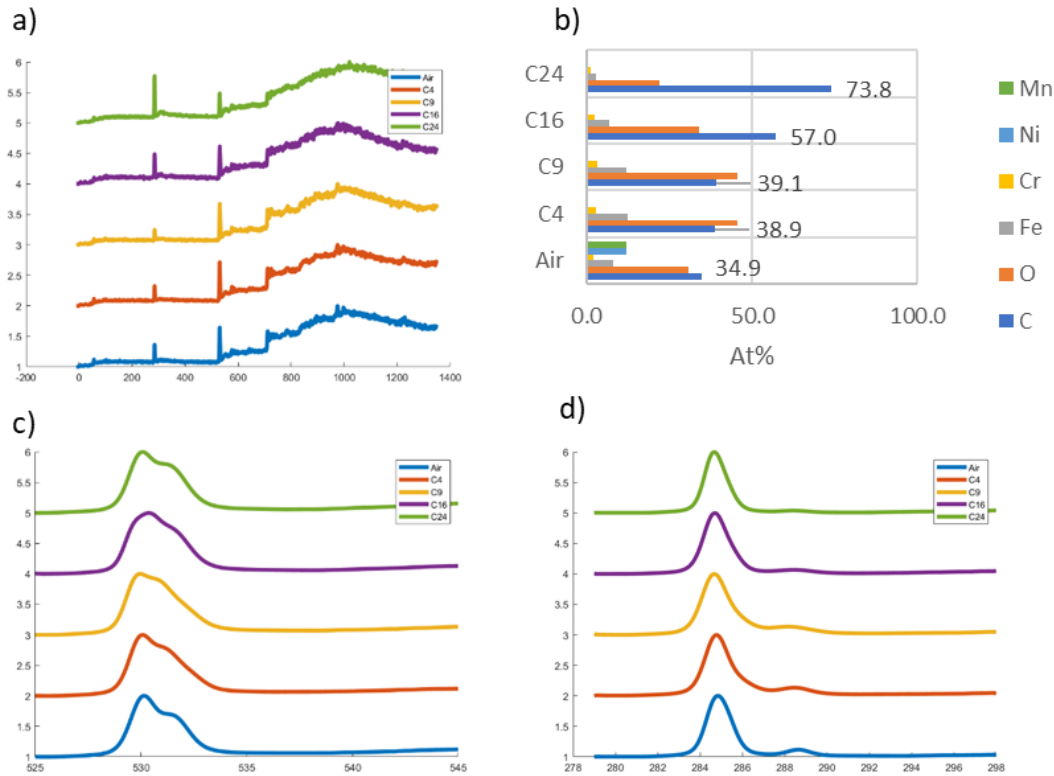


Figure 4.15: (a) XPS survey spectra of LIPSS surfaces after solution deposition of varying carboxylic acid chain length (b) At% composition of each surface, data labels are for Carbon At% (c) Oxygen element scans for each surface (d) Carbon element scans for each surface

Stearic acid (C16) modification was chosen as a suitable superhydrophobic treatment for further investigation. Stearic acid is a naturally occurring long chain fatty acid which is found in common household products such as soap and it is suitable for use in the food industry. This hydrophobic treatment was previously tested by Boinovich and Emelyanenko who found that it maintained hydrophobic properties in contact with water and saline solution but was degraded by acid and alkali solutions [188].

Further experiments investigated the duration of immersion of the nanosecond laser textured sample in the stearic acid solution. It was only possible to carry out this experiment for the nanosecond laser processed surface due to equipment availability. As shown in Figure 4.16, it was found that a similar transition in wetting properties occurred from hydrophilic to high adhesion hydrophobic, and then to superhydrophobic depending on the length of immersion. After only 10 seconds of immersion the contact angle transitioned from a superhydrophilic to hydrophilic (32.8°). After 10 minutes of immersion a high contact angle was measured, however no roll off behaviour was observed which indicated only partial coverage of the hydrophobic agent. An immersion time greater than 1 hour was

shown to be sufficient to produce superhydrophobic effects. This method allows for very rapid production of superhydrophobic surfaces using laser texturing whilst avoiding toxic chemicals.

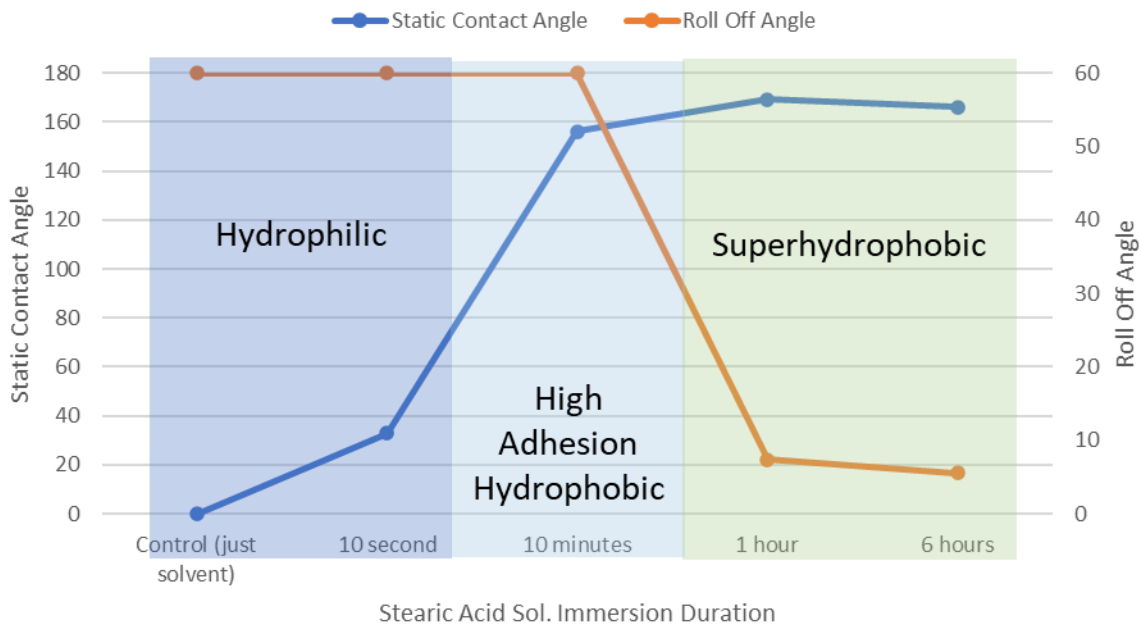


Figure 4.16: Wettability response of nanosecond laser processed surfaces with varied duration of immersion in stearic acid solution

4.6 Conclusion

In the research presented in this chapter, several manufacturing insights have been made which could influence the industrial adoption of the laser texturing for superhydrophobicity. This has implications for the selection of laser parameters, scaling the laser process to wide areas, handling and cleaning practices, the factory environment, and the use of chemical treatments.

Laser texturing processes were developed using both nanosecond and femtosecond pulsed fibre# lasers. The use of these sources gave rise to different modes of laser interaction and resultant texture morphology. The selection of laser source is determined by cost considerations, material properties and functional requirements. Currently nanosecond pulsed lasers are far less costly than femtosecond sources and it has only been recently that sufficiently powerful femtosecond lasers have become available for wide area operations involving fast scanning or beam parallelisation. The LIPSS fabrication approach used had a slower rate of areal coverage compared to the nanosecond processing strategy, to scale the process further the number of pulses per unit length has to be conserved requiring the development of femtosecond sources with MHz repetition rates. As an overall lower dose is required in the LIPSS patterning approach and a much lower amount of material is removed this means that the LIPSS approach may be more scalable as higher capacity femtosecond lasers

become available in the long term. The reduced thermal input to the material in the LIPSS approach may have specific benefits in applications which are heat sensitive such as post-assembly modification of exterior casing surfaces or modification of thin metal sheets.

The hydrophobic transition of the laser textured surfaces exposed to air were investigated, if air exposure is used in manufacturing the literature survey and experimental findings clearly pointed to LIPSS structures requiring far shorter air exposure transition period to form superhydrophobic wettability. This was attributed to the lower surface area of hydrophilic laser induced metal oxide compared to the rougher nanosecond laser processed surface. The measured duration for hydrophobic transition of the LIPSS surface was 6 days compared to 21 days for the nanosecond laser processed surface. XPS investigation supported the hypothesis that adsorption of hydrophobic organic molecules was responsible for the hydrophobic transition with air exposure. The interaction mechanism was investigated further by exposing the laser processed surfaces to atmospheres containing hydrocarbons with known functional groups. It was observed that the carboxylic acid group was effective to produce a hydrophobic surface, this was attributed to chemisorption to the polar metal oxide surface.

Several approaches to accelerate the transition process were investigated. The use of heat treatment, and exposure to CO₂ gas did not yield promising results due to poor repeatability and wettability. The application of post-process chemical treatments through solution or vapour deposition was observed to be a more effective approach to impart superhydrophobicity. The solution deposition of long chain fatty acids in an ethanol solvent was shown to be an effective treatment using safe, low cost precursors. By varying the chain length of the fatty acid, it was also observed that stronger hydrophobic properties were correlated with increasing hydrocarbon chain length.

Overall laser texturing for superhydrophobicity is in the development stage of technology readiness. The research levels Technology Readiness Levels 1-3 involving the basic principles underpinning the process and experimental proof of concepts have largely been achieved. The major challenge is now in validating and demonstrating the technology in relevant environments.

In this chapter a laser texturing approach was developed to fabricate superhydrophobic stainless steel surfaces. The literature review highlighted disagreement over the chemical mechanism responsible for the hydrophobic state, this was addressed experimentally through surface chemistry analysis. Further experiments explored acceleration of the transition rate through heat treatment and modifying the storage environment. The potential to create designer surfaces with tailored functionality through post-process chemical treatment was explored.

5 WETTABILITY MODIFICATION OF GLASS FOR INKJET DEPOSITION OF FUNCTIONAL MATERIAL

5.1 Introduction

Deposition of printed electronics through functional inkjet printing has gained interest both in research and industry due to its capability for digital pattern control and flexibility of materials selection. This chapter describes research into surface modification of glass surfaces to enable inkjet printing of functional material motivated by future applications in embedded electronics and sensors. Section 5.2 reviews the relevant principles of the inkjet printing process and research literature. A key aspect of the process which shaped the experimental work in this study is that to achieve precise control of deposit morphology it is necessary to engineer the interaction between the liquid ink droplet and the surface. This is determined by liquid properties such as viscosity and surface tension as well as surface properties such as surface free energy and roughness. Inkjet printing to flat glass surfaces brings specific challenges because of the need for controlled surface wettability to ensure high quality and adhesion of deposits. The focus of this work is on soda-lime glass supplied by the industrial partner of the project Pilkington-NSG, a major manufacturer of glass for display, architectural and automotive applications. In its pristine state, soda-lime glass has very high surface energy which results in a water contact angle of less than 10° and a loss of control over the printing process as droplets spread out rapidly to form uneven deposits. However, the pristine state of glass is unstable and quickly, due to hydrocarbon contamination, a water contact angle of $40\text{--}50^\circ$ is formed. This relatively high contact angle reduces the adhesion of inkjet printed deposits on glass [202] and can result in defects in the deposit. There is therefore a drive to understand the role of wettability modification when inkjet printing to glass and to design an optimum surface preparation process.

To judge deposition behaviour, an analysis process to test the spreading of droplets on flat glass with high repeatability was created based on sessile droplet profile imaging and contact angle analysis. This characterisation process was used to test the effect of different surface preparation methods on the liquid-surface interaction. Preparation of surfaces with novel heterogenous wettability was tested using corona plasma discharge treatment and ultrafast laser ablation to modify a hydrophobic coating on glass surfaces.

In order to address the environmental concerns of solvent usage in ink formulations, the printing industry is moving towards replacing the use of water as a carrier fluid. However, these experimental formulations pose challenges for printing to achieve the correct deposition behaviour. Printing tests used a water based silver nanoparticle ink to explore printing onto prepared surfaces with different wetting behaviour. The optimum print parameters to form consistent high-quality lines were investigated. The surface preparation and sintering cycles were evaluated in terms of the adhesion and conductivity of the print. Lift-off and abrasive loadings tests provided insight into the degradation of conductive properties of inkjet printed tracks in an end application. A new approach of embedding inkjet printed tracks in laser ablated microchannels to serve as an abrasion resistant topology was investigated.

5.2 Literature Review

In the literature review, firstly the fundamental mechanics of inkjet printing are outlined along with current industry approaches to preparation of glass surfaces. Secondly, current research into wettability patterning was outlined, this growing field has received increased research attention due to its potential value in fluidic manufacturing processes but effective patterning of glass surfaces with digital fabrication techniques has remained challenging. Finally, the characteristics and applications of functional inks used in printed electronics are discussed in order to guide material selection for inkjet printing experiments.

5.2.1 Inkjet printing principles

Inkjet printing involves production of picolitre sized liquid droplets by a printhead nozzle which are ejected and travel through an air gap to deposit on a substrate. There are many types of inkjet printing, differentiated by droplet production method such as continuous inkjet or thermal inkjet. In this thesis, experiments were conducted using piezoelectric actuated drop-on-demand printing. This technique is particularly applicable to materials and device prototyping for printed electronics because high patterning resolution can be achieved and only several millilitres of ink are required for test experiments [203]. Key advantages of functional inkjet printing include the flexible selection of deposited material, design customisability, low waste of valuable functional inks and the capability to print direct to shape. Disadvantages of the technique are that the ink formulations required to achieve the correct interaction between the liquid ink and substrate can add expense. There are process defects associated with the substrate surface interaction such as the coffee ring effect and defects associated with the printing process such as satellite drops and nozzle misfiring [61], the aerodynamics of the airborne droplets can result in misplaced droplets [204] and additionally the influence of flow dynamics on the inks such as the effect of high strain rates during jetting or recirculation [205].

Figure 5.1 illustrates the lifetime of a droplet in the piezoelectric drop-on-demand inkjet printing process. The stages are broken down into droplet generation (4-80 μs) [205], flight (80-330 μs) [206], spreading (4 μs -0.7 s)[207], drying (30-190 s) [207] and heat treatment (3-60 min) [208]. Images are adapted from cited studies and the timings are reproduced from [209]. Droplet generation involves the use of piezoelectric actuated nozzles which generate pressure waves to change the volume of the reservoir to eject individual droplets [53]. The process is controlled by applying a driving waveform which squeezes and deforms the chamber so that an ink meniscus is formed. The meniscus elongates to form a filament and then necking at the nozzle orifice results in separation of the filament. Ideally the filament converges to form a single large droplet although breakup of the filament into satellite drops is common. The duration of drop ejection is determined by the actuation waveform, optimally a trapezoidal waveform is used with rise, dwell and fall periods resulting in a typical time for the droplet to rupture from the nozzle of around 40 μs [210].

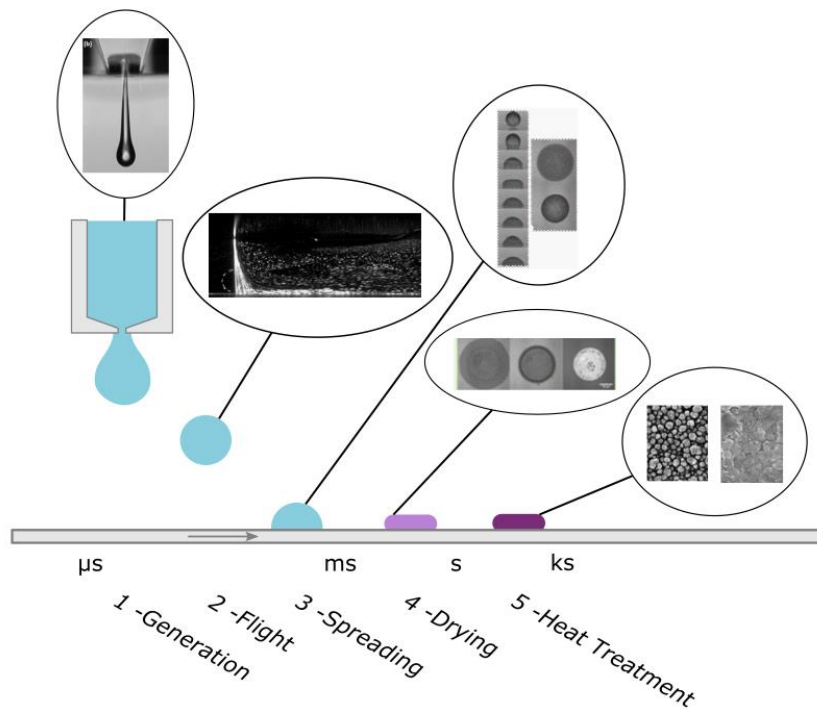


Figure 5.1: Illustration of the lifetime of a droplet from a drop-on-demand inkjet printing process. The stages are broken down into droplet generation [205], flight [206], spreading [207], drying [207], and heat treatment (3-60 min) [208].

By positioning the print nozzle relative to the substrate, the placement of the landing droplet can be precisely controlled to produce a 2D pattern. The flight path of the ejected droplet is determined by the kinetic properties of the droplet as well as air resistance and aerodynamics [204]. During high-rate industrial scale inkjet printing, eddies form between the printhead and substrate and can reduce drop placement accuracy. Gravity has a relatively minor influence because of the low volume of the individual droplets, this allows printing to be carried out with non-vertical throw angles [211].

In the spreading stage of the droplet lifetime, droplet-surface wetting interactions can include complete rebounding of the droplet, partial rebounding, breakup into smaller droplets, or most commonly impacting as single drop and spreading [212]. Upon impact of a single drop where no rebounding occurs, the droplet rapidly deforms and oscillates, and the oscillations viscously dissipate to form a stable spherical cap shape [213]. The diameter of the spread droplet is determined by the wettability of the substrate. A basic model can be formed to predict the morphology of the liquid track after coalescence depending on the interfacial parameters of the system. Using the assumption of negligible gravitation forces and a spherical cap shape, the diameter of the spread droplet on the substrate (D_{eqm}) can be determined from the droplet diameter D_0 and equilibrium contact angle [214]. Further droplets interact with the sessile droplet to form a stable liquid track through coalescence. A simple geometric model assuming droplets coalesce to form a track with a uniform spherical cap profile can be used to predict the deposited track width [214].

$$D_{eqm} = D_0 * \sqrt[3]{\frac{8}{\tan\frac{\theta_{eqm}}{2}(3+\tan^2\frac{\theta_{eqm}}{2})}} \quad (5.1)$$

Solid deposit formation is then governed by drying through evaporation and the effect of post-process techniques. Drying can be typified by either a pinned or a retracting contact line between surface and droplet. A retracting contact line behaviour requires a receding contact angle (CA_{rec}) which is greater than 0° . In this case as the droplet evaporates, dewetting occurs and the width of the spherical cap reduces whilst the contact angle remains fixed at CA_{rec} . In the case of a pinned droplet, CA_{rec} is 0° or very low, this means that as the droplet evaporates and reduces in volume the three-phase contact line and cap width remain fixed. A common print artefact resulting from the drying process is the preferential build-up of particles at the edge of the drop resulting in a detrimental coffee-ring effect. This is observed in Figure 5.1, stage 4, as a darker area at the edge of the deposit. This occurs due to a convective flow where particles are transported radially to the pinned droplet contact line during drying [54]. Initial contact line pinning may result from substrate heterogeneities or contamination but can be reinforced by the radial flow [213]. The resultant variation of deposit thickness is particularly deleterious in applications where a thin, uniform deposit is required such as organic light emitting diode (OLED) display fabrication [215]. Recent work by Hu *et al.* has been carried out to mitigate the coffee ring effect through binary solvent ink formulations [216]. The Marangoni enhanced spreading in these formulations inhibit pinning behaviour and deform the droplet shape during evaporation to prevent radial flow.

Some functional inkjet printed materials require further post-process steps such as sintering or UV curing. Sintering is used to enhance the conductivity of printed metallic nanoparticle inks. As seen in Figure 5.1, step 5 [217], sintering promotes necking between particles to form a continuous film.

Nanomaterials have much lower melting temperatures than the bulk material properties so relatively mild temperatures are used (100-200°C for Ag nanoparticles) [218]. Heat treatment post-processing may be used to remove nonconductive organic compounds used in the ink formation while also annealing the deposited material.

It is clear from this section that the surface preparation will be a key aspect to consider when printing and so this will be considered in more detail in the next section.

5.2.2 Surface preparation of glass

Surface contamination is a vital issue in inkjet printing because just a few atomic layers of contaminant can reduce adhesion by inhibiting chemical connection of the deposited material to the substrate. It is important to note that a bare glass surface continuously reacts with its environment during the overall manufacturing process. For example, immediately after flat glass production with the float glass process glass is typically stored with paper or polymer interlayers between single glass sheets. This can result in deposition of material to the glass surface and over a long time even corrosive reactions. Common contaminants such as residue from organic cleaning agents, fingerprints, greases and oils have low surface energy which results in poor ink wetting [219]. Further sources of contamination involve particles of dust or other solid matter and humidity. The goal of a cleaning or preparation process is to produce a reproducible, representative, and stable surface state amenable to successful printing.

The properties of silica glass surfaces can be very different from the bulk. The bulk matrix of silica glasses consists of interlinked tetrahedral SiO_4 arrays. Because the glass surface is very reactive after float glass production, a 10-100nm surface layer is typically formed through interaction of the surface with the air. The silica structure terminates either with a siloxane group or reactive silanol group. The siloxane group is inert, whereas the hydroxyl group of the silanol group is very reactive. Silanol groups (Si-OH) are formed by chemisorption of water with dangling silicon cations or Si-O^- anions, as well as through hydrolysis of siloxane linkages (Si-O-Si) and through ion exchange at non-bridging oxygen sites [220]. The processes of dehydration, dehydroxylation and rehydroxylation move between these two phases to tune surface reactivity. Organic contaminants react very quickly with surface hydroxyl groups in ambient conditions [221]. Cleaning is carried out to remove weak boundary layers and regenerate reactive silanol sites. This interaction with air is particularly important when processing is done offline such as in a secondary inkjet printing process as it determines the ink surface interaction mechanics [222].

In an industrial setting, a modular approach is typically used to clean and prepare flat glass surfaces. This may involve passing the glass panel through modules involving brushing, solvent treatment,

rinsing, ultrasonication, air-drying and plasma treatment. Brushing and ultrasonication act to mechanically remove solid particles and stimulate cleaning. This is typically used in conjunction with exposure to acid or alkali detergents, surfactants and solvents which help to remove solid particles and break down organic contamination. Rinsing with deionised water is used to remove any residues remaining from these cleaning agents. These processes are used both to remove macro scale contamination arising during flat glass production, remove chemical contaminants and activate the surface through reactive terminal group formation.

Wet chemical methods of cleaning are being replaced in some applications with plasma-based cleaning method which pose less environmental impact and safety hazards. Plasma treatment is a widely used industrial method to prepare a pristine surface for inkjet printing. The aim of plasma treatment is to eliminate surface impurities and to promote bonding of a coating [223]. Firstly, reactive species in the plasma react with surface contaminants to form volatile products which then escape from the surface into the atmosphere. Secondly, polar functional groups are formed on the glass surface [223]. Several types of plasma treatment for surface treatment are used which are differentiated by the elemental source of the plasma such as argon, nitrogen and oxygen. A specific type of plasma treatment which is used widely in the printing industry is corona discharge treatment. In this process, the substrate is separated from a high voltage electrode by a small air gap. The potential difference causes dielectric breakdown of air and the ionisation of air molecules, in particular forming reactive ozone (O_3). This treatment approach is very effective for sheet applications because it can be scaled to wide areas using roller electrodes. Because a homogenous flux of reactive species is supplied, surface cleanliness has a high degree of homogeneity [222]. An important consideration for a manufacturing environment is that an exhaust is required to remove ozone gas which is poisonous.

Yamamoto *et al.* showed that plasma treatment was an effective technique to lower the glass contact angle to less than 4° [224]. They found that treatment of 60 s with a voltage of 15 kV produced the maximum hydrophilicity possible. After leaving the plasma cleaned surface exposed to air for several days they found that the hydrophilic property was lost but did not provide further investigation into the cause. Homola *et al.* tested cleaning of glass surfaces with dielectric barrier discharge induced plasma, by treating the glass surface for 60 seconds they found the water contact angle reduced from 37° to lower than 4° . Using XPS analysis they found that this was associated with a reduction in C-H bond indicating removal of hydrocarbon contaminants and a rise in C-O=O/C-O peaks indicating polar functional group formation [225].

In common printing processes, engineering materials tend to have non-zero receding contact angles allowing for surface mobility after initial fluid-surface impact. Hsiao *et al.* showed that the retracting

angle of glass slides which had been cleaned and dried in an oven at 120°C for 2 hours was 20° [226]. This finite retracting angle meant that deposited droplets could coalesce and destabilize the printed geometry requiring careful control of drop spacing and print parameters to optimise deposition geometry avoiding necking and bulging. However, pinned droplet-surface interaction which exhibits contact angle 0°, whilst anchoring the droplets can lead to uneven spreading of droplets on surfaces and coffee ring formation.

Plasma cleaned surfaces readily adsorb contaminants from the surrounding atmosphere or packaging materials. This needs to be accounted for in manufacturing operations as this means printing must be carried out in a timely fashion if only a range of contact angles are viable for successful printing. There is not a clear guideline on the time interval for reabsorption of contaminants to glass after corona plasma treatment and limited research on the mechanism of hydrocarbon contamination; this is essential to qualify to ensure high quality and reproducibility of inkjet printing to glass in an industrial setting [172,227].

By understanding and controlling the wettability, there is then an opportunity to pattern it to deliver a specific function. This will be examined in more detail in the next section.

5.2.3 Wettability Patterning

Several opportunities exist for technologies and devices enabled by the ability to locally control liquid spreading and constrict movement. The use of programmable surface patterning techniques such as laser ablation allow for the creation of digital patterns with tailored control of wettability such as areas of both superhydrophobicity and superhydrophilicity in direct proximity. The production of patterns with contrasting wettability such as superhydrophobic surfaces with localised areas of superhydrophilicity or neutral wetting has been demonstrated for a range of substrate materials with different techniques including lithography, laser thermal treatment, laser printing and inkjet printing. The majority of studies have focused on medical or microfluidic device fabrication which has been reflected in bias of literature reports to substrate materials such as PDMS and paper.

In an example of medical device fabrication, nanosecond pulsed laser texturing of PDMS was used to fabricate droplet containment grids, the laser texturing acts to create surface roughness and a low surface energy chemical state resulting in textured areas of super hydrophobicity and untreated smooth hydrophobic PDMS [228]. Droplet formation was demonstrated by immersing the patterned surfaces vertically in water, by varying the grid patterning parameters and water withdrawal speed it was possible to control the size of droplets formed within the grid. The droplet microarrays produced were used to capture cells in microdroplet arrays for screening and culturing.

An additional route to patternable wettability control is to use laser or print based techniques to locally reduce the contact angle of an initially superhydrophobic surface [229–231]. Continuous wave laser processing of silicone paper was shown to reduce the contact angle from 115° to 20° allowing fluid to be contained in the textured areas [232]. A further coating of hydrophobic silica particles allowed lateral diffusion of the liquid to produce patterns showing capillary flow.

Chemi-luminescence tests showed that mice blood solution sprayed on a droplet array surface would luminesce in the laser textured areas which were patterned with luminol stock. Surfaces with binary superhydrophobicity-superhydrophilicity patterns with no substrate dependence were fabricated by Schutzius [233] through laser thermal treatment of dropcast polysilsequioxane (POSS). This technique leveraged the organic-inorganic hybrid nature of the POSS as thermal laser treatment of the dropcast coating acted to modify the ratio of polar to non-polar bonds modifying the wetting property from 165° to super hydrophilic. The POSS surface retained superhydrophobicity up to a temperature of 300°C suggesting potential use in harsh environments and for enhanced heat transfer applications.

A biomimetic example of patternable wettability is the Namib desert beetle which harvests water in the Namib desert fog with a surface of hydrophilic ridges and hydrophobic grooves. Laser patterning of a superhydrophobic porous TiO_2 -fluoroalkyl silane coating, Figure 5.2a, was used to mimic this effect by creating localised regions of hydrophilicity through localised smoothing of the film [234]. By texturing 2D arrays of microscale branch-like triangles arranged in a hierarchical tree shape a water harvesting device was fabricated on a silicon surface. Droplets forming on the tips of the triangle arrays were subjected to a capillary force imbalance and transported down the ‘stem’ of the tree pattern to a collection zone, the harvesting efficiency was enhanced by a factor of 36x compared to non-patterned films.

Gosh *et al.* used a process of UV exposure of a superhydrophobic coating through a photomask as shown in Figure 5.2b [235]. After exposure for 30 minutes the superhydrophobic coating becomes superhydrophilic. This process was developed as a fabrication tool for open microfluidics, a range of operations were demonstrated involving liquid transport along tracks, droplet bridges, droplet splitting and uphill travel.

As shown in Table 5.1, current literature reports show there is a deficiency of fabrication work in the superhydrophobic-superhydrophilic domain (larger than 150° of wetting contact angle difference). And there has been limited work into the use of intrinsically hydrophilic glass substrates. Several studies have explored wettability or topographically patterned substrates for use in inkjet printing. Keum investigated topography directed inkjet printing to produce functional tracks in flexible substrates [236]. The process involved molding a lithographically produced topography of ripples and grooves onto PDMS and then depositing a silver nanoparticle ink. The aim was to improve the

inherent resolution of inkjet printing, results were analysed in terms of print quality relative to channel geometry, force balances and track conductivity. This study showed the potential of hybrid topology modification before printing but did not investigate a real engineering material or scalable fabrication technique.

Table 5.1: Collation of studies investigating wettability contrast patterning. The substrate, fabrication techniques and range of contact angles reported are shown.

Paper Reference	Substrate	Maximum contact angle (°)	Minimum contact angle (°)	Fabrication Approach
[234]	Silicon	160	95.1	Hydrothermal NaOH for porous film. Silanized. Laser processing
[230]	Sandpaper	145	106	Superhydrophobic treatment. Inkjet printing
[40]	PDMS	162	~105 (est.)	Laser processing
[233]	Silica film	~145	0	Deposition. Thermal treatment through laser & flame
[232]	Hydrophobic Paper	115	20	Laser processing
[228]	PDMS	154	111	Laser ablation
[229]	Polyester sheet	>150	70	Roller Printing

Nguyen *et al.* developed a novel process of hydrophilic-hydrophobic coating onto PET films, then using a nickel stencil the films could be patterned to form selective regions of hydrophobic-hydrophilic [42]. Inkjet printing into the patterned surface showed that PEDOT:PSS ink spread into the high wettability tracks and it was possible to form continuous track features smaller than the printed drop diameter. Kant *et al.* investigated combined topographical and wettability patterning to investigate wetting of picolitre droplets into shallow recesses on an ITO-coated glass surface [237]. They found that the bounding topography encouraged fluid covering of the target recessed regions however containment was not assured. Wettability patterning ensured robust containment within the wetted regions but poor deposition coverage. The combination of topographic modification with hydrophobic fluoropolymer cavity walls produced a favourable wetting whilst maintaining droplet containment. A limitation of this study was the requirement for clean-room fabrication techniques.

An exciting demand for inkjet printing is found in manufacture of organic light-emitting displays. In this fabrication process the functional element is printed into a hydrophilic cavity with hydrophobic cavity walls. The key aim is to ensure a uniform particle deposition after carrier liquid evaporation and to ensure confinement of the droplet in the cavity. Jackson *et al.* carried out a numerical analysis of the printing process and identified the common failure modes for cavities with different combinations of wettabilities [238]. Broadly, it was found that the greater difference between the contact angle of the cavity wall and the substrate allowed for better cavity wetting. Using a wettability contrast between cavity and substrate it was possible to print with a maximum misalignment of greater than 90° of the droplet width and still achieve full cavity wetting. As well as patterning wettability, it is important to consider the patterning of functional materials onto glass, and this will be covered in the following section.

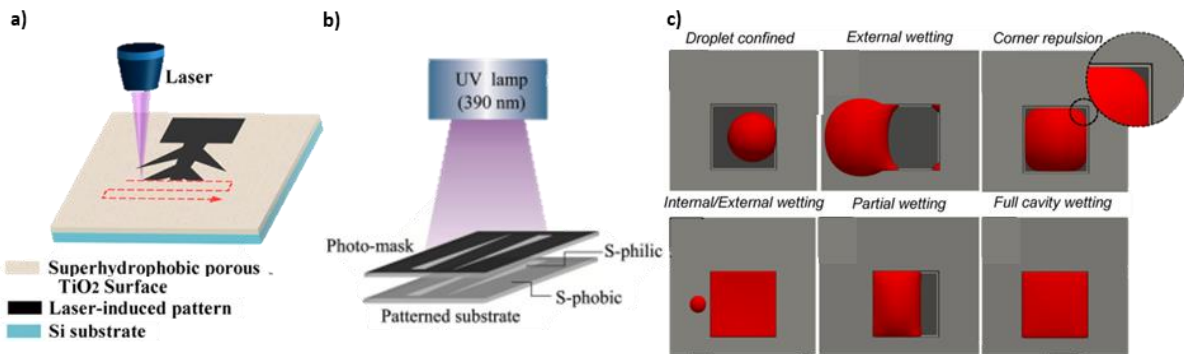


Figure 5.2: Experimental schematics of wettability patterning through (a) laser patterning [234], (b) masked UV treatment [235]. (c) Numerical simulation of inkjet printing into wettability patterned wells for OLED display fabrication [238].

5.2.4 Inkjet printing of functional material

In this section, the different types of functional inks prevalent in industry and research are outlined focusing on conductive ink formulations pertinent to embedded sensing and electronics applications. Three common types of functional ink are: dispersions of metal nanoparticles, dispersions of organic material and solutions containing a dissolved functional element. Table 5.2 collates commonly used conductive inkjet inks and describes their main advantages and disadvantages. As well as the functional component, inks must be formulated with the appropriate carrier fluid and dispersion properties to ensure printability. The critical properties of the ink are its surface tension and viscosity as these determine ejected droplet size and velocity as well as the stability of droplet generation [239]. For optimal inkjet printing these values should be around 10-12 cp and 28-33 dyne respectively at the jetting temperature [240].

Metal nanoparticle inks are the industry standard for the deposition of conductive tracks and interconnects. They provide the best conductivity which is broadly 2-4 orders of magnitude better than for conductive polymers, graphene or carbon [241]. The nanoparticles must be less than $1/10^{\text{th}}$ of the size of the inkjet printing nozzle to prevent clogging. The particles are usually dispersed in an organic solvent, with further formulation additives for anti-flocculation. Although this approach is effective there are environmental concerns due to the sensitivity of the organic solvents and the use of rare earth metals (silver, gold and indium). These environmental concerns have spurred research into alternative functional components and the use of water-based metal nanoparticle inks. In an important early study published in 2002, Fuller *et al.* printed a suspension of Ag nanoparticles dispersed in α -terpineol to achieve a very low resistivity of $3 \mu\Omega \text{ cm}$ which is approximately twice that of bulk silver [242]. However, the choice of solvent in this study would bring challenges for an industrial application due to the production of harmful volatile organic compounds [208]. Toluene is a commonly used solvent to formulate silver nanoparticle inks [239,243] but it is often classified as a toxic substance and can be incompatible with materials used in production processes such as the plastic housing of print heads.

Investigations into printing metal nanoparticle inks using environmentally friendly carrier fluids have been limited to date and none of the major ink suppliers offer commercially available water based inks. Several significant challenges are associated with this formulation such as forming a stable dispersion, avoiding particle flocculation, and ensuring the suitable surface tension and viscosity. Lee *et al.* [208] used a water-diethylene glycol (DEG) bisolvent to disperse Ag NPs in water. The DEG helped to reduce the evaporation rate of the solvent to reduce blocking of the print head, it also made the viscosity and surface tension of the ink more favourable for printing. The inkjet printing tests were carried out on a glass slide, although the surface preparation and wettability were not reported. The maximum concentration of silver nanoparticles tested was 25 wt% and the ink was printable for greater than 2 months after formulation. Sintering at 260°C resulted in an electrical resistivity of $1.6 \times 10^{-5} \Omega \text{ cm}$. Shen *et al.* [241] formulated an aqueous silver nanoparticle ink which involved synthesis of poly (acrylic acid) coated silver nanoparticles which were dispersed in a water-glycol solution at up to 25 wt%. This preparation method enabled very stable dispersive properties with simple, low cost and environmentally friendly manufacturing. In their printing tests it was possible to obtain an optimised resistivity of $3.7 \mu\Omega \text{ cm}$ on photographic paper with a relatively low sintering temperature of 180°C .

Table 5.2: Common conductive inkjet inks. Conductivities obtained from suppliers Sigma Aldrich, PV Nanocell and Ulvac in August 2020.

Ink	Conductivity	Advantages	Disadvantages	Ref.
Ag Nanoparticles	1.5 mΩ/sq	Very good conductivity. Resistant to heat and UV exposure.	Expensive. Particles can block the inkjet nozzles. Requirement for sintering limits applications for flexible substrates.	[244]
Tin-doped indium oxide (ITO) nanoparticles	250 Ω/sq	Industry standard transparent electrode material	Expensive. Environmental concerns.	[245]
Graphene	4 kΩ/sq	Cheap, flexible, easily printable and better for the environment	Can be damaged by heat and UV exposure.	[246]
SW-Carbon Nanotubes	400 Ω/sq	Novel electrical properties	Can be difficult to formulate CNT ink with stable dispersion properties. Post-processing is required to align CNT network. Toxicological effect.	[247]
PEDOT:PSS	1500 Ω/sq	High ductility. Low cost. Does not require sintering process.	Low conductivity. Vulnerable to degradation by heat, water, UV exposure and oxygen	[248,249]

To enhance adhesion of inkjet printed silver nanoparticle films, Jang *et al.* incorporated a nanosized frit glass into the ink formulation [250]. The formulation consisted of 0.16 vol% frit glass, 20 vol% silver nanoparticles, 5 vol% dispersant and remainder ethylene glycol. Incorporating frit glass enabled sintering of the deposit at a much higher temperature than when only silver nanoparticles were used by preventing cracking and delamination effects. Through the cross-hatch adhesion test they observed a much higher adhesion with the frit glass formulation whilst maintaining conductive properties of the film after sintering at 500°C. The enhanced adhesion was attributed to a liquid phase sintering effect in which the frit melted readily to wet between the Ag particles and bond the film to the substrate as a glassy film. This adhesion promotion mechanism is primarily physical in nature rather than chemical. Further research by Jeong *et al.* demonstrated chemical functionalisation of the glass surface prior to Ag ink printing with silane based molecular layer adhesion promoters [251]. In addition to improved

adhesion, a further benefit was that the low wettability of the silane layer allowed for narrow features to be printed (line width 45 μm).

The use of conductive polymers for integrated electronics applications is well established industrially. Conductive polymer materials reduce the disadvantages of using metals such as costs associated with mining, shipping and processing. Polymers are attractive industrially as they are lightweight, cheap and functionally versatile [252]. Additional novel properties involve the potential for chemistry modification through doping and high ductility for flexible electronics applications. PEDOT:PSS is a transparent conductive polymeric which is emerging as potential alternative to industry-standard rare earth metal compounds such as ITO. Example industrial applications of PEDOT:PSS involve interconnects for organic light-emitting diodes, organic solar cells, organic thin-film transistors and as transparent antistatic coatings. PEDOT:PSS solutions can be printed with a very high quality because no satellite drops are formed at high voltages [253]. To ensure the deposited films have conductive properties it is necessary for the polymer chains to swell and aggregate which is mediated by solvent choice and surfactant concentration [254]. Drying at 90°C and annealing at 150°C [255] have been used to improve the conductive properties of inkjet deposited PEDOT:PSS films. The temperature in the application environment must be controlled as degradation of conductive properties has been observed for temperatures above 55°C after 50 hours of exposure [249]. This is particularly important to consider for glass applications where the product may be exposed to direct sunlight and sharp thermal gradients. Specifically, this means alternative functional inks must be used in applications such as deposition of resistive heaters for automotive windshields or emerging thermoelectric energy generation applications. New ink formulations based on 2D and 3D nanostructured carbon allotropes have received substantial recent research attention. These inks are very attractive because of their combination of novel electrical properties [10], possibility of room temperature curing without heat treatment [256] and their potential to be very low cost in the future. Even now, the cost of CVD produced graphene is cost competitive in industrial applications such as flexible displays and solar cells [257]. Furthermore, these inks can be formulated with the use of water-based carrier fluids. Post-process heat treatment through thermal annealing or laser annealing is used to remove binders and solvents and sinter or weld graphene flakes together [258]. An example application of inkjet printed graphene was shown by Seekaew *et al.* who printed a graphene-PEDOT:PSS composite ink to fabricate ammonia sensors with sensitivity down to 25 ppm [259].

In addition to printing conductive inks, multilayer embedded electronic devices have been fabricated using inkjet printing including thin film transistors, photovoltaic cells and chemical sensing devices. In these multi-stage manufacturing processes inkjet printing can bring key patterning and material flexibility advantages. For example, in the manufacture of OLED displays, inkjet is highly sought as a lower cost alternative to the standard shadow mask evaporation deposition approach as no material is

wasted through depositing onto the mask. However, several research challenges must be addressed to enable commercial inkjet printed OLED displays such as optimal surface interaction to form flat deposits with high deposit density and quality [260]. Figure 5.3 shows the structures and compositions of a thin film transistor, a photovoltaic cell and an organic light emitting diode fabricated through multilayer inkjet printing.

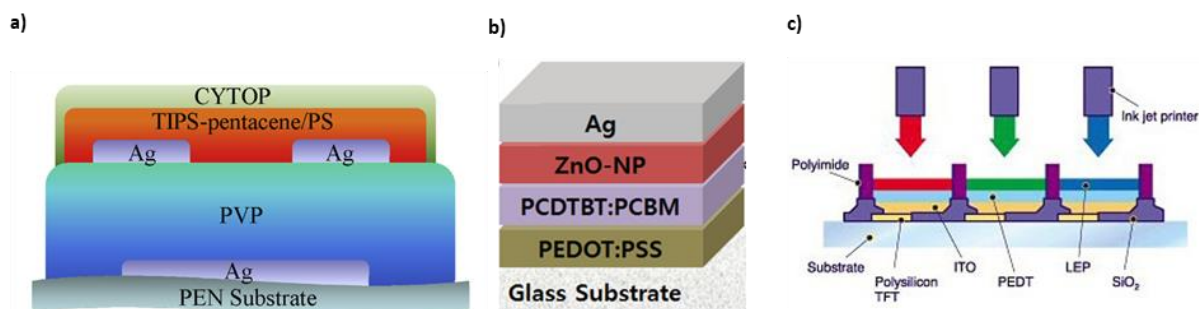


Figure 5.3: (a) Device structure of an inkjet printed thin film transistor [261]. (b) Device structure of an inkjet printed photovoltaic cell [262]. (c) Inkjet printing into wells for light emitting diode panel manufacture [263]

The literature presented evidence of the industrial value of fluid manufacturing techniques for printed electronics on glass surfaces. Emerging applications for functionalized and smart glass surfaces have created a market pull effect for scalable digital manufacturing processes in the glass industry. The key gaps in knowledge required for technology progression concerned the implications of cleaning and wettability modification techniques for functional inkjet printing. To obtain precise lateral and thickness control in additive fluid deposition processes it is essential to control surface wettability to match with the fluid properties.

There is growing desire to use water based conductive inks to ameliorate concerns associated with solvent based formulations. However, these inks bring new challenges because of the complex spreading and coalescence behaviour driven by their generally high surface tension. One approach to tailor surface-ink interaction is to modify surface wettability locally. There have been some initial studies into modification of glass surfaces to produce topographical or wettability patterns to enhance inkjet printing deposition. Currently lithographic approaches are used and there is a significant drive to explore digital modification approaches. Research gaps concerning the durability of functional inkjet printed tracks was highlighted both by the small number of research studies and through discussions with the industrial partner of the project.

5.3 Design of Experiments

This section describes how the research aim and literature findings were used to formulate research objectives and experimental approach.

5.3.1 Research Aim

To better understand the link between durability of printed functional inks and the tailoring of the wettability of glass surfaces.

5.3.2 Research Objectives

The literature review helps identify materials selection for printing electronic components to glass surfaces. In an industrial setting, silver nanoparticle inks are the most attractive way to inkjet print conductive tracks to function as interconnects or heating elements of resistive heater circuits. This is because they offer the highest conductivity and durability in comparison to alternative ink formulations with organic functional components. Research and industry have mainly focused on the use of solvent based ink formulations to deposit silver nanoparticles. The use of water-based inks is emerging because of the potential to reduce solvent usage however these inks bring printing challenges because of their high surface tension, that still need to be explored.

One key concern in inkjet printing is how to ensure the correct deposition behaviour to avoid coffee ring formation and low substrate adhesion. Because the functionality of a printed pattern can depend strongly on its geometric quality, experiments were carried out firstly to analyse the effect of surface preparation on droplet-surface interactions and then to optimise the printing of continuous tracks. The deposit morphology and conductive properties were analysed, and a print strategy was developed through optimisation of surface preparation, droplet spacing and number of printed layers.

Typical industrial approaches to modifying surface wettability involve air plasma treatment and deposition of self-assembled monolayers. If patterned control of wettability is needed, these are normally followed by lithographic approaches. Laser direct-write patterning and masked plasma treatment were used to modify glass surface chemistry and remove surface coatings. These capabilities were shown to enable the digital patterning of contrasting regions of hydrophilicity-hydrophobicity on glass surfaces, the operating window and limits of pattern resolution were tested. Finally, the effect of modifying glass surface wettability and structure on the adhesion and abrasion resistance of inkjet printed tracks was tested. This chapter also builds a capability that enables progression to inkjet printing combined with laser ablation to embed function within the glass surface.

This aim and the key research gaps noted above can be addressed by tackling the following objectives:

1. Characterise the effect of glass cleaning and plasma treatment on the surface parameters which impact surface interaction during inkjet printing.
2. Assess the use of wettability modifications processes such as solvent treatment, plasma treatment and functional chemistry deposition for use in a manufacturing environment.
3. Test the capability of laser and plasma patterning to produce surfaces with patterned wettability.
4. Study the dynamics of particle distribution and track formation of water based silver nanoparticle inks on a range of surface wettabilities.
5. Determine the feasibility of using a hybrid laser etching – inkjet printing process to embed conductive tracks below the glass surface and explore benefits to durability.

5.4 Method

This section outlines the materials, equipment and experimental procedure used.

5.4.1 Surface Modification

Three surface treatment approaches were tested which resulted in a range of surface wettabilities, from high attraction-superhydrophilic through to low attraction-hydrophobic. These treatment processes were (i) solvent cleaning, (ii) corona plasma treatment, and (iii) hydrophobic layer vapour transfer deposition.

The solvent cleaning process involved: firstly, brushing the surface with a scouring cleaning pad soaked in hot soapy water, then immersing the substrate in acetone (99.8%, Fisher) which was subjected to mechanical impulse in an ultrasonic bath for 5 minutes, followed by repetition with propan-2-ol (IPA) (99.8%, Fisher). These steps aim to remove most contaminants on a glass surface especially particulate matter such as dust. The surfaces were then rinsed with water (analytical reagent grade, Fisher) to remove any residue. Finally, the surfaces were dried with filtered compressed air.

To study the effect of corona plasma treatment on the wettability of glass surfaces an experimental matrix of applied power and treatment time was executed. A LabTEC Corona Lab System (tantec) HT-X01-28: 28 kW was used for experiments. The corona treater voltage was set to 20kV, the roller electrode was separated from the glass surface by a 1 mm spacer. To ensure an evenly applied dosage 15x 1 cm wide glass samples were prepared using the scribe and break method. The minimum

applied power for which a discharge plasma was formed was 13 W, applied powers of 50W and 200W were also tested. Following the results of this investigation into optimum applied parameters, the degradation of the surface conditioning over time was investigated by measuring the water contact angle in time intervals after treatment.

The hydrophobic coating was carried out by vacuum transfer of a 14 μ L droplet of Trichloro(1H,1H,2H,2H-perfluorooctyl)silane (97%, Sigma Aldrich) in a desiccator pumped to 7 mbar and left for over 12 hours. The surfaces were solvent cleaned and plasma treated prior to hydrophobic coating deposition to activate the surface and promote bonding.

Surfaces were characterised through profile imaging of deposited droplets, contact angle measurement (described in section 2.3.4), FTIR spectroscopy (PerkinElmer Frontier MIR/NIR Spectrometer) and XPS spectroscopy. The XPS system was a Thermofisher Escalab 250Xi. For survey scans: the pass energy was 100 eV, the step size was 1 eV and 10 scans were applied. For narrow scans: the pass energy was 50eV, the step size was 0.1eV and 50 scans were applied. The flood gun and 2 metal clips per sample were used.

Three probe liquids were used to measure the surface energy of the modified surfaces: deionized water, diiodomethane (Alfa Aesar, 99% stabilised) and ethylene glycol (Fisher 11428920). Drop volumes were fixed at 2 μ L. Contact angle measurements were used to calculate surface free energy using OWORK with the in-built KRUSS analysis software of the equipment [264,265].

5.4.2 Wettability patterning

Two novel processes to precondition the glass surface based on wettability patterning with plasma treatment and laser ablation.

5.4.2.1 Plasma treatment

Figure 5.4 shows a schematic of the experimental layout used for masked plasma treatment. The masks were fabricated by laser cutting polystyrene sheet of 0.5 mm thickness. A 60 W VLS CO₂ laser cutter was used operating with parameters 5% power, 1 mm/s and 500 pulses per inch. Several mask schematics were fabricated for experimental testing as shown in Figure 5.4(a).

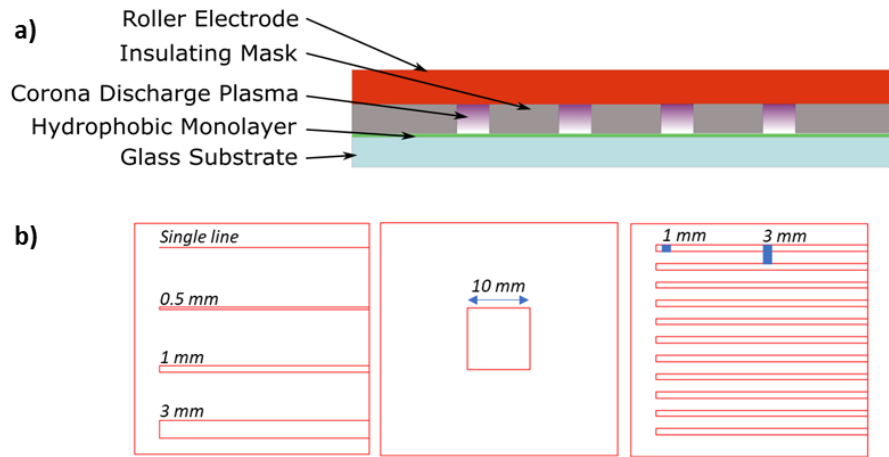


Figure 5.4: (a) Diagram of the masked plasma treatment process. (b) Schematic of masks used in masked plasma treatment experiments

5.4.2.2 Laser Processing

The ultrafast laser processing system was outlined in section 2.2.2 and patterning strategy described in section 3.3. The chosen parameters for glass patterning are summarised in table 5.3:

Table 5.3: Summary of laser processing parameters

Experiment	Laser	Objective	Pulse Energy	Scan Speed	Hatch Spacing	Number of layers
Microgroove formation	Satsuma Ultrafast Platform	Thorlams LMU 10x Spot-4.81 μm	70%	10 mm/s	5 μm	5
Wettability Modification	Satsuma Ultrafast Platform	COMAR 08 0X 05 Spot-1.92 μm	Ablation threshold 44%	50 mm/s	Varied 1-32 μm	1

5.4.3 Hardness and adhesion testing

To test the adhesion of the inks to the prepared glass surfaces a commercial cross cut adhesion test was used. The kit was Dyne CC3000 [266] which conforms with the test standards ISO/DIN 2409, ASTM D3359 [267]. In the testing process, two series of parallel cuts cross angled to each other are made in the coating with a 6-bladed cutting head. This produces a pattern of 25 regular squares of grid size 1 mm. Adhesive tape (SP3007, Dyne Testing) is then applied to the surface and removed by seizing the free end rapidly keeping the removal angle as close to 180° as possible. After lifting off, the degree of flaking and detachment is inspected under magnification and compared semi-

quantitatively using a ranking scale of 0-5 where 0 shows no detachment and 5 involves over 65% of the cross-cut area being detached. Figure 5.6 illustrates the cross-hatch adhesion testing process.

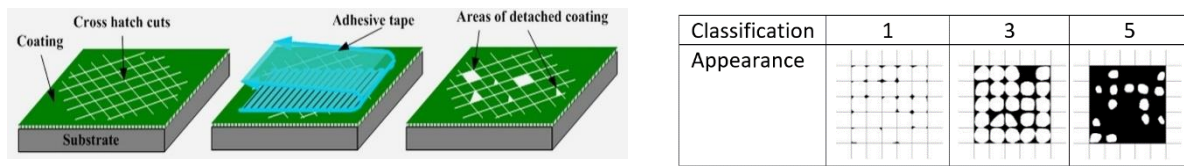


Figure 5.6: Schematic of the cross hatch adhesion testing and classification process [268].

To test the adhesion of inkjet printed tracks a tape peel off test was used. The standard adhesion tape (SP3007, Dyne Testing) was pressed firmly onto the surface perpendicularly to the tracks. The tape was then pulled off pulling as close to 180° as possible. The adhesive strength of the tape was measured by attaching a glass slide to a beaker, applying the tape to the glass slide and then adding water to the beaker in 100ml increments until the tape failed. The tape failed at a total mass of 1748g giving a bonding pressure to the glass slide of 2.74 N/cm².

In order to test abrasion resistance of the inkjet printed deposits, an experimental setup to apply a repeatable load was used. The system consisted of an 11.5mm strip of 600 grit sandpaper which was loaded by a 100g metal weight. The abrasion cycle consisted of pulling the weighted sandpaper across the surface at a rate of approximately 1 cm/s. After each cycle, the surface was imaged with optical microscopy and the track resistance was measured.



Figure 5.7: (a) Schematic of the adhesion peel off testing approach. (b) Schematic of the abrasion resistance testing approach.

5.5 Results & Discussion

In the results and discussion section, the effect of surface preparation of glass on surface wettability and chemistry was investigated. This is followed by a discussion of experiments concerning patterned modification of surface wettability using shadow masked plasma treatment and laser patterning. The properties of inkjet printed silver nanoparticle deposits on glass surfaces with modified wettability was analysed. The durability of the inkjet printed deposits were investigated through peel-off and abrasion tests.

5.5.1 Surface Preparation of Glass for Fluid Deposition

As surface wettability has a significant impact on the dynamics of a fluidic manufacturing approach such as inkjet printing, a full understanding and quantitative models of the cleaning and wettability modification processes are needed. After solvent cleaning, the glass surface showed an average water contact angle of $21.8 \pm 2.5^\circ$. This is classified as hydrophilic wettability and a high consistency was observed. However, pristine glass surfaces should have contact angle smaller than 10° . This indicates that after the solvent cleaning treatment there is likely still the presence of organic contamination chemically bound to the glass surface or the presence of organic residues from the solvents.

As discussed in literature review section 5.2.2, corona discharge plasma treatment is used to break down any organic surface contaminants as well as to activate the surface by generating high surface energy dangling hydroxyl (OH-) groups. The minimum applied power for which a stable discharge plasma was formed was 13 W. After 5 seconds of treatment with the minimum power a significant reduction in water contact angle was observed to an average of $8.47 \pm 1.6^\circ$. Figure 5.8(a) shows how droplet contact angle varied with applied corona treatment parameters. After 40s of treatment all surfaces showed an average contact angle less than 5° which remained low in longer treatment durations. This led to future experiments being carried out with an average power of 200 W and treatment time of 60 s/cm as this was within steady state conditions to ensure repeatability.

After plasma treatment it is essential to know the duration for which the surface remains activated, as this will be the time window for printing. This is particularly important in a factory setting where large batch numbers and long takt times may cause the negative consequences of any ageing effects to be encountered. To investigate the ageing of the plasma treated surface when exposed to an ambient air environment the contact angle was measured in time intervals after plasma treatment. Figure 5.8(b) shows the variance of contact angle compared to the untreated surface and the freshly treated surface. It was found that for the first 8 hours the contact angle remains on average below 5° . After 24 hours of air exposure the contact angle rose significantly outside of the critical superhydrophilic region to form

a contact angle of 9.2 ± 0.7 . Figure 5.8(c) shows example drop shapes for the different treatment methods used.

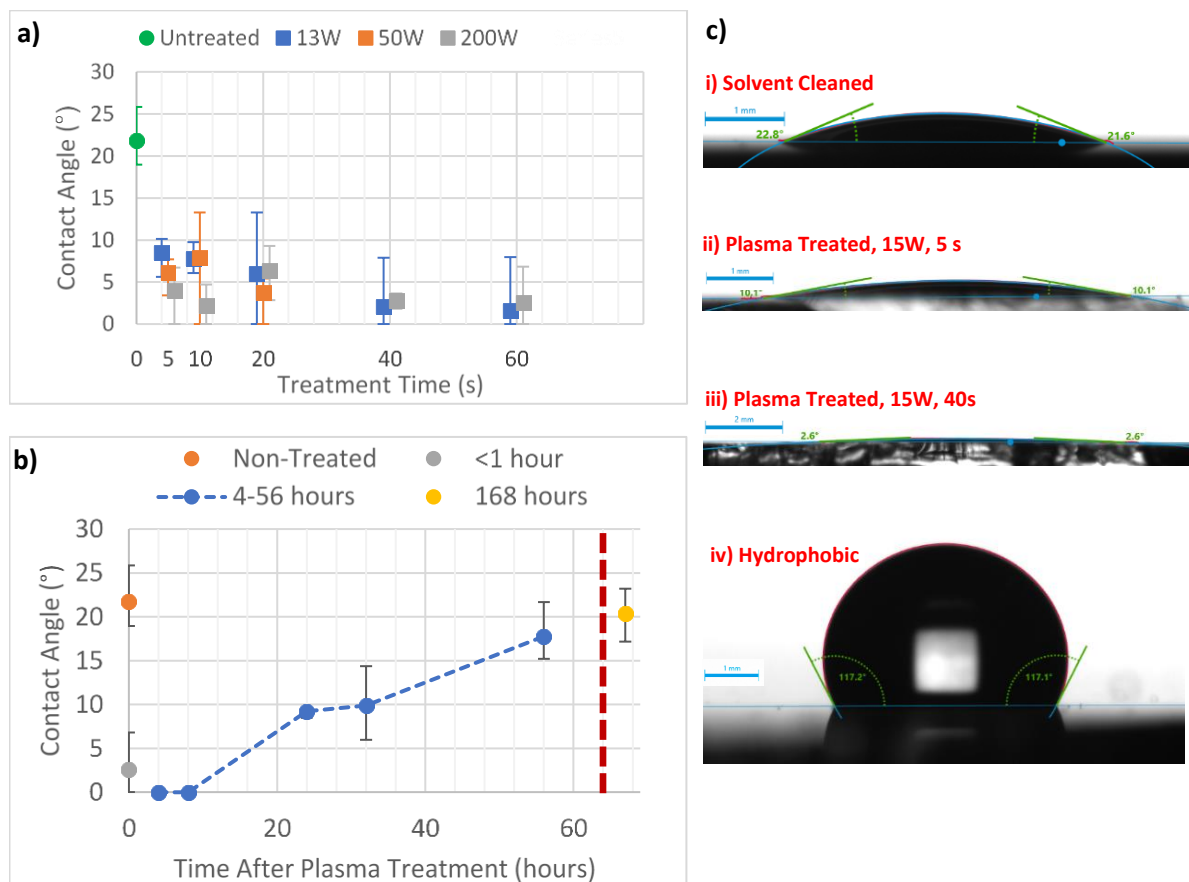


Figure 5.8: (a) Effect of varying plasma treatment power and time on measured contact angle, treatment times dodged by 1s to avoid overlapping of error bars. (b) Variation of contact angle with time exposed to air environment. (c i-iv) Drop shape images used for contact angle measurement.

The hydrophobic coating deposition resulted in a surface wettability of $114.3 \pm 1.6^\circ$. In order to inform the movement and drying behaviour of droplets on the surfaces the receding angle was measured using the needle-in method. The solvent and plasma cleaned surface showed pinned behaviour with receding angle of 0° . The hydrophobic surface exhibited a finite receding angle of 23° indicating a mobile contact line.

In order to qualify the wetting behaviour with respect to theoretical prediction water droplets of varying size ($1.25\text{--}10\ \mu\text{l}$) were deposited onto the prepared glass surfaces. The diameter of the deposited droplets was analysed using ImageJ [269] and compared to predicted results using the spherical cap model described in section 5.2.1, the contact angles measured in this section were used to supply the model along with the nominal droplet volumes defined by the syringe fluid dispensing unit of the contact angle measurement system. The spherical cap model produced a reasonable

prediction of the spread diameter of the droplets generally, within 5% as shown by the error bars in Figure 5.9.

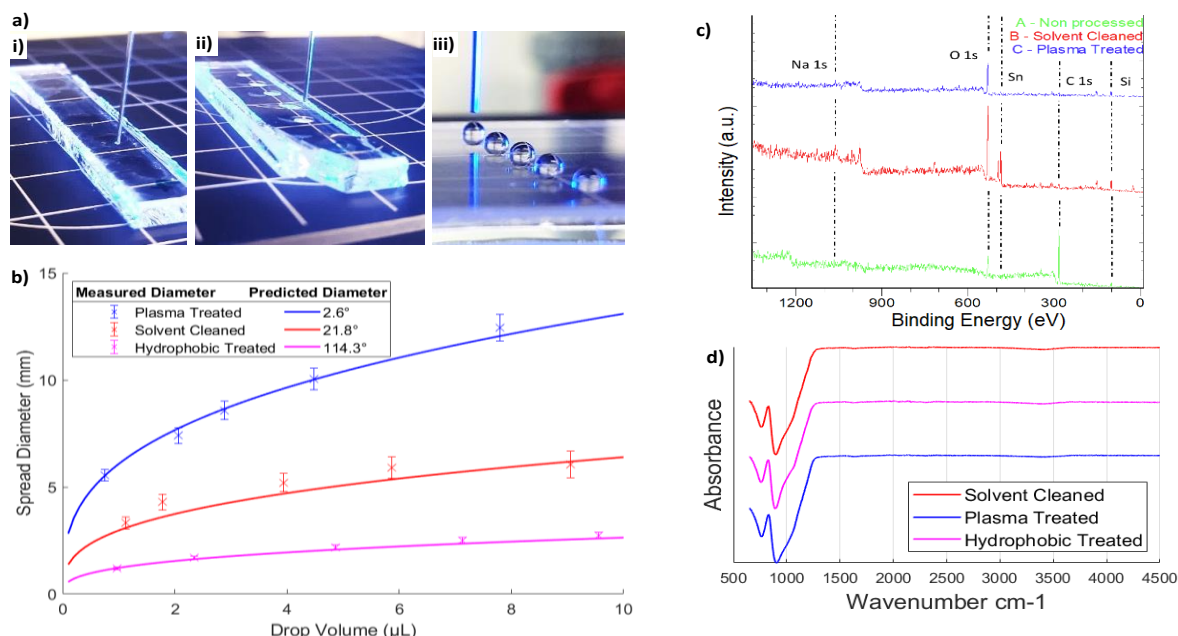


Figure 5.9: (a) Photographs of droplets dispensed on i) plasma treated surface ii) solvent cleaned surface iii) hydrophobic surface. (b) Plot of the measured droplet diameter compared to spherical cap predictions. (c) XPS Survey Spectra of the prepared surfaces. (d) FTIR Spectra of the prepared surfaces.

XPS spectroscopy was carried out on the non-processed surface ‘as received’ from the industrial supplier, the solvent cleaned, and the plasma treated surfaces. The atomic percent (At%) carbon content (C1s-248.8 eV) of the ‘as received’ surface was 79.3%, after solvent cleaning this reduced to 13.3%. The reduction in carbon content indicated that the solvent cleaning step removed carbonaceous debris and organic contamination. The At% of the plasma treated surface was even lower at 6.7% this indicated further removal of organic contamination. The presence of Tin (Sn metal - 485.2 eV) in the XPS spectrums indicated interaction with ions from the float bath process. Further elemental peaks visible include (Na 1s - 1071 eV, O 1s (SiO₂) - 532.9 eV, Si (SiO₂) - 103.5 eV). Although these peaks are identifiable in the overall spectrum, due to the insulating nature of the substrate the signal was poor and detailed bonding analysis was not possible. XPS has been used to give valuable insights into the surface chemistry after treatment and validation of contact angle measurements. However, XPS is a time-consuming, high vacuum technique so cannot be used as an in-line production process to assess glass cleanliness. FTIR spectroscopy in attenuated total reflection mode was carried out to assess its capability to rapidly characterize the surfaces.

Unfortunately, no difference between the spectrum obtained from each surface type was observed. This indicates the technique is not surface sensitive enough to use in this way.

This section has described the preparation and analysis of glass surfaces with a range of wettabilities. These findings are used as foundational knowledge for inkjet printing experiments as well as aid to research progression to an industrial application. The consequences of surface preparation on fluid interaction are very impactful when inkjet printing to glass substrates because of its influence on adhesion and deposit morphology. The wettability of glass in its pristine state has been demonstrated to be highly hydrophilic and droplet pinning is certain. In a production process it is vital to be able to rapidly characterize the surface condition of the substrate material. Contact angle analysis of water sessile drops is suggested as the best way to quickly assess surface cleanliness with reference to standards produce by offline measurements such as XPS.

5.5.2 Patterned wettability through modification of surface chemistry and topography

The next stage of experiments aimed to locally remove the hydrophobic coating in order to produce contrasting regions of surface wettability. In this study, the manufacturing potential of laser ablation and masked plasma treatment was investigated to produce wettability patterns on glass substrates through removal of a hydrophobic coating. This research aims in the future to help enhance inkjet printed deposit adhesion and resolution whilst eliminating artefacts such as the coffee ring effect or reduced morphology control when printing to hydrophilic surfaces. Firstly, the parameter space of the processes was explored by comparing the intensity of surface treatment to wetting contact angle. Then the dynamics of spatial confinement of water in track and square geometrical patterns was analysed. This, coupled with surface chemistry mapping, was used to produce an advanced understanding of wettability patterning based on analysis of advancing contact angle at the hydrophobic boundary.

5.5.2.1 Masked corona discharge plasma treatment

Firstly, it was necessary to obtain the optimal treatment parameters to remove the hydrophobic coating with corona discharge plasma treatment. To do this on the plasma treatment was applied to the coated glass substrates without any patterning as described in section 5.4.1. The effect of varying applied power and treatment time on the static water contact angle of the surface was measured and results are shown in Figure 5.10.

Without any plasma treatment, the hydrophobic coating deposition produced a water contact angle of $114.3^{\circ} \pm 1.6^{\circ}$. The minimum applied power for which a plasma was formed was 13 W, For treatment times between 0-40 s at this minimum power, the average contact angle remained above 78° and a

large range in the contact angle measurements was observed (as can be seen by the broad error bars). This indicated that the weak plasma only partially removed the hydrophobic coating. Increasing applied power to 50 W and 200 W resulted in consistent coating removal and contact angles below 20° for all treatment times as shown in Figure 5.10.

As consistent removal was observed, the parameters for experiments with a patterning mask were selected to minimise the process time. The power of 200 W was selected with a treatment time of 10 s per cm, this produced an average contact angle in exposed areas after plasma treatment of $11.6^\circ \pm 2.1^\circ$. To test the protective ability of the mask material for patterning experiments a layer of polystyrene sheet was placed between the corona discharge electrode and hydrophobic glass substrate. In masked areas, the hydrophobic property remained unchanged by plasma treatment, and so it was considered suitable as a masking material.

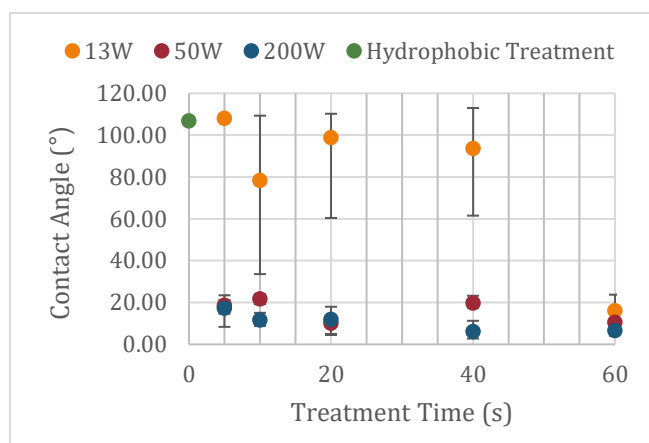


Figure 5.10: Plot of contact angle vs plasma treatment time for hydrophobic glass.

Several mask patterns were fabricated by laser cutting to test the capability of the masked plasma patterning approach for millimetre scale fluid entrapment. A comb pattern with a channel size of 1 mm and a pitch of 3 mm was tested to assess the capability for spontaneous pattern formation. After plasma treatment, the comb surface was immersed in water and withdrawn from the beaker, pulling in the long direction of the channels. After withdrawal, the fluid only adhered to the plasma treated pattern as shown in Figure 5.11(a-b). This initial experiment showed the immediate effectiveness of the technique to produce distinct regions of hydrophobicity and hydrophilicity with millimetre spatial definition. This capability for pattern self-alignment could be an exciting avenue in future research towards microfluidic device fabrication, when coupled with dispensed fluid. For example, fluid is dosed to a region treated using a square mask, as shown in the 10 mm diameter square in Figure 5.11(c). In order to test the limits of the patterning resolution, a mask with channels of nominal widths (3 mm, 1.5 mm, 0.5 mm and <0.5 mm using a single laser scan pass) were patterned. Figure 5.11(d) is a stitched image of the sample after fluid dispensing. All of the tracks showed preferential spreading into the patterned hydrophilic channel. A single water droplet was dispensed into the centre of each of

the patterned channels and the resultant width of the spread droplet was measured. Water droplets of varying size were dispensed in between the channels to show preservation of the hydrophobic quality in non-exposed areas.

Figure 5.11: (a-b) Images of comb surface after withdrawal from volume of water. (c) Photograph showing millimetric scale water confinement in 10mm square. (d) Confinement of fluid within patterned channels.

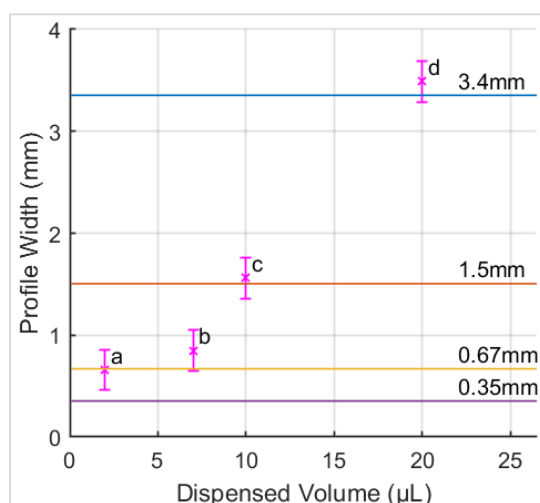
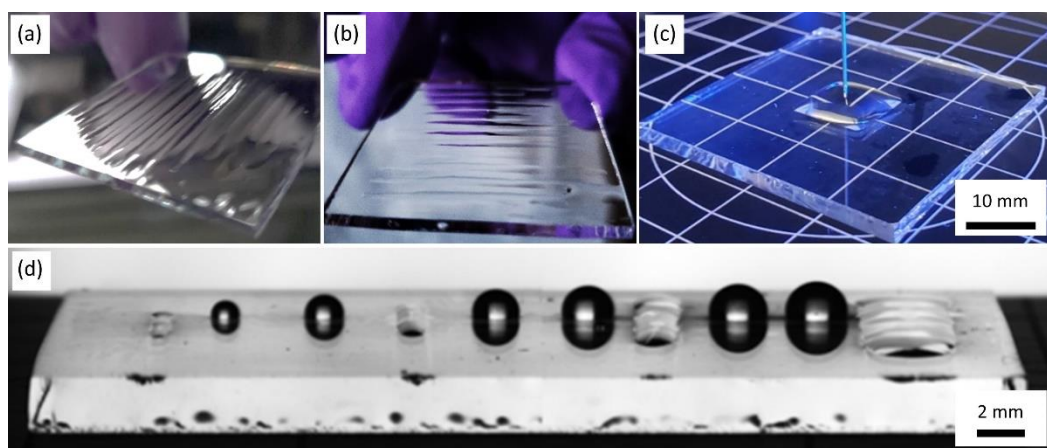


Figure 5.12 plots the measured width of the fluid in the channel compared to straight lines of constant width for the measured channel widths of the mask. The measured width of the channels exceeded the specified widths due to the laser cutting technique and are notated with straight lines. The dispensed fluid forms channels with width slightly greater than the channel size in all cases to within ± 0.3 mm. For the smallest track (a - 0.35 mm), the droplet spread in the direction of the track but the fluid profile was wider, measuring 0.65 mm. This represents the patterning resolution and analysis limit of this experimental arrangement which was limited by the width of the dispensing needle (0.51 mm) and minimum feature size of the laser cutter used for mask preparation.

Figure 5.12: Analysis of channel containment experiment.

1.5.2.2 Laser processing of hydrophobic coating

To move to a better controlled and finer resolution of patterning, laser ablation was explored because it is inherently direct-write and capable of modifying both surface topography and chemistry simultaneously through coating removal. A femtosecond laser source described in Section 2.2.2 was used to allow for absorption of the near-infrared laser light by the transparent substrate, as well as to minimise thermal damage to the glass [88].

Firstly, the impact of key laser parameters on surface wettability was assessed. The resolution of the available wettability analysis system requires patterning of areas with minimum dimensions of at least 8 mm. Squares were patterned onto the hydrophobic glass surface through a serpentine laser scan pattern with hatch spacing varied from 1-32 μm . In order to ensure an adequate number of samples could be fabricated in a timely manner for wettability analysis, a fast scan rate of 50 mm/s was used. The laser power of 0.63 W was tuned to the minimum value for which ablation occurred with the aim of minimising thermal input and the width of laser induced modification. Scanning the substrate with a power just below the ablation threshold was found to have no impact on the surface wettability. After laser patterning the surface was analysed to quantify wettability and morphology with comparison to hatch spacing. The contact angle was measured by imaging the profile of a droplet oriented perpendicular to the laser processed grooves, these values are recorded in Figure 5.13(a). Figure 5.13(b) shows the effect of modifying hatch spacing on surface morphology imaged with optical microscopy.

For hatch spacings smaller than 12 μm , a superhydrophilic response with complete droplet spreading was measured (CA_{las}). Loss of laser focus during processing resulted in a lower degree of ablation for the surface with 8 μm hatch spacing, this highlights the sensitivity to Z-axis positioning as explored in more detail in section 3.3. Laser patterning with hatch spacings greater than 12 μm resulted in an incremental reduction in wettability to produce water contact angles in the range 34-66.8°. A fill factor ratio for each hatch spacing was calculated, this represented the area of the surface which had been affected by the laser processing relative to the area of pristine hydrophobic glass ($\frac{\text{track width}}{\text{hatch spacing}}$). Because of the difference in wettability between the laser processed (CA_{las}) and pristine components of the surface (CA_{hpob}), the contact angle of the hatched surface ($CA_{hatched}$) varied depending on the proportion of the surface which had been laser patterned. The contact angles predicted by this model were compared to the measured values. The parameters of the model which produced the closest fit to experimental data were: Track width – 9 μm , CA_{hpob} -95°, CA_{las} -5°. The R^2 fit to the experimental data was calculated as - 0.985 indicating a close agreement.

$$CA_{hatched} = CA_{las} + \left(1 - \frac{\text{track width}}{\text{hatch spacing}}\right) * (CA_{hpob} - CA_{las}) \quad (5.2)$$

According to this analysis the track width of the wettability affected zone from a single laser scan ($9\text{ }\mu\text{m}$) was much larger than the calculated laser spot size of $1.92\text{ }\mu\text{m}$ ($M^2=1.15$, beam diameter - 6 mm and focal length - 8 mm). This effect may be due to thermal decomposition or vaporisation of the hydrophobic coating. Although a large covering of redeposited material was observed when patterning wider tracks, no difference in the contact angle in areas coated with redeposited material ($116.2\pm0.8^\circ$) was measured compared to the pristine hydrophobic coating ($114\pm1.6^\circ$).

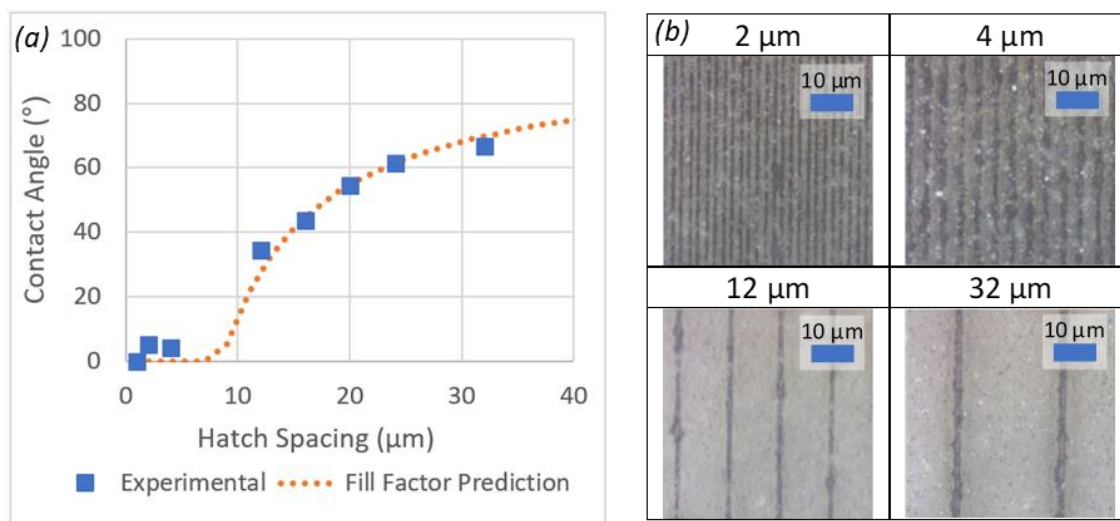


Figure 5.13(a) Plot of contact angle vs laser hatch spacing for glass with hydrophobic coating and prediction based on fill factor model. **(b)** Variance of surface morphology with laser hatch spacing .

To explore entrapment of fluid in a laser patterned geometry, spreading of a $5\text{ }\mu\text{L}$ droplet into a 1 mm wide and 20 mm long laser ablated pattern was analysed as shown in Figure 5.14. The droplet quickly spread along the length axis of the superhydrophilic track. Imaging the width profile of the track, the width of the fluid profile was measured to be 1.04 mm which was only 4% larger than the patterned track width. The spreading speed along the track was measured by capturing the displacement of the front of the fluid profile along the length profile of the track after droplet impact. It was found that the fluid front travelled with constant velocity of 16.3 mm/s between $0.046\text{--}0.564\text{ s}$. Initial droplet spreading from the width of the droplet (2.1 mm , 0 s) to the second collected data point (8.41 mm , 0.036 ms) was much faster but occurred too quickly to capture with the frame rate of the camera used. The profile expansion rate decelerated from 0.564 s until reaching the maximum length of the track at 1.107 s . The high rate of spreading occurs due to the very high wettability of the laser processed track.

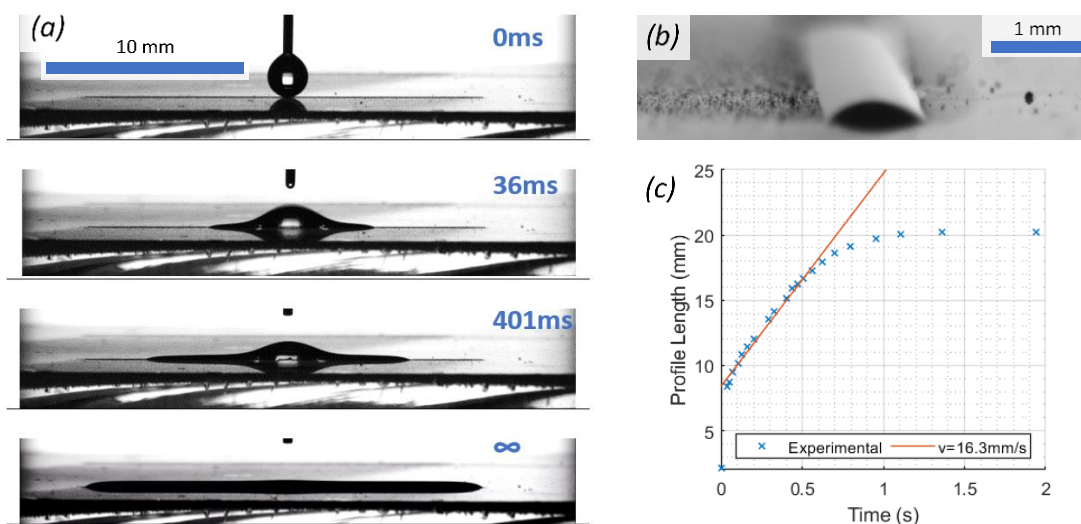


Figure 5.14: (a) Length profile and (b) width profile images of 5 μL drop spreading into hydrophilic laser patterned track. (c) Length of fluid profile variation with time during spreading

EDS spectrum analysis and mapping showed removal of the hydrophobic coating and exposure of the underlying glass substrate in the laser ablated grooves as shown in Figure 5.15. By comparing the element maps, it was seen that the elements present only in the coating (fluorine, carbon) were not present in the laser processed grooves. Similarly, the elements present in the substrate (sodium, silicon) were more prevalent in the laser ablated grooves. This was confirmed by spectrum analysis which showed the At% composition was in line with the mapping observations. A trace amount of silicon is present in the coating analysis, this may come from the trichloro-silane terminal group of the coating which bonds into the silica matrix of the glass, additionally the interaction volume of EDS is deeper than the coating thickness so some signal information is obtained from the bulk material. This investigation indicated that laser ablation was effective for removal of hydrophobic CF_2 groups and exposure of hydrophilic moieties in the glass substrate.

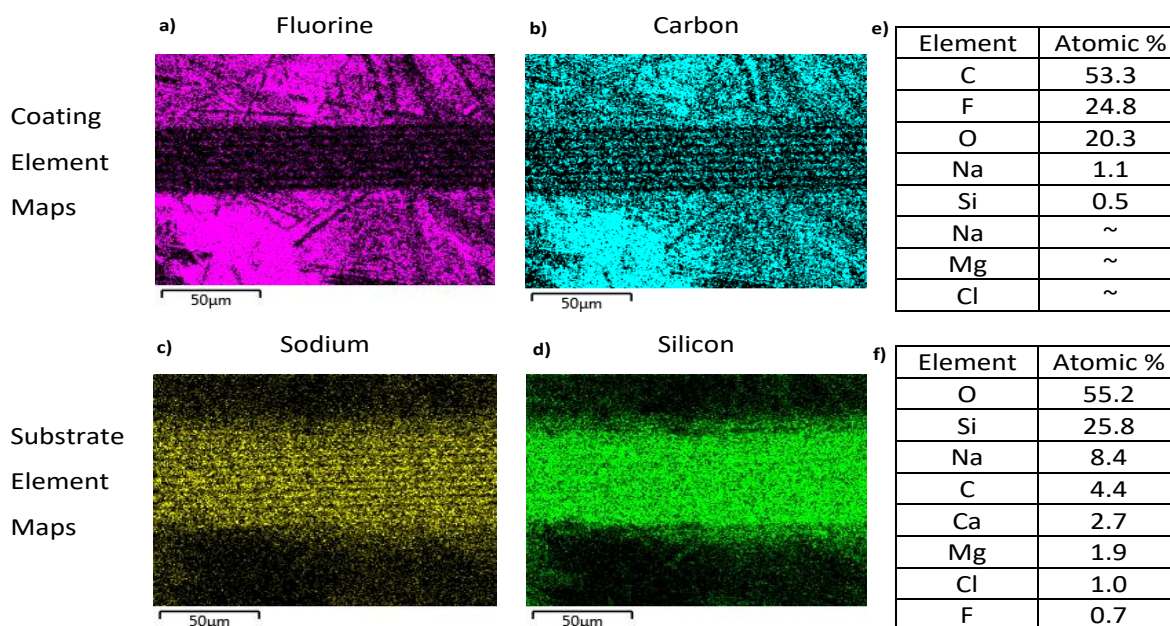


Figure 5.15: EDS analysis of laser ablated tracks (a-b) Maps of elements mainly found in hydrophobic coating (Fluorine and Carbon). (c-d) maps of elements mainly found in glass substrate (Sodium and Silicon). (e) Point scan composition of hydrophobic coating (f) Point scan composition of laser ablated track.

5.5.2.3 Comparison of wettability patterning approaches

In order to better understand the dynamics and reliability of the wettability patterning technique, a test case of water entrapment in a square was compared for both the laser patterned and plasma mask patterning approaches. The goal of this experiment was to analyse the maximum volume of the fluid which could be contained in the square before overflowing. The key parameters were the width of the fluid profile and the advancing contact angle (CA_{adv}) at the boundary of the wettability patterned square as illustrated in Figure 5.16. Water droplets were dispensed sequentially into the centre of the patterned area to produce entrapped liquid volumes of increasing size from 5-600 μL. After allowing the dispensed liquid volume to form a stable profile, the profile width and contact angle were measured. An equivalent experiment was carried out on the nonpatterned hydrophobic glass for validation of contact angle observations with large fluid volumes.

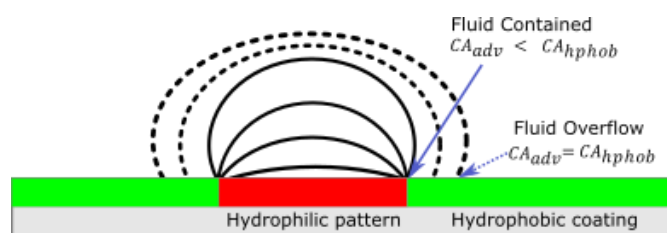


Figure 5.16: Schematic of fluid containment experiment. The fluid was predicted to remain contained within the pattern until the advancing contact angle matched that of the hydrophobic coating.

To produce an accurate comparison of the two patterning approaches the width of the fluid profile in each test was normalized to either the width of the laser patterned area (10 mm) or the width of the exposed area for plasma treatment (10.31 mm). Figure 5.15(a) plots the normalized width of fluid profile against dispensed volume. Figure 5.15(b) shows how the contact angle varied on the different surfaces with dispensed fluid volume. Figure 5.18 shows images of the fluid containment within the patterned areas.

In the initial spreading phase, the contact angle of the fluid profile remained close to that of the exposed hydrophilic pattern (0° & 11.6° for laser & plasma treatment respectively). This remained constant until the width of the fluid profile spread to match the width of the patterned area (marked as point P1). When the first drop was dispensed on the laser processed surface, the liquid spread out immediately through the superhydrophilic interaction to fill the patterned area. On the plasma treated surface, the contact angle stayed constant as the droplet volume increased from 5-50 μL .

When the normalized droplet width was equal to 1, the width of the fluid profile matched the width of the treated square. As the volume of liquid was increased further for both surfaces, the profile was prevented from expansion by the hydrophobic boundary. In this entrapped phase, contact angle increased continuously until it matched the hydrophobic surface. This represents the critical point between the entrapped and overflowing phases. The transition was most clearly observed at a normalized profile width equal to 1.1, beyond which the profile width grew rapidly. This critical point is represented in Figure 5.17(a) with markers at (340 μL -P2) for the masked plasma treatment and (370 μL -L2) for the laser ablation approach. These markers were transposed to corresponding droplet volumes on Figure 5.17(b).

The laser processed surface showed the distinction between the entrapped and overflowing phases most clearly. For droplet volumes in the range of 370 μL -600 μL , the contact angle remained within the range 100.9° - 108.1° whereas normalized droplet width increased from 1.1-1.4. The plasma treated surface showed a similar spreading effect except the overflowing phase initiated at the lower drop volume of 300 μL and a lower advancing contact angle was measured. Between 340-600 μL the contact angle varied in the range 82.9° - 90.9° . The lower contact angle was attributed to partial and uneven removal of the coating by the plasma treatment.

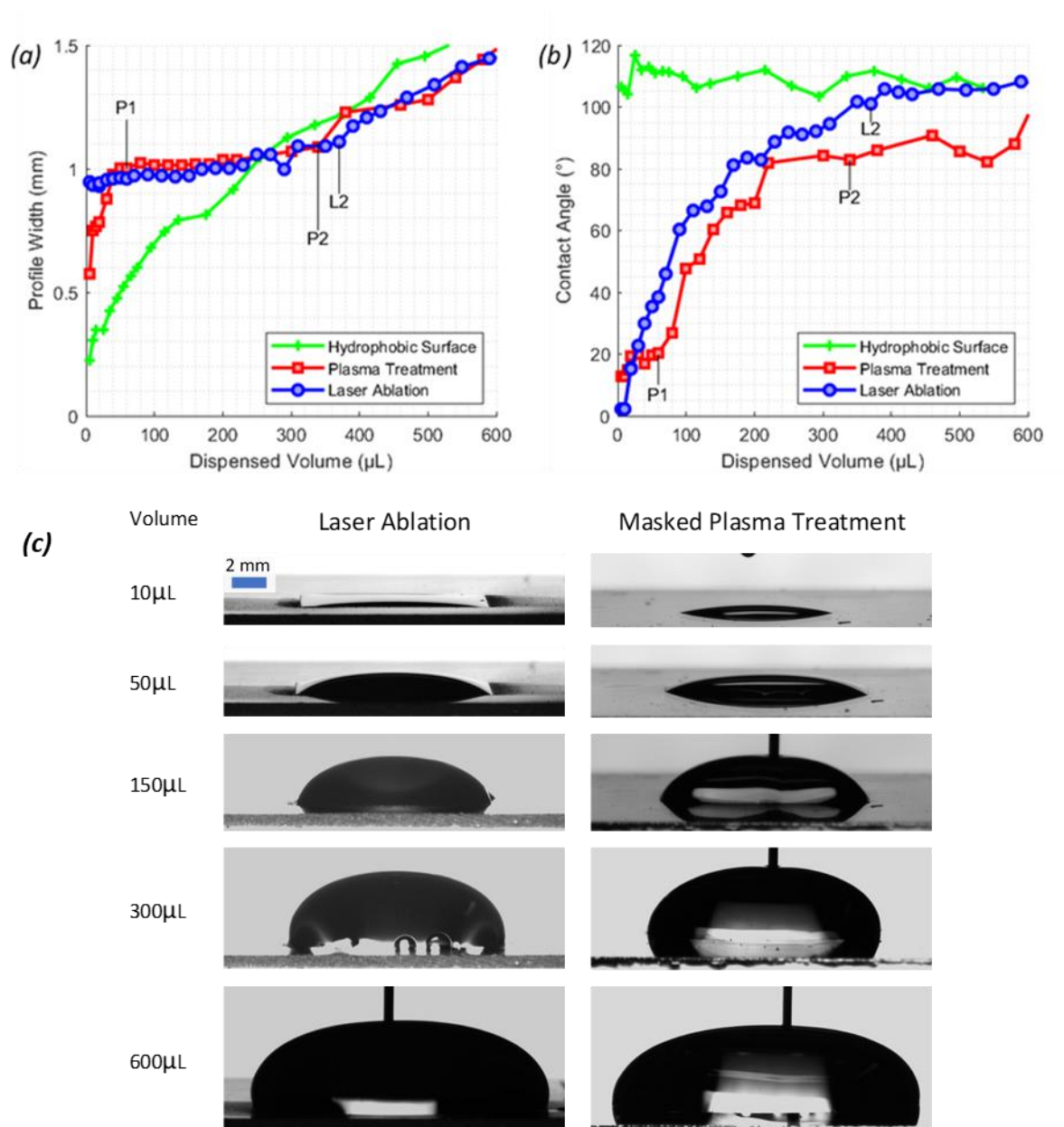


Figure 5.17: (a) Variation of contact angle with droplet volume. (b) Variation of normalized droplet width with droplet volume (c) Images of the fluid containment within the 10 mm square for the two patterning approaches.

Advantages of the ultrafast laser patterning technique are the very high patterning resolution possible, which overlaps in length scale with the minimum feature size possible with inkjet printing and aerosol jet printing. Additionally, the capability to modify both topology and chemistry in a single step allows for the creation of microstructure surfaces which display superhydrophilic film spreading into the ablated channels. However, the ablation threshold for surface modification is very sensitive with a short depth of focus. The texturing process used in this research has a slow areal rate of patterning. To progress the technique to an industrial scale, the laser and optics configuration could be improved by

using a laser source with an absorptive wavelength in the UV range, as well as coupling to a high-rate galvanometer scanning system.

Plasma treatment was also effective, but a more robust patterning and alignment approach is needed to boost precision. Overall laser patterning produced a more precise and effective localised surface modification which is evident in the higher contact angle and dispensed volume at the critical transition point L2 compared to P2. Future work could use a maskless plasma patterning approach which allows for 2D sample navigation with high resolution such as the use of needle electrodes for plasma generation or plasma jet technology [270,271]. A key benefit of masked plasma wettability patterning of glass substrates is the preservation of optical transparency.

An alternative approach using the method defined in chapter (4) of increasing hydrophobicity through heat treatment in an oven at 150°C for 2 hours was tested and was capable of raising the glass contact angle to $64.3 \pm 2.9^\circ$. The suggested mechanism of this is adsorption of organic contaminants [185]. This process could be used for equivalent wettability patterning in future work without the deposition of a hydrophobic coating. The maximum track retention volume would be reduced in line with experimental observations of the transition point between entrapped and overflowing phases relative to the hydrophobic boundary contact angle.

5.5.3 Inkjet deposition of conductive material to prepared glass surface

The literature review highlighted that surface wettability has a significant impact on the morphology and adhesion of inkjet printed deposits. So far experimental work in this chapter has aimed to produce surfaces with controlled and patternable wettability to investigate how these surface modifications can be used for inkjet printing of water-based metal nanoparticle inks onto glass. Inkjet printing experiments were conducted through analysis of morphology of single deposited droplets and linear track patterning, coupled with measurement of the electrical properties of the printed deposits. Critically, the influence of surface preparation (described in the previous section) on the distribution of particles in the deposit was tested.

Isolated droplets were printed on solvent and plasma treated surfaces with a spacing of 200 μm and the resultant deposits were imaged in an SEM. The high contrast between the conductive metal nanoparticle deposits and glass substrate allowed for analysis of particle coverage in ImageJ. A circular deposit was formed for both surfaces. The plasma treated surface resulted in formation of a much wider deposit in comparison to the solvent cleaned surface. The diameter and circularity of 5 deposited isolated droplets was measured, it was found that an average diameter of $37.6 \pm 2.4 \mu\text{m}$ and circularity of 0.52 was observed for the solvent cleaned surface. This compared to a diameter of $142.9 \pm 4.8 \mu\text{m}$ and circularity of 0.57 for the plasma treated surface. This showed that the circularity was

very similar for both surface preparation methods, but the droplet spread out much more on the plasma treated surface due to higher wettability.

At the nanoscale it was observed that the greater spreading on the plasma treated surface resulted in a low surface coverage of silver nanoparticles. On the solvent cleaned surface particle coverage was very high and averaged 97.8% across the measurements. On the plasma treated surface, a slightly higher density of particles at the edge of deposit was observed averaging 45.5% at +60 μm distance from the droplet centre compared to 26.4% at +20 μm . This was attributed to radial flow of silver nanoparticles to the pinned droplet contact line during evaporation. However, even for the very high wettability of the plasma treated surface, the overall deposit shape was relatively flat compared to typical coffee ring shapes observed using ink formulation with single organic solvent carrier fluids as observed in literature [272]. This is attributed to the bi-solvent evaporation mode with the mixture combination of water and DEG carrier fluids used in the ink formulation [216]. The implication of the low fill factor for functional inkjet printing is that when the substrate has very high wettability, multiple print layers are required to form a continuous deposit.

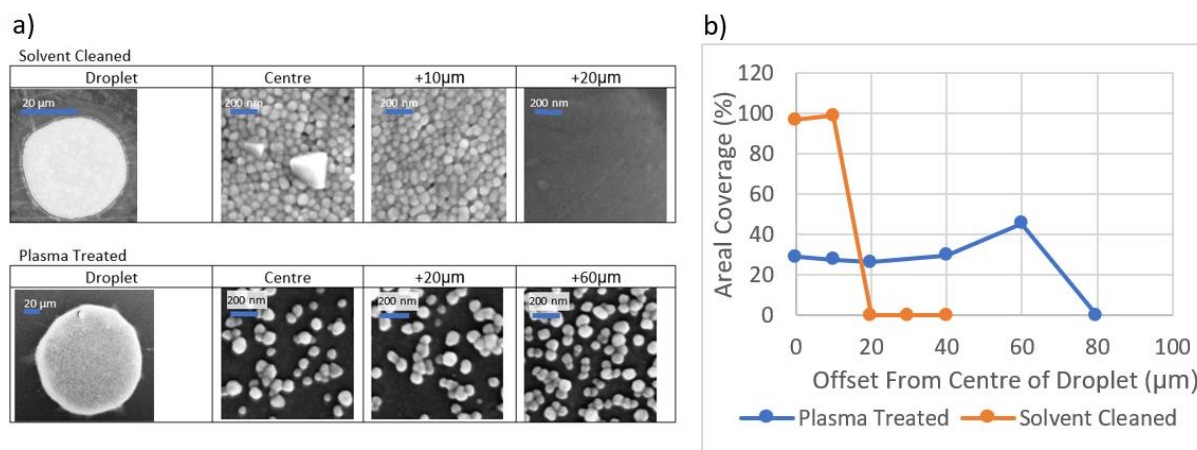


Figure 5.19: (a) SEM images showing particle distribution in single droplet printed deposits. (b) Plot of areal particle coverage over a 2.5 μm wide SEM field of view (100kx magnification) at specified offset from centre of circular deposit.

In order to form continuous tracks through droplet overlapping, it is necessary to tune the separation between drops for optimal coalescence and deposit formation. Inkjet printing experiments were conducted with varying drop spacing for solvent cleaned and plasma-treated surfaces. The width of the deposited track was measured using interferometry and several representative drop spacings were characterised with SEM imaging. The effect of varying drop spacing is discussed with respect to the ratio of drop spacing (p) to the deposited drop diameter (d).

At low droplet spacings, track width showed a high variance due to bulging as a result of unstable bead formation [273]. When drop spacing became close to the deposited width of an isolated droplet, resulting in a p/d ratio of 1, a smaller variance of track diameter was observed. This was observed for both surface preparation modes although was particularly present in the plasma treated surface.

On the plasma treated surface, droplets deposited to form discontinuous deposits. This was attributed to the extremely high surface energy of the surface. At very low contact angles droplets spread out until they interact with atomic contamination on the surface. Overall, much thinner tracks were produced for the solvent cleaned surface, this is favourable for printing of high-resolution conductive tracks because a more dense particle distribution is formed. A ratio of 0.80 p/d resulted in the highest quality track for the solvent cleaned surface and a drop spacing of $30\text{ }\mu\text{m}$ was selected for future experiments. The drop spacing was kept constant for the two surface preparation techniques in durability experiments to ensure preservation of mass.

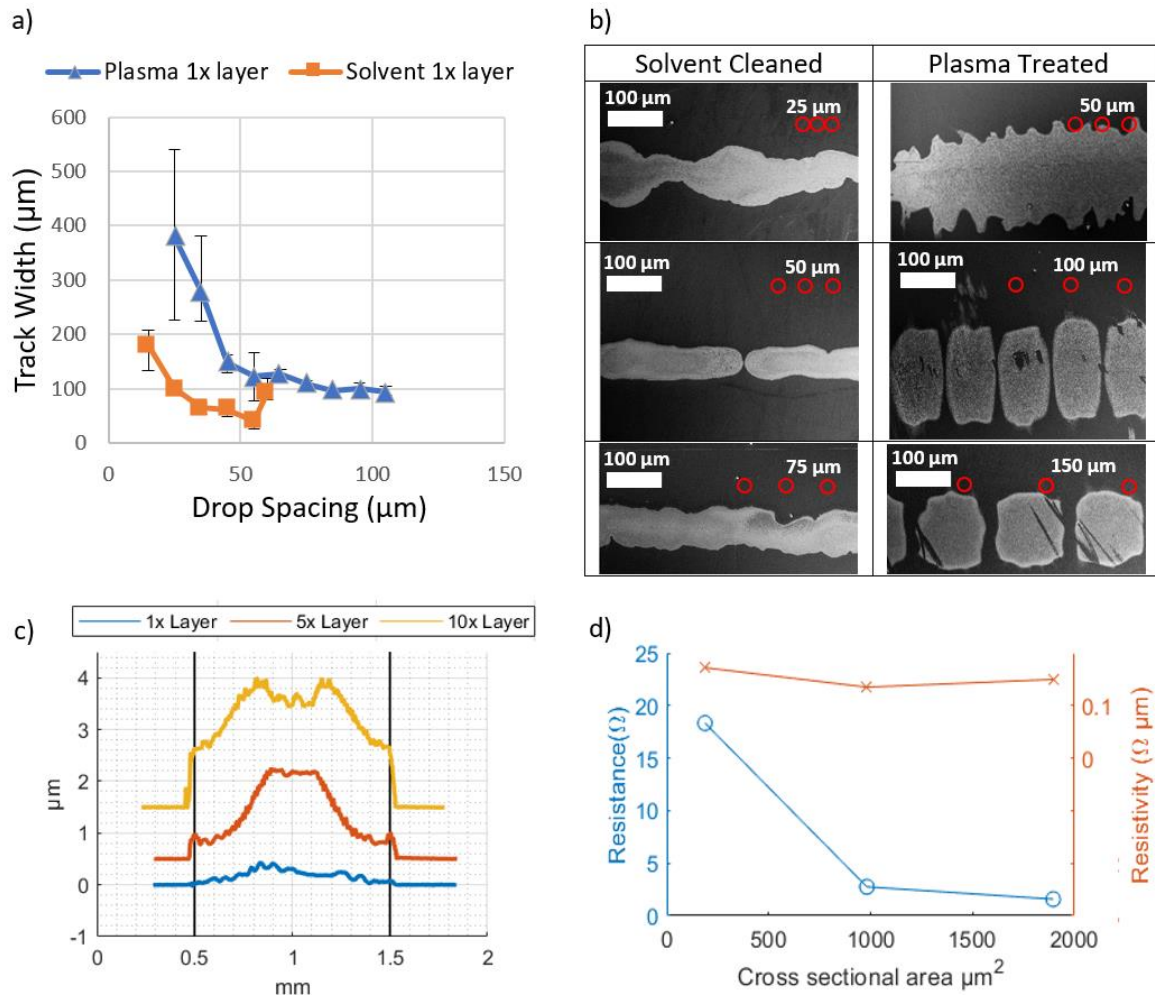


Figure 5.20: (a) Variation of track width with printing parameters and surface treatment method. (b) SEM images of deposited tracks, red circles are used to show drop spacing, diameter of red circle is

equivalent to the diameter of the spherical ejected droplet. **(c)** Variation of track morphology and, **(d)** electrical properties with increasing number of printed layers.

After investigating the spreading dynamics of inkjet printed tracks the next research stage was to test the conductive properties of the deposit. For this purpose, tracks were printed with increasing number of layers onto the solvent cleaned surface resulting in higher track cross sectional area. Interferometry was used to measure the profile of the printed track and track resistance was measured with a 2-point probe technique. Figure 5.20(c) shows the morphology profile of the printed tracks, a favourable profile was formed avoiding coffee ring formation. The width of the printed track was close to the specified track width of 1 mm indicated by black lines and the morphology profile of all tracks showed less than 100 μm overlap. This indicates that when a solvent cleaned surface is used excessive spreading isn't problematic for printing conductive tracks of this thickness and width.

Without sintering, no conductive properties were measured as there is no necking or continuous conductive pathway between silver nanoparticles. Using a sintering profile of 150°C for 30 minutes the track resistance was measured and resistivity was calculated. The resistivity of the deposits was measured as 168 $\text{m}\Omega\mu\text{m}$ which is around $\sim 10\times$ greater than bulk silver (15.9 $\text{m}\Omega\mu\text{m}$). Other studies exploring inkjet printing of Ag NP inks with aqueous formulations (reviewed in section 5.2.4) reported resistivities of 160 $\text{m}\Omega\mu\text{m}$ [208] and 37 $\text{m}\Omega\mu\text{m}$ [241]. The low resistivity obtained by [241] suggests the benefit of their nanoparticle functionalisation technique to improve ink dispersion and stability. The experimentally obtained resistivity was slightly higher than a commercial solvent based Ag NP ink with specification of 100 $\text{m}\Omega\mu\text{m}$ [274] Modelling research of solar cell efficiency suggests a resistivity of around $2\times$ the bulk value (32 $\text{m}\Omega\mu\text{m}$) is needed for efficient and cost effective inkjet fabrication of Ag solar cell busbars [275].

This section has investigated inkjet printing of a water based conductive silver nanoparticle ink to glass surfaces with modified wettability. The morphology and electrical properties of the printed tracks were measured in order to select system parameters for further experiments into the durability of inkjet printed deposits.

5.5.4 Investigations into the substrate-deposit interface and deposit robustness

In order to progress the use of water based silver nanoparticles inks towards usage in the rigours of an application environment. Four investigations were carried out to investigate the durability of inkjet printed silver nanoparticle tracks. Firstly, the measurement of surface free energy produced by the modification techniques using fluids with varying polar and dispersive components of surface tension quantified the effect of plasma treatment on fluid-ink interaction. To investigate adhesion of the inkjet printed deposits with reference to a certified industrial standard, a destructive cross hatch testing

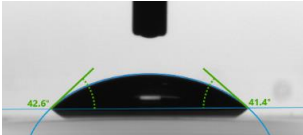
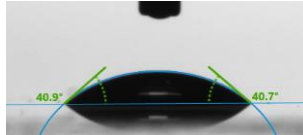

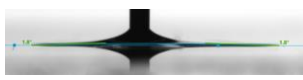


process was used on the inkjet printed films. To explore degradation of functional properties, peel off and abrasion tests were carried out on deposited tracks.

5.5.4.1 Influence of surface preparation on deposit adhesion

Surface free energy indicates the energy required to form new surface area and can be calculated from the sum of different intermolecular bonding components. A widely used approach is to consider only the dispersive and polar components [265]. The total surface free energy or energy difference for a solid molecule to reside at the surface is calculated using the extended Fowkes equation. This requires the use of multiple probe liquids with known dispersive and polar components, this measurement and calculation was described in section 5.41. Table 5.5 presents the measurements and surface free energy calculation results.

After solvent cleaning the surface free energy of the ink was 64.8 mN/m compared to the 40 mN/m ink surface tension. This indicates favourable interaction as the adhesive forces outweigh the cohesive forces of the ink. Plasma treatment significantly enhanced the surface free energy of the glass substrate to 99.2 mN/m which suggests even greater interfacial attraction to the inkjet printed fluid. This enhancement of surface free energy was mainly attributed to the polar component of surface free energy through generation of hydrophilic surface hydroxyl groups.

Table 5.5: Measurements and calculation of surface free energy

Measurement	Solvent Cleaned		Plasma Treated	
Diiodo-methane (°)	41.2		39.4	
Ethylene Glycol (°)	6.2		1.8	
Water (°)	14.5		4.6	
Surface Free Energy (mN/m)	64.8		99.2	
Disperse component (mN/m)	31.5		0.1	

Polar component (mN/m)	33.3	99.1
------------------------	------	------

To enable standardised cross hatch adhesion testing of inkjet printed deposit adhesion, square films of 30 mm width were printed onto different surfaces including the solvent cleaned, plasma treated and plasma mask wettability patterned surfaces. All of the results showed complete removal of the printed film through transfer of material to the adhesive tape. This meant that a qualitative investigation into adhesion within the range given by ISO2409 was not possible beyond applying classification 5 which describes a degree of flaking higher than 65%. The reason for this failure may be because the deposit thickness was thinner than the range recommended by the test manufacturer.

5.5.4.2 Degradation of surface conductivity by peeling

Track lift-off experiments with adhesive tape were carried out with the method described in Section 5.3. Figure 5.21(a) plots the measured track resistance as the peel off cycle was repeated 10 times. The 1 mm wide track printed onto the plasma treated surface did not show conductive properties when sintered at 150°C. This was attributed to the low density of particle distribution observed earlier. By raising the sintering temperature to 350°C the track exhibited conductive properties which was attributed to increased necking between particles at the higher temperature. The plasma treated surface sintered at 350°C showed substantial delamination during peel off tests and a large part of the track was removed. However, a conductive path remained so a track resistance of 6.6 Ω was measured. After lift-off tests, the solvent cleaned surfaces-maintained conductivity with track resistance values within the range of 5.1-6.6 Ω .

No clear trend was observed between sintering temperature and deposit adhesion using this test configuration. However, an important finding was that the duration of the thermal profile impacts the adhesion behaviour. When the samples were left to cool slowly in the hot oven instead of being removed after the nominal 30 minute exposure time delamination occurred after a single pull off cycle indicating low deposit adhesion. So in further experiments samples were removed from the oven after the nominal sintering time and left to cool on a metal plate. Figure 5.21(b) shows the morphology of tracks during the pull off tests. The dark material is residue liquid stuck to the surface from the adhesion tape. The underlying metal deposit of the solvent cleaned surface was visually unchanged by the lift-off tests.

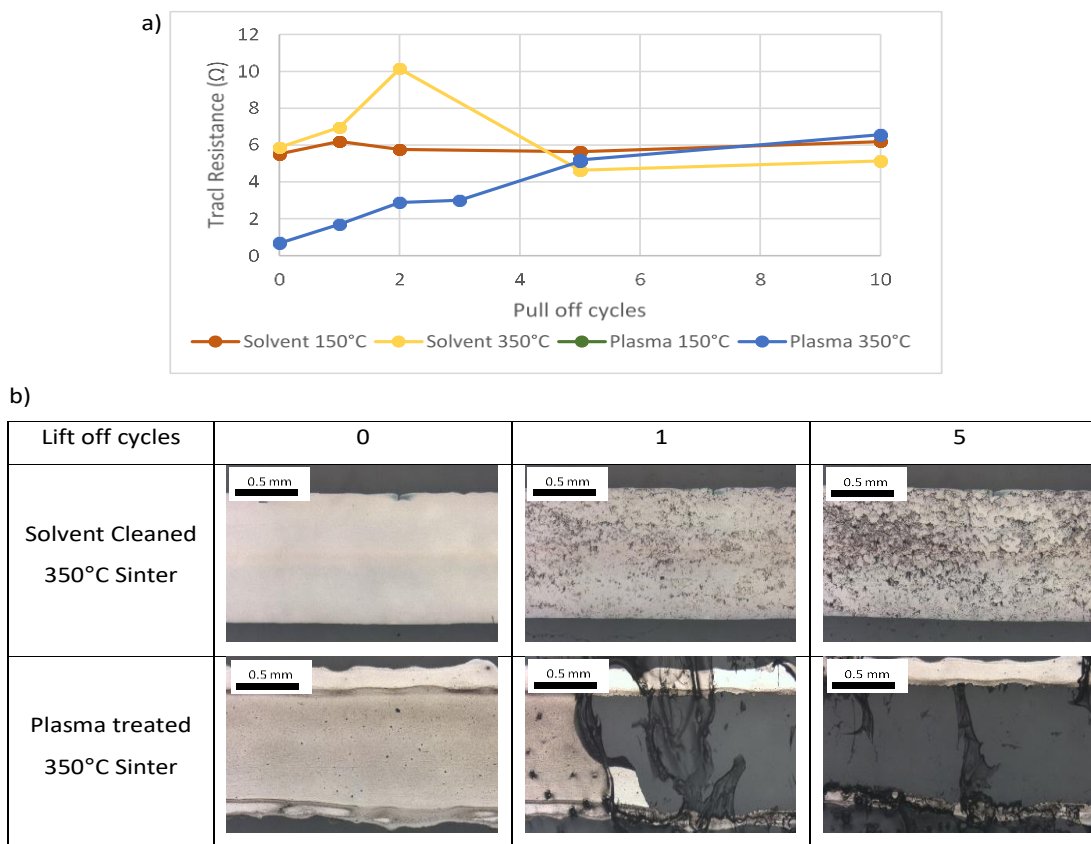


Figure 5.21: (a) Variation of inkjet printed Ag track resistance with pull off cycles for difference surface treatment and sintering methods. (b) Optical microscopy images of track surface morphology.

5.5.4.3 Abrasion resistance of printed deposits and laser etched topology

To produce embedded silver tracks in laser ablated grooves it was necessary to explore the interaction of the ink with the laser induced microstructure. In order to calibrate deposition parameters, 1mm squares were laser etched and squares were printed on top with varying volume of deposited material

controlled by varying the number of printed layers. Figure 5.22 shows SEM images at 50° tilt and 3D interferometry profiles of the resultant morphology.

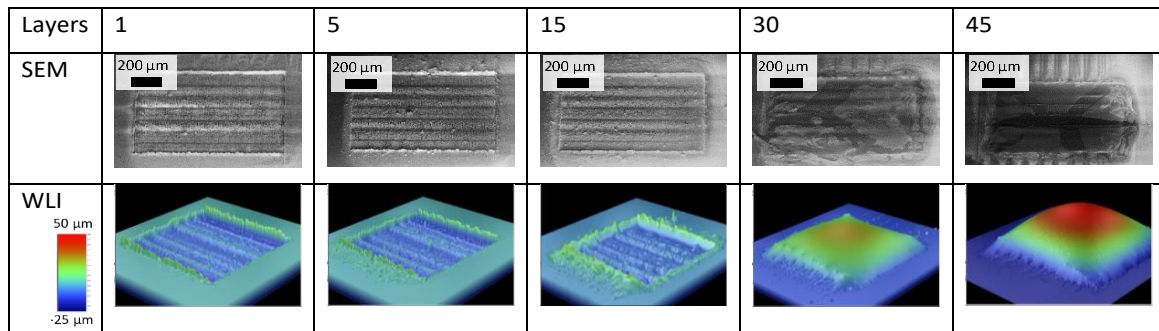


Figure 5.22: SEM morphology of deposits with variable number of print layers into laser etched groove.

The average height of the centre of the profile was measured as shown in Figure 5.23(a), the number of layers to produce a flat deposit with average profile height of 0 was calculated from the graph x-axis intersection as 16.5 layers. 20 printed layers was used in subsequent experiments to ensure total filling of the laser ablated grooves.

In order to qualify the abrasion resistance of the hybrid laser-inkjet patterning with comparison to a standard inkjet printed track. A 20 mm long track with 1 mm width and 20x printed layers track was deposited onto a flat glass surface. An equivalent track was deposited onto a laser ablated microchannel which had equal dimensions. This was repeated once for each system producing 4 analysis tracks in total. Figure 5.23(b) compares the profile of the track printed to the flat glass surface with the hybrid laser & inkjet surface and the profile of the laser ablated groove with no printing.

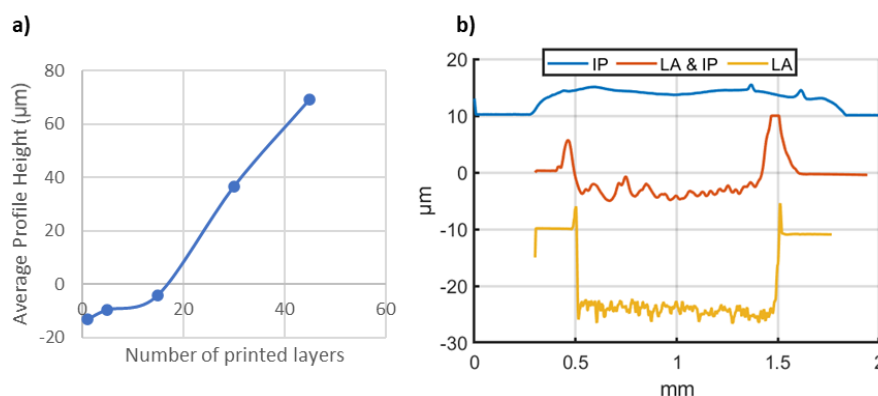


Figure 5.23: (a) Graph used for interpolation of number of printed layers (b) WLI profiles of inkjet printed track (IP), inkjet deposited track in laser ablated channel (LA&IP), laser ablated groove (LA)

The abrasion test system described in Section 5.4.4 was used to investigate the degradation of conductivity with abrasion. Figure 5.24 shows how track morphology and electrical resistance varied with number of abrasion cycles. Firstly, for the tracks printed to the flat glass surface it was found that after 1-2 abrasion cycles the tracks were damaged enough to break the continuous pathway resulting in no measured track resistance. In contrast, the tracks deposited into the laser ablated grooves- maintained conductivity over the 10 cycles tested with equivalent abrasive loading. During these abrasion cycles the measured track resistance remained within $\pm 0.5 \Omega$ of the original value. A 0.6Ω difference in track resistance was measured between the two tracks deposited onto the laser ablated microchannels. This suggests further optimisation is needed to tune deposition behaviour and deposit morphology to ensure a repeatable track resistance.

After each abrasion cycle the morphology of each track was inspected with optical microscopy. Figure 5.24(a) shows surface morphology changes during the abrasion testing process for the two deposition systems. For the track deposited onto flat glass, large areas of printed deposit were removed and the continuous conductive path was clearly broken. The laser textured surface showed the printed silver nanoparticle deposit was effectively contained within the channel; black material was attributed to redeposited material from laser machining. After the application of 5x abrasion cycles the excess printed material and laser induced burrs on each side of the channel had been removed. The deposited material in the central printed channel was preserved which suggests that the topology provided physical protection against abrasion for the loading conditions considered. Further work is needed to examine the effect of a high number of abrasion cycles with an automated abrasive loading technique and variation of surface topology.

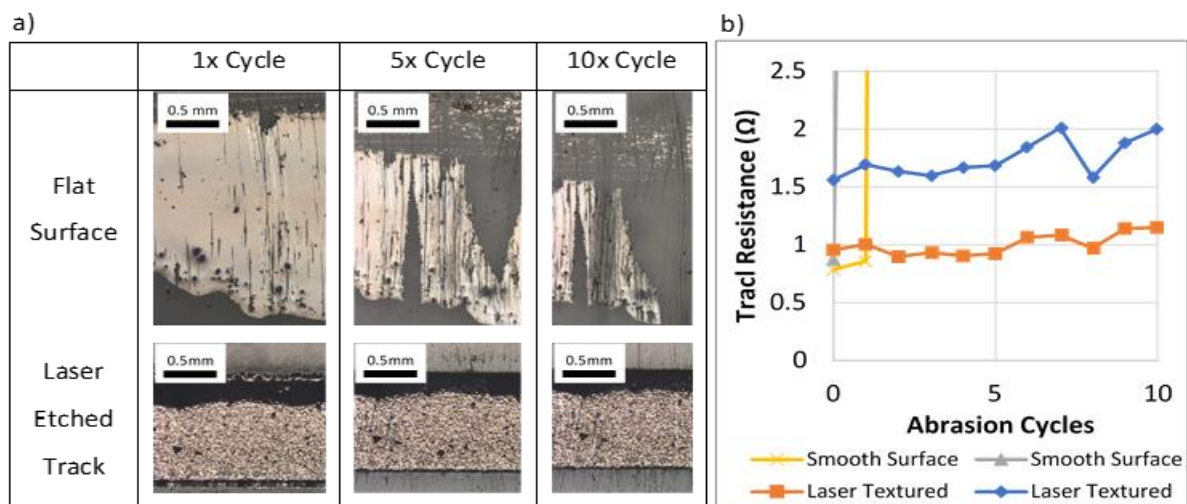


Figure 5.24 (a) Optical microscopy of track morphology degradation with abrasion cycles. (b) Track resistance variation with number of abrasion cycles

This section has investigated the adhesion and abrasion resistance of inkjet printed conductive tracks. The surface energy of the modified glass surfaces was measured through contact angle analysis of 3 different fluids. In peel off tests however no clear trend was observed between surface energy or sintering temperature and adhesive strength of the coating. Subsequently experiments were carried out to investigate hybrid inkjet printing onto a laser structured topology to create abrasion resistant embedded conductive tracks. First the number of printed layers was optimised to fill the ablated cross-sectional area and then tracks of dimension 20x1 mm were fabricated for abrasion testing. It was found that an equivalent track printed to a flat glass surface immediately lost its conductive pathway due to abrasive material removal whereas the embedded track remained conductive over 10 abrasion cycles.

5.6 Conclusion

The results in this chapter present new knowledge in modification of glass surfaces to enable industrial scale functional inkjet printing. The investigation into surface preparation showed that solvent cleaning and plasma treatment remove carbonaceous contamination from glass surfaces, the effect of this is to increase the hydrophilicity of the glass. The average measured sessile water droplet contact angle for solvent cleaning was 21.5°. For plasma treatment with treatment exposure time of 0.1 cm/s the contact angle was consistently less than 5°. A spherical cap analysis was used to predict deposited droplet geometry based on the sessile contact angle with good agreement to experimental data. Sessile contact analysis was found to be an effective and repeatable method to probe the cleanliness of glass surfaces.

Wettability patterns were fabricated on glass substrates through local removal of a hydrophobic coating by selective plasma treatment and laser ablation. Through plasma treatment the contact angle of hydrophobic glass was reduced from 114.3° to 11.6°. This difference in wettability was sufficient to produce self-aligned comb patterns of water and containment of fluid within millimetric square and track patterns. The laser ablation process resulted in a superhydrophilic wettability with contact angle of close to 0° when a high fill factor of laser texturing was used. EDS chemical mapping indicated that laser ablation caused removal of hydrophobic CF₂ groups and exposure of hydrophilic moieties in the glass substrate. The velocity profile of a droplet spreading into a 20 mm long track was analysed and after the initial impact stage a constant fluid front velocity of 16.3 mm/s was measured. The two treatments were compared by imaging the profile of entrapped fluid in a confined 10 mm square. This approach provided a design guideline in terms of the advancing contact angle for fluid deposition to surfaces with wettability patterns based on the restrictive hydrophobic boundary.

Inkjet printing concerned the deposition of a novel water based silver nanoparticle ink formulation. After inkjet printing the morphology of the printed deposits was investigated. It was found that with

the high wettability plasma treated surface, single deposited droplets spread to 143 μm , around 5x the diameter of the spherical jetted droplet. This high spreading resulted in a low surface coverage of nanoparticles and formation of uneven continuous printed tracks. The solvent cleaned surface showed more favourable spreading behaviour and an average surface coverage of 97.8% was formed. After sintering the resistivity of printed tracks was measured as 168 $\text{m}\Omega\mu\text{m}$ which is around $\sim 10\text{x}$ greater than bulk silver (15.9 $\text{m}\Omega\mu\text{m}$). This result was reasonably comparative to other studies which used water-based Ag NP inks [208,241] and to a current commercial solvent-based Ag NP ink[274], further improvements to deposit resistivity are needed to meet requirements for an application in printed solar cell busbars [275].

Finally, the durability of inkjet printed deposits were tested for use in an end application environment. The surface preparation method and sintering temperature did not exhibit a measurable benefit to adhesion using the test methods considered. This suggests that the solvent cleaned surface was the best selection for manufacturing as it avoided the problems associated with excessive spreading found with the plasma treated surface modification. By printing into laser ablated grooves a protective topology was fabricated which preserved the conductive pathway of the conductive tracks. Future research will combine this finding with the high-rate glass laser structuring experiments in section 3.4.2.3 to enable scale up of the technique.

6 LASER INDUCED REVERSE TRANSFER OF FUNCTIONAL MATERIAL

6.1 Introduction

Laser induced reverse transfer (LIRT) is a direct-write technique to deposit materials, and to-date mostly metals, onto transparent substrates. This chapter presents research into the use of LIRT as a manufacturing approach for scalable direct write deposition to glass substrates. In this chapter, an overview of the LIRT process is given in the introduction, then the literature review highlights the state-of-the-art and also gaps in understanding. The remainder of the chapter looks at the methods, results and finally the conclusions, where the new findings are highlighted.

The LIRT process involves transmitting a pulsed laser through a transparent substrate to a donor target material surface, producing an ablation plume of vaporized species. The vaporized species traverse a small air gap and deposit on the underside of the receiver substrate and by scanning the laser across the target surface a 2-D pattern can be transferred. Figure 6.1 shows a labelled schematic of the LIRT process. The technique has also received different names in research literature such as Laser Induced Backwards Transfer (LIBT) and has common features with other processes like Laser Induced Forward Transfer (LIFT) and Laser-Induced Plasma-Assisted Ablation (LIPAA). Before 2018 there were 10 published research papers utilising the technique Laser Induced Backwards (or Reverse) Transfer with 11 additional publications arising during the timespan of PhD research. There have been 44 published research papers using the closely related process of Laser Induced Plasma Assisted Ablation, based on search using Scopus in Aug 2020.

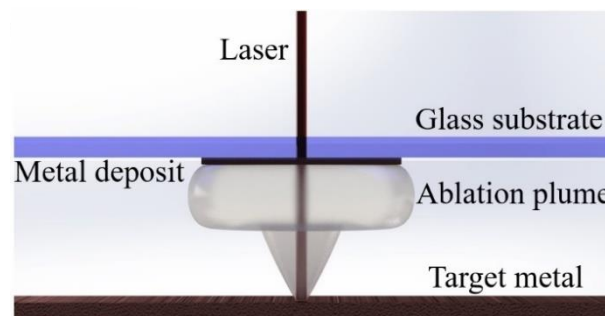


Figure 6.1: Overview schematic of the LIRT process, direct-writing a thin film from a metal target to the glass surface above by laser ablation.

In Section 6.2, the current understanding of the dynamics of material ejection and transfer dynamics are introduced, the technique is compared to other laser direct-write deposition approaches and recent research studies are described to showcase the state-of-the-art in deposition capabilities using LIRT. Laser ablation in the nanosecond pulse regime is a mainly thermally driven material ejection process. The ablation plume generated consists of a mixture of energetic plasma, gas and solid debris. The review in Section 6.2 was carried out to identify where additional understanding is required about the behaviour and content of this plume and to provide a focus of the experimental work. Digital holographic imaging in combination with micro- and nano-scale surface characterisation was used to gain key insights into the mechanism of LIRT when using long nanosecond pulses. The research here employs silver, graphite and copper donor materials and uses both static and scanned beam experiments to explore the challenges in using LIRT for conformal coating and specifically the susceptibility to surface damage in the patterned substrate and the difficulty in delivering overlapping deposits.

The work shows that there is great potential for facile, reliable fabrication of conductive patterns and digitally controlled customisation of glass products using LIRT, with some applications-focused experiments also presented. It is anticipated that this research will excite further study of this rarely explored technique for applications such as embedded sensors and electronics.

6.2 Literature review

6.2.1 Laser direct-write deposition processes

Laser-based direct-write deposition approaches include laser induced forward transfer (LIFT), matrix assisted pulsed laser evaporation (MAPLE), laser enhanced chemical vapour deposition (LECVD), and laser induced reverse transfer (LIRT). LECVD has been demonstrated to have the highest resolution of these deposition approaches in an industrial setting with sub-micron tungsten track width patterning demonstrated [276]. LIFT involves ablation and transfer of a thin film coated on a transparent holder. In LIFT, the processing laser transmits through the holder from the non-coated side. The film can be both a solid film prepared by techniques such as PVD or a liquid film of viscous ink [277,278]. LIFT has been used to deposit metallic nanodroplets of diameter 300 nm [279]. Drawbacks of these approaches include the relatively complex preparation steps required such as production of donor or sacrificial thin films in the case of LIFT [280] and preparation of suitable reactant gases in the case of LECVD [4]. In LIRT, the donor target can either be a bulk solid or thin film. This ease of target preparation means there is a reduced number of manufacturing steps and higher flexibility in the selection of transfer materials.

6.2.2 LIRT Process dynamics

From analysis by Karpman *et al.* [282], the steps involved for transfer of material by a single pulse with LIRT involves i) the absorption of laser energy by the target material, ii) mechanical expansion effects in the target material to produce an ablation plume, iii) transport of ejected species from target to the substrate and iv) condensation on the substrate. This framework has been used to analyse research literature relevant to the LIRT process as the individual steps are common with other research areas such as laser micromachining and pulsed laser deposition. The laser is scanned across the target surface to transfer a continuous track. It is known that pulse overlapping means each subsequent laser pulse will interact with the lingering ablation plume from earlier pulses and also previously deposited material [283], however there are few reports examining this interaction.

6.2.2.1 Target interaction and ejection

The laser materials interaction theory section, Chapter 2a, introduced the fundamentals of laser ablation through explanation of laser light absorption and the processes which couple light absorption to thermal energy. In LIRT, the energy transfer processes involved in ablative material ejection govern the deposit morphology and composition. Laser processing with low fluence results in direct heating effects which can be analysed with static conditions. In these conditions, material phase transitions are relatively continuous, as material exceeds its melting temperature, it transitions to a liquid state resulting in the formation of a melt pool and then vaporisation. The resultant morphology after solidification is governed by hydrodynamic flow and heat transfer processes [284]. When the laser intensity becomes high enough, such as with the use of pulsed lasers, strongly non-static effects result in material ejection as illustrated in Figure 6.2(a). Immediately after pulse energy delivery, a pressure shockwave emanating from the focal spot is observed, this results from the high pressures induced by the expanding target material on the atmosphere. Molten material is ejected through phase explosion when the material heating process is fast enough that homogenous vapour bubble nucleation is kinetically favoured over heterogenous nucleation of small vapour bubbles. Phase explosion results in the ejection of large droplets from the ablation zone [285]. Ejected molten material typically redeposits next to the machining zone forming burr-like structures. Similarly, through the concentrated local forces created by rapid heating in the ablation zone solid particles can be fragmented and ejected from the target surface. In ultrafast laser ablation, a vapour plume is formed by direct sublimation. With increasing laser intensity the species in the vapour become ionized and are described as a plasma [88]. When long nanosecond laser pulse durations are used, or the process is operating at high fluence; ablation is a mainly thermally driven process.

6.2.2.2 Transfer

The ablation of the target generates a plume of airborne species, the plume forms a classic ‘mushroom cloud’ shape as it expands into the atmosphere driven by the Rayleigh-Taylor instability for mixing fluids [286]. The expansion and propagation of unconfined ablation plumes has been previously investigated using optical and emission spectroscopy approaches [287,288], Figure 6.2(b) shows an example of high speed imaging of an expanding ablation plume [289]. The expansion rate of the leading edge of an ablation plume has been shown to decelerate according to viscous forces, where ejected species experience a viscous drag force proportional to their velocity [290]. Kerdja *et al.* found that increasing pressure of the atmosphere in their test chamber from vacuum conditions to 10 mbar resulted in higher air resistance and deceleration of the ablation plume as shown in Figure 6.2(c) [288]. High speed imaging of plasma plumes generated by nanosecond ablation has shown they consist of a fast wave of primarily atomic plasma with a peak density in the velocity distribution of 10^4 m/s and a slower wave of evaporated species with velocity of around 10^2 m/s [280]. Across a 100 μm transfer gap this would give a time of flight estimate of between 0.1-10 μs .

So far, there has been relatively limited research into the effect of the confined geometry on the LIRT process. Time resolved shadowgraphy was used to directly image the morphology of flyers in the LIFT process by Fardel *et al.* as shown in Figure 5.2(d) [291]. The transfer dynamics of thin aluminium film flyers with a polymer release layer were investigated for different film thicknesses and transfer separation distances. An interesting observation which is highly relevant to the LIRT process was the presence of a rebounding pressure shockwave in the confined geometry. When the rebounding pressure shockwave met the thin film flyer it caused deformation and deceleration of the thin film flyer. The confinement of an ablation plume in a 50 μm air gap has been investigated with emission spectroscopy, in the confined geometry the plasma lifetime was shown to be sustained at high densities for much longer than the case of free ablation [292]. It is anticipated that confinement will significantly affect the behaviour of the shockwave, the ablation plume and ultimately the quality of deposition.

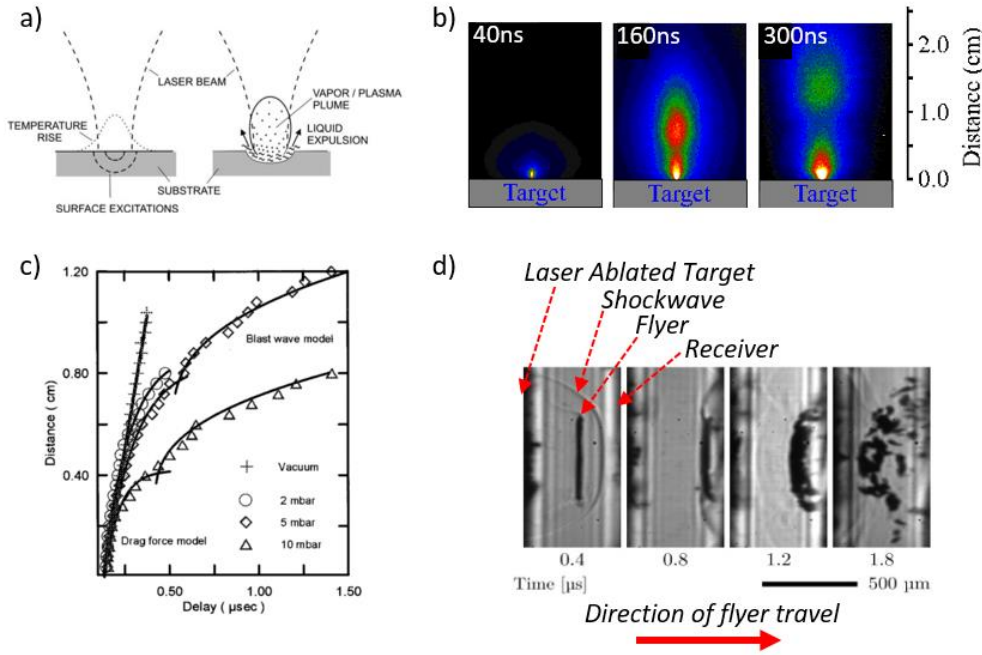


Figure 6.2: (a) Schematic of the processes involved in laser ablation material ejection [88] (b)

Intensified-CCD Camera images of the ablation plume produced by femtosecond ablation of silicon [289] (c) Displacement-time graph of the leading edge of a graphite ablation plume in atmospheres with varying pressure (d) Shadowgraphy imaging of a thin film flyer produced by LIFT travelling from target to receiver [291]. Labels have been added to show the components of the system and the direction of flyer travel.

6.2.2.3 Deposition

The transferred species condense and solidify on the underside surface of the substrate in the final deposition stage of LIRT. This deposition process is relatively complex due to the kinetics of the energetic plume and the interaction of the deposit with subsequent laser pulses. Dhimi *et al.* reported LIRT transfer of gold tracks in the range of 15–40 μm onto quartz substrate using a 215 fs pulsed laser [280]. They found that a deposition process was only obtained within a small experimental range of laser fluence values which was related to the dynamics of the ablation process. Below a threshold pulse-energy of 36 nJ no transfer occurred. Above the upper threshold of 82 nJ, the process was constrained by a reduction in sticking coefficient due to higher operating temperatures and a removal effect associated with the more energetic ablation plume. A similar observation was presented by Xu *et al.* for transfer experiments of graphite using a 100 ns pulsed laser. Tuning of the applied laser fluence allowed the process to be controlled between material removal and micromachining of the substrate or sputtering of the graphite target [293].

Hanada *et al.* tested the role of plasma generated substrate absorption sites during plasma assisted laser ablation surface structuring. The use of double-pulse femtosecond irradiation with varied inter-pulse-delay of 3 ps-10 ns was used to probe the plasma-substrate interaction. For small target-substrate separations, material removal was dominated by a transient absorption site generated on the substrate, the dominating mechanism of substrate material removal for larger separations (70 μm) was a deposited thin metal film which results in direct absorption on the substrate surface [294]. This research suggests that removal of material from the substrate is due to ablation of deposited species by subsequent laser pulses. Zhang *et al.* also reported this ablation mechanism to describe their process of high speed micromachining machining of glass using a non-absorbing laser wavelength [295].

6.2.3 Applications and device fabrication demonstrations

Several studies have targeted the production of conductive films with a recent report showing deposition of copper on single crystal sapphire to produce sheet resistances in the range of 0.5 $\text{M}\Omega/\text{sq}$ [15]. Lu *et al.* used a nanosecond pulsed fibre laser to investigate LIPAA based metallization of single-crystal sapphire (SCS) as shown in Figure 6.3(a) [296]. The behaviour of the generated plasma was considered as a time-of-flight spectra of a shifted Maxwell-Boltzman distribution related to the substrate-target separation and the velocity and energy of excited plasma. With longer time of flight, the shape of the plasma plume and resultant deposit were less controlled. Pulse width was limited to 1-5 ns to avoid micro-thermal cracks on SCS and high overlapping of 99.25-99.9% was used. The resistance of the deposit decreased with increasing repetition rate and fluence. The minimum deposit sheet resistance was not reported numerically but was read from a graph in the presented results to be in the range of $<1 \text{ M}\Omega/\text{mm}$. In the work of Mir-Hosseini *et al.*, films were produced through LIRT of metallic targets [297]. No conductive properties were reported in the case of copper deposition. The reflectivity measurements of the deposited films suggested that the copper film was mainly composed of copper oxide and also that the low reflectivity values were due to non-uniformities and poor surface coverage of the film. The authors suggested that the oxidation pathway of the metals was due to interaction with the background air whilst ‘in transit’ between the target and substrate.

A recent study involving transfer of AZO showed the capability to deposit electrode patterns with optimised resistivity of 34.75 Ω/sq [298]. LIRT has also been used to deposit graphite to fabricate patterns with resistivity of 444.44 $\text{m}\Omega.\text{cm}$, with subsequent nickel electroplating used to improve the resistivity to 22 $\mu\Omega.\text{cm}$ [16]. Importantly, this work also demonstrated the use of LIRT for device prototyping, with the fabrication of an embedded electrofluidics chips and resistive heaters as shown in Figure 6.3(b).

In addition to electronic functionality, LIRT has been used to deposit optical elements such as: generation and transfer of gold nanoparticles for nanooptics devices Figure 6.3(c) [299], phase-

diffraction gratings [300] and plasmonically active films (McCann *et al.*, 2017). One report investigated ablation of different transition metal compounds to deliver RGB colour marking Figure 6.3(d) [302]. Further novel applications involve decontamination of radioactive surfaces without the use of chemicals [303], and by switching to a hydrogel suspension target material LIRT has been used to pattern mammalian cells with a high survival rate [304,305]. These studies have shown the capability of LIRT to transfer functional materials both as a film, tracks or even as isolated droplets. More research is required to validate the unanswered questions arising from these studies such as material compatibility in a manufacturing context, chemical behaviour of ejected material during transfer and selection of laser processing approach for optimal conductivity.

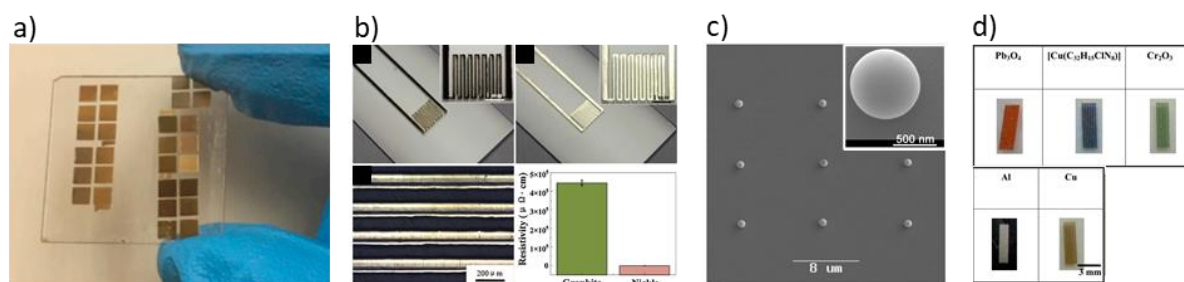


Figure 6.3: Research demonstrations of LIRT applications: (a) deposition of conductive copper films [296], (b) fabrication of a resistive heater with tracks deposited by LIRT then electroplated [293], (c) deposition of gold nanoparticles for plasmonic and metamaterial applications [299], (d) RGB colour marking with variation of target material [302].

The literature shows that laser direct-write deposition approaches offer significant potential in manufacturing due to their versatility, patterning rate and high resolution. However, current techniques such as LIFT and LECVD require relatively complex preparation steps. LIRT has received less research attention because it is only suitable for transparent substrates such as glass. The deposit morphology is a product of the material ejection dynamics which is complex and multiphase in nature. A key research gap is in understanding the interaction of the ablation plume with the air environment and substrate in the confined LIRT system. Current studies have demonstrated the use of LIRT to fabricate basic embedded electronic devices however this has required high hatching overlaps which can cause excessive damage to the substrate or the use of post-process steps such as electroplating. Therefore, experiments will focus firstly on the dynamics of ablation plume interaction in LIRT geometry using high-speed digital holography to capture plasma plume morphology and composition changes. This approach is used to inform the study of single spot and linear track deposition of silver, copper and graphite. The deposited morphology, composition and electrical properties are analysed to gain insight into the capabilities of LIRT for direct-write material deposition and improve the potential of this technique to transition from the lab to the manufacturing environment.

6.3 Design of experiments

This section describes how the research aim and literature findings were synthesized to formulate research objectives and experimental approach.

6.3.1 Research Aim

- Determine the viability of laser induced reverse transfer using a nanosecond pulsed fibre laser for deposition of functional material to flat glass surfaces

The literature review shows that the processes of ablation plume production, transfer and laser energy deposition occur on overlapping timescales. This temporal profile of the process may result in complex interactions such as plasma shielding which affect the characteristics of the deposit. The use of holographic camera imaging aims to characterise the temporal profile of the process, plume morphology and probe plasma behaviour. Building on this understanding of transfer mechanics a process of high laser incidence angle transfer can be then tested to avoid deleterious laser-deposit interactions.

Copper, silver, and graphite target materials are explored as candidates for conductive path patterning. Copper and silver are both widely used materials for patterning of interconnects in microelectronics applications. Although their conductivity and applications are similar, they have different oxidation and laser interaction properties which affect their interaction in the LIRT system. Graphite was selected because of its applications in electronics and sensing devices. Published research has also shown room temperature laser ablation synthesis of graphene [306] and carbon nanotubes [307]. Additionally, graphite has a high absorption and is easily ablated by near infrared lasers to enable transfer experiments at lower laser intensities than when metal targets were used. For the selected target materials, the structure, chemical composition, and electrical properties of deposits were analysed and related to the laser interaction mechanics.

6.3.2 Research Objectives

1. Analyse the material ejection mode of LIRT using nanosecond laser pulses.
2. Test the use of target materials with different ablation responses for functional material deposition and device fabrication.
3. Use holographic camera imaging to assess the temporal profile of the process and the morphology and compositional changes of the ablation plume.

6.4 Experimental approach and methodology

6.4.1 Materials and surface preparation

The work focuses on three donor materials which were obtained as solid targets to investigate the potential for transfer from solid targets. The sacrificial target materials selected were silver (1 mm thick, 72 nm Ra, 99.97% purity), graphite (0.8 mm thick, 386nm Ra, 99.5% purity), copper (0.9 mm thick, 134 nm Ra, C11000 grade). Figure 6.4 shows interferometry measurements of target surface roughness. Standard 1 mm thick microscope slides (Thermo Scientific) were used as the substrate material.

The separation distance between target and substrate was spaced using stainless-steel feeler gauge of 102 μm thickness. In early experiments targeting copper film production, a fixture with the requisite separation between target and substrate was CNC machined from aluminium. This aimed to improve heat removal by conduction from the processing zone and prevent warpage.

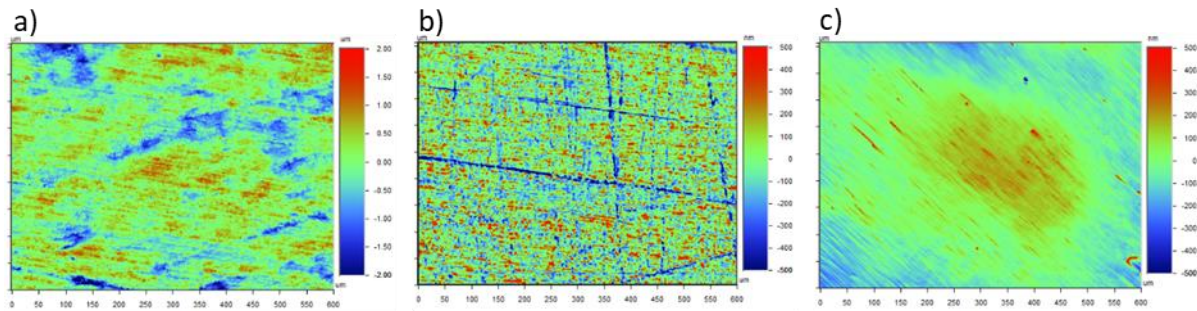


Figure 6.4: White light interferometry surface roughness measurements of target materials (a) graphite (b) silver and (c) copper used for LIRT experiments.

6.4.2 Patterning system approach

Track patterning and single pulse exposure experiments were carried out with an SPI™ G3 laser marker system with power of 20 W, repetition rate of 25 kHz, Pulse duration of 200 ns, wavelength of 1064 nm and spot size of 40 μm as described fully in Section 2.2. The effect of static overlapping pulses with varying power were tested to investigate process dynamics. A range of laser energy profiles were investigated for track production which involved variance of power and scan speed to modify the linear dose of energy (J/cm). The power of the defocused laser beam was measured before and after being transmitted through the substrate using an Ophir 30A-SH-V1 laser power sensor and showed negligible attenuation due to substrate absorbance although a small loss of power is expected due to reflection losses at the air-glass interface.

Characterisation equipment has been fully introduced in the experimental tools and analytical techniques section of this thesis (Chapter 2). Deposit morphology was investigated using optical microscopy, white light interferometry and focused ion beam imaging. Deposit chemistry was investigated using EDS and Raman spectroscopy. Deposit conductivity was tested using a four point probe test.

6.4.3 Holographic camera imaging system

A digital holographic imaging system was used to image the dynamics of ablation plumes created by individual pulses in the laser induced transfer geometry. A TEEM photonics frequency-doubled Q-switched PowerChip series platform (PNP-M08010) was used as the imaging laser operating at 532 nm wavelength. The system operates with a pulse duration of 400 ps which determines the temporal resolution of the images. The imaging laser passes through a beam splitter (BS1) to produce the reference and object beam paths. The object beam is expanded and propagates through the laser induced ‘event’. The two beams are then recombined on the camera CCD chip where they form an interference pattern. From this intensity distribution holographic reconstruction is carried out to extract phase plots. A full description of the imaging system is provided in [308]. To ablate the target materials an SPI™ G4 laser was used, producing single pulses of energy 158 μJ and 125 ns. The processing laser was focused to the surface with a 100 mm FL lens to a spot size of 29.0 μm .

A signal generator is used to trigger the processing laser and imaging laser sequentially, the imaging time delay is determined with integrated photodiodes. Several hundred hologram frames were captured in the time range of 10^{-9} to 10^{-4} seconds for unconfined and LIRT geometries with a 1 mm target-substrate separation, after each pulse the target surface was translated so fresh surface was exposed. The holograms were processed to produce unwrapped plots of phase and reconstructed as a time resolved sequence of images. These images show the evolution of plume morphology with the imaging signal capturing both the solid and liquid ablation products and also the plasma of the ablation plume. Refractive index was inferred using numerical methods to approximate the Abel inversion [309]. Plotting contours of refractive index allowed the measurement of the presence of a plasma ($n < 1$) in the ablation plume. ImageJ [269,310] was used to measure the width and height of the propagating ablation plumes.

6.5 Results and Discussion

6.5.1 Plume dynamics insights through Holographic camera analysis

Fundamental studies were carried out to better understand the LIRT process, focusing on the plume dynamics and deposition behaviour, prior to more application-focused experiments examining single pulse and continuous line deposition. For these fundamental studies, holographic imaging was carried out to observe laser ablation of a graphite target. This recently developed technique enables imaging of the ablation plume propagation at the ablation event (t_0) and for 500 μs afterwards to capture the process lifetime, using nanosecond temporal resolution. This included analysis of unconfined plumes that propagate into an open environment and confined plumes, where the glass substrate to be coated was close to the graphite surface. Figure 6.5(a) shows a sequence of frames over the time period for the unconfined plume. A rapid pressure wave is observed emitting from the location of the laser pulse. This manifests as a bright white emission in the images, that dissipates quickly. A slower ablation plume is then observed to form and propagate normal to the target surface, seen as the darker component in the images. This is an unconfined geometry and so these two separate waves do not interact again or impinge on any surface. While the LIRT process normally takes place with microscale gaps between the target metal and the substrate to be patterned, these gap sizes are not feasible for imaging. To help understand the behaviour of plume dynamics in a confined spacing, the gap size was reduced to the minimum that could be reliably imaged, and Figure 6.5(b) shows a sequence of frames in this confined geometry of a 1 mm gap.

As can be seen from Figure 6.5(a), a pressure shockwave is generated after the 150 ns laser pulse. Heating and material ejection effects result in compressive forces acting on the air [88]. Over the timescale 0 – 3.4 μs , this shockwave is seen to expand with hemispherical symmetry. While this dissipates in the unconfined system, in the confined system the leading edge of the shockwave is observed to reach the substrate surface at 1.6 μs . It is then reflected and dissipates. Over the scale of several microseconds a dense plume of ablated target material is produced and then expands upwards. In the confined geometry with the conditions described, the plume front first reaches the substrate at around 35 μs and by around 140 μs the plume detaches from the target surface. The vaporised material in the confined geometry condenses on the substrate surface with evidence of the lingering ablation plume seen even 400 μs after the laser pulse.

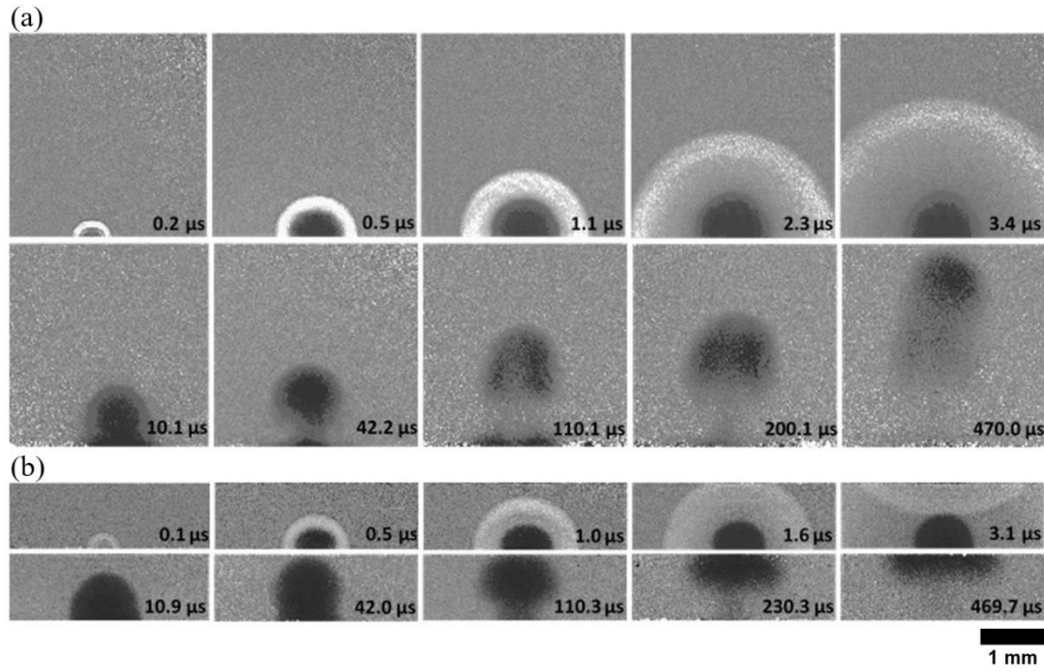


Figure 6.5: (a) Holographic imaging of the evolution of plume morphology during unconfined laser ablation. A rapid pressure wave is seen as a light colour, with the mass transfer of ablated material indicated by the dark colour. (b) Holographic imaging of the evolution of plume morphology in confined geometry, showing pressure wave reflection and plume spreading. Times shown are relative to the triggering of the laser pulse.

The displacement of the leading edge of the ablation plumes was measured for both confined and unconfined geometries. As shown in Figure 6.6(a), the ablation plumes were observed to decelerate rapidly in both cases. The rapid deceleration is attributed to viscous drag forces acting on the expanding ablation plume. Classical drag force models have been applied to plume expansion in previous studies to produce displacement-time variance of the form $Y = (\alpha/\beta)(1 - e^{(-\beta t)})$ for up to 8 μs after the ablation event [290,311]. When this modelling approach was tested in this study, it was not found to capture the dynamics of the entire plume lifetime and account for both short and long timescales simultaneously with a single set of fitting parameters. To provide a basic qualification of the plume displacement curve, the unconfined data set was fitted with regression analysis to produce the relationship, $Y = 53.18t^{0.2913}$ with $R^2 = 0.9605$.

While the approach above focuses on the vertical motion of the plume, Figure 6.6(b) plots the width of the confined and unconfined plumes over time. Both plumes expand laterally at the same rate initially. When the plumes reach the 1 mm separation distance, they have a measured width in the range of 800-1000 μm. The unconfined plume does not show significant further widening and stays within this range as it propagates vertically. The confined plume expands laterally after reaching the substrate as pressure is dissipated, a maximum width of 1751 μm was measured at 470 μs.

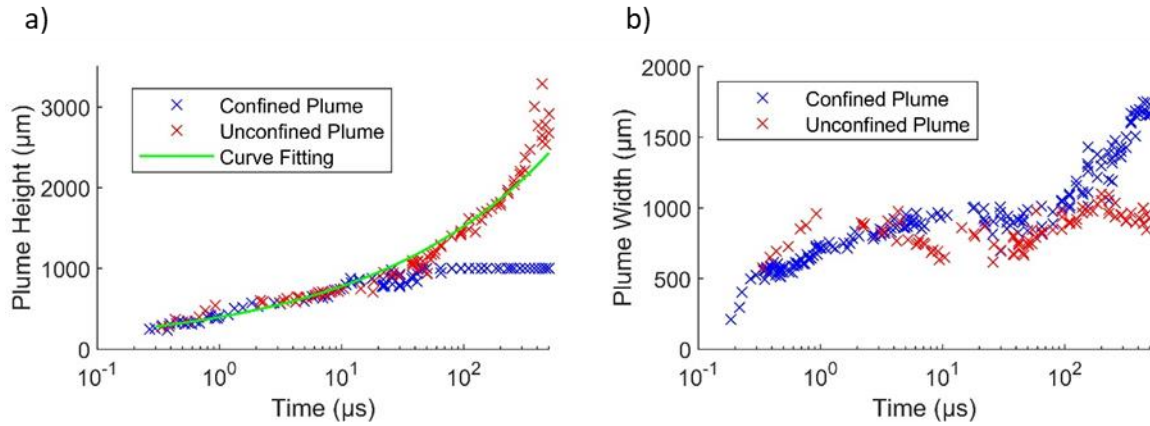


Figure 6.6: (a) Progression in plume leading edge vertical displacement with time. (b) Measured plume width over time.

Refractive index mapping of the ablation plume was used to measure the propagation of the energetic plasma core of the ablation plume and estimate its lifetime, as described earlier in Section 6.3. This is critical to understand because there is no longer just a single pulse when translating the technique to manufacturing. It is anticipated that there will be attenuation of pulse energy while travelling through the plume that is already present due to previous pulses. There is also expected to be an etching effect of the plasma on the transparent substrate. It was found that the plasma core was significantly slowed by the confined geometry. Figure 6.7(b) plots the height of the leading edge of the plasma component of the ablation plumes. Both confined and unconfined plumes display an initial velocity of approximately 440 ms^{-1} for $1 \mu\text{s}$, after which the confined plume begins to slow. It has been shown that ablation plumes have shorter stopping distances and decelerate more rapidly in pressurised atmospheres [288]. The deceleration of the plasma plume in the confined geometry occurs due to increased atmospheric pressure and coincides with the presence of the rebounding pressure shockwave. This observation concurs with the study of Fardel *et al.* [291] who observed deformation and deceleration of a thin film flyer due to a rebounding shockwave in the LIFT process. In the unconfined geometry, no regions with refractive index less than 1 (indicating the presence of the plasma) were observed after $125 \mu\text{s}$. In the confined geometry the plasma lifetime was found to be $230 \mu\text{s}$, which indicated an 81% longer plasma lifetime associated with densification effects when the plume impinges on the substrate. This finding is supported by the emission spectroscopy experiments of Donnelly *et al.* [292], who observed that the plasma in confined ablation was sustained at high density for longer times than in free ablation. An important implication of our imaging experiments is that the laser induced plasma persists for the duration of multiple laser pulses at a typical kHz repetition rate. As subsequent pulses interact with the ablation plume this could result in plume shielding and incubation effects. Future research should seek to optimise repetition rate selection through this knowledge of plume dynamics, for example, by selecting an interval between pulses which allows the plasma to dissipate.

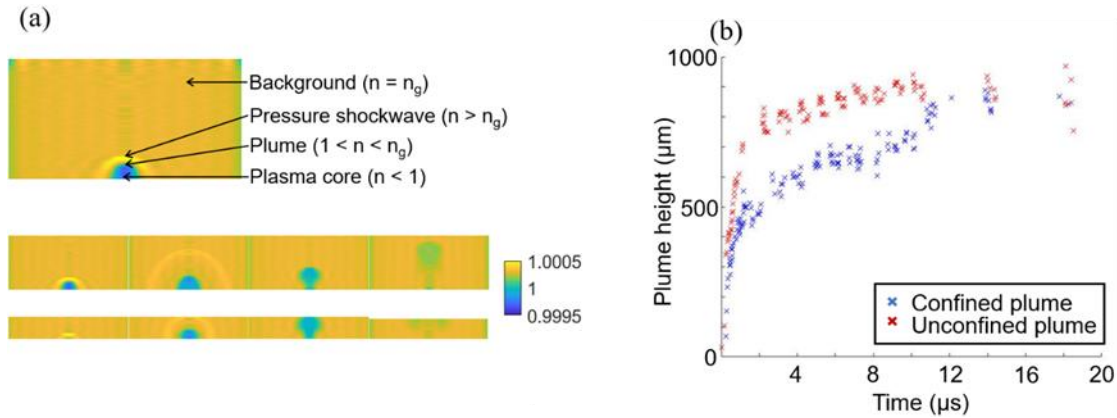


Figure 6.7: (a) Refractive index plot of graphite ablation plume, with processing pulse incident in an unconfined geometry and at a 1 mm confinement. (b) Measurement of the plasma core plume height during processing

6.5.2 Single pulse deposition

With the goal of better understanding how to fabricate repeatable conductive tracks with LIRT, the new understanding of plume dynamics described here was used to explore the mechanism of material deposition in the LIRT geometry. No deposition was observed in experiments using the 1 mm separation distance. One insight from the holographic camera imaging was that the expansion velocity of the ablation plume is a factor of 3.5 slower at the position of 1 mm compared to 100 μm according to the derived displacement-time curve. This loss in kinetic energy and further cooling effects are likely to be responsible for reducing the sticking probability of impinging species. As noted in Section (6.6), a G3 laser patterning system was used with 100 μm target-substrate separation for deposition studies. Sequences of static laser pulses were triggered at constant pulse energy with target ablation observed in all cases. After processing, the receiving side of the glass substrate was inspected with optical microscopy, as shown in Figure 6.8. Experiments examined single pulse, 10 pulses and 100 pulses. Graphite was easily ablated and showed a small amount of deposited material after a single pulse. Single pulse ablation of silver and copper did not produce substantial deposition, indicating the LIRT deposition threshold is higher than the material ablation threshold. This observation suggests that the optimum processing regime requires laser fluence high enough to trigger explosive material ejection, which has enough energy to stick to the substrate, whilst not so high as to damage the glass substrate.

After 10 pulses, deposited material was observed for all the tested target materials. The deposits consisted of a central circular feature with a width equivalent to the incident laser spot size, surrounded by scattered particles. The presence of deposited material after multiple pulses is attributed to an increase in material ejection as target absorptivity and temperature rise during the pulse train. The 200 ns pulse duration is much longer than the typical electron-lattice relaxation time

of metals (1-10ps) [312], which means that a significant portion of the incident laser energy diffuses into the target material as heat. As multiple pulses arrive, a damage feature at the centre of the deposit region becomes more pronounced, suggesting that deposited material produces a laser absorption site on the glass surface and subsequent laser pulses are partially absorbed by this site resulting in ablation to the glass substrate [294,313]. Zhang *et al.* demonstrated that this damage mechanism could be exploited with the use of higher pulse energies for micromachining or drilling of the glass substrate [295]. No damage was observed to the glass when the laser was focused to its surface without a target in place. This indicates that not enough energy is directly absorbed by the glass to cause ablation and the central circular feature is produced by interaction with the laser ablation plume. The results indicate that the mass transfer of the fine vapour produced by a single pulse is superseded by explosive particle ejection of subsequent pulses and the dominant additive mechanism in LIRT using nanosecond laser pulses is fragmentation of solid or molten particles.

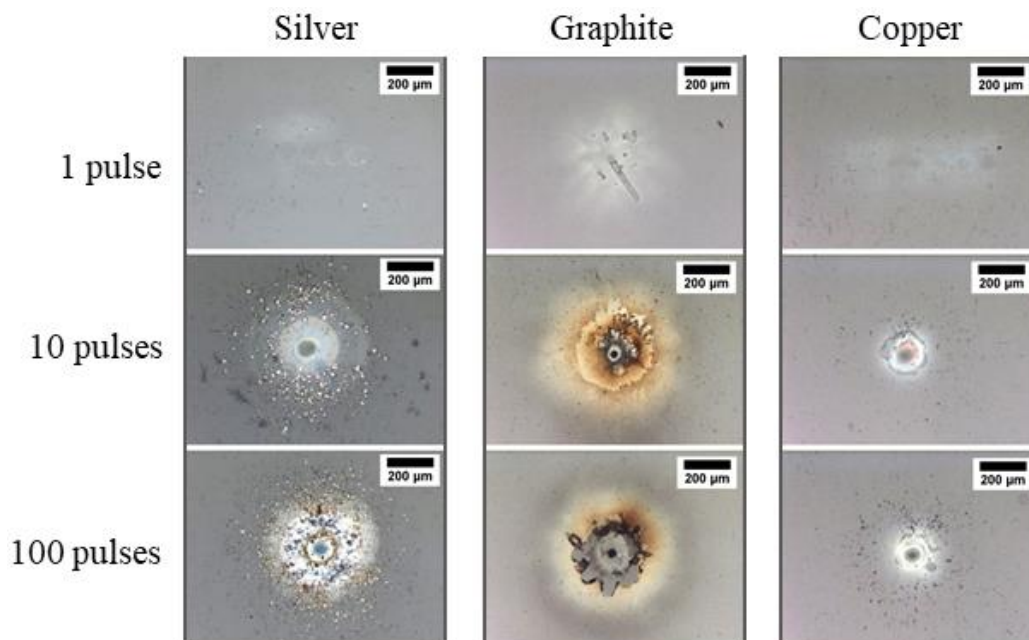


Figure 6.8: Optical imaging of silver, graphite and copper deposits produced by static laser beam with 1 pulse, 10 pulses and 100 pulses.

6.5.3 Conductive Track LIRT deposition

The next experimental steps were to generate understanding of the industrial applications, the characteristics of patterned track depositions and to maximise deposit conductivity. Up to now the potential of LIRT as a direct-write technology to produce conductive tracks through single pass laser scanning calls for further attention due to the small number of current studies [298]. Application-targeted experiments aimed to form continuous conductive tracks using three commonly used conductive materials, namely silver, graphite and copper.

6.5.3.1 Comparison of 3 target materials

Initial experiments used fixed laser parameters to compare the characteristics of the selected materials. These experiments were carried out using an incident laser beam scanned at 100 mm/s to produce a 90 % overlap between pulses. Figure 6.9(a) shows the micro and nanoscale morphology of the fabricated tracks across a range of magnifications. At the macro scale it was found that tracks in the range of 200-700 μm were formed. A central depression was observed in the channels which is particularly visible in the FIB imaging of copper shown in Figure 6.9(a). Based on the plume observations noted earlier we believe the depressions were caused by pulse overlap etching. In the case of the metallic target materials, silver and copper, the deposited tracks were mainly composed of molten microparticles which had fused together and solidified. The copper deposit showed less material deposition, which is attributed to the low absorption at the laser wavelength of 1.064 μm . The morphology of the graphite deposit was observed to be a dense covering of clustered nanoparticles as shown in Figure 6.9(a). EDS measurements were used to probe the composition of the deposited material to assess the deposition quality and degree of oxidation. Figure 6.9(b) shows the EDS spectra for the deposited tracks produced by scanning areas of 20 μm^2 in the center of each track. The spectra are mainly composed of the respective target element, silicon, oxygen and other elements from the glass.

A composition analysis was also applied to the graphitic deposit. In the EDS measurement the high percentage of carbon indicated good surface coverage. Raman spectroscopy was used to probe the structure of the deposit, with spectra collected for the graphite target and for LIRT deposited graphite, as shown in Figure 6.9(c). In the spectra for the deposit the D (1308cm^{-1}) and G (1578cm^{-1}) peaks have broadened, shifted and merged to form a broad band which indicates a transition to an amorphous carbon structure [314].

Four probe resistivity measurements of deposited tracks were carried out to measure electrical resistivity, and these measurements are summarised in Figure 6.9(d). The silver track shows the best electrical performance, with a resistivity of 0.03 $\mu\Omega\text{m}$, around twice the bulk resistivity value. The resistivity of the graphite was measured to be 340 $\mu\Omega\text{m}$, around ten times the bulk resistivity value. One possible effect is that the fusing of the molten droplets produces more continuous electrical pathways compared to the clustered particles observed with the graphite deposit. The deposited copper tracks did not have a measurable resistivity, this was attributed to the low volume of transferred material and a lack of continuous electrical pathway. EDS experiments also indicated that the transferred copper track exhibited a higher level of oxidation than the silver track resulting in the formation of nonconductive copper oxide. It is likely that the oxidation process occurs due to reaction of the metal elements in the ablation plume with the oxygen in the background air [297]. The

measured resistivity correlates with the composition of each sample because less oxidation was linked to better resistivity.

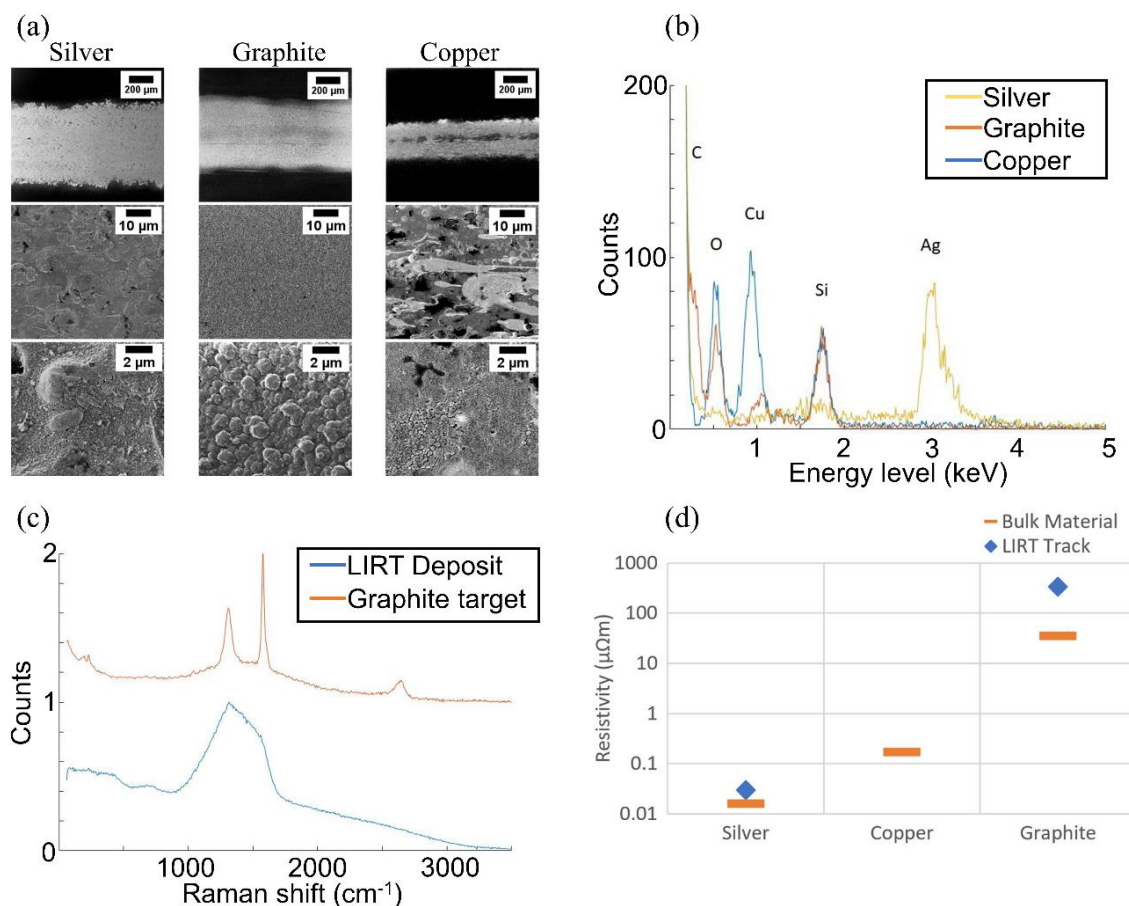


Figure 6.9: (a) Helium GFIS FIB imaging of tracks deposited by LIRT. (b) EDS spectra for the LIRT deposits. (c) Raman spectra of the graphite LIRT deposit and the graphite target. (d) Four-point probe resistivity measurements of the LIRT deposits compared to the bulk material.

Table 6.1 summarises the composition of the target material in the scanned area. A much higher relative percentage of metallic component was observed for the silver target compared to the copper target.

This section analysed the behaviour of each target material with constant laser parameters to produce a direct comparison. Because each material interacted differently in the LIRT process there is the potential to gain insight through experiments which are specific to the interaction behaviour highlighted such as the nanocluster formation during transfer of graphite and low deposition yield of copper. Now each material is studied in more detail to address these challenges and optimise the functional properties of deposits.

Table 6.1 : Comparison of deposited track elemental composition measured with EDS.

Element (At%)	Silver	Graphite	Copper
Ag	67.3		
Cu	0.0		18.5
C	8.0	73.8	26.1
O	21.0	20.3	41.9
Si	3.7	5.9	13.5

6.5.3.2 Graphite Deposition

Graphite was selected as a candidate target material because of its applications in electronics and sensing devices. Initial LIRT deposition with graphite in Section 6.6.1 showed that it had a high deposition rate and a deposit morphology consisting of nanostructured clusters of amorphous carbon. Further experiments were carried with the aim of gaining a more detailed understanding of how varying laser parameters influenced the nano and micro scale deposition morphology. This aimed to achieve an optimum laser patterning approach for high deposit conductivity and device fabrication.

To explore the effect of varying pulse energy from 150-400 μJ tracks were fabricated and deposit width and thickness was measured with interferometry. Significant micro-structure morphology variance was found in this range as evidenced in Figure 6.10. Both track width and thickness were found to increase with pulse energy, this was attributed to stronger target ablation producing a higher volume of ejected material. Width and thickness increased from an average of 189 μm at 100 μJ pulse energy up to 279 μm at 400 μJ pulse energy. Over the same range deposit thickness increased from 55.8 nm up to 396 nm. At higher pulse energy there was more substantial variation in deposit thickness as observed with range bars in Figure 6.10(b). This was attributed to a more chaotic thermally driven processing regime and the potential for more material removal from the deposited track due to laser pulses overlapping.

The deposit morphology at the nanoscale was also investigated, this was characterised through a combination of SEM imaging and ImageJ thresholding as shown in Figure 6.10(c). As laser pulse energy was increased from 150 to 400 μJ , the size range (25th-75th percentile) of the carbon clusters deposited on the surface increased from 45-65 nm to 106-164 nm. This effect was attributed to the laser interaction mechanics, during laser ablation solid clusters may be directly ejected from the target surface or formed by condensation of atoms and molecules during the ablation plume expansion [88]. Numerical analysis by Ohkubo *et al.* suggested that the trend of increasing cluster size with laser light intensity is due to the higher density of vapour and therefore a higher frequency of collisions between species in the plume [315].

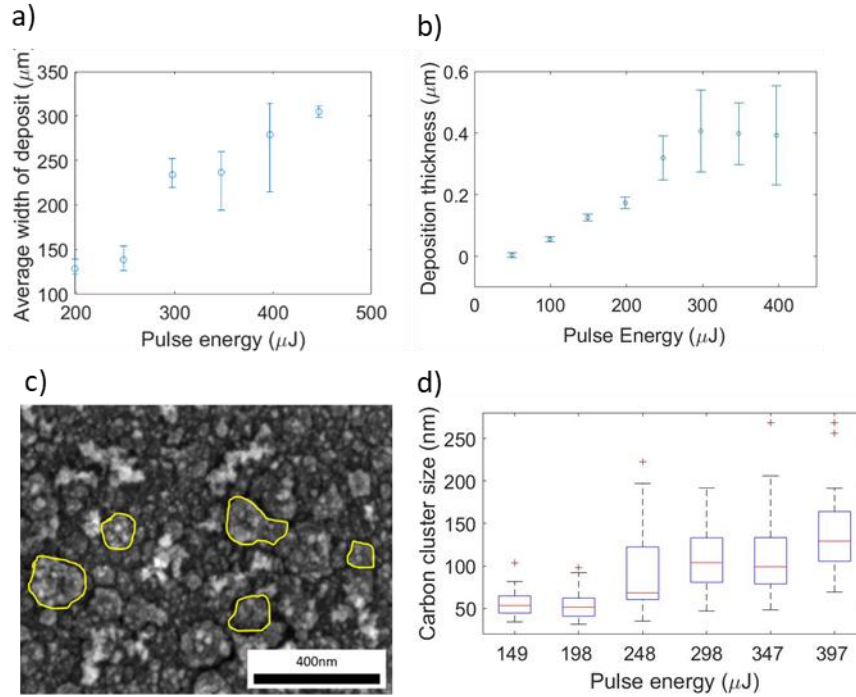


Figure 6.10: Variance of laser pulse energy with (a) deposit width and (b) deposit thickness. (c) Identification of carbon cluster size using thresholding in ImageJ. (d) Variance of carbon cluster size with pulse energy

The resistivity of the deposited tracks was measured using the four-point probe analysis technique, Figure 6.11 plots resistivity against laser pulse energy for LIRT deposition of graphite tracks. The minimum threshold to form a track with which conductive properties could be measured was 100 μJ pulse energy. The resistivity of the deposited tracks remained relatively constant with increase of laser intensity beyond this threshold, with the measured average resistivity varying between 420 to 1860 $\mu\Omega\text{m}$. This suggests that the chemical composition does not change substantially in the range of applied laser parameters and variation is mainly due to the discussed differences in morphology and resultant conductive pathways.

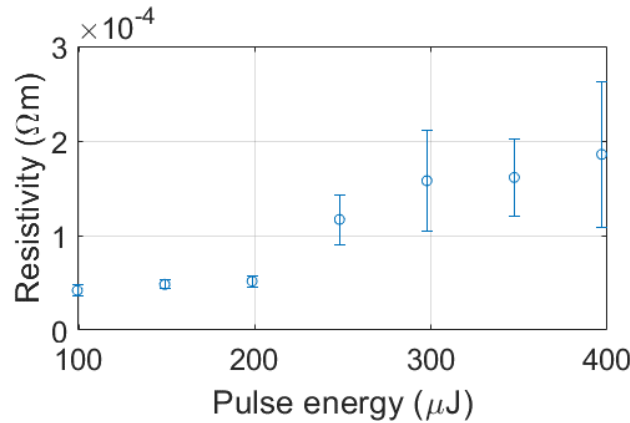


Figure 6.11: Variation of track resistivity with applied laser parameters.

6.5.3.3 Deposition of a noble metal (silver)

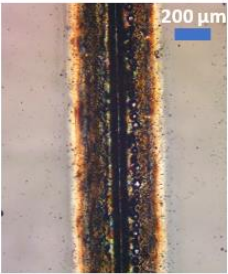
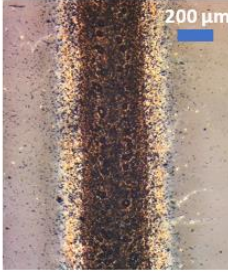

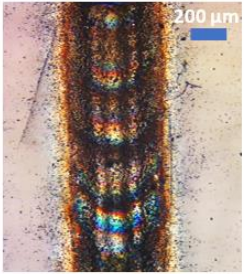




Silver is a widely used material for electrodes in common devices such as LEDs, batteries, photovoltaic panels and touch screens [316]. Typically, silver electrodes are deposited by mask based physical vapour deposition approaches such as sputtering or analog printing techniques such as screen printing. Silver was selected as a candidate in transfer experiments because of its very high electrical conductivity and chemical inertness. It was also used to contrapose the transfer dynamics of copper which is more readily oxidized. The objective of these deposition experiments was to assess the range of parameters for which a conductive track was formed, gain insight into the LIRT process and to explore the deposition behaviour of a noble metal.

To achieve these objectives a parameter sweep was carried out involving variance of laser pulse energy from 200-800 μJ and scan speed from 1-100 mm/s. Deposition experiments were carried out with both a 100 μm target-substrate standoff and with no separation in contact. The lowest laser power for which track deposition observed was 600 μJ , which indicated the deposition threshold using this combination of laser system and material. Because a much higher deposition threshold was observed compared to graphite deposition there was a restricted scope to observe the effect of varying laser parameters with the maximum power of the laser available. Table 6.2 shows the morphology of the silver tracks characterised using optical microscopy and interferometry. Firstly, observations are made about the interaction of specific deposits before moving to general trends from the wider experiment.

In parameter set Ag-1 the target and substrate were placed in contact without a separation. In this case the deposit profile showed that the central ablation channel resulting from laser overlapping was very pronounced and resulted in excessive damage to the substrate. This behaviour is attributed to plasma generated by ablation of the target directly etching the glass substrate [295]. In comparison, sample

Ag-2 used the same laser parameters but with a 100 μm standoff. Here, the central etched track in the deposit was still present but it was smaller and a continuous deposit was formed. In comparison to Ag-1 there was also more scattered particulate debris outside of the main area of the track which could indicate the influence of plume widening observed in the holographic camera experiments in Section 6.5. Sample Ag-3 used a lower power of 15W but with a 100 μm standoff, in this case the material removal effect from the glass substrate were also avoided. A narrower deposited track was observed reducing from an average width of 534 μm for parameter set Ag-2 to 342 μm for parameter set Ag-3.

Table 6.2 Optical images of deposited silver tracks compared to laser parameters and resistivity.

	Ag-1	Ag-2	Ag-3	Ag-4
Parameters	200ns, 20W, 0 μm separation 25mm/s	200ns, 20W, 100 μm separation 25mm/s	200ns, 15W, 100 μm separation 25mm/s	200ns, 20W, 100 μm separation 5mm/s
				
				
Width	423 μm	534 μm	342 μm	739 μm
Thickness	2.42 μm	1.49 μm	0.89 μm	2.52 μm
Resistivity	$1.95 \times 10^7 \mu\Omega\text{m}^{-1}$	$0.62 \mu\Omega\text{m}^{-1}$	$3.39 \mu\Omega\text{m}^{-1}$	$1.48 \times 10^7 \mu\Omega\text{m}^{-1}$

In parameter set, Ag-4 the same laser power as Ag-2 was used but scanning speed was reduced to 5 mm/s resulting in a higher pulse overlap and energy dose per unit length. This resulted in significant damage to the glass substrate and microcracks around the tracks were observed. For the tracks Ag-1 and Ag-4 where significant damage to the glass substrate was observed a high deposit resistivity was measured. The resistivity of the deposits was low for tracks Ag-2 and Ag-3 with values of $0.62 \mu\Omega\text{m}^{-1}$ and $3.39 \mu\Omega\text{m}^{-1}$ respectively.

Several trends were observed by looking at the experimental data set more broadly. Figure 6.12(a) plots the deposit thickness against scan speed. Reducing scan speed and increasing power resulted in continual increase to deposit thickness. Figure 6.12(b) plots deposit width against laser scan speed. At the lowest scan speed of 1 mm/s the deposit width increased with power. However, at higher scan speeds width this trend was less clear.

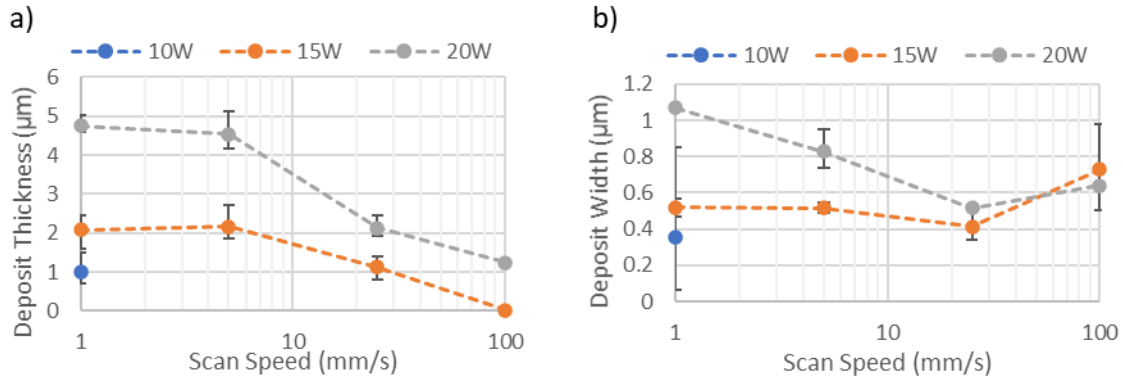


Figure 6.12: Plots of (a) deposit thickness and (b) deposit width for LIRT of Ag track deposits with varying laser parameters

Figure 6.13 plots the laser parameters with varying scan speed and laser power against their measured track resistivity. High resistivities were measured when using scan speeds slower than 25 mm/s , this is attributed to the removal effect at high laser overlaps. The set of parameters investigated indicate that a small experimental range is available to deposit silver tracks with conductive properties whilst avoiding material removal effects. Broadly two regimes were observed with resistivity in the range of 10^7 - $10^9 \Omega\text{m}$ and resistivity values which were less than $1 \mu\Omega\text{m}$. There is not a clear reason for this partition in measured resistivities, although it is attributed primarily to a morphology effect. One potential mechanism is that a critical density of molten particles is required to produce a continuous path otherwise conductivity is limited to the vapor driven thin film.

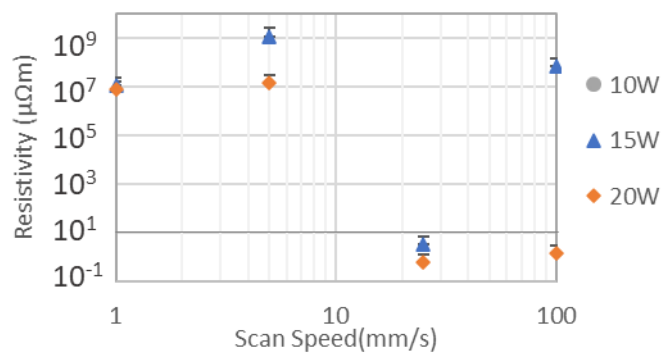


Figure 6.13: Variation of resistivity with applied laser parameters for Ag track deposition

6.5.3.4 Deposition of an oxidizing metal (copper)

Copper is a metallic material possessing high thermal conductivity of 401 W/(m.K) and high electrical resistivity of 16.8 nΩ.m [317]. It is highly reflective in the near IR wavelength reflecting >95% of incident light, which reduces rapidly as copper heats up or melts, or as copper oxide is formed during laser ablation [318]. It was tested in transfer experiments because of its common use in electronics applications and value as a lower cost alternative to silver interconnects.

In initial transfer experiments using a copper target reported in Section 6.6.1, the copper track showed lower volume of transfer material in comparison to graphite and silver. This was attributed to high reflectivity at the laser wavelength. In total, 96 parameter sets were tested for track patterning with copper varying power (5-20W), scan speed (1-100 mm/s), and standoff (0-300 μm) conductive properties were not observed for any of the deposited copper tracks. This was attributed to low deposition yield and oxidation during transfer.

In order to investigate this oxidation process more closely surface chemistry analysis was carried out on copper film deposits. Sample W13 was processed with the target and substrate in contact, sample W14 was processed with a separation of 125 μm. XPS analysis was used to probe the bonding state, EDS analysis was used to measure the deposit elemental composition.

As illustrated in XPS spectra Figure 6.14(a-b), sample W13 (0 μm standoff) showed the presence of the Cu metal peaks in the Cu₂p spectrum and diminished CuO peaks, whereas sample W14 (100 μm standoff) showed much larger CuO peaks. EDS composition analysis reported in Figure 6.14(c) showed a greater copper Wt% in sample W14 indicating more deposited metal with the use of a standoff. The greater Wt% of glass substrate elements (Si,O) in W13 was attributed to the lower deposition yield and redeposited ablated substrate material mixing with the metallic deposit. Simplistically, a ratio of approximately 2:1 Oxygen:Silicon could be expected for the glass silica matrix [319]. The ratio of Oxygen:Silicon in both samples was higher than could be accounted for by the glass matrix indicating the presence of copper oxide compounds. These two analyses confirm oxidation of copper during LIRT. As more CuO was formed when an air gap was used, it is likely that the oxidation process occurs due to reaction of the metal elements in the ablation plume with the oxygen in the background air [297].

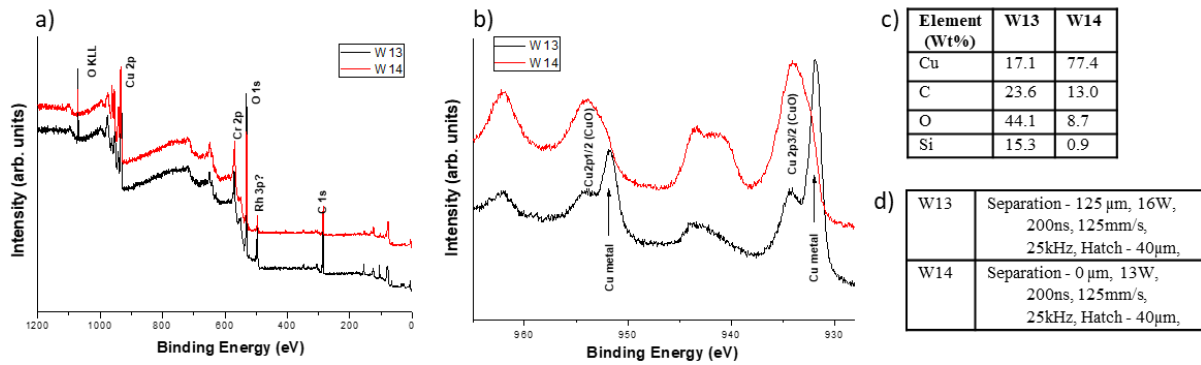
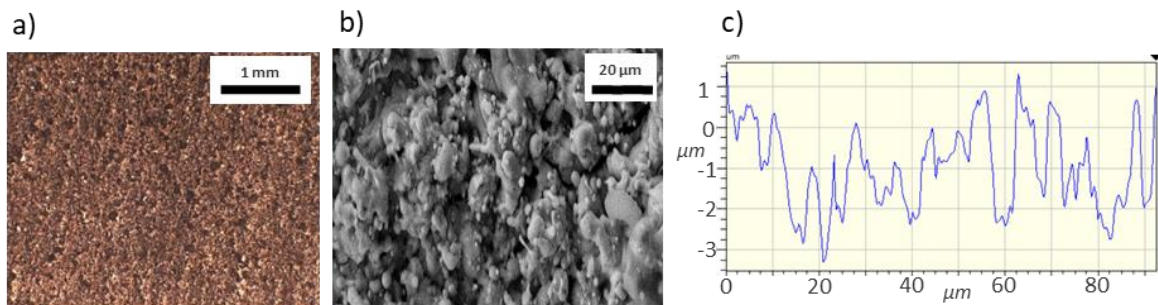


Figure 6.14: (a) Comparison of XPS sample survey for samples W13 and W14. (b) Comparison of Cu₂p spectra. (c) Comparison of EDS elemental composition measurements. (d) Summary of laser parameters.

In order to assess the functional properties of the deposited copper films the film morphology and electrical properties were characterised. As shown in Figure 6.15 the surface structure of the copper film W14 was characterised with optical microscopy, SEM imaging and interferometry. The deposited copper film retained the orange colour of the copper target, a periodicity was observed in the film with equal width to the laser scanning pattern. At the microscale, the deposit was very rough and consisted of solidified globules of molten material. The average roughness was measured as Ra



0.86 μ m with total profile height of 4.64 μ m.

Figure 6.15: Morphology analysis of W14 deposit through (a) Optical Microscopy (b) SEM (c) Interferometry roughness measurement

As no conductivity was measured with track scanning, areal deposits were patterned with serpentine scanning to characterise the electrical properties of copper deposits. The patterned areas had dimensions of 10x4 mm, a hatching separation of 40 μ m between tracks was used for patterning. A parameter sweep consisting of variance of target-separation distance and applied average power was carried out, scanning speed was kept constant at 150 mm/s.

Variance of resistivity with comparison to laser power and target separation is shown in Figure 6.16. LIRT areal film deposition of copper with pulse energy less than 0.52 mJ did not produce enough

deposited material to measure conductive properties. It was found that the most conductive deposits were produced by operating in the range 0.64-0.76 mJ pulse energy. The sample with closest equivalent laser parameters to W13 had among the lowest resistivity of $2.24 \mu\Omega\cdot\text{m}$ 0.64 mJ, 16W pulse energy and 230 μm standoff. All films deposited with no separation (similarly to sample W14) did not produce conductive properties. Areal deposit production with no separation at the highest pulse energy of 0.76 mJ even resulted in cracking or shattering of the glass.

This experiment showed that a narrow operating window was available to produce sufficient deposited material whilst avoiding thermal damage. The lowest resistivity recorded was $1.28 \mu\Omega\cdot\text{m}$ which is approximately 7.5x the value for bulk copper [317]. The high conductivity effects observed when depositing films instead of tracks is mainly attributed to better morphology. Additionally the high number of scanning passes of the laser may result in an annealing effect which contributes to the significantly improved resistivity [320].

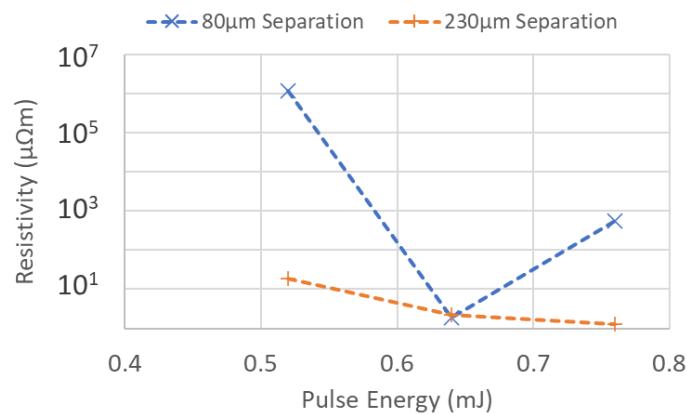


Figure 6.16: Variation of LIRT deposited copper film resistivity with laser pulse energy and standoff

6.5.3.5 High incidence angle transfer of copper

To improve the overall low net deposition when patterning copper, a process adaption was tested which utilised a high laser incidence angle to avoid overlapping of the laser and the deposit. The aim of the strategy was to scan the beam at a sufficiently high incident angle to prevent interaction with the deposited track. In principle, the plume produced by laser ablation is directionally normal to the target surface irrespective of incidence angle. Because a laser pulse has insignificant momentum the preservation of momentum results in a density gradient maximum in the normal direction. Specifically for copper, laser absorption and coupling coefficient at 1064 nm have been shown experimentally to exhibit minor dependency up to an incidence angle of 60° [321].

Microscope images from earlier track patterning experiments reported in Section 6.6.1 showed the approximate deposited track width to be $200\text{ }\mu\text{m}$ with focused beam spot size of $36.4\text{ }\mu\text{m}$. The minimum angle of incidence required to eliminate deposit-beam overlapping was calculated geometrically to be 40° . The beam was assumed to be collimated as the calculated depth of focus of 3.9 mm was much larger than the target-substrate separation. Figure 6.17 shows the experimental arrangement and labelling of axis. A 3D printed fixture was placed onto an alignment pattern on a flat support surface. By interrogating the CAD model of the fixture, the height on the target surface could be ascertained to focus the laser. It proved to be very difficult to focus the laser to a highly inclined surface so only proof of concept tests were possible for high incident angle LIRT deposition.

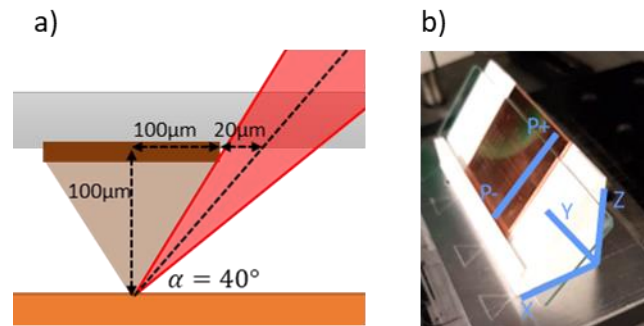


Figure 6.17: (a) geometric arrangement of high incident angle LIRT patterning (b) labelling of machining axes

Figure 6.18 shows optical microscopy and FIB imaging characterisation of the deposits. Processing at 0° incidence resulted in a central channel in the deposit indicating ablation due to pulse overlapping. Compared to the deposit produced by scanning at a high angle of incidence, no material removal of the glass surface was observed. This showed successful demonstration of the high incidence angle deposition process.

Further evidence of the proposed mechanism was given by scanning a cross pattern in the intersection of the P and Y axis shown in Figure 6.18(c). The track in the Y Axis showed pure deposition, the intersecting track machined in P Axis showed removal of deposited material at the intersection of the tracks. This demonstrates that laser ablation can remove the deposited material. A scanning strategy using this approach could allow for sequential build-up to produce thick or multilayer depositions in future research.

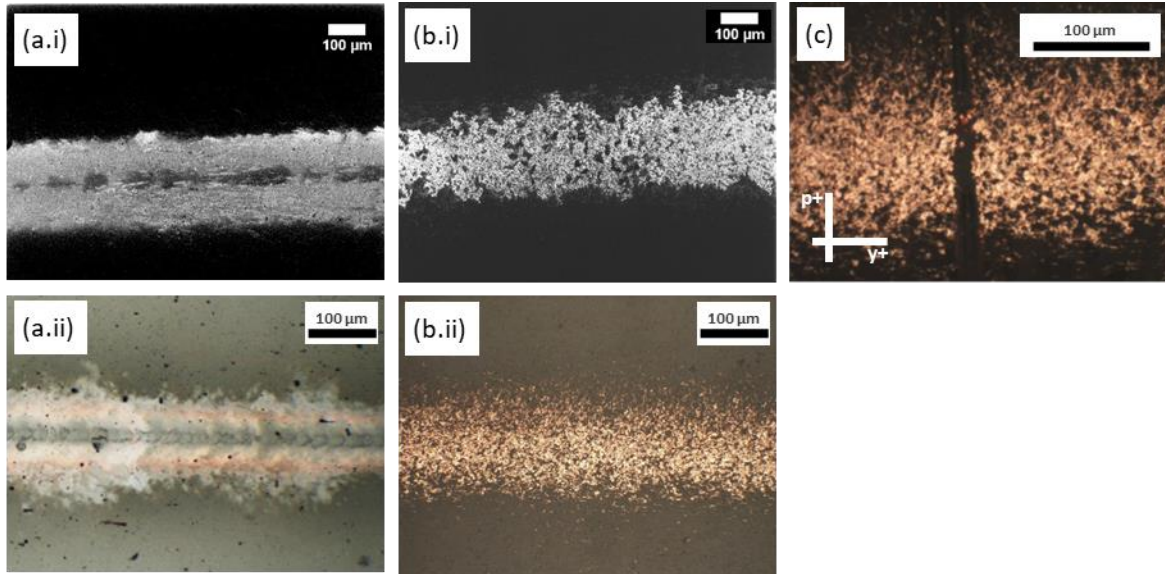


Figure 6.18: Morphology characterisation of deposits created with varying laser inclination angle **(a.i)** FIB image **(a.ii)** optical microscope image of track machined at 0° inclination. **(b.i)** FIB image **(b.ii)** optical microscope image of track machined at 50° inclination. **(c)** Center of cross pattern machined on axes Y-P with 60° inclination and separation ~100μm

Holographic camera imaging was used to investigate the material ejection at a high incidence angle. Figure 6.19 shows holographic camera frames for unconfined plumes for times 1.9 μs - 255.9 μs after the ablation event. The camera was aligned to the transfer gap across axis Y and the laser was incident in the Z axis which is vertically straight in the frames shown. Graphite was used as the target material in order to achieve ablation at low energy although the expected plume morphology is similar. Very similar behaviour was observed to the experiment in Section 6.5.1 on flat target surfaces. The key finding was that the ablation plume propagated at an angle broadly normal to the target surface evidencing the mechanics of the high incident angle transfer technique.

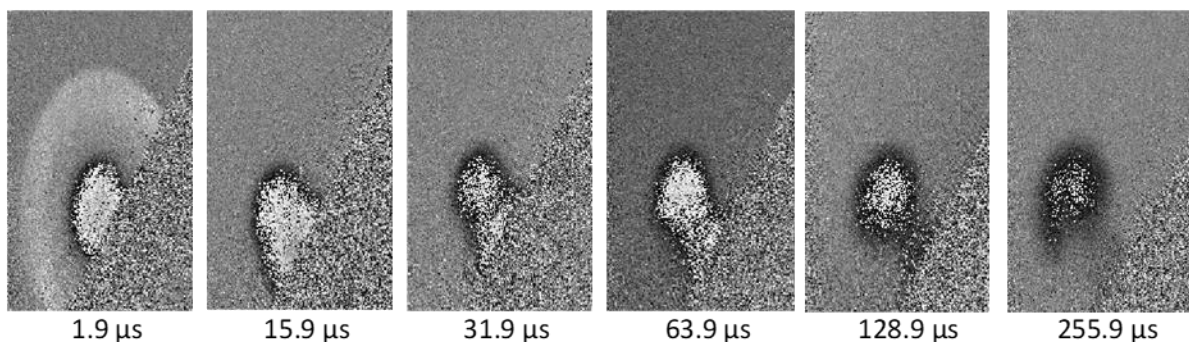


Figure 6.19: Holographic imaging of plume morphology during unconfined laser ablation at 60° laser incidence angle

6.5.3.6 Device Fabrication

In order to explore routes for progression of the LIRT technique a series of application focused experiments were conducted which involved fabrication of embedded devices. These targeted applications were logo colour marking, fabrication of a capacitive touch sensor and a temperature dependant resistor.

Although copper tracks were not suitable for conductive interconnects, they were visibly homogenous on a macroscopic level. With digital control of the laser scanning pattern, LIRT could be used for colour marking of glass surfaces. Figure 6.20(a) shows text patterning onto a glass microscope slide using LIRT of copper.

To demonstrate an application of conductive track patterning, a capacitive touch sensing grid was deposited to a glass microscope slide. The parameters Ag-2 defined in Section 6.6.3 were used for silver deposition to produce a grid with 2 mm pitch. The Arduino capacitive sensing library was used to write the code for this device [322]. Figure 6.20(b-c) shows the device being used to switch an LED based on touch.

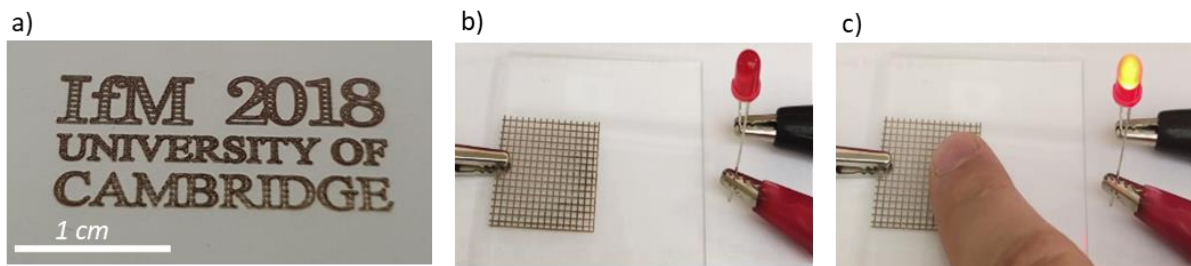


Figure 6.20: (a) Colour marking to a glass slide (b-c) A capacitive touch sensing grid patterned with the LIRT process to a glass microscope slide.

Graphitic carbon and graphene compounds have been used as the functional material in the fabrication of different sensors including humidity [323], gas sensing [324] and temperature [325]. The use of graphite is particularly attractive as a low cost and environmentally friendly alternative to conventional thermal sensors [326]. A simple circuit pattern was deposited onto a glass slide to form a thermoresistive sensor. Inkjet printed silver electrodes were deposited on top of the graphite deposit to ensure good electrical contact with the probe tips using the parameters outlined in Section 5.5.4. Figure 6.21(a) shows the deposited pattern and equipment setup. The characterisation setup consisted of a probe station touching the deposit, a resistive heater which allowed for sample heating up to 60°C and thermocouple glued to the device surface.

Figure 6.21(b) shows the variation of electrical resistance with temperature. As temperature increased from 29 to 74°C it was seen that the resistance decreased with a total resistance change of 435 Ω , with the reverse behaviour observed on cooling. The temperature dependent coefficient of resistance for a best fit line was calculated as: -1257 ppm/°C. This was broadly in line with other investigations into graphitic thermoresistive sensors [325], however the unique contribution here is to establish the use of LIRT for sensing device fabrication. Previous investigators of graphite based thermoresistive sensors have attributed the decrease in electrical resistance with temperature to thermionic emission. Because the resistance of the boundaries between graphite grains is usually much higher than the resistance of the grains, boundary resistance is the dominant component of the measured resistance. The low potential barrier of graphite (33 mEV) favours a thermionic emission mechanism of temperature dependence, where thermally excited carriers can pass through or over the barrier between graphite clusters [326].

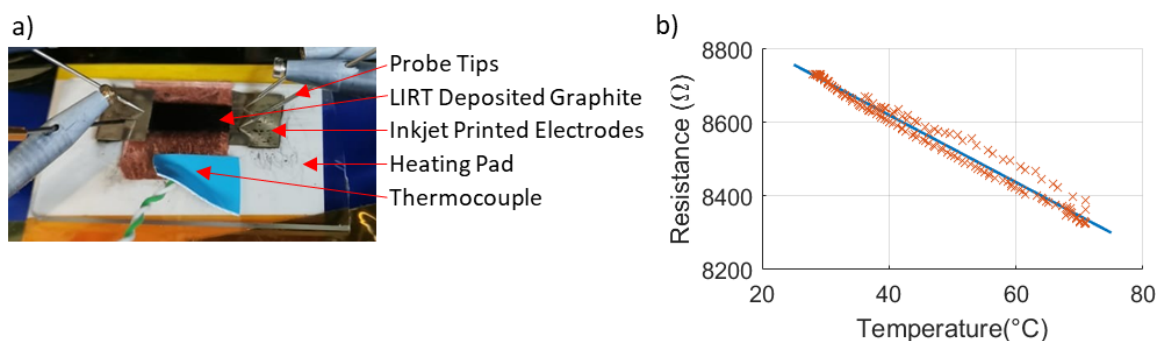


Figure 6.21: (a) Fabrication of a temperature sensor device using LIRT deposition of graphite tracks and characterisation setup. (b) Variation of resistance with temperature over a heating and cooling cycle

6.6 Conclusion

The results in this chapter present new knowledge in the use of LIRT deposition of functional material to glass substrates. The results prove the feasibility of the technique for functional material patterning however there are substantial challenges to progress LIRT to an industrial process which is competitive with other direct write deposition approaches.

The unique capabilities of holographic phase contrast imaging was used with nanosecond temporal resolution to study LIRT in open and confined geometries, revealing previously unseen phenomena. The deceleration of the plasma plume in confined environments was recorded and the influence of the rebounding pressure wave observed. The speed of plume propagation was found to decelerate exponentially from an initial velocity of over 400 m/s. Observation of the plasma core of the ablation plume showed densification and plume widening effects due to the confined geometry. There is >80%

longer plasma lifetime in the confined geometry, and we discussed the importance in terms of plume shielding and incubation effects. This will become more important as the process develops towards applications and the production rate and patterning resolution need to be improved. Static beam experiments with silver, copper and graphite were informative when studying the mechanism of transfer and it was observed that multiple pulses are required to produce deposited material and this deposit is primarily composed of fused particles. In the case of graphite transfer, the deposits consisted of nanostructured carbon clusters. The average size of these clusters was found to increase with laser pulse energy.

Tests into producing direct-write patterns through overlapped pulses showed that the technique could produce conductive tracks suitable for fabrication of embedded components in late-stage customisation of glass products. Fabrication of a capacitive touch sensing device, colour marking of a brand logo and a simple temperature sensing circuit were used to demonstrate the industrial value of LIRT as a simple and effective printed electronics fabrication technique. The uneven morphology, poor uniformity, inhomogeneous chemical composition and material damage highlight the challenges in using LIRT for applications but these are all challenges that can be addressed and would lead to a facile, reliable fabrication of conductive patterns and digitally controlled customisation of glass products for applications such as embedded sensors and electronics.

Future research should explore process optimisation through control of the temporal energy deposition profile in combination with a controlled atmosphere. As the target metal surface requires minimal preparation and the environmental and process control are minimal, the new insights into the mechanism and track formation are a step towards delivering a reliable alternative approach to direct-writing metals.

7 RESEARCH OUTCOMES AND FUTURE WORK

In this work new aspects of digital surface modification have been investigated and presented, adding to the knowledge described in the literature and bringing new capabilities for future manufacturing processes. In the stainless steel and glass industries in particular, there is significant demand for innovative product functionalities. These functionalities need to be imparted using scalable ultra-precision manufacturing techniques, with digital processing techniques such as inkjet and laser processing offering particular advantages such as customizability, low input resource usage and the avoidance of harsh chemicals and processing conditions. This thesis has focused on surface modification using digital manufacturing techniques involving direct laser texturing, inkjet printing of functional material and laser induced reverse transfer. This chapter firstly summarises the main outcomes of the work presented and then describes recommended future work that will be important based on the findings in this thesis.

7.1 Research outcomes

A core aim of the research was to find insights through literature analysis to identify where progress was needed in laser textured superhydrophobic surfaces. This led to fundamental studies assessing the chemical nature of the hydrophobic transition and how this time-consuming process could be accelerated.

Two laser processing techniques were identified of LIPSS production and ablative surface structuring. Both surfaces were found to be capable of superhydrophobicity. The major difference between the two techniques was that the rougher surface required longer to transition to hydrophobic, it also unsuitable for processing of thin sheets. The LIPSS modification improved on these aspects however it is currently a slower and more expensive approach.

The hydrophobic transition of laser textured stainless steel was investigated to high level of detail. A range of conditions after laser processing was tested, the use of low temperature annealing at (250°C) was found to decrease the hydrophilicity-phobicity transition from over 30 days to 24 hours however this did not result in a stable modification. Vapour transfer and solution deposition of food safe fatty carboxylic acids was capable of forming effective superhydrophobic surfaces. XPS surface chemistry analysis was used to understand the transition mechanism which was attributed to chemisorption of hydrocarbons through polar interaction with the high surface energy metal oxide.

The main advantages of the laser texturing technique which were found in this study were:

- The very strong superhydrophobic effects possible
- Economic and fast-throughput processing
- The avoidance of toxic coating chemicals which may degrade or peel off into the end-use environment or supply chain.
- The capability for digital wettability patterning production

Chapter 5 aimed to use surface wettability and topology modification approaches to enable functional inkjet printing with enhanced adhesion and durability on glass surfaces. The literature review showed that the state of the art in inkjet printing is rapidly expanding, improved performance and novel functionalities may be enabled by hybrid processes which combine laser or plasma treatment with inkjet printing. Advanced material deposition capabilities are sought for applications including solar technology and embedded in electronics in automotive glass.

To build understanding into the impact of surface preparation processes, solvent cleaning and plasma treatment were analysed for the effect on wettability and surface chemistry. Solvent cleaning produced a hydrophilic water contact angle of 21.8° which was reduced further to less than 5° through plasma treatment. Through XPS analysis, this reduction in contact angle was attributed to removal of organic contaminants. Surface free energy measurement showed that the plasma treatment raised surface free energy substantially which was attributed to generation of polar hydroxyl groups on the glass surface. Both of these processes could be readily integrated into a production line prior to inkjet printing to enable tailoring of fluid-ink interaction.

Inkjet printing of a water-based silver nanoparticle ink formulation was used to pattern conductive tracks on glass. The printed tracks were analysed for morphology and electrical properties. Experiments did not show a clear benefit of plasma treatment when used as an approach to increase the adhesion of the printed silver tracks. However due to the very high wettability after treatment, this surface type led to a loss of control over deposit morphology and a low coverage of nanoparticles.

Wettability patterning was explored as a technique with the motivation of combining a high surface energy surface with a hydrophobic boundary to overcome these spreading difficulties. Masked plasma treatment showed exciting capabilities and proved to be an effective approach but a more refined technique is needed for microscale modification. When the fluid profile was analysed with respect to increasing fluid volume one drawback was that the plasma technique suffered from a less clearly defined hydrophobic boundary definition and the contrast in wettability between exposed and nonexposed areas was smaller. The laser treatment was precise and resulted in a superhydrophilic wettability in the patterned area. In particular the use of printing into a 1 mm track showed very

effective containment in the spreading of the inkjet printed deposit. The major limitation on these techniques for inkjet printing was the inconsistency of the printing which resulted in droplets misplacement. Laser patterning of microgrooves showed an effective protection against surface abrasion resulting in preservation of track conductivity.

In chapter 6, fundamental studies were carried out with the aim of improving understanding and testing the viability of LIRT process for functional material deposition to flat glass surfaces. The experiments focused on the plume dynamics and deposition behaviour, prior to more application-focused experiments examining single pulse and continuous track deposition.

Understanding of the process mechanics when nanosecond pulsed lasers are used was developed with optimisation of applied laser energy, scanning parameters, and target-substrate separation. By using a long pulse width of 200 ns and a standoff of 100 μm mainly evaporation driven deposits were produced. Holographic camera imaging provided unprecedented insight into the plume dynamics in the confined LIRT geometry including observed effects of shock wave rebound and plasma incubation. 3 different target materials were tested and the most conductive deposits were formed through deposition of silver which displayed conductivity in the range of 2x the bulk value. This was attributed to reduced oxidation and a favourable deposit morphology consisting of fused molten particles. A future processing regime utilising an incident laser tilted to scan out with the central ablation plume and deposit area was demonstrated to eliminate laser pulse absorption by deposits from preceding pulses. This could allow for more uniform deposits to be formed and eliminate thermal damage to the glass substrate. The technique was shown to be capable of basic colour marking and patterned functional deposition. A capacitive touch sensing circuit and temperature dependant resistor were fabricated as application demonstrations.

Novel findings and capabilities using LIRT have been achieved in this project Although this progress is significant, the challenges for LIRT remain large. In particular, the uneven morphology, poor uniformity, inhomogeneous chemical composition and material damage.

7.2 Future Work

7.2.1 Laser Textured Superhydrophobic Surfaces

Future research into laser textured superhydrophobic surfaces should target gaining further insight into the surface chemistry after laser processing and industrial progression. The investigation with XPS produced exciting results such as influence of hydrocarbon terminal group and chain length. However, the analysis was limited because of the overlap with other carbon sources and obscuration

of the relevant carbon bonding state peaks. An interesting experiment would be the use of FTIR solution depletion isotherms [199]. This could allow measurement of adsorption rate of different hydrocarbons as well as monolayer binding characteristics.

To increase the processing rate of LIPSS laser texturing a system was outlined which required the use of a high repetition rate femtosecond laser which is accessible with the current state of the art. Further opportunities include the use of multi beam processing [118] and direct laser interference patterning [327].

7.2.2 Functional Inkjet Printing to Glass

To increase the durability of the inkjet printed deposits on glass surfaces several strategies could be examined in future research. One might be to print onto a polymer sheet which is then sandwiched between laminated glass plates [328], secondly may be to deposit a protective encapsulating layer on the deposit such as a rigid polymer [329], third would be through chemical functionalisation such as application of a primer bonding layer [251].

Additionally, alternative digital manufacturing opportunities may be sought. The industry standard process is to screen print a high viscosity frit paste which consists of a mix of silver and glass particles. After firing the glass and silver particles fuse into the surface to produce a tightly bonded and abrasion resistant deposit. This is challenging to implement with inkjet printing because of the frit glass particle size and fluid viscosity. Investigating microextrusion [330] or LIFT [278,331] may be an interesting opportunities to recreate this process digitally.

7.2.3 Laser Induced Reverse Transfer

Further research into LIRT would allow for further exploration of manufacturing related challenges and novel deposit properties.

Based on findings into the temporal profile of process, future research should seek to optimise repetition rate selection through the knowledge of plume dynamics. In particular, the use of burst pulse processing with burst duration shorter than the plume accumulation could be used to avoid shielding effects [332]. It will also be vital to investigate other aspects of device fabrication such as the interface of the LIRT deposit with soldered connections.

Although crack free deposition was observed when fast scanning speed and a standoff were used, this factor should be investigated further in wide area translation due to the potential to reduce the mechanical strength of the glass. Standard 1 mm thick microscope slides were used in experimental work because of their availability and for the ease of configuring in the laser processing system. The

translation of the deposition technique to glass with different thicknesses calls for further investigation, for example thicker glass may reduce the laser power incident on the target due to absorption by the substrate, very thin glass may be more susceptible to cracking due to thermal effects.

Deposition of a transparent superhydrophobic coating on glass has been demonstrated using areal pulsed laser deposition of PTFE in high vacuum conditions [49]. LIRT deposition of PTFE could be a unique opportunity to enable transparent superhydrophobic patterns using a laser direct write technique. Initial experimental work suggest that a femtosecond laser source is required for this process due to the low absorption of PTFE at NIR wavelengths.

Overall, the work presented has provided additional understanding and developed new techniques for the field of functionalising glass and stainless-steel surfaces. The research was carried out while still ensuring a clear route to large-scale digital manufacture was considered at every stage. The findings and guidance made in this thesis should be useful potential routes forward to further advance these technologies further towards industrial realisation and applications.

8 REFERENCES

- [1] M. Gannon, N.E. | J. 8, 2014 02:06am ET, Ancient Greeks Used Portable Grills at Their Picnics, Live Science. (n.d.). <https://www.livescience.com/42414-ancient-cooking-mycenaeans-portable-grills.html> (accessed August 16, 2017).
- [2] Heat Treatment of Metals: History and Objectives | Metallurgy, Engineering Notes India. (2017). <https://www.engineeringenotes.com/metallurgy/heat-treatment/heat-treatment-of-metals-history-and-objectives-metallurgy/25554> (accessed February 8, 2021).
- [3] Bhaktivedanta Vedabase Online, Bg 5.10, 2011. <http://www.vedabase.com/en/bg/5/10> (accessed August 16, 2017).
- [4] A.M. Worthington, R.B. Clifton, XXVIII. On the forms assumed by drops of liquids falling vertically on a horizontal plate, Proceedings of the Royal Society of London. 25 (1877) 261–272. <https://doi.org/10.1098/rspl.1876.0048>.
- [5] W. Barthlott, C. Neinhuis, Purity of the sacred lotus, or escape from contamination in biological surfaces, Planta. 202 (1997) 1–8. <https://doi.org/10.1007/s004250050096>.
- [6] R.J. Plunkett, Tetrafluoroethylene polymers, US2230654A, 1941. <https://patents.google.com/patent/US2230654A/en> (accessed February 8, 2021).
- [7] F. Harvey, Are we running out of water?, The Guardian. (2018). <http://www.theguardian.com/news/2018/jun/18/are-we-running-out-of-water> (accessed June 19, 2018).
- [8] K. Werner, ID Asks/Dongsheng Wang, Information Display. 35 (2019) 18–22. <https://doi.org/https://doi.org/10.1002/msid.1073>.
- [9] Secure by Design, GOV.UK. (n.d.). <https://www.gov.uk/government/publications/secure-by-design> (accessed August 12, 2018).
- [10] K. Suganuma, Introduction to Printed Electronics, Springer-Verlag, New York, 2014. <https://doi.org/10.1007/978-1-4614-9625-0>.
- [11] Stainless Steel Market Size | Industry Analysis Report, 2018-2025, (n.d.). <https://www.grandviewresearch.com/industry-analysis/stainless-steel-market> (accessed July 19, 2018).
- [12] Flat Glass Manufacturing, Eurotherm by Schneider Electric | Temperature Control, Process Control, Measurement and Data Recording Solutions. (n.d.). <https://www.eurotherm.com/flat-glass> (accessed July 18, 2018).
- [13] An industrial policy for the European glass sector, European Economic and Social Committee. (2014). <https://www.eesc.europa.eu/en/our-work/opinions-information-reports/opinions/industrial-policy-european-glass-sector> (accessed July 18, 2018).
- [14] The History of Stainless Steel – Celebrating 100 Years, AZoM.Com. (2013). <https://www.azom.com/article.aspx?ArticleID=8307> (accessed February 16, 2021).

- [15] dairyreporter.com, Dairies could slash cleaning costs with AI cleaning system, Dairyreporter.Com. (n.d.).
<https://www.dairyreporter.com/Article/2016/09/14/Dairies-could-slash-cleaning-costs-with-AI-cleaning-system> (accessed July 21, 2018).
- [16] S.J. Fleming, Roman Glass; reflections on cultural change, University of Pennsylvania Museum of Archaeology and Anthropology., Philadelphia, 1999.
- [17] One of the world's oldest products faces the digital future, The Economist. (2017).
<https://www.economist.com/science-and-technology/2017/10/12/one-of-the-worlds-oldest-products-faces-the-digital-future> (accessed July 18, 2018).
- [18] Automotive Overview, (n.d.). <http://www.pilkington.com/en-gb/uk/automotive/original-equipment/automotive-overview> (accessed July 21, 2018).
- [19] T. Sun, L. Feng, X. Gao, L. Jiang, Bioinspired Surfaces with Special Wettability, Acc. Chem. Res. 38 (2005) 644–652. <https://doi.org/10.1021/ar040224c>.
- [20] O. Pedersen, T.D. Colmer, Physical gills prevent drowning of many wetland insects, spiders and plants, Journal of Experimental Biology. 215 (2012) 705–709.
<https://doi.org/10.1242/jeb.065128>.
- [21] T. Onda, S. Shibuichi, N. Satoh, K. Tsujii, Super-Water-Repellent Fractal Surfaces, Langmuir. 12 (1996) 2125–2127. <https://doi.org/10.1021/la950418o>.
- [22] T. Nishino, M. Meguro, K. Nakamae, M. Matsushita, Y. Ueda, The Lowest Surface Free Energy Based on -CF₃ Alignment, LANGMUIR. 15 (1999) 4321–4323.
- [23] C.-H. Xue, S.-T. Jia, J. Zhang, J.-Z. Ma, Large-area fabrication of superhydrophobic surfaces for practical applications: an overview, Sci. Technol. Adv. Mater. 11 (2010) 033002.
<https://doi.org/10.1088/1468-6996/11/3/033002>.
- [24] N. Menga, R. Di Mundo, G. Carbone, Soft blasting of fluorinated polymers: The easy way to superhydrophobicity, Materials & Design. 121 (2017) 414–420.
<https://doi.org/10.1016/j.matdes.2017.02.074>.
- [25] Mechanically robust superhydrophobic porous anodized AA5083 for marine corrosion protection | Elsevier Enhanced Reader, (n.d.).
<https://doi.org/10.1016/j.corsci.2019.06.031>.
- [26] H. Wang, D. Dai, X. Wu, Fabrication of superhydrophobic surfaces on aluminum, Applied Surface Science. 254 (2008) 5599–5601. <https://doi.org/10.1016/j.apsusc.2008.03.004>.
- [27] A.-M. Kietzig, S.G. Hatzikiriakos, P. Englezos, Patterned Superhydrophobic Metallic Surfaces, Langmuir. 25 (2009) 4821–4827. <https://doi.org/10.1021/la8037582>.
- [28] F. Chen, D. Zhang, Q. Yang, J. Yong, G. Du, J. Si, F. Yun, X. Hou, Bioinspired Wetting Surface via Laser Microfabrication, ACS Appl. Mater. Interfaces. 5 (2013) 6777–6792.
<https://doi.org/10.1021/am401677z>.
- [29] S.A. Mahadik, M.S. Kavale, S.K. Mukherjee, A.V. Rao, Transparent Superhydrophobic silica coatings on glass by sol–gel method, Applied Surface Science. 257 (2010) 333–339.
<https://doi.org/10.1016/j.apsusc.2010.06.062>.

- [30] J.-D. Brassard, D.K. Sarkar, J. Perron, Fluorine Based Superhydrophobic Coatings, *Applied Sciences*. 2 (2012) 453–464. <https://doi.org/10.3390/app2020453>.
- [31] G.R.J. Artus, S. Seeger, Scale-Up of a Reaction Chamber for Superhydrophobic Coatings Based on Silicone Nanofilaments, *Ind. Eng. Chem. Res.* 51 (2012) 2631–2636. <https://doi.org/10.1021/ie202129z>.
- [32] www.neverwet.com, NeverWet Partners & Product Uses | Toilet Brushes, Clothing, Covers & More, (n.d.). <https://www.neverwet.com/applications/partner-product-uses.php> (accessed May 30, 2020).
- [33] GLASS PRO, (n.d.). <https://hendlex.com/my-product/glass-pro/> (accessed February 8, 2021).
- [34] Super Hydrophobic Nano Coating Spray Protects Auto Windshield Glass, Superhydrophobic Nano-Coating Expert. (n.d.). <https://ultrahydrophobiccoating.com/product/super-hydrophobic-nano-coating-spray-protects-auto-windshield-glass-car-glass/> (accessed February 8, 2021).
- [35] International Convention on the Control of Harmful Anti-fouling Systems on Ships (AFS), (n.d.). [http://www.imo.org/en/About/Conventions/ListOfConventions/Pages/International-Convention-on-the-Control-of-Harmful-Anti-fouling-Systems-on-Ships-\(AFS\).aspx](http://www.imo.org/en/About/Conventions/ListOfConventions/Pages/International-Convention-on-the-Control-of-Harmful-Anti-fouling-Systems-on-Ships-(AFS).aspx) (accessed May 29, 2020).
- [36] Health and Safety Executive, RR1112 - Summary of evidence – solvent-based hydrophobic coatings and risks for acute respiratory toxicity, (2017). <http://www.hse.gov.uk/research/rrhtm/rr1112.htm> (accessed June 19, 2018).
- [37] X. Tian, T. Verho, R.H.A. Ras, Moving superhydrophobic surfaces toward real-world applications, *Science*. 352 (2016) 142–143. <https://doi.org/10.1126/science.aaf2073>.
- [38] T. Verho, C. Bower, P. Andrew, S. Franssila, O. Ikkala, R.H.A. Ras, Mechanically Durable Superhydrophobic Surfaces, *Advanced Materials*. 23 (2011) 673–678. <https://doi.org/10.1002/adma.201003129>.
- [39] L. Zhai, M.C. Berg, F.Ç. Cebeci, Y. Kim, J.M. Milwid, M.F. Rubner, R.E. Cohen, Patterned Superhydrophobic Surfaces: Toward a Synthetic Mimic of the Namib Desert Beetle, *Nano Lett.* 6 (2006) 1213–1217. <https://doi.org/10.1021/nl060644q>.
- [40] S. Xing, R.S. Harake, T. Pan, Droplet-driven transports on superhydrophobic-patterned surface microfluidics, *Lab Chip*. 11 (2011) 3642–3648. <https://doi.org/10.1039/C1LC20390H>.
- [41] D. Tian, Y. Song, L. Jiang, Patterning of controllable surface wettability for printing techniques, *Chem. Soc. Rev.* 42 (2013) 5184–5209. <https://doi.org/10.1039/C3CS35501B>.
- [42] P.Q.M. Nguyen, L.-P. Yeo, B.-K. Lok, Y.-C. Lam, Patterned Surface with Controllable Wettability for Inkjet Printing of Flexible Printed Electronics, *ACS Appl. Mater. Interfaces*. 6 (2014) 4011–4016. <https://doi.org/10.1021/am4054546>.
- [43] S.K. Karunakaran, G.M. Arumugam, W. Yang, S. Ge, S.N. Khan, X. Lin, G. Yang, Recent progress in inkjet-printed solar cells, *J. Mater. Chem. A*. 7 (2019) 13873–13902. <https://doi.org/10.1039/C9TA03155C>.

- [44] A. Ellison, I.A. Cornejo, Glass Substrates for Liquid Crystal Displays, *International Journal of Applied Glass Science*. 1 (2010) 87–103.
<https://doi.org/https://doi.org/10.1111/j.2041-1294.2010.00009.x>.
- [45] S. Garner, S. Glaesemann, X. Li, Ultra-slim flexible glass for roll-to-roll electronic device fabrication, *Appl. Phys. A*. 116 (2014) 403–407. <https://doi.org/10.1007/s00339-014-8468-2>.
- [46] M.L. Crozier, A.N. Brunton, A. Abbas, J.W. Bowers, P.M. Kaminski, J.M. Walls, J.D. Shephard, One step thin-film PV interconnection process using laser and inkjet, in: 2013 IEEE 39th Photovoltaic Specialists Conference (PVSC), 2013: pp. 3411–3415.
<https://doi.org/10.1109/PVSC.2013.6745181>.
- [47] K. Gesheva, T. Ivanova, G. Bodurov, I.M. Szilágyi, N. Justh, O. Kéri, S. Boyadjiev, D. Nagy, M. Aleksandrova, Technologies for deposition of transition metal oxide thin films: application as functional layers in “Smart windows” and photocatalytic systems, *J. Phys.: Conf. Ser.* 682 (2016) 012011. <https://doi.org/10.1088/1742-6596/682/1/012011>.
- [48] Y. Paz, Z. Luo, L. Rabenberg, A. Heller, Photooxidative self-cleaning transparent titanium dioxide films on glass, *Journal of Materials Research*. 10 (1995) 2842–2848.
<https://doi.org/10.1557/JMR.1995.2842>.
- [49] R.A. Alawajji, Fabrication of transparent superhydrophobic polytetrafluoroethylene coating, *Applied Surface Science*. 444 (2018) 208–215.
- [50] W. Wang, Y.-W. Su, C. Chang, Inkjet printed chalcopyrite $\text{CuIn}_x\text{Ga}_{1-x}\text{Se}_2$ thin film solar cells, *Solar Energy Materials and Solar Cells*. 95 (2011) 2616–2620.
<https://doi.org/10.1016/j.solmat.2011.05.011>.
- [51] Alberto Pique, Douglas Chrisey, *Direct-Write Technologies for Rapid Prototyping Applications - 1st Edition*, Academic Press, 2001.
- [52] Hutchings, Ian, *Inkjet Technology for Digital Fabrication*, Wiley.Com. (n.d.).
<https://www.wiley.com/en-gb/Inkjet+Technology+for+Digital+Fabrication-p-9780470681985> (accessed August 27, 2018).
- [53] K.K.B. Hon, L. Li, I.M. Hutchings, Direct writing technology—Advances and developments, *CIRP Annals*. 57 (2008) 601–620. <https://doi.org/10.1016/j.cirp.2008.09.006>.
- [54] Y. Shams, *Designing a Hybrid Inkjet and Laser Manufacturing System for the Digital and Non-Contact Fabrication of Emerging Nanotechnology Based Devices*, Thesis, University of Cambridge, 2019. <https://doi.org/10.17863/CAM.40169>.
- [55] J.A. Lewis, G.M. Gratson, Direct writing in three dimensions, *Materials Today*. 7 (2004) 32–39. [https://doi.org/10.1016/S1369-7021\(04\)00344-X](https://doi.org/10.1016/S1369-7021(04)00344-X).
- [56] *Electrochemical Micromachining for Nanofabrication, MEMS and Nanotechnology*, Elsevier, 2015. <https://doi.org/10.1016/C2014-0-00027-5>.
- [57] *Functional and Industrial Print to 2022 | Market Reports | Smithers Pira*, (n.d.).
<https://www.smitherspira.com/industry-market-reports/printing/functional-and-industrial-print-to-2022> (accessed August 21, 2018).
- [58] Pvnanocell, *PVNanocell: Mass Production of Printed Electronics Made Possible With Conductive Digital Inkjet Technology*, PVNanocell. (2015).

- <http://pvnanocell.blogspot.com/2015/11/printed-electronics.html> (accessed October 10, 2020).
- [59] (8) Lasersonic® LIFT Process for Large Area Digital Printing, ResearchGate. (n.d.). https://www.researchgate.net/publication/270225895_LasersonicR_LIFT_Process_for_Large_Area_Digital_Printing (accessed April 30, 2020).
 - [60] H. Ujiie, *Digital Printing of Textiles*, Woodhead Publishing, 2006.
 - [61] W. Zapka, Pros and Cons of Inkjet Technology in Industrial Inkjet Printing, in: *Handbook of Industrial Inkjet Printing*, John Wiley & Sons, Ltd, 2017: pp. 1–6. <https://doi.org/10.1002/9783527687169.ch1>.
 - [62] T.H. Maiman, Stimulated Optical Radiation in Ruby, *Nature*. 187 (1960) 493–494. <https://doi.org/10.1038/187493a0>.
 - [63] R.W. Ryan, R.F. Spetzler, M.C. Preul, Aura of technology and the cutting edge: a history of lasers in neurosurgery, *Neurosurgical Focus*. 27 (2009) E6. <https://doi.org/10.3171/2009.6.FOCUS09125>.
 - [64] C.K.N. Patel, Continuous-Wave Laser Action on Vibrational-Rotational Transitions of $\text{C}\{\mathrm{O}\}_{2}$, *Phys. Rev.* 136 (1964) A1187–A1193. <https://doi.org/10.1103/PhysRev.136.A1187>.
 - [65] J.G. Siekman, Cutting of thin metal films with a CO₂-gas laser beam, *Microelectronics Reliability*. 7 (1968) 305-306, IN9-IN12, 307-311. [https://doi.org/10.1016/0026-2714\(68\)90117-0](https://doi.org/10.1016/0026-2714(68)90117-0).
 - [66] Laser Market Data, Optech Consulting. (n.d.). <http://optech-consulting.com/laser-market-data/> (accessed February 8, 2021).
 - [67] P. Balling, J. Schou, Femtosecond-laser ablation dynamics of dielectrics: basics and applications for thin films, *Rep. Prog. Phys.* 76 (2013) 036502. <https://doi.org/10.1088/0034-4885/76/3/036502>.
 - [68] C.V. Shank, Generation of Ultrashort Optical Pulses, in: W. Kaiser (Ed.), *Ultrashort Laser Pulses and Applications*, Springer, Berlin, Heidelberg, 1988: pp. 5–34. https://doi.org/10.1007/978-3-662-02546-8_2.
 - [69] OSA | Fiber lasers and their applications [Invited], (n.d.). <https://www.osapublishing.org/ao/abstract.cfm?uri=ao-53-28-6554> (accessed February 8, 2021).
 - [70] Four reasons to choose fiber lasers, *Industrial Laser Solutions*. (2017). <https://www.industrial-lasers.com/home/article/16490241/four-reasons-to-choose-fiber-lasers> (accessed February 8, 2021).
 - [71] A. Temmler, E. Willenborg, K. Wissenbach, Laser polishing, in: *Laser Applications in Microelectronic and Optoelectronic Manufacturing (LAMOM) XVII*, International Society for Optics and Photonics, 2012: p. 82430W. <https://doi.org/10.1117/12.906001>.
 - [72] V.P. Veiko, G.V. Odintsova, M.Y. Gazizova, Y.Y. Karlagina, S.S. Manokhin, R.M. Yatsuk, S.D. Vasilkov, Y.R. Kolobov, The influence of laser micro- and nanostructuring on the wear resistance of Grade-2 titanium surface, *Laser Phys.* 28 (2018) 086002. <https://doi.org/10.1088/1555-6611/aac05a>.

- [73] D.V. Ta, A. Dunn, T.J. Wasley, R.W. Kay, J. Stringer, P.J. Smith, C. Connaughton, J.D. Shephard, Nanosecond laser textured superhydrophobic metallic surfaces and their chemical sensing applications, *Applied Surface Science*. 357 (2015) 248–254. <https://doi.org/10.1016/j.apsusc.2015.09.027>.
- [74] M.F. Ashby, K.E. Easterling, The transformation hardening of steel surfaces by laser beams—I. Hypo-eutectoid steels, *Acta Metallurgica*. 32 (1984) 1935–1948. [https://doi.org/10.1016/0001-6160\(84\)90175-5](https://doi.org/10.1016/0001-6160(84)90175-5).
- [75] R. Singh, D. Kumar, S.K. Mishra, S.K. Tiwari, Laser cladding of Stellite 6 on stainless steel to enhance solid particle erosion and cavitation resistance, *Surface and Coatings Technology*. 251 (2014) 87–97. <https://doi.org/10.1016/j.surfcoat.2014.04.008>.
- [76] Pilkington Optiwhite™, (n.d.). <http://www.pilkington.com/en-gb/uk/products/product-categories/special-applications/pilkington-optiwhite> (accessed February 15, 2021).
- [77] J.N. Israelachvili, 17 - Adhesion and Wetting Phenomena, in: *Intermolecular and Surface Forces* (Third Edition), Academic Press, San Diego, 2011: pp. 415–467. <https://doi.org/10.1016/B978-0-12-375182-9.10017-X>.
- [78] R.N. Wenzel, Resistance of solid surfaces to wetting by water, *Ind. Eng. Chem.* 28 (1936) 988–994. <https://doi.org/10.1021/ie50320a024>.
- [79] R.W. Lloyd, *Laser Generation and Applications of Micron and Submicron Scale Features on Metals*, [Thesis]. Manchester, UK: The University of Manchester; 2011. (2011). <https://www.escholar.manchester.ac.uk/uk-ac-man-scw:121291> (accessed August 5, 2017).
- [80] U. Trdan, M. Hočevár, P. Gregorčič, Transition from superhydrophilic to superhydrophobic state of laser textured stainless steel surface and its effect on corrosion resistance, *Corrosion Science*. 123 (2017) 21–26. <https://doi.org/10.1016/j.corsci.2017.04.005>.
- [81] M. Zhang, S. Feng, L. Wang, Y. Zheng, Lotus effect in wetting and self-cleaning, *Biotribology*. 5 (2016) 31–43. <https://doi.org/10.1016/j.biotri.2015.08.002>.
- [82] A.F. Stalder, G. Kulik, D. Sage, L. Barbieri, P. Hoffmann, A snake-based approach to accurate determination of both contact points and contact angles, *Colloids and Surfaces A: Physicochemical and Engineering Aspects*. 286 (2006) 92–103. <https://doi.org/10.1016/j.colsurfa.2006.03.008>.
- [83] M. Malinauskas, A. Žukauskas, S. Hasegawa, Y. Hayasaki, V. Mizeikis, R. Buividas, S. Juodkazis, Ultrafast laser processing of materials: from science to industry, *Light: Science & Applications*. 5 (2016) e16133–e16133. <https://doi.org/10.1038/lsa.2016.133>.
- [84] Krste Pangovski, Temporal pulse design and analysis of silicon ablation using advanced pulse shaping and digital holography in the nanosecond domain, PhD Thesis, University of Cambridge, 2014.
- [85] W. Steen, *Laser Material Processing*, 3rd ed., Springer-Verlag, London, 2003. <https://doi.org/10.1007/978-1-4471-3752-8>.
- [86] Refractive index of Fe (Iron) - Johnson, (n.d.). <https://refractiveindex.info/?shelf=main&book=Fe&page=Johnson> (accessed April 7, 2020).

- [87] G. Wang, C. Wang, Y. Zhang, X. Xiong, X. Tang, The absorptivity of low-carbon steel under Nd:YAG CW laser loading, in: XVII International Symposium on Gas Flow, Chemical Lasers, and High-Power Lasers, International Society for Optics and Photonics, 2009: p. 71311N. <https://doi.org/10.1117/12.816999>.
- [88] D.W. Bäuerle, Laser Processing and Chemistry, 4th ed., Springer-Verlag, Berlin Heidelberg, 2011.
- [89] A Study Optical and Physical Properties of Soda Lime Silica Glass Doped with V2O5 | Alsalam university Journal, (n.d.). <http://alsalam.edu.sd/journal/index.php/suj/article/view/50> (accessed May 29, 2020).
- [90] S. Nolte, Micromachining with Femtosecond Lasers Short Course, (n.d.). <https://spie.org/education/courses/coursedetail/SC743?f=Online&SSO=1> (accessed May 29, 2020).
- [91] L.V. Keldysh, Ionization in the field of a strong electromagnetic wave, Sov. Phys. JETP. 20 (1965) 1307–1314.
- [92] B.C. Stuart, M.D. Feit, S. Herman, A.M. Rubenchik, B.W. Shore, M.D. Perry, Nanosecond-to-femtosecond laser-induced breakdown in dielectrics, Phys. Rev. B. 53 (1996) 1749–1761. <https://doi.org/10.1103/PhysRevB.53.1749>.
- [93] K. Sugioka, M. Meunier, A. Piqué, eds., Laser Precision Microfabrication, Springer-Verlag, Berlin Heidelberg, 2010. <https://doi.org/10.1007/978-3-642-10523-4>.
- [94] S. Nolte, C. Momma, H. Jacobs, A. Tünnermann, B.N. Chichkov, B. Wellegehausen, H. Welling, Ablation of metals by ultrashort laser pulses, J. Opt. Soc. Am. B, JOSAB. 14 (1997) 2716–2722. <https://doi.org/10.1364/JOSAB.14.002716>.
- [95] P.T. Mannion, J. Magee, E. Coyne, G.M. O'Connor, T.J. Glynn, The effect of damage accumulation behaviour on ablation thresholds and damage morphology in ultrafast laser micro-machining of common metals in air, Applied Surface Science. 233 (2004) 275–287. <https://doi.org/10.1016/j.apsusc.2004.03.229>.
- [96] D.P. Adams, V.C. Hodges, D.A. Hirschfeld, M.A. Rodriguez, J.P. McDonald, P.G. Kotula, Nanosecond pulsed laser irradiation of stainless steel 304L: Oxide growth and effects on underlying metal, Surface and Coatings Technology. 222 (2013) 1–8. <https://doi.org/10.1016/j.surfcoat.2012.12.044>.
- [97] D.R. Paschotta, Gaussian Beams, (n.d.). https://www.rp-photonics.com/gaussian_beams.html (accessed March 1, 2021).
- [98] F. Korte, J. Serbin, J. Koch, A. Egbert, C. Fallnich, A. Ostendorf, B.N. Chichkov, Towards nanostructuring with femtosecond laser pulses, Appl Phys A. 77 (2003) 229–235. <https://doi.org/10.1007/s00339-003-2110-z>.
- [99] R.F.W. Herrmann, J. Gerlach, E.E.B. Campbell, Ultrashort pulse laser ablation of silicon: an MD simulation study, Appl Phys A. 66 (1998) 35–42. <https://doi.org/10.1007/s003390050634>.
- [100] L.V. Zhigilei, Z. Lin, D.S. Ivanov, Atomistic Modeling of Short Pulse Laser Ablation of Metals: Connections between Melting, Spallation, and Phase Explosion, J. Phys. Chem. C. 113 (2009) 11892–11906. <https://doi.org/10.1021/jp902294m>.

- [101] A.H.A. Lutey, L. Romoli, Surface topography following pulsed laser texturing: Implications for adhesion and wettability, *Surf. Topogr.: Metrol. Prop.* 7 (2019) 045023. <https://doi.org/10.1088/2051-672X/ab5c82>.
- [102] H.M. van Driel, J.E. Sipe, J.F. Young, Laser-Induced Periodic Surface Structure on Solids: A Universal Phenomenon, *Phys. Rev. Lett.* 49 (1982) 1955–1958. <https://doi.org/10.1103/PhysRevLett.49.1955>.
- [103] J. Bonse, S. Höhm, S.V. Kirner, A. Rosenfeld, J. Krüger, Laser-Induced Periodic Surface Structures— A Scientific Evergreen, *IEEE Journal of Selected Topics in Quantum Electronics*. 23 (2017). <https://doi.org/10.1109/JSTQE.2016.2614183>.
- [104] R.J. Nemanich, D.K. Biegelsen, W.G. Hawkins, Aligned, coexisting liquid and solid regions in laser-annealed Si, *Phys. Rev. B*. 27 (1983) 7817–7819. <https://doi.org/10.1103/PhysRevB.27.7817>.
- [105] J. Bonse, S. Baudach, J. Krüger, W. Kautek, M. Lenzner, Femtosecond laser ablation of silicon—modification thresholds and morphology, *Appl Phys A*. 74 (2002) 19–25. <https://doi.org/10.1007/s003390100893>.
- [106] M. Ardron, N. Weston, D. Hand, A practical technique for the generation of highly uniform LIPSS, *Applied Surface Science*. 313 (2014) 123–131. <https://doi.org/10.1016/j.apsusc.2014.05.154>.
- [107] S. Faas, R. Weber, T. Graf, Heat accumulation controlled surface functionalization of stainless steel with structuring rates up to 500 mm²/s, *Procedia CIRP*. 74 (2018) 324–327. <https://doi.org/10.1016/j.procir.2018.08.125>.
- [108] M.V. Shugaev, I. Gnilitzkiy, N.M. Bulgakova, L.V. Zhigilei, Mechanism of single-pulse ablative generation of laser-induced periodic surface structures, *Phys. Rev. B*. 96 (2017) 205429. <https://doi.org/10.1103/PhysRevB.96.205429>.
- [109] A.R. de la Cruz, R. Lahoz, J. Siegel, G.F. de la Fuente, J. Solis, High speed inscription of uniform, large-area laser-induced periodic surface structures in Cr films using a high repetition rate fs laser, *Opt. Lett., OL*. 39 (2014) 2491–2494. <https://doi.org/10.1364/OL.39.002491>.
- [110] I. Gnilitzkiy, T.J.-Y. Derrien, Y. Levy, N.M. Bulgakova, T. Mocek, L. Orazi, High-speed manufacturing of highly regular femtosecond laser-induced periodic surface structures: physical origin of regularity, *Scientific Reports*. 7 (2017) 8485. <https://doi.org/10.1038/s41598-017-08788-z>.
- [111] C. Momma, B.N. Chichkov, S. Nolte, F. von Alvensleben, A. Tünnermann, H. Welling, B. Wellegehausen, Short-pulse laser ablation of solid targets, *Optics Communications*. 129 (1996) 134–142. [https://doi.org/10.1016/0030-4018\(96\)00250-7](https://doi.org/10.1016/0030-4018(96)00250-7).
- [112] B.C. Stuart, M.D. Feit, S. Herman, A.M. Rubenchik, B.W. Shore, M.D. Perry, Optical ablation by high-power short-pulse lasers, *J. Opt. Soc. Am. B, JOSAB*. 13 (1996) 459–468. <https://doi.org/10.1364/JOSAB.13.000459>.
- [113] High Power Ultrafast Laser Tangor, Amplitude. (n.d.). <https://amplitude-laser.com/produit/tangor/> (accessed April 4, 2020).

- [114] Mega-speed and precision laser micromachining, Industrial Laser Solutions. (2014). <https://www.industrial-lasers.com/micromachining/article/16484883/megaspeed-and-precision-laser-micromachining> (accessed February 3, 2021).
- [115] R.D. Loor, L. Penning, R. Slagle, Polygon Laser Scanning, *Laser Technik Journal*. 11 (2014) 32–34. <https://doi.org/10.1002/latj.201400033>.
- [116] L. Parellada-Monreal, I. Castro-Hurtado, M. Martínez-Calderón, A. Rodríguez, S.M. Olaizola, D. Gamarra, J. Lozano, G.G. Mandayo, Study of sputtered ZnO modified by Direct Laser Interference Patterning: Structural characterization and temperature simulation, *Applied Surface Science*. 441 (2018) 331–340. <https://doi.org/10.1016/j.apsusc.2018.02.031>.
- [117] A. Khan, Z. Wang, M.A. Sheikh, D.J. Whitehead, L. Li, Laser micro/nano patterning of hydrophobic surface by contact particle lens array, *Applied Surface Science*. 258 (2011) 774–779. <https://doi.org/10.1016/j.apsusc.2011.08.089>.
- [118] S. Bruening, M. Jarczyński, K. Du, et al, Large Scale Ultrafast Laser Micro Texturing with Multi-Beams, *Journal of Laser Micro/Nanoengineering. Online Journal*. 13 (2018) 254–262.
- [119] M. Bieda, C. Schmädicke, T. Roch, A. Lasagni, Ultra-Low Friction on 100Cr6-Steel Surfaces After Direct Laser Interference Patterning, *Adv. Eng. Mater.* 17 (2015) 102–108. <https://doi.org/10.1002/adem.201400007>.
- [120] Z. Wang, Q. Zhao, C. Wang, Reduction of Friction of Metals Using Laser-Induced Periodic Surface Nanostructures, *Micromachines*. 6 (2015) 1606–1616. <https://doi.org/10.3390/mi6111444>.
- [121] A. Dunn, J.V. Carstensen, K.L. Włodarczyk, E.B. Hansen, J. Gabzdyl, P.M. Harrison, J.D. Shephard, D.P. Hand, Nanosecond laser texturing for high friction applications, *Optics and Lasers in Engineering*. 62 (2014) 9–16. <https://doi.org/10.1016/j.optlaseng.2014.05.003>.
- [122] M. Duarte, A. Lasagni, R. Giovanelli, J. Narciso, E. Louis, F. Mücklich, Increasing Lubricant Film Lifetime by Grooving Periodical Patterns Using Laser Interference Metallurgy, *Advanced Engineering Materials*. 10 (2008) 554–558. <https://doi.org/10.1002/adem.200700321>.
- [123] A. San-Blas, N. Casquero, N. Pérez, M. Martínez-Calderon, L.M. Sanchez-Brea, J. Buencuerpo, S.M. Olaizola, A. Rodríguez, Polarization conversion on nanostructured metallic surfaces fabricated by LIPSS, in: U. Klotzbach, R. Kling, A. Watanabe (Eds.), *Laser-Based Micro- and Nanoprocessing XIII*, SPIE, San Francisco, United States, 2019: p. 53. <https://doi.org/10.1117/12.2506982>.
- [124] L.B. Boinovich, A.M. Emelyanenko, K.A. Emelyanenko, A.G. Domantovsky, A.A. Shiryaev, Comment on “Nanosecond laser textured superhydrophobic metallic surfaces and their chemical sensing applications” by Duong V. Ta, Andrew Dunn, Thomas J. Wasley, Robert W. Kay, Jonathan Stringer, Patrick J. Smith, Colm Connaughton, Jonathan D. Shephard (*Appl. Surf. Sci.* 357 (2015) 248–254), *Applied Surface Science*. 379 (2016) 111–113. <https://doi.org/10.1016/j.apsusc.2016.04.056>.
- [125] B. Wu, M. Zhou, J. Li, X. Ye, G. Li, L. Cai, Superhydrophobic surfaces fabricated by microstructuring of stainless steel using a femtosecond laser, *Applied Surface Science*. 256 (2009) 61–66. <https://doi.org/10.1016/j.apsusc.2009.07.061>.

- [126] A.-M. Kietziga, M.N. Mirvakilia, S. Kamalb, P. Englezosa, S.G. Hatzikiriakosa, Nanopatterned Metallic Surfaces: Their Wettability and Impact on Ice Friction, *Journal of Adhesion Science and Technology*. 25 (2011) 1293–1303. <https://doi.org/10.1163/016942411X555872>.
- [127] B. Liu, W. Wang, G. Jiang, X. Mei, Z. Wang, K. Wang, J. Cui, Study on hierarchical structured PDMS for surface super-hydrophobicity using imprinting with ultrafast laser structured models, *Applied Surface Science*. 364 (2016) 528–538. <https://doi.org/10.1016/j.apsusc.2015.12.190>.
- [128] G. Mincuzzi, L. Gemini, M. Faucon, R. Kling, Extending ultra-short pulse laser texturing over large area, *Applied Surface Science*. 386 (2016) 65–71. <https://doi.org/10.1016/j.apsusc.2016.05.172>.
- [129] C.W. Extrand, Criteria for Ultralyophobic Surfaces, *Langmuir*. 20 (2004) 5013–5018. <https://doi.org/10.1021/la036481s>.
- [130] V.D. Ta, A. Dunn, T.J. Wasley, J. Li, R.W. Kay, J. Stringer, P.J. Smith, E. Esenturk, C. Connaughton, J.D. Shephard, Laser textured superhydrophobic surfaces and their applications for homogeneous spot deposition, *Applied Surface Science*. 365 (2016) 153–159. <https://doi.org/10.1016/j.apsusc.2016.01.019>.
- [131] J. Long, M. Zhong, H. Zhang, P. Fan, Superhydrophilicity to superhydrophobicity transition of picosecond laser microstructured aluminum in ambient air, *Journal of Colloid and Interface Science*. 441 (2015) 1–9. <https://doi.org/10.1016/j.jcis.2014.11.015>.
- [132] G.-W. Römer, C. Del, R.C.J. Sipkema, M.N.W. Groenendijk, I. 't V. Huis, Ultra short pulse laser generated surface textures for anti-ice applications in aviation, in: 2009: pp. 30–37.
- [133] L.B. Boinovich, A.M. Emelyanenko, A.D. Modestov, A.G. Domantovsky, K.A. Emelyanenko, Synergistic Effect of Superhydrophobicity and Oxidized Layers on Corrosion Resistance of Aluminum Alloy Surface Textured by Nanosecond Laser Treatment, *ACS Appl. Mater. Interfaces*. 7 (2015) 19500–19508. <https://doi.org/10.1021/acsami.5b06217>.
- [134] R. Qiu, Z. Wu, J. Xu, Study of anti-corrosion and anti-wear properties on superhydrophobic aluminium alloy surfaces, *Materials Science and Technology*. 0 (2018) 1–7. <https://doi.org/10.1080/02670836.2018.1495879>.
- [135] K. Sun, H. Yang, W. Xue, A. He, D. Zhu, W. Liu, K. Adeyemi, Y. Cao, Anti-biofouling superhydrophobic surface fabricated by picosecond laser texturing of stainless steel, *Applied Surface Science*. 436 (2018) 263–267. <https://doi.org/10.1016/j.apsusc.2017.12.012>.
- [136] N. Epperlein, F. Menzel, K. Schwibbert, R. Koter, J. Bonse, J. Sameith, J. Krüger, J. Toepel, Influence of femtosecond laser produced nanostructures on biofilm growth on steel, *Applied Surface Science*. 418 (2017) 420–424. <https://doi.org/10.1016/j.apsusc.2017.02.174>.
- [137] N. Miljkovic, E.N. Wang, Condensation heat transfer on superhydrophobic surfaces, *MRS Bulletin*. 38 (2013) 397–406. <https://doi.org/10.1557/mrs.2013.103>.
- [138] S. Ye, Q. Cao, Q. Wang, T. Wang, Q. Peng, A highly efficient, stable, durable, and recyclable filter fabricated by femtosecond laser drilling of a titanium foil for oil-water separation, *Scientific Reports*. 6 (2016) 37591. <https://doi.org/10.1038/srep37591>.

- [139] TresClean | Home, (n.d.). <https://www.tresclean.eu/> (accessed June 23, 2020).
- [140] Laser for mass production of functionalised metallic surfaces, Laser4surf. (n.d.). <https://www.laser4surf.eu/> (accessed June 23, 2020).
- [141] B.N. Chichkov, C. Momma, S. Nolte, F. von Alvensleben, A. Tünnermann, Femtosecond, picosecond and nanosecond laser ablation of solids, *Appl. Phys. A*. 63 (1996) 109–115. <https://doi.org/10.1007/BF01567637>.
- [142] Nano to pico to femto: Pulse widths for optimal laser micromachining outcomes, Industrial Laser Solutions. (2017). <https://www.industrial-lasers.com/micromachining/article/16485073/nano-to-pico-to-femto-pulse-widths-for-optimal-laser-micromachining-outcomes> (accessed February 4, 2021).
- [143] D. Metzner, M. Olbrich, P. Lickschat, A. Horn, S. Weißmantel, Experimental and Theoretical Determination of the Effective Penetration Depth of Ultrafast Laser Radiation in Stainless Steel, *Lasers Manuf. Mater. Process.* 7 (2020) 478–495. <https://doi.org/10.1007/s40516-020-00129-9>.
- [144] P. Gregorčič, B. Šetina-Batič, M. Hočevár, Controlling the stainless steel surface wettability by nanosecond direct laser texturing at high fluences, *Appl. Phys. A*. 123 (2017) 766. <https://doi.org/10.1007/s00339-017-1392-5>.
- [145] F.D. Niso, C. Gaudiuso, T. Sibillano, F.P. Mezzapesa, A. Ancona, P.M. Lugarà, Role of heat accumulation on the incubation effect in multi-shot laser ablation of stainless steel at high repetition rates, *Opt. Express*, OE. 22 (2014) 12200–12210. <https://doi.org/10.1364/OE.22.012200>.
- [146] B. Neuenschwander, B. Jaeggi, M. Schmid, A. Dommann, A. Neels, T. Bandi, G. Hennig, Factors controlling the incubation in the application of ps laser pulses on copper and iron surfaces, in: *Laser Applications in Microelectronic and Optoelectronic Manufacturing (LAMOM) XVIII*, International Society for Optics and Photonics, 2013: p. 86070D. <https://doi.org/10.1117/12.2004136>.
- [147] S.K. Lawrence, D.P. Adams, D.F. Bahr, N.R. Moody, Environmental resistance of oxide tags fabricated on 304L stainless steel via nanosecond pulsed laser irradiation, *Surface and Coatings Technology*. 285 (2016) 87–97. <https://doi.org/10.1016/j.surfcoat.2015.11.021>.
- [148] M. Gomez-Aranzadi, N. Casquero, M. Martínez-Calderon, A. San Blas, S. Olaizola, A. Rodríguez, Innovative method to enhance the control over the fabrication of LIPSS on metallic surfaces, 2019.
- [149] J. Schille, L. Schneider, P. Lickschat, U. Loeschner, R. Ebert, H. Exner, High-pulse repetition frequency ultrashort pulse laser processing of copper, *Journal of Laser Applications*. 27 (2015) S28007. <https://doi.org/10.2351/1.4906482>.
- [150] High-power ultrafast Ytterbium (1 μ m) - Active Fiber Systems GmbH in Jena, Active Fiber Systems GmbH. (n.d.). <https://www.afs-jena.de/products/high-power-ultrafast-ytterbium/> (accessed February 12, 2021).
- [151] K. Itoh, W. Watanabe, S. Nolte, C.B. Schaffer, Ultrafast Processes for Bulk Modification of Transparent Materials, *MRS Bulletin*. 31 (2006) 620–625. <https://doi.org/10.1557/mrs2006.159>.

- [152] R.E. Samad, N.D. Vieira, Geometrical method for determining the surface damage threshold for femtosecond laser pulses, *Laser Phys.* 16 (2006) 336–339. <https://doi.org/10.1134/S1054660X06020228>.
- [153] P.R. Herman, R. Marjoribanks, A. Oetl, Burst-ultrafast laser machining method, US6552301B2, 2003. <https://patents.google.com/patent/US6552301B2/en> (accessed February 10, 2021).
- [154] J.J. Azkona, J.J. Azkona, M. Gómez-Aranzadi, M. Gómez-Aranzadi, A. Rodriguez, A. Rodriguez, T. Morlanes, J.L. de la Peña, S.M. Olaizola, S.M. Olaizola, Femtosecond laser fabrication of monolithic double volume phase-gratings in glass, *Opt. Express*, OE. 28 (2020) 29054–29063. <https://doi.org/10.1364/OE.402275>.
- [155] H. Ma, R.A. Zakoldaev, A. Rudenko, M.M. Sergeev, V.P. Veiko, T.E. Itina, Well-controlled femtosecond laser inscription of periodic void structures in porous glass for photonic applications, *Opt. Express*, OE. 25 (2017) 33261–33270. <https://doi.org/10.1364/OE.25.033261>.
- [156] R. Knappe, Applications of picosecond lasers and pulse-bursts in precision manufacturing, in: *Laser Applications in Microelectronic and Optoelectronic Manufacturing (LAMOM) XVII*, SPIE, 2012: pp. 96–102. <https://doi.org/10.1117/12.913626>.
- [157] C. Moorhouse, Advantages of Picosecond Laser Machining for Cutting-Edge Technologies, *Physics Procedia*. 41 (2013) 381–388. <https://doi.org/10.1016/j.phpro.2013.03.091>.
- [158] J. Shin, K. Nam, Groove Formation in Glass Substrate by a UV Nanosecond Laser, *Applied Sciences*. 10 (2020) 987. <https://doi.org/10.3390/app10030987>.
- [159] P. Bizi-bandoki, S. Valette, E. Audouard, S. Benayoun, Time dependency of the hydrophilicity and hydrophobicity of metallic alloys subjected to femtosecond laser irradiations, *Applied Surface Science*. 273 (2013) 399–407. <https://doi.org/10.1016/j.apsusc.2013.02.054>.
- [160] One step fabrication and characterisation of stainless steel superhydrophobic surfaces using laser ablation, *Euspen*. (n.d.). <https://www.euspen.eu/resource/one-step-fabrication-and-characterisation-of-stainless-steel-superhydrophobic-surfaces-using-laser-ablation/> (accessed December 16, 2018).
- [161] T. Min, Design & Fabrication of Super-Hydrophobic Surfaces by Laser Micro/Nanoprocessing, Thesis, 2012. <https://scholarbank.nus.edu.sg/handle/10635/43410> (accessed May 22, 2017).
- [162] L. Gemini, M. Faucon, L. Romoli, R. Kling, High throughput laser texturing of superhydrophobic surfaces on steel, in: U. Klotzbach, K. Washio, R. Kling (Eds.), 2017: p. 100921G. <https://doi.org/10.1117/12.2252649>.
- [163] Góra, Wojciech, Laser texturing of superhydrophobic surfaces on stainless steel: influence of storage conditions on the anti-wetting transition, in: *Proceedings of Lasers in Manufacturing 2019*, Munch, Germany, n.d.
- [164] A. Samanta, Q. Wang, S.K. Shaw, H. Ding, Roles of chemistry modification for laser textured metal alloys to achieve extreme surface wetting behaviors, *Materials & Design*. 192 (2020) 108744. <https://doi.org/10.1016/j.matdes.2020.108744>.

- [165] Y. Tian, L. Jiang, Intrinsically robust hydrophobicity, *Nature Materials*. 12 (2013) 291–292. <https://doi.org/10.1038/nmat3610>.
- [166] C.-V. Ngo, D.-M. Chun, Control of laser-ablated aluminum surface wettability to superhydrophobic or superhydrophilic through simple heat treatment or water boiling post-processing, *Applied Surface Science*. 435 (2018) 974–982. <https://doi.org/10.1016/j.apsusc.2017.11.185>.
- [167] M.M. Gentleman, J.A. Ruud, Role of Hydroxyls in Oxide Wettability, *Langmuir*. 26 (2010) 1408–1411. <https://doi.org/10.1021/la903029c>.
- [168] D.-M. Chun, C.-V. Ngo, K.-M. Lee, Fast fabrication of superhydrophobic metallic surface using nanosecond laser texturing and low-temperature annealing, *CIRP Annals - Manufacturing Technology*. 1 (2016) 519–522. <https://doi.org/10.1016/j.cirp.2016.04.019>.
- [169] C. Zhang, S. Li, L. Wang, T. Wu, S. Peng, Studies on the decomposing carbon dioxide into carbon with oxygen-deficient magnetite, *Materials Chemistry and Physics*. 62 (2000) 52–61. [https://doi.org/10.1016/S0254-0584\(99\)00168-6](https://doi.org/10.1016/S0254-0584(99)00168-6).
- [170] Y. Wan, C. Xi, H. Yu, Fabrication of self-cleaning superhydrophobic surface on stainless steel by nanosecond laser, *Mater. Res. Express*. 5 (2018) 115002. <https://doi.org/10.1088/2053-1591/aadbf2>.
- [171] D.J. Miller, M.C. Biesinger, N.S. McIntyre, Interactions of CO₂ and CO at fractional atmosphere pressures with iron and iron oxide surfaces: one possible mechanism for surface contamination?, *Surface and Interface Analysis*. 33 (2002) 299–305. <https://doi.org/10.1002/sia.1188>.
- [172] D.J. Preston, N. Miljkovic, J. Sack, R. Enright, J. Queeney, E.N. Wang, Effect of hydrocarbon adsorption on the wettability of rare earth oxide ceramics, *Appl. Phys. Lett.* 105 (2014) 011601. <https://doi.org/10.1063/1.4886410>.
- [173] C. Mücksch, C. Rösch, C. Müller–Renno, C. Ziegler, H.M. Urbassek, Consequences of Hydrocarbon Contamination for Wettability and Protein Adsorption on Graphite Surfaces, *J. Phys. Chem. C*. 119 (2015) 12496–12501. <https://doi.org/10.1021/acs.jpcc.5b02948>.
- [174] R.A. Erb, Wettability of Metals under Continuous Condensing Conditions, *J. Phys. Chem.* 69 (1965) 1306–1309. <https://doi.org/10.1021/j100888a035>.
- [175] P. Liu, L. Cao, W. Zhao, Y. Xia, W. Huang, Z. Li, Insights into the superhydrophobicity of metallic surfaces prepared by electrodeposition involving spontaneous adsorption of airborne hydrocarbons, *Applied Surface Science*. 324 (2015) 576–583. <https://doi.org/10.1016/j.apsusc.2014.10.170>.
- [176] G. Goldfinger, K.E. Johnson, Clean Surfaces: Their Preparation and Characterization for Interfacial Studies, *J. Electrochem. Soc.* 117 (1970) 411C. <https://doi.org/10.1149/1.2407351>.
- [177] J.T. Cardoso, A. Garcia-Girón, J.M. Romano, D. Huerta-Murillo, R. Jagdheesh, M. Walker, S.S. Dimov, J.L. Ocaña, Influence of ambient conditions on the evolution of wettability properties of an IR-, ns-laser textured aluminium alloy, *RSC Adv.* 7 (2017) 39617–39627. <https://doi.org/10.1039/C7RA07421B>.

- [178] S. Takeda, M. Fukawa, Y. Hayashi, K. Matsumoto, Surface OH group governing adsorption properties of metal oxide films, *Thin Solid Films*. 339 (1999) 220–224.
[https://doi.org/10.1016/S0040-6090\(98\)01152-3](https://doi.org/10.1016/S0040-6090(98)01152-3).
- [179] A.-M. Kietzig, M.N. Mirvakili, S. Kamal, P. Englezos, S.G. Hatzikiriakos, Laser-patterned super-hydrophobic pure metallic substrates: Cassie to Wenzel wetting transitions, *Journal of Adhesion Science and Technology*. 25 (2012) 2789–2809.
<https://doi.org/10.1163/016942410X549988>.
- [180] J. Long, M. Zhong, P. Fan, D. Gong, H. Zhang, Wettability conversion of ultrafast laser structured copper surface, *Journal of Laser Applications*. 27 (2015) S29107.
<https://doi.org/10.2351/1.4906477>.
- [181] C.-V. Ngo, D.-M. Chun, Fast wettability transition from hydrophilic to superhydrophobic laser-textured stainless steel surfaces under low-temperature annealing, *Applied Surface Science*. 409 (2017) 232–240. <https://doi.org/10.1016/j.apsusc.2017.03.038>.
- [182] C.-V. Ngo, D.-M. Chun, Effect of Heat Treatment Temperature on the Wettability Transition from Hydrophilic to Superhydrophobic on Laser-Ablated Metallic Surfaces, *Advanced Engineering Materials*. 20 (2018) 1701086.
<https://doi.org/10.1002/adem.201701086>.
- [183] A. He, W. Liu, W. Xue, H. Yang, Y. Cao, Nanosecond laser ablated copper superhydrophobic surface with tunable ultrahigh adhesion and its renewability with low temperature annealing, *Applied Surface Science*. 434 (2018) 120–125.
<https://doi.org/10.1016/j.apsusc.2017.10.143>.
- [184] S. Moradi, N. Hadesfandiari, S.F. Toosi, J.N. Kizhakkedathu, S.G. Hatzikiriakos, Effect of Extreme Wettability on Platelet Adhesion on Metallic Implants: From Superhydrophilicity to Superhydrophobicity, *ACS Appl. Mater. Interfaces*. 8 (2016) 17631–17641.
<https://doi.org/10.1021/acsami.6b03644>.
- [185] T.-H. Dinh, C.-V. Ngo, D.-M. Chun, Direct laser patterning for transparent superhydrophobic glass surfaces without any chemical coatings, *Appl. Phys. A*. 126 (2020) 462. <https://doi.org/10.1007/s00339-020-03653-9>.
- [186] K.M.T. Ahmmed, A.-M. Kietzig, Drag reduction on laser-patterned hierarchical superhydrophobic surfaces, *Soft Matter*. 12 (2016) 4912–4922.
<https://doi.org/10.1039/C6SM00436A>.
- [187] L. Li, B. Li, J. Dong, J. Zhang, Roles of silanes and silicones in forming superhydrophobic and superoleophobic materials, *J. Mater. Chem. A*. 4 (2016) 13677–13725.
<https://doi.org/10.1039/C6TA05441B>.
- [188] L.B. Boinovich, A.M. Emelyanenko, The behaviour of fluoro- and hydrocarbon surfactants used for fabrication of superhydrophobic coatings at solid/water interface, *Colloids and Surfaces A: Physicochemical and Engineering Aspects*. 481 (2015) 167–175.
<https://doi.org/10.1016/j.colsurfa.2015.05.003>.
- [189] M. Ruan, J.W. Wang, Q.L. Liu, F.M. Ma, Z.L. Yu, W. Feng, Y. Chen, Superhydrophobic and anti-icing properties of sol-gel prepared alumina coatings, *Russ. J. Non-Ferrous Metals*. 57 (2016) 638–645. <https://doi.org/10.3103/S1067821216060122>.

- [190] F. Guo, Z. Guo, Inspired smart materials with external stimuli responsive wettability: a review, *RSC Adv.* 6 (2016) 36623–36641. <https://doi.org/10.1039/C6RA04079A>.
- [191] J. Yong, F. Chen, Q. Yang, U. Farooq, X. Hou, Photoinduced switchable underwater superoleophobicity–superoleophilicity on laser modified titanium surfaces, *J. Mater. Chem. A* 3 (2015) 10703–10709. <https://doi.org/10.1039/C5TA01782C>.
- [192] H.-Y. Ryu, S.H. Yoon, D.-H. Han, H. Hafeez, N.R. Paluvai, C.S. Lee, J.-G. Park, Fabrication of hydrophobic/hydrophilic switchable aluminum surface using poly(N-isopropylacrylamide), *Progress in Organic Coatings* 99 (2016) 295–301. <https://doi.org/10.1016/j.porgcoat.2016.06.008>.
- [193] W.E. Delpont, J.P. Roux, The surface segregation and oxidation of chromium and palladium in high chromium stainless steel, *Corrosion Science* 26 (1986) 407–417. [https://doi.org/10.1016/0010-938X\(86\)90136-8](https://doi.org/10.1016/0010-938X(86)90136-8).
- [194] U. Çaydaş, S. Ekici, Support vector machines models for surface roughness prediction in CNC turning of AISI 304 austenitic stainless steel, *J Intell Manuf.* 23 (2012) 639–650. <https://doi.org/10.1007/s10845-010-0415-2>.
- [195] G. Attard, C. Barnes, *Surfaces*, Oxford University Press, Oxford, New York, 1998.
- [196] B. Bhushan, E.K. Her, Fabrication of Superhydrophobic Surfaces with High and Low Adhesion Inspired from Rose Petal, *Langmuir* 26 (2010) 8207–8217. <https://doi.org/10.1021/la904585j>.
- [197] Y. Lai, F. Pan, C. Xu, H. Fuchs, L. Chi, In Situ Surface-Modification-Induced Superhydrophobic Patterns with Reversible Wettability and Adhesion, *Advanced Materials* 25 (2013) 1682–1686. <https://doi.org/10.1002/adma.201203797>.
- [198] B.H. Luo, P.W. Shum, Z.F. Zhou, K.Y. Li, Preparation of hydrophobic surface on steel by patterning using laser ablation process, *Surface and Coatings Technology* 204 (2010) 1180–1185. <https://doi.org/10.1016/j.surfcoat.2009.10.043>.
- [199] R.M. Alloway, J. Mong, I.W. Jephson, M.H. Wood, M.T.L. Casford, P. Grice, S.V. Filip, I.E. Salama, C. Durkan, S.M. Clarke, Adsorption of 4-n-Nonylphenol, Carvacrol, and Ethanol onto Iron Oxide from Nonaqueous Hydrocarbon Solvents, *Langmuir* 35 (2019) 11662–11669. <https://doi.org/10.1021/acs.langmuir.9b01863>.
- [200] L.B. Boinovich, A.M. Emelyanenko, Hydrophobic materials and coatings: principles of design, properties and applications, *Russ. Chem. Rev.* 77 (2008) 583. <https://doi.org/10.1070/RC2008v077n07ABEH003775>.
- [201] A.A. Thorpe, V. Peters, J.R. Smith, T.G. Nevell, J. Tsibouklis, Poly(methylpropenoxyfluoroalkylsiloxane)s: a class of fluoropolymers capable of inhibiting bacterial adhesion onto surfaces, *Journal of Fluorine Chemistry* 104 (2000) 37–45. [https://doi.org/10.1016/S0022-1139\(00\)00225-6](https://doi.org/10.1016/S0022-1139(00)00225-6).
- [202] L. Parthier, T. Wiegell, C. Ottermann, F. Prince, Glass Substrates for Industrial Inkjet Printing Applications, in: *Handbook of Industrial Inkjet Printing*, John Wiley & Sons, Ltd, 2017: pp. 391–408. <https://doi.org/10.1002/9783527687169.ch21>.
- [203] Inkjet Technology | Fujifilm Global, (n.d.). https://www.fujifilm.com/products/graphic_systems/inkjet_technology/ (accessed August 24, 2020).

- [204] C. Rodriguez-Rivero, J.R. Castrejón-Pita, I. Hutchings, Aerodynamic effects in industrial inkjet printing, (2015). <https://doi.org/10/254482>.
- [205] N. Willis-Fox, E. Rognin, T.A. Aljohani, R. Daly, Polymer Mechanochemistry: Manufacturing Is Now a Force to Be Reckoned With, *Chem.* 4 (2018) 2499–2537. <https://doi.org/10.1016/j.chempr.2018.08.001>.
- [206] H.J.J. Staat, A. van der Bos, M. van den Berg, H. Reinten, H. Wijshoff, M. Versluis, D. Lohse, Ultrafast imaging method to measure surface tension and viscosity of inkjet-printed droplets in flight, *Exp Fluids*. 58 (2016) 2. <https://doi.org/10.1007/s00348-016-2284-8>.
- [207] H. Yoo, C. Kim, Experimental studies on formation, spreading and drying of inkjet drop of colloidal suspensions, *Colloids and Surfaces A: Physicochemical and Engineering Aspects*. 468 (2015) 234–245. <https://doi.org/10.1016/j.colsurfa.2014.12.032>.
- [208] H.-H. Lee, K.-S. Chou, K.-C. Huang, Inkjet printing of nanosized silver colloids, *Nanotechnology*. 16 (2005) 2436–2441. <https://doi.org/10.1088/0957-4484/16/10/074>.
- [209] Fundamentals of Inkjet Printing: The Science of Inkjet and Droplets | Wiley, Wiley.Com. (n.d.). <https://www.wiley.com/en-ad/Fundamentals+of+Inkjet+Printing%3A+The+Science+of+Inkjet+and+Droplets-p-9783527337859> (accessed September 9, 2020).
- [210] C. Gao, T. Xing, G. Chen, Research on micro mechanism of water-based disperse ink and optimization of driving waveform for inkjet ink, *Colloids and Surfaces A: Physicochemical and Engineering Aspects*. 606 (2020) 125237. <https://doi.org/10.1016/j.colsurfa.2020.125237>.
- [211] M. Singh, H.M. Haverinen, P. Dhagat, G.E. Jabbour, Inkjet Printing—Process and Its Applications, *Advanced Materials*. 22 (2010) 673–685. <https://doi.org/10.1002/adma.200901141>.
- [212] R. Rioboo, C. Tropea, M. Marengo, OUTCOMES FROM A DROP IMPACT ON SOLID SURFACES, *AAS*. 11 (2001). <https://doi.org/10.1615/AtomizSpr.v11.i2.40>.
- [213] Y. Sun, V. Bromberg, S. Gawande, S. Biswas, T. Singler, Transport processes associated with inkjet printing of colloidal drops for printable electronics fabrication, in: 2009 59th Electronic Components and Technology Conference, 2009: pp. 1349–1355. <https://doi.org/10.1109/ECTC.2009.5074188>.
- [214] J. Stringer, B. Derby, When the Drop Hits the Substrate, in: *Inkjet Technology for Digital Fabrication*, John Wiley & Sons, Ltd, n.d.: pp. 113–139. <https://doi.org/10.1002/9781118452943.ch5>.
- [215] X. Yu, R. Xing, Z. Peng, Y. Lin, Z. Du, J. Ding, L. Wang, Y. Han, To inhibit coffee ring effect in inkjet printing of light-emitting polymer films by decreasing capillary force, *Chinese Chemical Letters*. 30 (2019) 135–138. <https://doi.org/10.1016/j.cclet.2018.09.007>.
- [216] G. Hu, L. Yang, Z. Yang, Y. Wang, X. Jin, J. Dai, Q. Wu, S. Liu, X. Zhu, X. Wang, T.-C. Wu, R.C.T. Howe, T. Albrow-Owen, L.W.T. Ng, Q. Yang, L.G. Occhipinti, R.I. Woodward, E.J.R. Kelleher, Z. Sun, X. Huang, M. Zhang, C.D. Bain, T. Hasan, A general ink formulation of 2D crystals for wafer-scale inkjet printing, *Science Advances*. 6 (2020) eaba5029. <https://doi.org/10.1126/sciadv.aba5029>.

- [217] A. Roshanghias, M. Krivec, M. Baumgart, Sintering strategies for inkjet printed metallic traces in 3D printed electronics, *Flexible and Printed Electronics*. 2 (2017) undefined-undefined.
- [218] K.-S. Moon, H. Dong, R. Maric, S. Pothukuchi, A. Hunt, Y. Li, C.P. Wong, Thermal behavior of silver nanoparticles for low-temperature interconnect applications, *Journal of Elec Materi.* 34 (2005) 168–175. <https://doi.org/10.1007/s11664-005-0229-8>.
- [219] G. Liebel, M. Beß, Surface Pretreatment for Wettability Adjustment, in: *Handbook of Industrial Inkjet Printing*, John Wiley & Sons, Ltd, 2017: pp. 507–528. <https://doi.org/10.1002/9783527687169.ch29>.
- [220] J. Banerjee, S.H. Kim, C.G. Pantano, Elemental areal density calculation and oxygen speciation for flat glass surfaces using x-ray photoelectron spectroscopy, *Journal of Non-Crystalline Solids*. 450 (2016) 185–193. <https://doi.org/10.1016/j.jnoncrysol.2016.07.029>.
- [221] O. Sneh, S.M. George, Thermal Stability of Hydroxyl Groups on a Well-Defined Silica Surface, *J. Phys. Chem.* 99 (1995) 4639–4647. <https://doi.org/10.1021/j100013a039>.
- [222] M. Šimek, M. Černák, O. Kylián, R. Foest, D. Hegemann, R. Martini, White paper on the future of plasma science for optics and glass, *Plasma Processes and Polymers*. 16 (2019) 1700250. <https://doi.org/10.1002/ppap.201700250>.
- [223] K. Terpilowski, D. Rymuszka, Surface properties of glass plates activated by air, oxygen, nitrogen and argon plasma, *Glass Phys Chem.* 42 (2016) 535–541. <https://doi.org/10.1134/S1087659616060195>.
- [224] T. Yamamoto, M. Okubo, N. Imai, Y. Mori, Improvement on Hydrophilic and Hydrophobic Properties of Glass Surface Treated by Nonthermal Plasma Induced by Silent Corona Discharge, *Plasma Chemistry and Plasma Processing*. 24 (2004) 1–12. <https://doi.org/10.1023/B:PCPP.0000004878.61688.4d>.
- [225] T. Homola, J. Matoušek, M. Kormunda, L.Y.L. Wu, M. Černák, Plasma Treatment of Glass Surfaces Using Diffuse Coplanar Surface Barrier Discharge in Ambient Air, *Plasma Chem Plasma Process.* 33 (2013) 881–894. <https://doi.org/10.1007/s11090-013-9467-3>.
- [226] W.-K. Hsiao, G.D. Martin, I.M. Hutchings, Printing Stable Liquid Tracks on a Surface with Finite Receding Contact Angle, *Langmuir*. 30 (2014) 12447–12455. <https://doi.org/10.1021/la502490p>.
- [227] Z. Li, Y. Wang, A. Kozbial, G. Shenoy, F. Zhou, R. McGinley, P. Ireland, B. Morganstein, A. Kunkel, S.P. Surwade, L. Li, H. Liu, Effect of airborne contaminants on the wettability of supported graphene and graphite, *Nature Materials*. 12 (2013) 925–931. <https://doi.org/10.1038/nmat3709>.
- [228] B. Farshchian, J.R. Gatabi, S.M. Bernick, S. Park, G.-H. Lee, R. Droopad, N. Kim, Laser-induced superhydrophobic grid patterns on PDMS for droplet arrays formation, *Applied Surface Science*. 396 (2017) 359–365. <https://doi.org/10.1016/j.apsusc.2016.10.153>.
- [229] C.-V. Ngo, D.-M. Chun, Laser Printing of Superhydrophobic Patterns from Mixtures of Hydrophobic Silica Nanoparticles and Toner Powder, *Scientific Reports*. 6 (2016) 36735. <https://doi.org/10.1038/srep36735>.

- [230] M. Elsharkawy, T.M. Schutzius, C.M. Megaridis, Inkjet patterned superhydrophobic paper for open-air surface microfluidic devices, *Lab Chip*. 14 (2014) 1168–1175. <https://doi.org/10.1039/C3LC51248G>.
- [231] S. Nishimoto, A. Kubo, K. Nohara, X. Zhang, N. Taneichi, T. Okui, Z. Liu, K. Nakata, H. Sakai, T. Murakami, M. Abe, T. Komine, A. Fujishima, TiO₂-based superhydrophobic-superhydrophilic patterns: Fabrication via an ink-jet technique and application in offset printing, *Applied Surface Science* (1985). 255 (2009) 6221–6225. <https://doi.org/10.1016/j.apsusc.2009.01.084>.
- [232] G. Chitnis, Z. Ding, C.-L. Chang, C.A. Savran, B. Ziaie, Laser-treated hydrophobic paper: an inexpensive microfluidic platform, *Lab Chip*. 11 (2011) 1161–1165. <https://doi.org/10.1039/C0LC00512F>.
- [233] T.M. Schutzius, I.S. Bayer, G.M. Jursich, A. Das, C.M. Megaridis, Superhydrophobic-superhydrophilic binary micropatterns by localized thermal treatment of polyhedral oligomeric silsesquioxane (POSS)-silica films, *Nanoscale*. 4 (2012) 5378–5385. <https://doi.org/10.1039/c2nr30979c>.
- [234] M. Wang, Q. Liu, H. Zhang, C. Wang, L. Wang, B. Xiang, Y. Fan, C.F. Guo, S. Ruan, Laser Direct Writing of Tree-Shaped Hierarchical Cones on a Superhydrophobic Film for High-Efficiency Water Collection, *ACS Appl. Mater. Interfaces*. 9 (2017) 29248–29254. <https://doi.org/10.1021/acsami.7b08116>.
- [235] A. Ghosh, R. Ganguly, T.M. Schutzius, C.M. Megaridis, Wettability patterning for high-rate, pumpless fluid transport on open, non-planar microfluidic platforms, *Lab Chip*. 14 (2014) 1538–1550. <https://doi.org/10.1039/C3LC51406D>.
- [236] C.-M. Keum, I.-H. Lee, H.-L. Park, C. Kim, B. Lüssem, J.S. Choi, S.-D. Lee, Principle of topography-directed inkjet printing for functional micro-tracks in flexible substrates, *Journal of Applied Physics*. 121 (2017) 244902. <https://doi.org/10.1063/1.4989837>.
- [237] P. Kant, A.L. Hazel, M. Dowling, A.B. Thompson, A. Juel, Sequential deposition of microdroplets on patterned surfaces, *Soft Matter*. 14 (2018) 8709–8716. <https://doi.org/10.1039/C8SM01373J>.
- [238] F.F. Jackson, K.J. Kubiak, M.C.T. Wilson, M. Molinari, V. Stetsyuk, Droplet Misalignment Limit for Inkjet Printing into Cavities on Textured Surfaces, *Langmuir*. 35 (2019) 9564–9571. <https://doi.org/10.1021/acs.langmuir.9b00649>.
- [239] J.B. Szczech, C.M. Megaridis, D.R. Gamota, Jie Zhang, Fine-line conductor manufacturing using drop-on demand PZT printing technology, *IEEE Transactions on Electronics Packaging Manufacturing*. 25 (2002) 26–33. <https://doi.org/10.1109/TEPM.2002.1000480>.
- [240] FujiFilm, DIMATIX DMP-2800 SERIES USER MANUAL, (2006). <https://www.manualslib.com/manual/1238531/Dimatix-Dmp-2800-Series.html> (accessed October 3, 2020).
- [241] W. Shen, X. Zhang, Q. Huang, Q. Xu, W. Song, Preparation of solid silver nanoparticles for inkjet printed flexible electronics with high conductivity, *Nanoscale*. 6 (2014) 1622–1628. <https://doi.org/10.1039/C3NR05479A>.

- [242] S.B. Fuller, E.J. Wilhelm, J.M. Jacobson, Ink-jet printed nanoparticle microelectromechanical systems, *Journal of Microelectromechanical Systems*. 11 (2002) 54–60. <https://doi.org/10.1109/84.982863>.
- [243] N.R. Bieri, J. Chung, S.E. Haferl, D. Poulikakos, C.P. Grigoropoulos, Microstructuring by printing and laser curing of nanoparticle solutions, *Appl. Phys. Lett.* 82 (2003) 3529–3531. <https://doi.org/10.1063/1.1575502>.
- [244] M.Y. Chuang, Inkjet Printing of Ag Nanoparticles using Dimatix Inkjet Printer, No 2, *Protocols and Reports*. (2017). https://repository.upenn.edu/scn_protocols/40.
- [245] D. Ito, K. Masuko, B.A. Weintraub, L.C. McKenzie, J.E. Hutchison, Convenient preparation of ITO nanoparticles inks for transparent conductive thin films, *J Nanopart Res.* 14 (2012) 1274. <https://doi.org/10.1007/s11051-012-1274-x>.
- [246] Cambridge Graphene, (n.d.). <http://www.cambridgegraphene.com/#graphinks> (accessed August 24, 2020).
- [247] R.P. Tortorich, J.-W. Choi, Inkjet Printing of Carbon Nanotubes, *Nanomaterials (Basel)*. 3 (2013) 453–468. <https://doi.org/10.3390/nano3030453>.
- [248] X. Fan, W. Nie, H. Tsai, N. Wang, H. Huang, Y. Cheng, R. Wen, L. Ma, F. Yan, Y. Xia, PEDOT:PSS for Flexible and Stretchable Electronics: Modifications, Strategies, and Applications, *Advanced Science*. 6 (2019) 1900813. <https://doi.org/10.1002/advs.201900813>.
- [249] L. Stepien, A. Roch, R. Tkachov, B. Leupolt, L. Han, N. van Ngo, C. Leyens, Thermal operating window for PEDOT:PSS films and its related thermoelectric properties, *Synthetic Metals*. 225 (2017) 49–54. <https://doi.org/10.1016/j.synthmet.2016.11.017>.
- [250] D. Jang, D. Kim, B. Lee, S. Kim, M. Kang, D. Min, J. Moon, Nanosized Glass Frit as an Adhesion Promoter for Ink-Jet Printed Conductive Patterns on Glass Substrates Annealed at High Temperatures, *Advanced Functional Materials*. 18 (2008) 2862–2868. <https://doi.org/10.1002/adfm.200800238>.
- [251] S. Jeong, H.C. Song, W.W. Lee, Y. Choi, S.S. Lee, B.-H. Ryu, Combined Role of Well-Dispersed Aqueous Ag Ink and the Molecular Adhesive Layer in Inkjet Printing the Narrow and Highly Conductive Ag Features on a Glass Substrate, *J. Phys. Chem. C*. 114 (2010) 22277–22283. <https://doi.org/10.1021/jp106994t>.
- [252] J.S.R. Wheeler, S.G. Yeates, *Polymers in Inkjet Printing*, in: *Fundamentals of Inkjet Printing*, John Wiley & Sons, Ltd, 2015: pp. 117–140. <https://doi.org/10.1002/9783527684724.ch5>.
- [253] S.D. Hoath, S. Jung, W.-K. Hsiao, I.M. Hutchings, How PEDOT:PSS solutions produce satellite-free inkjets, *Organic Electronics*. 13 (2012) 3259–3262. <https://doi.org/10.1016/j.orgel.2012.10.004>.
- [254] S.H. Eom, S. Senthilarasu, P. Uthirakumar, S.C. Yoon, J. Lim, C. Lee, H.S. Lim, J. Lee, S.-H. Lee, Polymer solar cells based on inkjet-printed PEDOT:PSS layer, *Organic Electronics*. 10 (2009) 536–542. <https://doi.org/10.1016/j.orgel.2009.01.015>.
- [255] Z. Xiong, C. Liu, Optimization of inkjet printed PEDOT:PSS thin films through annealing processes, *Organic Electronics*. 13 (2012) 1532–1540. <https://doi.org/10.1016/j.orgel.2012.05.005>.

- [256] H. Menon, R. Aiswarya, K.P. Surendran, Screen printable MWCNT inks for printed electronics, *RSC Adv.* 7 (2017) 44076–44081. <https://doi.org/10.1039/C7RA06260E>.
- [257] The Price Of Graphene, Graphenea. (n.d.). <https://www.graphenea.com/pages/graphene-price> (accessed August 30, 2020).
- [258] S.R. Das, S. Srinivasan, L.R. Stromberg, Q. He, N. Garland, W.E. Straszheim, P.M. Ajayan, G. Balasubramanian, J.C. Claussen, Superhydrophobic inkjet printed flexible graphene circuits via direct-pulsed laser writing, *Nanoscale.* 9 (2017) 19058–19065. <https://doi.org/10.1039/C7NR06213C>.
- [259] Y. Seekaew, S. Lokavee, D. Phokharatkul, A. Wisitsoraat, T. Kerdcharoen, C. Wongchoosuk, Low-cost and flexible printed graphene–PEDOT:PSS gas sensor for ammonia detection, *Organic Electronics.* 15 (2014) 2971–2981. <https://doi.org/10.1016/j.orgel.2014.08.044>.
- [260] OLED ink jet printing: introduction and market status | OLED-Info, (n.d.). <https://www.oled-info.com/oled-inkjet-printing> (accessed January 26, 2021).
- [261] L. Feng, C. Jiang, H. Ma, X. Guo, A. Nathan, All ink-jet printed low-voltage organic field-effect transistors on flexible substrate, *Organic Electronics.* 38 (2016) 186–192. <https://doi.org/10.1016/j.orgel.2016.08.019>.
- [262] S. Jung, A. Sou, K. Banger, D.-H. Ko, P.C.Y. Chow, C.R. McNeill, H. Sirringhaus, All-Inkjet-Printed, All-Air-Processed Solar Cells, *Advanced Energy Materials.* 4 (2014) 1400432. <https://doi.org/10.1002/aenm.201400432>.
- [263] O. Nowak, Active OLEDs close in on mobile phone market, *MEMS Journal -- The Largest MEMS Publication in the World.* (2006). http://www.memsjournal.com/2006/07/active_oleds_cl.html (accessed July 15, 2018).
- [264] D.K. Owens, R.C. Wendt, Estimation of the surface free energy of polymers, *Journal of Applied Polymer Science.* 13 (1969) 1741–1747. <https://doi.org/https://doi.org/10.1002/app.1969.070130815>.
- [265] Quantifying Enhanced Wettability and Time-dependency of Plasma-treated Polypropylene, *Nanoscience Instruments.* (n.d.). <https://www.nanoscience.com/applications/materials-science/enhanced-wettability-plasma-treated-polypropylene/> (accessed January 30, 2021).
- [266] Cross Hatch Paint Adhesion Test Kit UK CC3000 | UK Dyne Testing, (n.d.). <https://dynetesting.com/cross-hatch-adhesion-testing/cross-hatch-adhesion-test-kit-with-guide-wheel-cc3000-range/> (accessed September 9, 2020).
- [267] ASTM International, Test Methods for Rating Adhesion by Tape Test, ASTM International, n.d. <https://doi.org/10.1520/D3359-17>.
- [268] Test the Resistance of Coating to Separation with Cross Hatch Tester, Prestogroup. (n.d.). <https://www.prestogroup.com/articles/test-the-resistance-of-coating-to-separation-with-cross-hatch-tester> (accessed September 9, 2020).
- [269] C.A. Schneider, W.S. Rasband, K.W. Eliceiri, NIH Image to ImageJ: 25 years of image analysis, *Nat Methods.* 9 (2012) 671–675. <https://doi.org/10.1038/nmeth.2089>.

- [270] L.J. Tinsley, R.A. Harris, A Novel Computer-Controlled Maskless Fabrication Process for Pneumatic Soft Actuators, *Actuators*. 9 (2020) 136. <https://doi.org/10.3390/act9040136>.
- [271] M.H.A. van Dongen, E. Nieuwenhuis, L. Verbraeken, R. verkuijlen, P. Ketelaars, J.P.C. Bernards, Digital printing of μ Plasmas to selectively improve wetting behavior of functional inks for printed electronics, (2012). <https://surfsharekit.nl/publiek/fontys/1f830db4-9a01-4892-b960-c7274bec006b> (accessed August 24, 2020).
- [272] Z. Zhang, X. Zhang, Z. Xin, M. Deng, Y. Wen, Y. Song, Controlled Inkjetting of a Conductive Pattern of Silver Nanoparticles Based on the Coffee-Ring Effect, *Advanced Materials*. 25 (2013) 6714–6718. <https://doi.org/https://doi.org/10.1002/adma.201303278>.
- [273] J. Stringer, B. Derby, Formation and Stability of Lines Produced by Inkjet Printing, *Langmuir*. 26 (2010) 10365–10372. <https://doi.org/10.1021/la101296e>.
- [274] Solar, Ceramic & Glass, PV Nano Cell. (n.d.). <https://www.pvnanocell.com/solar-ceramic--glass.html> (accessed December 29, 2021).
- [275] N. Chen, A. Chowdury, E. Ahmad, V. Unsur and A. Ebong, Assessing the impact of multi-busbars on metallization cost and efficiency of solar cells with digital inkjet-printed gridlines | IEEE Conference Publication | IEEE Xplore, in: 2013: pp. 60–65. <https://doi.org/doi:10.1109/HONET.2013.6729758>.
- [276] J.S. Ten, M. Sparkes, W. O'Neill, Femtosecond laser-induced chemical vapor deposition of tungsten quasi-periodic structures on silicon substrates, *Journal of Laser Applications*. 30 (2018) 032606. <https://doi.org/10.2351/1.5040637>.
- [277] M.L. Levene, R.D. Scott, B.W. Siryj, Material Transfer Recording, *Appl. Opt.*, AO. 9 (1970) 2260–2265. <https://doi.org/10.1364/AO.9.002260>.
- [278] E. Breckenfeld, H. Kim, R.C.Y. Auyeung, A. Piqué, Laser-induced Forward Transfer of Ag Nanopaste, *J Vis Exp*. (2016) e53728. <https://doi.org/10.3791/53728>.
- [279] D.P. Banks, C. Grivas, J.D. Mills, R.W. Eason, I. Zergioti, Nanodroplets deposited in microarrays by femtosecond Ti:sapphire laser-induced forward transfer, *Appl. Phys. Lett.* 89 (2006) 193107. <https://doi.org/10.1063/1.2386921>.
- [280] G. Dhami, B. Tan, K. Venketakrishnan, Laser induced reverse transfer of gold thin film using femtosecond laser, *Optics and Lasers in Engineering*. 49 (2011) 866–869. <https://doi.org/10.1016/j.optlaseng.2011.02.019>.
- [281] C. Duty, D. Jean, W.J. Lackey, Laser chemical vapour deposition: materials, modelling, and process control, *International Materials Reviews*. 46 (2001) 271–287. <https://doi.org/10.1179/095066001771048727>.
- [282] J. Karpman, M.N. Libenson, E.M. Minaeva, Laser-induced transfer of precoated films, in: *Laser Radiation Photophysics*, International Society for Optics and Photonics, 1993: pp. 2–10. <https://doi.org/10.1117/12.147608>.
- [283] V.P. Veiko, E.A. Shakhno, Ablation and condensation of material during the local laser transfer of films, *J. Opt. Technol.* 67 (2000) 389. <https://doi.org/10.1364/JOT.67.000389>.

- [284] J. Mazumder, Laser-aided direct metal deposition of metals and alloys, in: M. Brandt (Ed.), *Laser Additive Manufacturing*, Woodhead Publishing, 2017: pp. 21–53.
<https://doi.org/10.1016/B978-0-08-100433-3.00001-4>.
- [285] A. Mazzi, A. Miotello, Simulation of phase explosion in the nanosecond laser ablation of aluminum, *Journal of Colloid and Interface Science*. 489 (2017) 126–130.
<https://doi.org/10.1016/j.jcis.2016.08.016>.
- [286] S. Mahmood, R.S. Rawat, Y. Wang, S. Lee, M. Zakaullah, T.L. Tan, S.V. Springham, P. Lee, Effects of laser energy fluence on the onset and growth of the Rayleigh–Taylor instabilities and its influence on the topography of the Fe thin film grown in pulsed laser deposition facility, *Physics of Plasmas*. 19 (2012) 103504.
<https://doi.org/10.1063/1.4763555>.
- [287] I. Zergioti, D.G. Papazoglou, A. Karaiskou, C. Fotakis, E. Gamaly, A. Rode, A comparative schlieren imaging study between ns and sub-ps laser forward transfer of Cr, *Applied Surface Science*. 208–209 (2003) 177–180. [https://doi.org/10.1016/S0169-4332\(02\)01363-6](https://doi.org/10.1016/S0169-4332(02)01363-6).
- [288] T. Kerdja, S. Abdelli, D. Ghobrini, S. Malek, Dynamics of laser-produced carbon plasma in an inert atmosphere, *Journal of Applied Physics*. 80 (1996) 5365–5371.
<https://doi.org/10.1063/1.363477>.
- [289] F. Claeysens, Fundamental studies of pulsed laser ablation, (2001).
http://inis.iaea.org/Search/search.aspx?orig_q=RN:33042040 (accessed August 17, 2020).
- [290] F. Kokai, K. Takahashi, K. Shimizu, M. Yudasaka, S. Iijima, Shadowgraphic and emission imaging spectroscopic studies of the laser ablation of graphite in an Ar gas atmosphere, *Appl Phys A*. 69 (1999) S223–S227. <https://doi.org/10.1007/s003399900216>.
- [291] R. Fardel, M. Nagel, F. Nüesch, T. Lippert, A. Wokaun, Laser-Induced Forward Transfer of Organic LED Building Blocks Studied by Time-Resolved Shadowgraphy, *J. Phys. Chem. C*. 114 (2010) 5617–5636. <https://doi.org/10.1021/jp907387q>.
- [292] T. Donnelly, J.G. Lunney, Confined laser ablation for single-shot nanoparticle deposition of silver, *Applied Surface Science*. 282 (2013) 133–137.
<https://doi.org/10.1016/j.apsusc.2013.05.083>.
- [293] S. Xu, B. Liu, C. Pan, L. Ren, B. Tang, Q. Hu, L. Jiang, Ultrafast fabrication of micro-channels and graphite patterns on glass by nanosecond laser-induced plasma-assisted ablation (LIPAA) for electrofluidic devices, *Journal of Materials Processing Technology*. 247 (2017) 204–213. <https://doi.org/10.1016/j.jmatprotec.2017.04.028>.
- [294] Y. Hanada, K. Sugioka, I. Miyamoto, K. Midorikawa, Double-pulse irradiation by laser-induced plasma-assisted ablation (LIPAA) and mechanisms study, *Applied Surface Science*. 248 (2005) 276–280. <https://doi.org/10.1016/j.apsusc.2005.03.050>.
- [295] J. Zhang, K. Sugioka, K. Midorikawa, High-speed machining of glass materials by laser-induced plasma-assisted ablation using a 532-nm laser, *Appl Phys A*. 67 (1998) 499–501.
<https://doi.org/10.1007/s003390050810>.

- [296] X. Lu, F. Jiang, T. Lei, R. Zhou, C. Zhang, G. Zheng, Q. Wen, Z. Chen, Laser-Induced-Plasma-Assisted Ablation and Metallization on C-Plane Single Crystal Sapphire (c-Al₂O₃), *Micromachines*. 8 (2017) 300. <https://doi.org/10.3390/mi8100300>.
- [297] N. Mir-Hosseini, M.J.J. Schmidt, L. Li, Growth of patterned thin metal oxide films on glass substrates from metallic bulk sources using a Q-switched YAG laser, *Applied Surface Science*. 248 (2005) 204–208. <https://doi.org/10.1016/j.apsusc.2005.03.113>.
- [298] C.-F. Ding, L. Li, H.-T. Young, Laser-induced backward transfer of conducting aluminum doped zinc oxide to glass for single-step rapid patterning, *Journal of Materials Processing Technology*. 275 (2020) 116357. <https://doi.org/10.1016/j.jmatprotec.2019.116357>.
- [299] A.I. Kuznetsov, A.B. Evlyukhin, C. Reinhardt, A. Seidel, R. Kiyan, W. Cheng, A. Ovsianikov, B.N. Chichkov, Laser-induced transfer of metallic nanodroplets for plasmonics and metamaterial applications, *J. Opt. Soc. Am. B, JOSAB*. 26 (2009) B130–B138. <https://doi.org/10.1364/JOSAB.26.00B130>.
- [300] M.T. Flores-Arias, A. Castelo, C. Gomez-Reino, G.F. de la Fuente, Phase diffractive optical gratings on glass substrates by laser ablation, *Optics Communications*. 282 (2009) 1175–1178. <https://doi.org/10.1016/j.optcom.2008.11.067>.
- [301] R. McCann, C. Hughes, K. Bagga, A. Stalcup, M. Vázquez, D. Brabazon, Pulsed laser deposition of plasmonic nanostructured gold on flexible transparent polymers at atmospheric pressure, *J. Phys. D: Appl. Phys.* 50 (2017) 245303. <https://doi.org/10.1088/1361-6463/aa7193>.
- [302] Y. Hanada, K. Sugioka, I. Miyamoto, K. Midorikawa, Colour marking of transparent materials by laser-induced plasma-assisted ablation (LIPAA), *Journal of Physics: Conference Series*. 59 (2007) 687–690. <https://doi.org/10.1088/1742-6596/59/1/145>.
- [303] V.P. Veiko, E.A. Shakhno, V.N. Smirnov, A.M. Miaskovski, G.D. Nikishin, Laser-induced film deposition by LIFT: Physical mechanisms and applications, *Laser and Particle Beams*. 24 (2006) 203–209. <https://doi.org/10.1017/S0263034606060289>.
- [304] M. Duocastella, J.M. Fernández-Pradas, J.L. Morenza, D. Zafra, P. Serra, Novel laser printing technique for miniaturized biosensors preparation, *Sensors and Actuators B: Chemical*. 145 (2010) 596–600. <https://doi.org/10.1016/j.snb.2009.11.055>.
- [305] J. Zhang, B. Hartmann, J. Siegel, G. Marchi, H. Clausen-Schaumann, S. Sudhop, H.P. Huber, Sacrificial-layer free transfer of mammalian cells using near infrared femtosecond laser pulses, *PLOS ONE*. 13 (2018) e0195479. <https://doi.org/10.1371/journal.pone.0195479>.
- [306] R. Ye, D.K. James, J.M. Tour, Laser-Induced Graphene, *Accounts of Chemical Research*. (2018). <https://doi.org/10.1021/acs.accounts.8b00084>.
- [307] T.F. Kuo, C.C. Chi, I.N. Lin, Synthesis of Carbon Nanotubes by Laser Ablation of Graphites at Room Temperature, *Jpn. J. Appl. Phys.* 40 (2001) 7147. <https://doi.org/10.1143/JJAP.40.7147>.
- [308] K. Pangovski, M. Sparkes, W. O'Neill, A holographic method for optimisation of laser-based production processes, *Advanced Optical Technologies*. 5 (2016) 177–186. <https://doi.org/10.1515/aot-2015-0057>.
- [309] G. Pretzier, A New Method for Numerical Abel-Inversion, *Zeitschrift Für Naturforschung A*. 46 (2014) 639–641. <https://doi.org/10.1515/zna-1991-0715>.

- [310] M.D. Abràmoff, P.J. Magalhães, S.J. Ram, Image processing with imageJ, *Biophotonics International*. 11 (2004) 36–41.
- [311] D.B. Geohegan, Fast intensified-CCD photography of YBa₂Cu₃O_{7-x} laser ablation in vacuum and ambient oxygen, *Appl. Phys. Lett.* 60 (1992) 2732–2734. <https://doi.org/10.1063/1.106859>.
- [312] Y. Hirayama, M. Obara, Heat-affected zone and ablation rate of copper ablated with femtosecond laser, *Journal of Applied Physics*. 97 (2005) 064903. <https://doi.org/10.1063/1.1852692>.
- [313] Y. Hanada, K. Sugioka, K. Obata, S.V. Garnov, I. Miyamoto, K. Midorikawa, Transient electron excitation in laser-induced plasma-assisted ablation of transparent materials, *Journal of Applied Physics*. 99 (2006) 043301. <https://doi.org/10.1063/1.2171769>.
- [314] D.R. Tallant, T.A. Friedmann, N.A. Missert, M.P. Siegal, J.P. Sullivan, Raman Spectroscopy of Amorphous Carbon, *MRS Online Proceedings Library Archive*. 498 (1997). <https://doi.org/10.1557/PROC-498-37>.
- [315] T. Ohkubo, M. Kuwata, B. Luk'yanchuk, T. Yabe, Numerical analysis of nanocluster formation within ns-laser ablation plume, *Appl Phys A*. 77 (2003) 271–275. <https://doi.org/10.1007/s00339-003-2135-3>.
- [316] Silver In Electronics, The Silver Institute. (n.d.). <https://www.silverinstitute.org/silver-in-electronics/> (accessed August 17, 2020).
- [317] Table of Resistivity, (n.d.). <http://hyperphysics.phy-astr.gsu.edu/hbase/Tables/rstiv.html> (accessed August 28, 2018).
- [318] Edward D. Palik, *Handbook of Optical Constants of Solids*, Academic Press, 1985.
- [319] M. Hasanuzzaman, A. Rafferty, M. Sajjia, A.-G. Olabi, Properties of Glass Materials, in: *Reference Module in Materials Science and Materials Engineering*, Elsevier, 2016. <https://doi.org/10.1016/B978-0-12-803581-8.03998-9>.
- [320] V. Figueiredo, E. Elangovan, G. Gonçalves, P. Barquinha, L. Pereira, N. Franco, E. Alves, R. Martins, E. Fortunato, Effect of post-annealing on the properties of copper oxide thin films obtained from the oxidation of evaporated metallic copper, *Applied Surface Science*. 254 (2008) 3949–3954. <https://doi.org/10.1016/j.apsusc.2007.12.019>.
- [321] D. Bergström, J. Powell, A.F. h. Kaplan, The absorption of light by rough metal surfaces—A three-dimensional ray-tracing analysis, *Journal of Applied Physics*. 103 (2008) 103515. <https://doi.org/10.1063/1.2930808>.
- [322] Arduino Playground - CapacitiveSensor, (n.d.). <https://playground.arduino.cc/Main/CapacitiveSensor/> (accessed August 17, 2020).
- [323] A. Watanabe, J. Cai, Laser direct writing of reduced graphene oxide micropatterns and sensor applications, in: *Laser-Based Micro- and Nanoprocessing XII*, International Society for Optics and Photonics, 2018: p. 105200P. <https://doi.org/10.1117/12.2288355>.
- [324] D. Wu, Q. Peng, S. Wu, G. Wang, L. Deng, H. Tai, L. Wang, Y. Yang, L. Dong, Y. Zhao, J. Zhao, D. Sun, L. Lin, A Simple Graphene NH₃ Gas Sensor via Laser Direct Writing, *Sensors*. 18 (2018) 4405. <https://doi.org/10.3390/s18124405>.

- [325] T. Dinh, H.-P. Phan, D.V. Dao, P. Woodfield, A. Qamar, N.-T. Nguyen, Graphite on paper as material for sensitive thermoresistive sensors, *J. Mater. Chem. C*. 3 (2015) 8776–8779. <https://doi.org/10.1039/C5TC01650A>.
- [326] T. Dinh, H.-P. Phan, A. Qamar, P. Woodfield, N.-T. Nguyen, D.V. Dao, Thermoresistive Effect for Advanced Thermal Sensors: Fundamentals, Design Considerations, and Applications, *Journal of Microelectromechanical Systems*. 26 (2017) 966–986. <https://doi.org/10.1109/JMEMS.2017.2710354>.
- [327] D.W. Müller, T. Fox, P.G. Grützmacher, S. Suarez, F. Mücklich, Applying Ultrashort Pulsed Direct Laser Interference Patterning for Functional Surfaces, *Scientific Reports*. 10 (2020) 3647. <https://doi.org/10.1038/s41598-020-60592-4>.
- [328] J. Lauri, E. Hannila, T. Fabritius, Non-Destructive Characterization of Glass Laminated Electronics, in: 2019 IEEE International Instrumentation and Measurement Technology Conference (I2MTC), 2019: pp. 1–5. <https://doi.org/10.1109/I2MTC.2019.8827057>.
- [329] M.-C. Choi, Y. Kim, C.-S. Ha, Polymers for flexible displays: From material selection to device applications, *Progress in Polymer Science*. 33 (2008) 581–630. <https://doi.org/10.1016/j.progpolymsci.2007.11.004>.
- [330] S.K. Parupelli, S. Desai, Hybrid additive manufacturing (3D printing) and characterization of functionally gradient materials via in situ laser curing, *Int J Adv Manuf Technol*. 110 (2020) 543–556. <https://doi.org/10.1007/s00170-020-05884-9>.
- [331] D. Munoz-Martin, C.F. Brasz, Y. Chen, M. Morales, C.B. Arnold, C. Molpeceres, Laser-induced forward transfer of high-viscosity silver pastes, *Applied Surface Science*. 366 (2016) 389–396. <https://doi.org/10.1016/j.apsusc.2016.01.029>.
- [332] O.A. Ranjbar, Z. Lin, A.N. Volkov, Plume accumulation effect and interaction of plumes induced by irradiation of a copper target with a burst of nanosecond laser pulses near the ionization threshold, *Journal of Applied Physics*. 127 (2020) 223105. <https://doi.org/10.1063/5.0007786>.

APPENDIX A

A1 - LIPSS Hatch Spacing

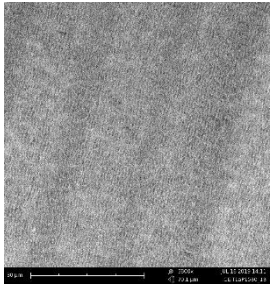
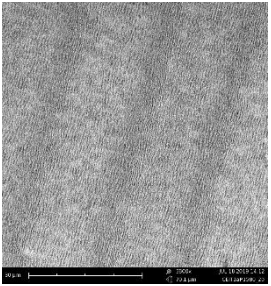
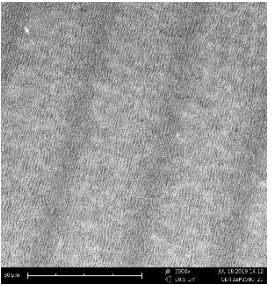

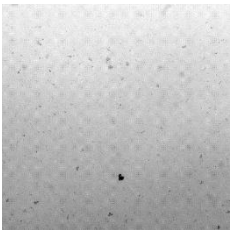
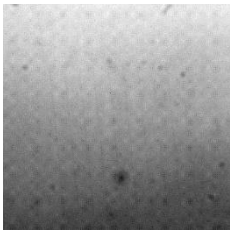
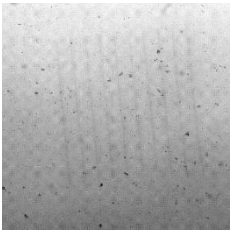
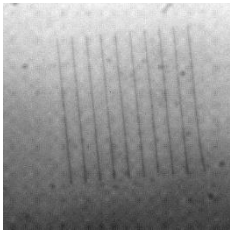
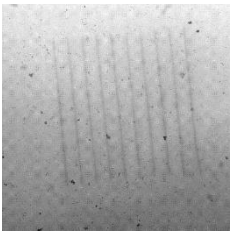
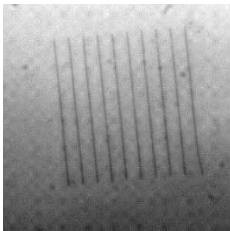
			
18 μm	19 μm	20 μm	21 μm

Figure A1: Comparison of LIPSS surface textures with varied hatch spacing

A2 - In-volume Modification

All tracks patterned with 10 mm/s scanning speed and 8 μm spot size

Microscope Focus	Top Surface	Track
0.39		
0.81		
1.23		

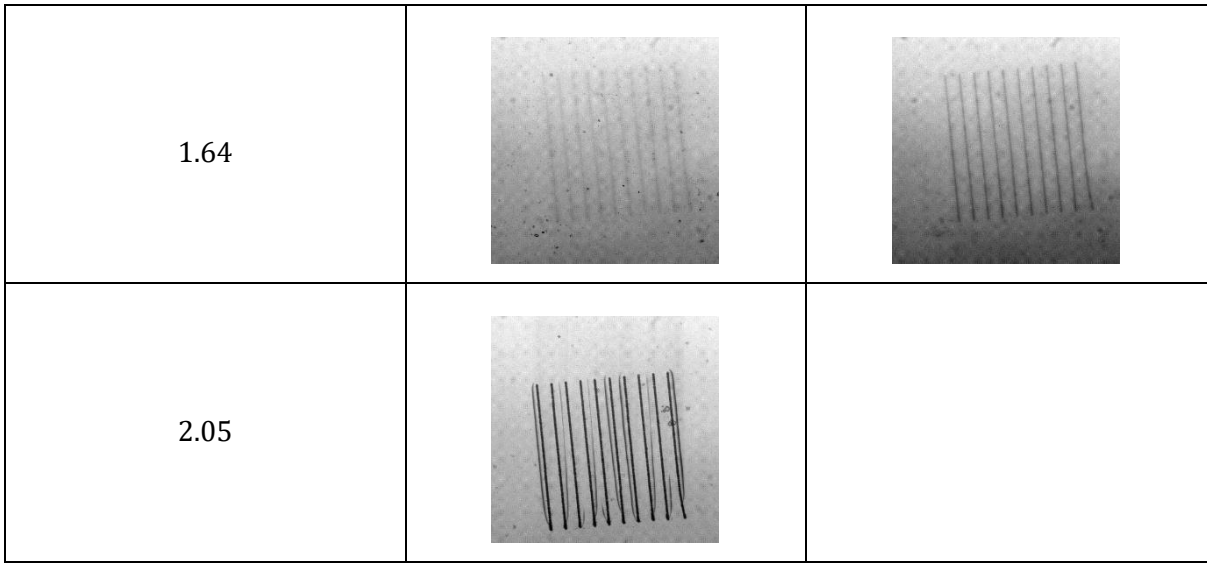


Figure A2: Formation of in-volume tracks when using laser fluence below surface damage threshold

APPENDIX B

B1 - Heat Treatment

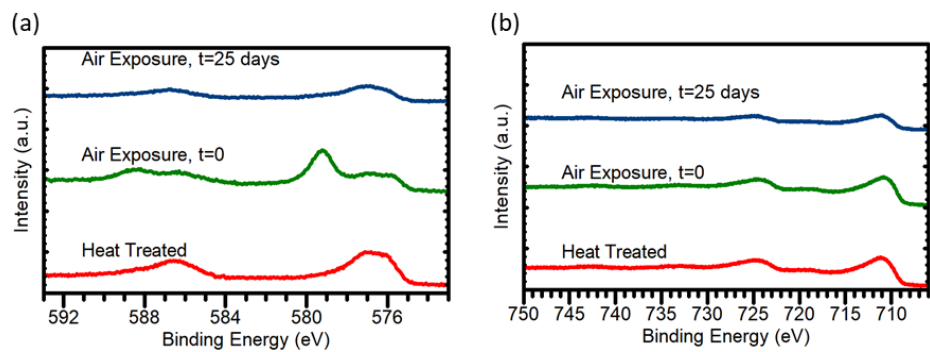


Figure B1: XPS spectra of (a) Fe & (b) Cr regions

B2 - Terminal Group Variance

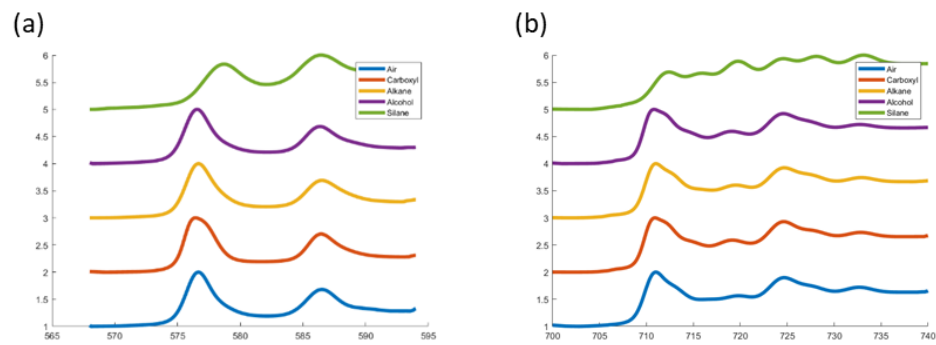


Figure B2: Normalized XPS spectra of (a) Fe & (b) Cr regions with terminal group variation.

B3 - Chain Length Variance

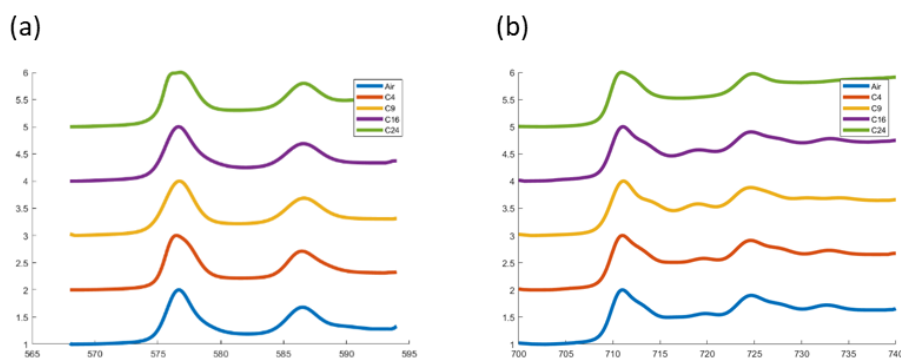


Figure B3: Normalized XPS spectra of (a) Fe & (b) Cr regions with Chain Length variance

B4 - Deposition of 1-Octanoic acid

The experiment used in section (4.5.2.2) concerning variation of hydrocarbon terminal group was repeated using 1-Octanoic acid (method detailed in section 4.4). As seen below a superhydrophobic contact of 164.8 ± 3.0 was measured. The roll off angle was measured as 6.2° .

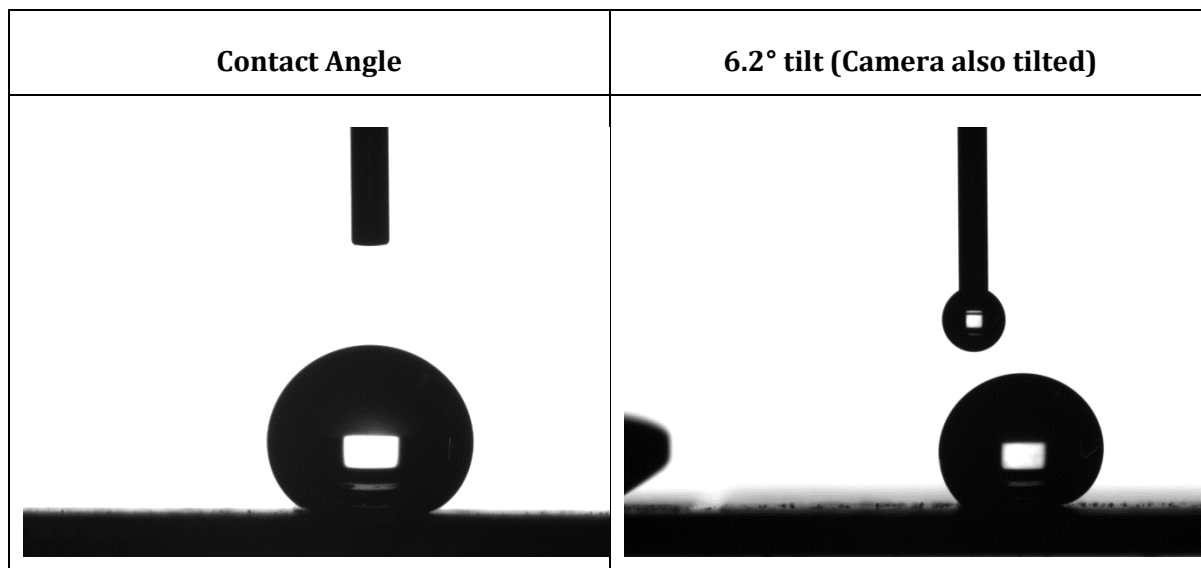


Figure B4: Contact angle and roll off angle using 1-Octanoic acid